Photophysical and Theoretical Studies of Aza-heterocycles: Mechanistic Pathways to Excited State Proton Transfer Phenomenon

A dissertation as partial fulfilment for the degree of

Doctor of Philosophy in Chemistry

by

Gulshan Kumar

(Roll No. 901409007)

Under the Supervision

of

Dr Vijay Luxami

Associate Professor

School of Chemistry & Biochemistry

Thapar Institute of Engineering & Technology,

Patiala-147004

November 2020

Certificate

It is certified that the work contained in the thesis entitled "**Photophysical and Theoretical Studies of Aza-heterocycles: Mechanistic Pathways to Excited State Proton Transfer Phenomenon**" by Gulshan Kumar in fulfilment of the degree of Doctor of Philosophy, is an authentic record of candidate's own independent and original research work carried out under my supervision in the School of Chemistry and Biochemistry, Thapar Institute of Engineering and Technology, Patiala, Punjab-India. The material embodied in this thesis has not been submitted in part or full to any other University or Institute for the award of any degree.

Vijay Luxami 20/11/2020

Vijay Luxami

(Supervisor)

Associate Professor

School of Chemistry and Biochemistry,

Thapar Institute of Engineering and Technology,

Patiala – 147004, Punjab (India)

20/11/2020

Dr Amjad Ali

(Head of SCBC)

Associate Professor

School of Chemistry and Biochemistry,

Thapar Institute of Engineering and Technology,

Patiala – 147004, Punjab (India)

Candidate's Declaration

I, hereby declared that the presented work in the thesis entitled "**Photophysical and Theoretical Studies of Aza-heterocycles: Mechanistic Pathways to Excited State Proton Transfer Phenomenon**" in fulfilment of degree of Doctor of Philosophy is outcome of research work carried out by me under the supervision of Dr Vijay Luxami, Associate Professor, School of Chemistry and Biochemistry, Thapar Institute of Engineering & Technology, Patiala, Punjab (India). In keeping with general practice of reporting scientific observations, due acknowledgements have been made whenever work described here has been based on findings of other investigator. This work has not been submitted in part or full to any other University or Institute for the award of any degree.

Gulshan Kumar

Gulshan Kumar

Reg. No. 901409007

School of Chemistry and Biochemistry,

Thapar Institute of Engineering and Technology,

Patiala – 147004, Punjab (India)

Vijay Luxami 20/11/2020

Vijay Luxami

(Supervisor)

Associate Professor

School of Chemistry and Biochemistry,

Thapar Institute of Engineering and Technology,

Patiala – 147004, Punjab (India)

I may halt for a while to place on record my gratefulness to all those who have made a contribution towards the successful completion of this thesis. Above all, I express my gratitude to the family members for their blessings and support. I am acknowledging the gratitude towards my respected supervisor Dr Vijay Luxami, Associate professor, School of Chemistry and Biochemistry (SCBC), Thapar Institute of Engineering & Technology, Patiala (Punjab, India) for the opportunity to work in her group. Her inspiring guidance, intellectual support encouragement and motivation for working on new research problems is what made this work possible. She also established successful collaborations, which gave me the opportunity to gain knowledge in a wide range of research problems. I thank her for help in writing of this dissertation, other research articles and improving me at scientific communication and style.

I express my gratitude to Director, Thapar Institute of Engineering & Technology, Patiala, Dr. Rafat Siddique, Dean of Research and Sponsored Projects (RSP), Prof. O. P. Pandey former Dean RSP, Dr Amjad Ali (Head of SCBC), Prof. Bonamali Pal (Former Head of SCBC) for all facilities which have been immensely helpful in completing my work.

I am also thankful to all my respected teachers of the School of Chemistry and Biochemistry (SCBC) and my doctoral committee members Prof. Haripada Bhunia, Dr Manmohan Chhibber, Dr Bhupesh Goyal, Dr Satyendra Pandey, Dr Rajesh Kumar for their valuable suggestion and motivation at each and every step during my whole thesis work.

During my PhD studies, I had the opportunity to work in close collaborations with other research groups. I would like to express my sincere thank to Dr Kamaldeep Paul for initial days of collaboration and inspiring me to rotameric isomeric chemistry. I learned a great deal about a conformational analysis problem. I thank his group members, especially Dr Richa Goel, for their support and discussion.

I would also like to thank Dr Akul Sen Gupta, Dr Alka Sharma, Dr Meenakshi Verma, Dr Prinka Singla, and Dr Richa Rani for scientific and non-scientific help during the PhD studies. Time flew by in the company of good friends and therefore, a special thanks to Iqubal Singh, Rayees Ahmad Rather, Richa Bansal, Ruhi Mehta, Sudesh Rani, Dinesh Singla, and Aastha Palta. I would also like to extend the expression of thanks to other colleagues Nehal Gupta, Manveer Kaur, Charu Goyal, Prince Benipal, Aanchal Sharma, Rekha Thakur, Swati Rana, Rohini, Geetika, Saurabh Gupta, Nandan Sarkar for creating a great work

atmosphere and help at different stages during my course study. I extend my gratitude to other research scholars of Santosh Kumar Rath, Anirudh Sharma, Amanpreet Kaur, Aadil Bathla, Ashok Kumar, Sanjeev and others who are not mentioned by name for their support and encouragement. I express my warm thanks to my colleagues and friends with whom I spent and enjoyed scientific and social activities. I now have a forever collection of stories and a lot of everlasting memories to tell.

Another round of thanks for friends away from here; Dr Sunil Kumar, Dr Manoj Kumar, Gaurav, Lalit Singh Somavanshi, Rajdeep Jaswal, Varun Suryavanshi, Nishant Sharma, Renu Sharma, Aarti Sharma, Meenakshi Sharma, Priyanka Sharma, Vinod Kumar, Pankaj Kumar, Parmanand Sharma, Rakesh Kumar, Raj Bhardwaj, Hare Ram Yadav Gurpreet Kaur, and Sukhwinder Dhiman for a laugh whenever possible.

I am also thankful to Prof. Subodh Kumar, Department of Chemistry, Guru Nanak Dev University, Amritsar- Punjab (India) for introducing new dimension of research challenges and scientific discussion.

I acknowledge the help of Mr Mayank Sharma, office staff and Chander Singh Thakur, Chandar Shekhar, Hemant Sharma, and Vishwanath Dass, technical staff of School of Chemistry and Biochemistry for their support in various aspects.

I extend my thankful acknowledgement to SAI Labs, Thapar Institute of Engineering & Technology, Patiala; SAIF Lab, Panjab University, Chandigarh; CIL, IIT Ropar; Sprint Testing solution, Mumbai for providing experimental instrumentation. I extend my gratitude to Mr Mukesh Aggarwal, SAI Labs, Thapar Institute of Engineering & Technology, Patiala for their cooperation during NMR/CHN data collection.

I thankfully acknowledge Thapar Institute of Engineering & Technology, Patiala for providing me teaching assistantship during my course. I am also thankful to DST-SERB, New Delhi (EMR/2016/002464) for financial assistant.

Finally, none of this would have been possible without the constant love, support, guidance and patience of all my family members. I owe my gratitude to my respected Father-Mother and Uncle-Aunty, whose blessings, belief and encouragement have shown me the path to pursue goals in my life. I thank my sisters and brothers for everything they have done for me. They all have been amazing and always been there for me. I cannot thank them enough. Thank you for your everlasting love and support. **This is for you!**

I want to dedicate this thesis to my younger brother Rutash Kumar, who left us during his doctoral study in Bioinformatics. Your skills at computational biology & chemistry along with potential discussion always enriched me with scientific information and thus, assisted me to get solution of different research problems. Your belief in me and other chit-chat deepen me with positivity and thus, made this journey possible.

Gulshan Kumar

1 Table of Contents

Abbreviation

ACQ	Aggregation-caused quenching
AIE	Aggregation-induced emission
CHEF	Chelation-enhanced fluorescence
Cys	Cysteine
DFT	Density Functional Theory
DLS	Dynamic light scattering
DMSO	Diethyl sulphoxide
ESICT	Excited state intramolecular charge transfer
ESIPT	Excited state intramolecular proton transfer
FESEM	Field-emission scanning electron microscope
HOMO	Highest occupied molecular orbital
HB	Hydrogen bonding
FESEM	Field emission scanning electron microscopy
ct-DNA	Calf thymus-Deoxyribonucleic acid
HEPES	(4-hydroxyethyl)-1-piprazineethanesulfonic acid
ICT	Intramolecular charge transfer
IraHB	Intramolecular hydrogen bonding
IraPT	Intramolecular proton transfer
IEFPCM	Integral equation of formalism polarized continuum model
LEDs	Light emitting diodes
LOD	Limit of detection
LUMO	Lowest unoccupied molecular orbital
MeOH	Methanol
MLCT	Metal to ligand charge transfer

LMCT	Ligand to metal charge transfer
m.pt.	Melting point
OLEDs	Organic light emitting diodes
PET	Photo-induced electron transfer
PT	Proton transfer
PPI	Pyrophosphate
TBAX	Tetrabutyl ammonium halide
TICT	Twist intramolecular charge transfer
ESTICT	Excited state twisted intramolecular charge transfer
TDDFT	Time-dependant density functional theory
TLC	Thin-layer chromatography

Symbols

K	Binding constant
H	HOMO (Highest occupied molecular orbital)
L	LUMO (Lowest unoccupied molecular orbital)
ϕ	Quantum yield
μM	Micromolar
nM	Nanomolar
λ_{ex}	Absorption peak
λ_{em}	Emission peak
λ_{calc}	Calculated absorption peak

Chapter 1

Introduction and review of literature

Proton transfer is a very fundamental process, occurs in a large variety of chemical reactions as well as in biological systems such as acid-base neutralization and enzymatic reactions, DNA etc.[1-5] There are varieties of proton transfer reactions which could occur in the ground or excited-states, either adiabatically or non-adiabatically. However, excited state proton transfer (ESPT) have more application in many branches of sciences such as photophysics, photochemistry, and photobiology. Also, an increasing number of proton transfer based chromophores have application in fluorescent probes, laser dyes, organic optoelectronic materials, and white light-emitting materials.[6-10] Due to its significant application potential in various aspects of sciences, proton transfer phenomenon was studied extensively.[11, 12]

The prerequisite condition for ESPT was the existence of hydrogen bonding (D−H···A; where D−H defined as hydrogen donor and A defined as hydrogen acceptor units). The hydrogen bonding categorized into two types based on the interactions existing in molecular architecture: Intermolecular hydrogen-bonded (IerHB**)** molecular architecture and intramolecular hydrogen-bonded (IraHB**)** molecular architecture. The IerHB could be defined as interaction in two different molecular systems (Z–H···X ↔ Z-····H–X+), whereas in IraHB could exist within the same molecular system.

The hydrogen bonding has relative weak nature, and therefore, with the application of some external stimuli such as electric field, magnetic field, and an electromagnetic field, it could be formed/broken easily. The electromagnetic field induced the electronic redistribution of charges in the hydrogen-bonded molecular system, and thus, the molecular architecture became more polar and therefore, charge transfer can occur in the form of a proton within the molecular system or with the surrounding environment. This process is recognized as proton transfer (PT) whereas proton gets transferred directly from the acidic site to the basic site of a molecular system. The site which allowed the proton transfer called as the proton donor site, while the receiving site called as a proton acceptor site. Therefore, hydrogen bonding is a significant intermediate in the proton transfer reaction. Based on the hydrogen bonding interaction within the molecular systems, the ESPT phenomenon categorized into two types: Excited state intramolecular

Proton Transfer (ESIPT) and excited state intermolecular Proton Transfer (ESIerPT). Among these two processes, the ESIPT is one studied experimentally and theoretically due to its applications in molecular chemosensors, fluorescence probes, luminescent materials, UV stabilizers, OLEDs and molecular logic gates.[9, 13-22]

In general, the ESIPT process requires hydrogen bond between proton donor (–OH, –NH_2, or –NHR, etc.) and proton acceptor groups (–C=O, –N=, etc.), which must be at an interacting distance to each other in a molecule. During the ESIPT process, the proton attached covalently to the donor groups in the electronic ground state got transferred to acceptor groups in the excited state. In the electronic ground state, ESIPT molecules exist in the standard enol form (E), and it is stabilized by intramolecular hydrogen bonding. Upon photoexcitation, the singlet-excited state of the enol form is populated without geometry relaxation, according to the Franck–Codon principle. Further, geometry relaxation resulting in tautomeric conversion to keto form (K), which is further stabilized by the hydrogen bond. The photoinduced excitation is accompanied by the redistribution of electronic charge, causing an increase in the acidity of the proton donor and the basicity of the proton acceptor. These electronic changes result in the proton transfer from the proton donor to the proton acceptor, leading to a tautomeric transformation from the excited enol form (^{1}E*) to the excited keto form (^{1}K*) (Figure 1.1). The geometry of excited keto tautomer (K*) is utterly different from the excited enol (E*) form and therefore, leading to broad Stokes shifted emission. The large Stokes' shift provided the spectrum window to investigate different processes in a particular range such as sensing or cell imaging etc. During ESIPT, single or dual emissions may be observed, due to the existence of isomeric forms in solution state and energy barrier of ESIPT process. The ESPT process can be influenced by IraHB strength, pH, solvent, and interaction with other molecules and therefore, determining the energy barrier for the ESIPT process under different environments is critical. This goal could be accomplished with theoretical calculation directly.[7-12, 23-29] Generally, the band appears at lower wavelength ascribed due to enolic form while one appears at higher wavelength assigned to be due to tautomeric keto form produced after hydrogen bond. ESIPT process also depends upon the distance of hydrogen bonding, i.e. separation between the hydrogen acceptor and donor atoms in molecules, the strength of IraHB, and acidity of hydrogen. The phenomenon can be understood with the following example

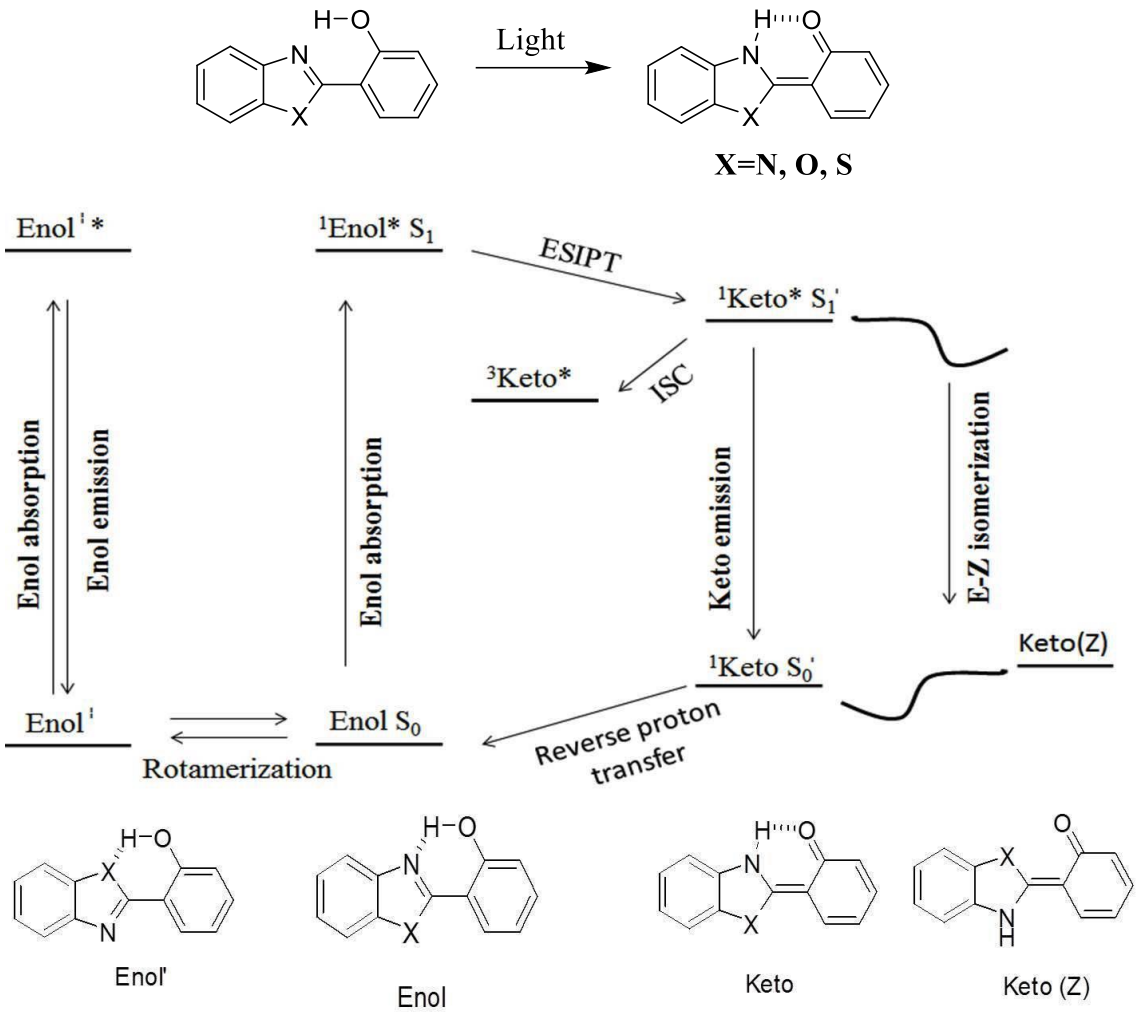

Figure 1.1 Photophysical process of ESIPT labeled with different conformation generated during the process

The relocation of charges on interaction with the electromagnetic field does not only drive ESIPT but also favored the weak interactions such as dipole-dipole interactions or induced dipolar interactions due to change in polarization in the excited state. These changes sometimes led ESIPT along with charge transfer and electron transfer.

1.1 The factors affecting ESIPT

The ESIPT process is sensitive and depends upon the strength of hydrogen bond, polarity, protic nature of solvents, the heterogeneous medium, and the nature of substituents. These factors perturb the ESIPT phenomenon in several molecular architectures and therefore, discussed below:

1.1.1 Effect of substituent:

The ESIPT process significantly depends upon the acidity of the proton donor unit and basicity of proton acceptor unit. On the modification of molecular architecture, the process of proton transfer can be controlled or/and modified. The substitution of electronegative/electron acceptor unit on the side of proton donor site, will increase the acidity of group and therefore, facilitate the proton transfer process with significant tautomeric emission. However, the substitution of electron-donating unit decreased the acidity of proton donor and thus, further discommode the proton transfer process. In a similar way, the electron-donating substitution on the side of proton acceptor unit increase the basicity and thus ease the proton transfer process, however, substitution of electron-accepting group will decrease the basicity and thus, harden the proton transfer process.

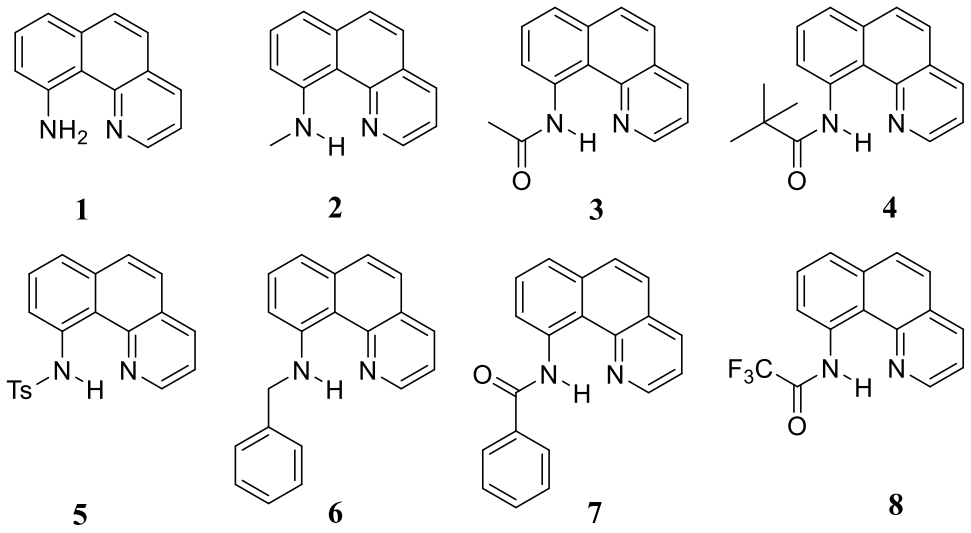

Tseng and co-workers have synthesized the derivatives of 10-aminobenzo[h]quinoline (**1-8**).[30] Different substitution in the form of electron-withdrawing and donating units were introduced to parent compound **1**. The compound **1** exhibited an emission at 770 nm with a Stokes shift of 11500 cm^{-1}, originated from the ESIPT phenomenon. The presence of electron-donating units decreased the acidity of NH proton and thus, shifted the emission spectra towards blue end. On the other hand, the introduction of electron-withdrawing units increased the acidity of NH proton; however, these groups stabilized the HOMO and thus, lead to blue shift.

Mutui and co-workers studied the substitution effect on the ESIPT response of imidazo[1,2-*a*]pyridine (**9-22**).[31] All the derivatives displayed dual emission in solution forms with small quantum yield. However, the emission properties were enhanced in the

polymer matrix. The introduction of electron-donating groups and electron-withdrawing groups at imidazopyridine unit displayed a red and blue shift, respectively in emission bands. However, introduction of electron-donating groups and electron-withdrawing groups at phenyl unit displayed a blue and redshift in emission bands, respectively. Also, the established linearity between calculated energies for frontier molecular orbitals and Hammett substituent constant supported the varied emission response for different derivative.

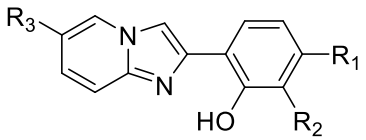

9-22

	R_1	R_2	R_3		R_1	R_2	R_3
9	H	H	H	**16**	H	H	Cl
10	H	OCH_3	H	**17**	H	H	Br
11	H	CH_3	H	**18**	H	H	CF_3
12	H	Cl	H	**19**	H	H	CN
13	H	Br	H	**20**	OCH_3	H	H
14	H	F	H	**21**	H	CH_3	Cl
15	H	H	CH_3	**22**	H	CH_3	CF_3

1.1.2 Effect of solvents:

The driving force for the ESIPT phenomenon is the strength of intramolecular hydrogen bonding (IraHB) at excited state. The strength of intramolecular HB relatively independent of aprotic solvents, and thus, the phenomenon is favorable in aprotic medium. On the other hand, on increasing the polarity of medium, the IraHB strength perturbed and sometimes led to formation of intermolecular hydrogen bonding with the solvent molecules. The gradient of HB strength further act as prime key for the molecular configuration alteration and therefore, affects the keto-enol tautomerism. These changes further hamper the ESIPT significantly and thus, the relative intensity of standard enol and tautomeric emission was also altered with variation in the polarity. Hence, the nonpolar solvents favor the ESIPT process relative to polar and protic solvents. However in some cases, the proton donor and acceptor sites were located long distances, and thus, intramolecular proton transfer is not possible. But, in the presence of protic solvents, the molecule formed the intermolecular hydrogen bonding and thus, mediated the solvent assisted intermolecular proton transfer.[32-34]

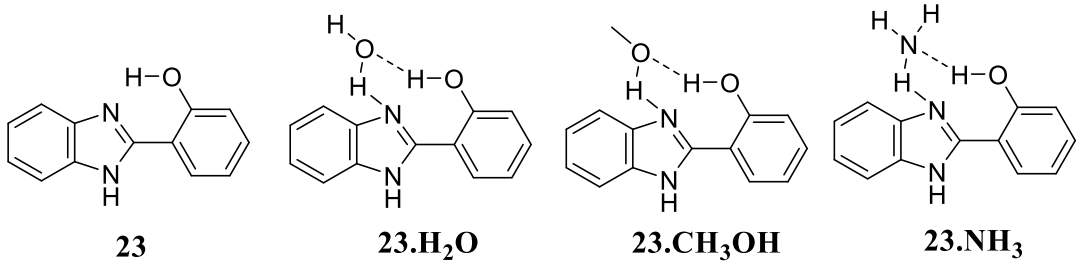

23 **23.H_2O** **23.CH_3OH** **23.NH_3**

The compound **23** displayed ESIPT phenomenon in aprotic solvents, however in the presence of protic polar solvents, the IraHB was distorted, and formation of intermolecular hydrogen bonding was taken place with solvents (**23**.H_2O, **23**.NH_3, and **23**.CH_3OH). These intermolecular hydrogen bonding restrict the intramolecular proton transfer and therefore, the disturb ESIPT process of compound **23.**

1.1.3 Intramolecular Charge Transfer

The molecular architectures containing functional units with a capacity of electron-donating and electron-accepting could push or pull the electron density and led to the origin of the intramolecular charge transfer phenomenon.[35, 36] The presence of such functionality along with the presence of proton donor and accepting moiety, could lead dual phenomenon as ESICT and ESIPT. The ESICT and ESIPT could assist each other, could co-occur or in following manner to each other. The phenomenon could be distinguished by measuring the steady-state absorption and emission spectroscopy in varying environmental polarity.[37-39]

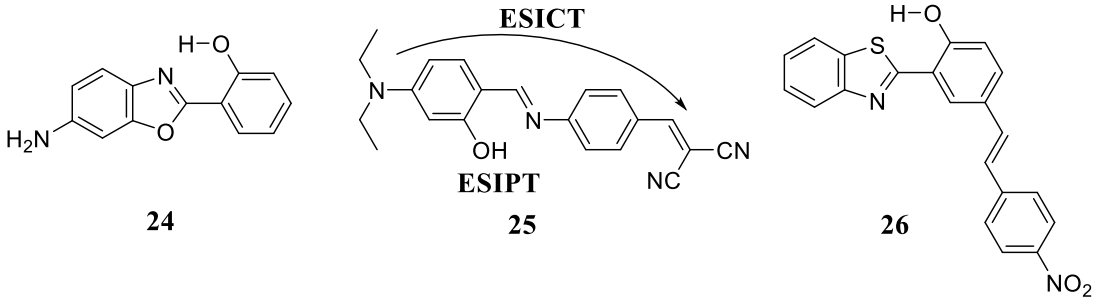

24 **25** **26**

Gutierrez and co-workers studied compound **24**, which exhibited ESICT followed by ESIPT phenomenon. An ultrafast ESICT phenomenon was occurred due to the presence of $–NH_2$ group, and the process occurred in the time domain of 80-140 fs, followed by solvent relaxation. The ESIPT process in solvent relaxation form occurred in the time range of 40-175 ps depending upon the solvent systems. Compound **25** was studied by Lin and co-workers, which displayed strong solvatochromism effect with emission color tuning. The compound **25** was further utilized as ratiometric chemosensor towards CN^-

ions. Further, compound **26** was studied by Niu and co-workers for ESIPT/ESICT phenomenon. The compound **26** exhibited dual emission; however, in the presence of polar solvents, enol solvatochromism was observed. Compound **26** was highly planar and formed H-aggregate in its crystalline state.

Further, these ESIPT/ESICT-coupled systems could occur three ways as ESICT states can be involved prior to, concurrently with, or following ESIPT. In literature, there are some reports of rational design of ESIPT/ESICT-coupled systems. In the current scenario, the reported ESIPT/ESICT-coupled molecular systems can be categorized into two classes. In class I, the proton and charge acceptors are in the same moiety, whereas the charge and proton donors are in the different moiety. On the other hand, in class II, the proton and charge donors are in the same moiety, but the proton and charge acceptors are at different sites.[11, 39-41] Further, the study of environmental effect on the steady-state emission spectra could help to determine the nature of ESICT/ESIPT phenomena. The two limiting cases determined the competitive priority of ESICT or ESIPT. Whenever there is the rise of high energy emission intensity with increasing the polarity of the environment, there must be ESICT/ESIPT process, however, an increase in tautomeric emission with rising of polarity lead ESIPT/ESICT phenomenon.[42-44]

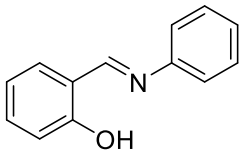

27

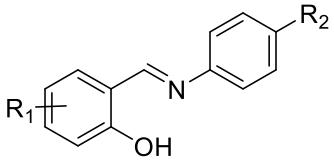

28-30

	R_1	R_2
28	NEt_2	NMe_2
29	NEt_2	F
30	NMe_2	NO_2

Salicylideneaniline based Schiff bases **28-30** were studied extensively and were known to exhibit ESIPT and AIE phenomenon.[45-48] Different functional groups were introduced on parent compound, and resulted compounds also displayed the ESIPT and high emission properties through AIE phenomena. Further, these compounds **28-30** were used as a potential ratiometric fluorescence sensor for pH and Zn^{2+} ions.[49]

Further, the structurally related and double analog of Salicylideneaniline compound **31** contained double IraHBs and exhibited the ESIPT and AIE phenomena.[50, 51]; Compound **31** displayed yellow emission (λ_{em} = 542 nm), which was further tuned by introducing electron-donating and accepting groups at different positions. These functional groups strongly influenced the electronic environment and thus, tuned the ESIPT and AIE emission properties. Ma and co-workers studied the compounds **32-37**, and obtained the

blue, green and red emission colors and further utilized as fluorescence pH probes with range of 2-14. After deprotonation, compounds **33-35**, and **37** displayed ratiometric response however, compound **32** and **36** were non-emissive.[52] Compound **36** was studied elaborately by Jana and co-workers, and their experimental and theoretical observation established that the $–NEt_2$ unit pushed the electron density and thus, promote the charge-coupled proton transfer.[53] Also, compound **36** displayed switchable solid-state emission. Compound **36** exists in two crystalline forms with emission at 550 nm and 529 nm, while its amorphous forms have emission at 529 nm with a shoulder peak at 550 nm.[54] Compound **38** and **39** were studied by Tang and co-workers and established the AIE-characteristics for compounds. The emissions of compound **38** and **39** displayed emission in green (λ_{em} = 513 nm) and red (λ_{em} = 570 nm) regime, respectively.[55]

The emission of compound **39** was quenched on interaction with Cu^{2+} ions. Complex **39**.Cu^{2+} was used as *turn-on* chemosensor for PPi in the aqueous medium. The preferential and strong interaction of PPi towards Cu^{2+} ions displaced the compound **39** and recovered the AIE and ESIPT emission. Also, the complex was demonstrated in serum samples for the detection of PPi. The detection limit towards PPi ions was 64 μM.[56]

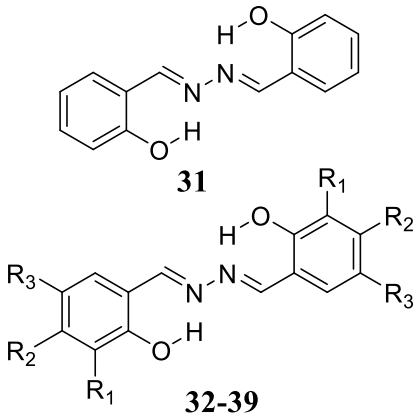

	R_1	R_2	R_3
32	NO_2	H	H
33	F	H	H
34	Cl	H	H
35	OMe	H	H
36	H	NEt_2	H
37	H	OMe	H
38	H	OH	H
39	H	H	Cl

Zhau and co-workers established the coordination of compound **31** and **40**, towards Cu^{2+} ions through chelation with phenolic and imine group. This coordination ended the IraHBs and thus, lead to chelation caused emission quenching. Further, the addition of S^{2-} ions disrupt the coordinated network of [**31**.Cu^{2+}]$_n$ and [**40**.Cu^{2+}]$_n$ and regenerated the AIE-ESIPT emission. No other ions could disrupt the coordinated network. The compounds were demonstrated for emission quenching due to complexation with Cu^{2+} ions and subsequent rise of emission by S^{2-} ions in KYSE510 live cells.[57]

Peng and co-workers introduced the dinitrobenzenesulfonyl unit to compound **40** to form compound **41**. On the introduction of cysteine exhibited the emission enhancement at 558 nm with broad Stokes' shift of 170 nm. Compound **41** was successfully demonstrated for fabrication on test paper and detection of thiols. The good permeability of compound **41** allowed the imaging of thiols in HEK 293 T cells.[58] Also, compound **41** was utilized as auxiliary *turn-on* sensor for β-lactamase in solution and paper strip with a detection limit of 10 $mUmL^{-1}$.[59] Likewise, compound **42** also exhibited the AIE-ESIPT emission with Stokes' shift of 148 nm and selectivity towards cysteine and homocysteine. The compound **42** was utilized for the detection of Cys and HCys in PC12 for live-cell imaging.[60]

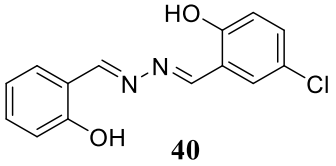

40

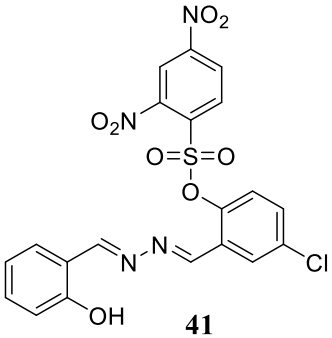

41

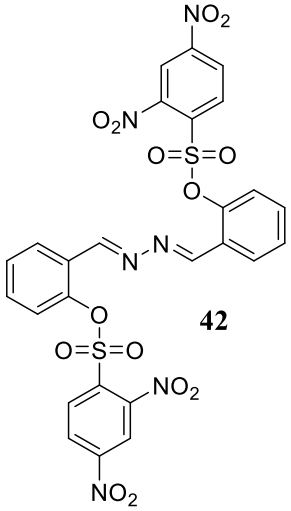

42

Compound **43** with the extension of π-conjugation was studied as a pH sensor by Ma and co-workers. The emission of compound **43** was remained constant between pH 3-11 and decreased on increasing the alkalinity.[52] Further, Yao and co-workers studied compound **43** for its piezochromism behavior. The powder form of compound **43** displayed yellow emission at 543 nm, however on grinding green emission was released at 530 nm. The annealing technique also leads the solid-state transformation and emission switching from yellow to green. The grinding of compound **43** in THF and 1,4-dioxane solvent resulted in new emission peak at 566 nm.[61]

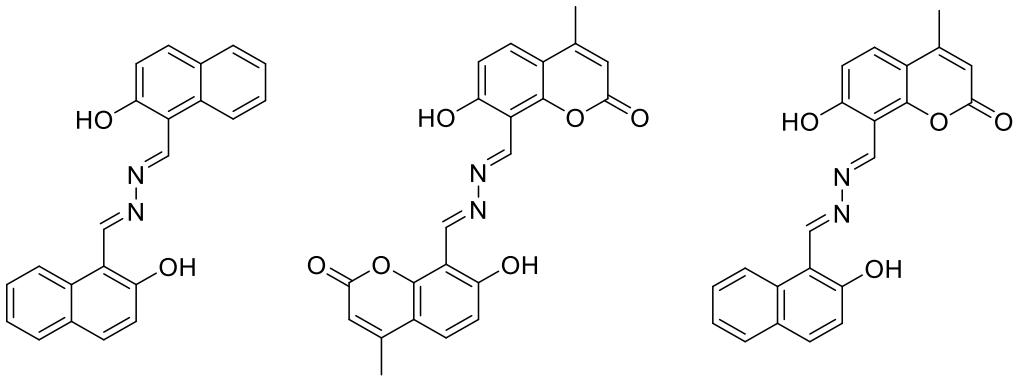

43 **44** **45**

Compounds **44** and **45** displayed ESIPT emission with large Stokes' shift of 270 nm (λex =335 nm) and 240 nm (λex =340 nm). Both compounds exhibited the AIE phenomenon, and the measured quantum yields of aggregates were 0.827 and 0.546, respectively. Further, good thermal stability and biocompatibility allowed these compounds to be used in cell staining.[62] The ESIPT phenomenon of these compounds was elaborated through theoretical calculations. Hao and co-workers established that the compound **44** exhibited emission from excited state intramolecular double proton transfer through the concerted mechanism. However, the dual emission of compound **45** exhibited from the ESIPT mechanism *via* a single proton transfer. The potential energy profile indicated that proton transfer on naphthalene unit was more feasible than at coumarin unit.[63]

Further, the introduction of phenyl rings at azine center for compound **46** and **47** did not change its ESIPT and AIE properties and behaved very similar to compound **31**. For compound **46**, the IraHBs afforded the structural based polymorphism and exit in two crystalline forms. The different crystalline forms (green and yellowish-green) have different ESIPT emission. The annealing/melting treatment allowed the switching of crystalline forms and thus, tuned their solid-state emission with good stability.[64]

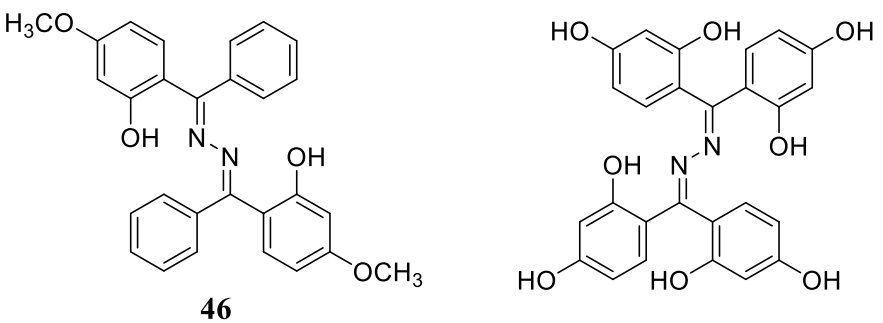

46 **47**

The free rotation of compound **47** was ceased in the hydrophobic medium, and a resulted blue emission was due to AIE/ESIPT phenomena. Further, compound **47** was utilized as a ratiometric fluorescent sensor toward BSA, HSA, and casein, with emission at 518 nm. The detection limits for BSA, HSA and casein were determined to be 16.2 μgmL^{-1}, 10.5 μgmL^{-1}, and 5.7 μgmL^{-1} respectively.[65]

Peng and co-workers synthesized flavone based compound **48**, which presented flexibility through azine linkage and therefore, exhibited the AIE-phenomenon and emission originated from ESIPT phenomenon. Compound **48** selectively displayed ratiometric emission change with Al^{3+} ions and the linear response of emission intensity ratio ($I_{461/537}$) determined the detection limit of 0.29 μM. The compound **48** demonstrated for practical applicability of detection of Al^{3+} ions in test paper strips and live-cell imaging.[66]

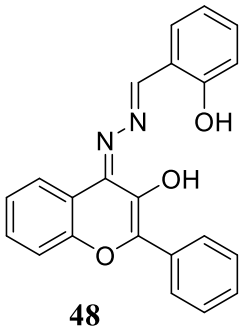

48

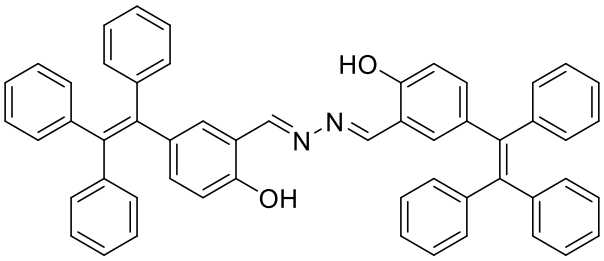

49

Compound **49** was a highly conjugated system and had yellow emission at 581 nm due to ESIPT phenomenon. On the introduction of Cu^{2+} ions, a complex formed in the stoichiometry of 2:1 as (Compound **49**)$_2$Cu. The coordination of Cu^{2+} ions with phenolic and imine groups break the IraHBs, and thus, quenched the ESIPT emission of compound **49**. The detection limit towards Cu^{2+} ion was determined to be 30 nM. Further, the complex was used to detect the cysteine due to more chemical reactivity and preferential binding of cysteine with Cu^{2+} ions and regeneration of emission of parent compound **49**. The detection limit was lower than 30-200 μM intercellular concentration.[67]

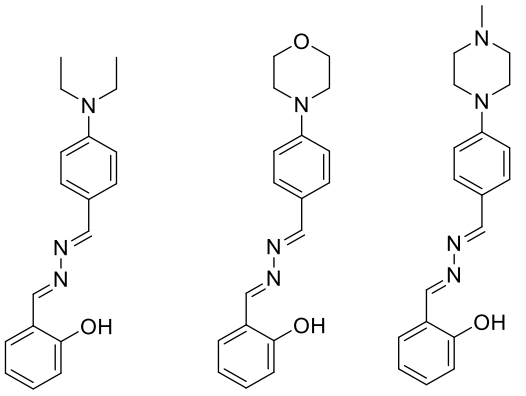

50 **51** **52**

Ni and co-workers have synthesized azine based Schiff bases (**50**-**52**) with characteristics of ESIPT and AIE.[68] The compounds **50**-**52** have been used as lipid droplet tracker, lyso-trackers and endoplasmic reticulum trackers, respectively. The compounds **50**-**52** displayed absorption peaks at 391 nm, 372 nm, and 376 nm, respectively. On excitation, compound **50** displayed dual keto-enol emission at 457 nm, 535 nm, compound **51** at 433 nm and 541 nm, and compound **52** at 435 nm and 541 nm, respectively. The listed absorption peaks have π-π* and CT character. Further, the substitution variation tuned the AIE properties. The aggregated form benefits the hydrogen bonding and thus, resulted in enhancement of keto emission.

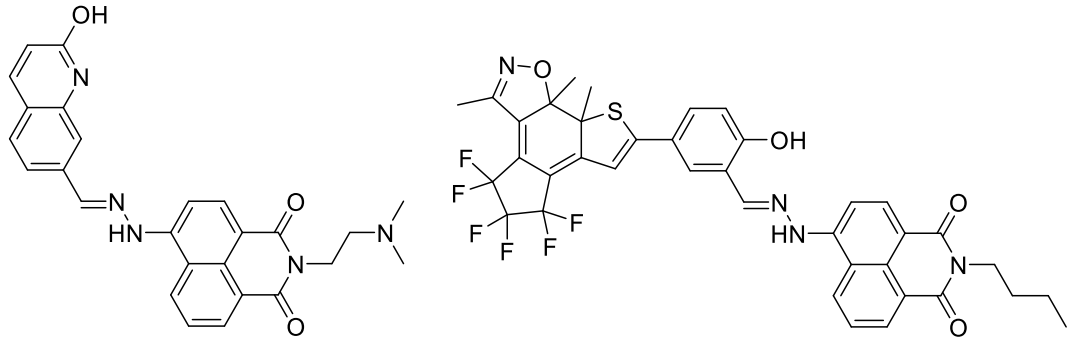

53 **54**

Naphthalimide-based compound **53** contained the quinoline unit linked through the azine linkage.[69] The compound **53** (λ_{abs} = 448 nm) displayed a ratiometric increased in absorption intensity at 628 nm on interaction with CN^- and F^- ions. The detection limit for CN^- and F^- ions were determined to be 20 nM and 24 nM, respectively. The weakly emissive compound **53** displayed emission enhancement on interaction with Hg^{2+} ions with the lowest detection limit of 240 nM.

Compound **54** displayed selectivity towards Cu^{2+} ions and F^- ions.[70] In the presence of Cu^{2+} ions, the absorption peak at 440 nm and emission peaks at 542 nm was decreased, with color variation from yellowish-green to colorless. The determined limit of detection was 2.4 μM. However, in the presence of F^- ions, the new absorption peak appeared ratiometrically at 580 nm and consequently, the color of the solution changed from yellowish-green to blue.

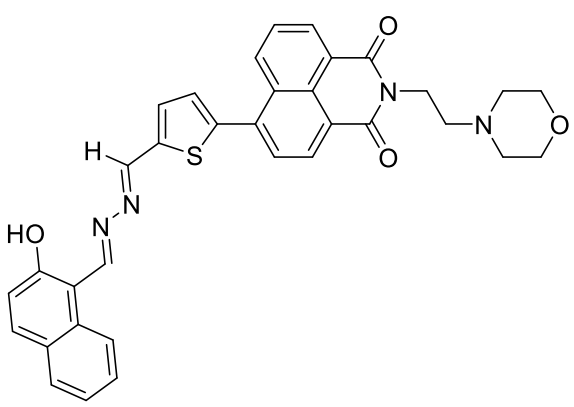

55

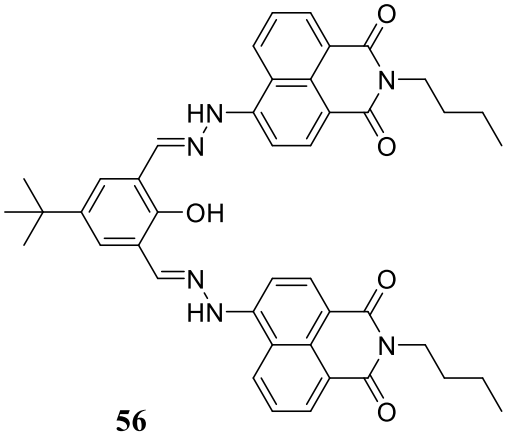

56

Compound **55** exhibited emission at 593 nm with Stokes' shift of 173 nm and displayed selectivity towards F^- ions.[71] The interaction of F^- ions, increased the absorption peak at 500 nm and 590 nm ratiometrically and accompanied by a color change from yellow to light purple. The abstraction of the hydroxy proton by F^- ions inhibit the ESIPT, and thus, quenched the emission. The determined detection limit was 15 nM.

Another, naphthalimide based compound **56** exhibited emission at 560 nm, accompanied with Stokes' shift of 94 nm in CH_3CN/H_2O (4:1; v/v) and displayed selectively towards Cu^{2+} ions.[72] On interaction with Cu^{2+} ions, the absorption peak at 466 nm was decreased, and new peak appeared at 600 nm ratiometrically. However, the emission peak of compound **56** was decreased by 30-folds in the presence of Cu^{2+} ions. The determined detection limit was 64 ppb. Further, compound **56** was utilized in microscopy imaging of MCF-7 live cells.

The compound **57** displayed AIE-ESIPT emission at 559 nm with Stokes' shift of 179 nm and found to be very selective towards Al^{3+} ions.[73] On interaction with Al^{3+} ions, the absorption peaks of compound **57** (H_2O/DMSO; 9:1; v/v) at 310 nm and 360 nm were decreased. On the other hand, the emission spectra rise at 453 nm ratiometrically with respect to ESIPT peak at 559 nm. The emission intensity ratio ($I_{453/559}$) increased linearly

and determined the limit of detection was 2.82 μM. Further, compound **57** was utilized as portable paper strips for detection of Al^{3+} ions. The application of compound **57** was extended to *in-vitro* and *in-vivo* study and brain tissue imaging.

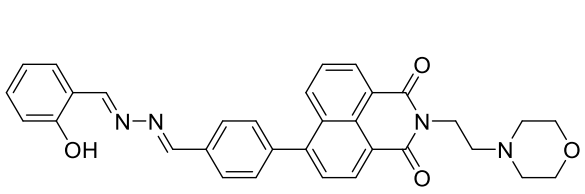

57

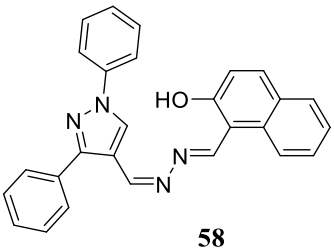

58

Compound **58** exhibited dual emission at 440 nm and 503 nm due to the ESIPT phenomenon and selectively responded to tryptamine and F^- ions. On the interaction of tryptamine, the absorption and emission intensity was increased at 282 nm and 440 nm, respectively. However, on interaction with F^- ions, the absorption peak at 384 nm was decreased, while a new peak at 422 nm was increased ratiometrically and color of compound **58** changed from yellow to orange. The determined detection limit for tryptamine and F^- ions were 0.04 nM and 0.03 nM, respectively.

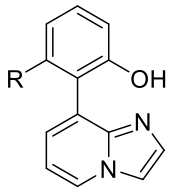

59 : R = H
60 : R = F

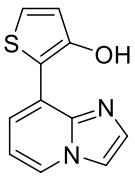

61

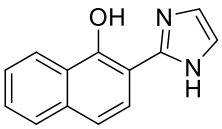

62

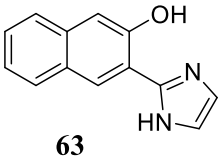

63

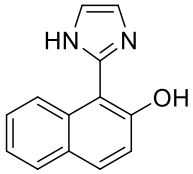

64

Mutui and co-workers have synthesized imidazo[1,2-a]pyridine derivatives (**59**-**61**) containing potential seven-membered IraHBs with different hydroxyaryl units.[74] The crystal structure determined that the compound **59** and **61** have planar structure, while compound **60** has a twisted structure. Therefore, due to structural planarity, only compound **59** and **61** exhibit the ESIPT emissions at 528 nm (Φ = 0.32) and 471 nm (Φ = 0.45), respectively.

Thais and co-workers studied compound **62**-**64** for the ESIPT phenomenon. Among these, compound **62** has the strongest IraHB and thus, highest ground state acidity. The structural optimization suggested that the compound **62** and **63** have planarity at IraHBs center, while compound **64** displayed no planarity at IraHB center. Therefore, compound **62** and **63** were having small barrier for ESIPT process; however, compound **64** was

measured with the highest barrier. The proton transferred configuration of compound **63** also displayed the intramolecular charge transfer coupled with ESIPT.

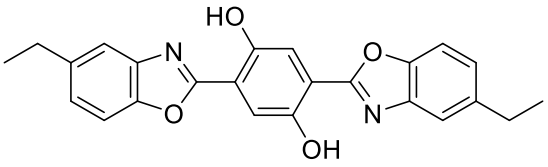

65

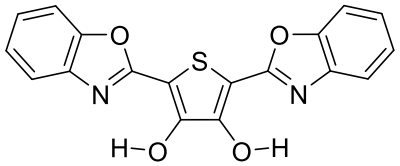

66

Dual emission of compound **65** was studied by Pawel and co-workers through experimental and theoretical techniques.[75] Time correlated single photon counting methods suggested that the ultrafast (~100fs) tautomeric conversion from the enolic form of mono-keto form. The dual emission was solely affected by solvent polarity. The calculated potential energy curves suggested that the di-keto form was relatively higher in energy than mono-keto form and also, followed by a higher energy barrier too. Therefore, the calculation also supported the formation of mono-keto form only.

Thiophene based compound **66** exhibited an absorption peak at 354 nm, 372 nm and 395 nm, while excitation at 395 nm compound 66 displayed four emission peaks at 412 nm , 430 nm, 475 nm and 550 nm.[76] The complexity in emission spectra were originated from the three tautomeric forms resulted due to single or/and double proton transfer tautomeric conversion.[21]

A series of imidazole-based derivatives **67-75** have been synthesized, which exhibited the tuned ESIPT emission.[77] A simple strategy of extension of sufficient conjugation length and variation of heterocyclic rings were adopted for different compounds (**67-75**). All these compounds displayed no absorption color; however, displayed diverse colors of strong photoluminescence over broad visible regions from 450 nm to 630 nm. The DFT calculation also predicted these emissions from tautomeric conformations.

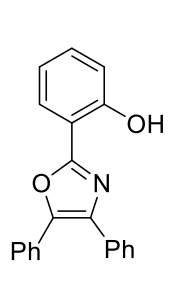

67

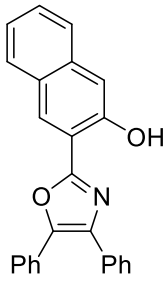

68

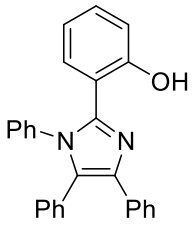

69

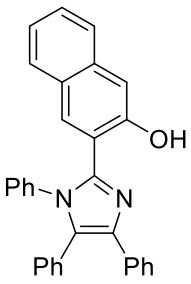

71

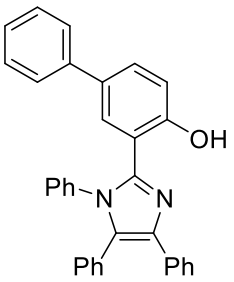

72

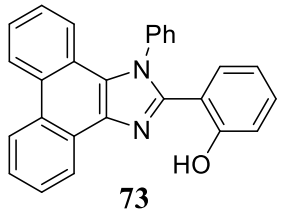

73

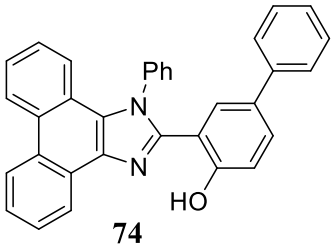

74

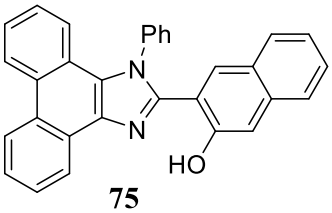

75

Compound **76** exhibited emission at 554 nm with Stokes' shift of ~200 nm.[78] The theoretical calculation depicted that the resulted emission was due to ESIPT process through N−H···N proton transfer. The introduced F^- ions, abstracted the proton adjacent to ESIPT proton, which decreased the acidity of ESIPT proton and thus, inhibits of ESIPT process.

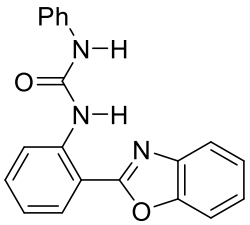

76

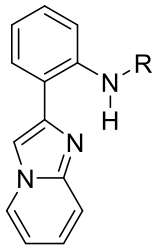

77-81

77 = R= H

78 = R = $COCH_3$

79 = R = $COCF_3$

80 = R =

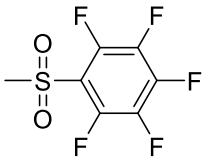

81 = R =

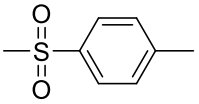

Imidazo[1,2-a]pyridin-based derivatives (**77-81**) have been synthesized, which exhibited the N−H···N-type IraHB.[79] The amino group was substituted with groups of different electronic properties and thus, altered the acidity of NH proton and therefore, improved IraHB strengths. On inducing the EWG –R groups, the emission was hypsochromically shifted from 700 nm (compound **77**) to 510 nm (compound **79**). This was due to the formation of zwitterionic forms, which was located over the hydrogen donor and acceptor units.

Compound **82** and **83** displayed dual emission at 430 nm and 500 nm. The high energy emission was ascribed due to standard enol emission, while the low energy emission was ascribed due to ESIPT emission.[80] The ESIPT emission of compound **82** and **83** displayed

positive solvatochromism, and thus, emission peak was shifted to longer wavelengths in polar solvents. The solvatochromism was proposed due to ESICT process originated from the extension of π-conjugation framework and following the ESIPT phenomenon.

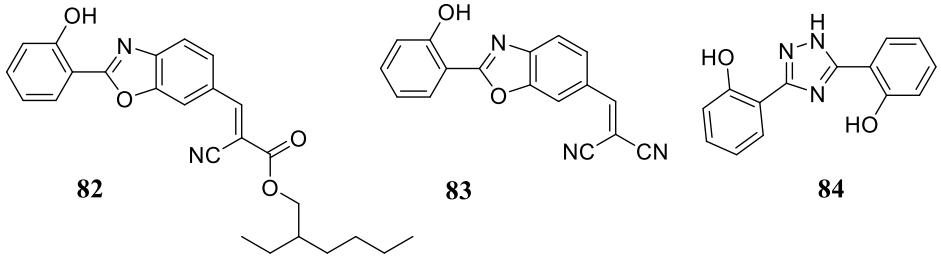

82 **83** **84**

Compound **84** displayed an absorption peak at 308 nm and an emission peak at 460 nm in dioxane. Compound **84** contained double intramolecular hydrogen bonding, which underwent a rare type of twin ESIPT. Interestingly, only single hydrogen donor-acceptor site was active for ESIPT, initially. However, the first proton transfer activates another hydrogen donor-acceptor site for ESIPT. The process of proton transfer triggered proton transfer was established by steady-state and time-resolved spectroscopy. In case of solid-state, both the hydrogen donor sites transferred the proton to acceptor sites.

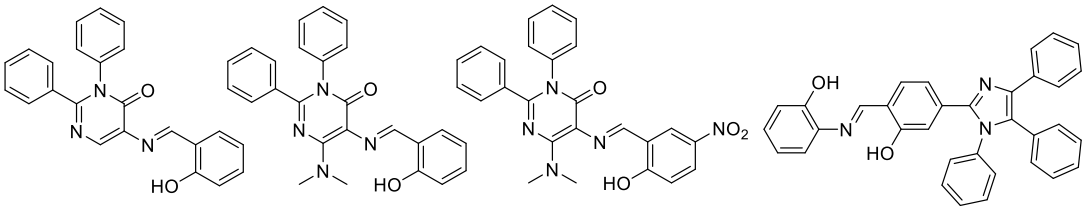

85 **86** **87** **88**

Compound **85-87** displayed the AIE and ESIPT properties. Compound **85** displayed red-orange AIE-ESIPT emission at 564 nm.[81] On the other hand, yellow-colored AIE-ESIPT emission of compound **86** and **87** were centred at 526 nm with Φ = 0.237 and Φ = 0.068,respectively.[82] The AIE features of compound **85-87** were utilized for fingerprinting on aluminum, metal currency coins, and stainless steel. These compounds were established for gathering information of fingerprinting at level one (loop or whorl, the pattern of the arch) and level two (dots, delta, bifurcation, ridge ending, and core).

The compound **88** displayed dual emission at 461 nm and 575 nm. This compound was used as potential chemodosimeter towards CN^- ions selectively with "turn-on' emission behavior and lowest detection limit of 15.34 ppb.[83] Further, compound 88 was studied for the origin of its photophysical properties, where electronic spectra calculation described that the compound **88** dominantly excited to first and second excited state. Also, the

intramolecular hydrogen bonding was strengthened at first and second state. Further, the calculated potential energy curves for ESIPT process at first and second excited state illustrated that the tautomeric conversion could only be possible at second excited state. Thus, the low energy emission at 575 nm was originated from the ESIPT process at second excited state.[84]

1.2 The motivation for the present work

In recent years, different molecular architectures were explored for ESIPT, AIE-ESIPT, ESICT phenomena, and studies were extended for chemo-sensing properties.[85-102] The ESIPT-based molecular architectures have attracted much attention due to their promising applications in ultra-fast reaction rate and extremely large fluorescence Stokes shift. The excited state intramolecular charge-transfer (ESICT) molecules are potential candidates for single-molecule spectroscopy, cell imaging, laser dyes, biomarkers, solar cells, in photosynthesis, etc. Further, the coupling of the AIE phenomenon with ESIPT and ESICT mechanisms have exhibited remarkable advantages, such as no self-quenching at high concentrations, strong emission with a large Stokes shift, and avoidance of hydrophilic modification.

During the literature survey, we have found reports based on azine or tetra-phenylethylene compounds which exhibited the AIE phenomenon while the Schiff base linkage allow the ESIPT phenomenon. Thus, we designed the symmetrical azine-based compound incorporating the tetraphenyl units, exhibiting the ESIPT and AIE phenomenon on single platform. The interplay of two phenomena has been studied by experimental and theoretical methods. Additionally, the compounds were successfully utilized for detection of common metal ions with approach of real-world applications. Further, the naphthalimide-derived Schiff bases were designed due to high photostability, and chromo-fluorescent nature and found application in antiviral, anticancer activity, analgesic, etc. Further, Imidazo[1,2-*a*]pyrazine acts as a versatile scaffold with application in chemiluminescence, bioluminescence and drug development. Therefore, the considered molecular architectures are potential organic candidates with versatile applications. Despite the potential application, the literature reports limit the theoretical insight of phenomena. The literature limits an experimental and theoretical study on the phenomenon of ESIPT/ESIDPT of azine and heterocycles-based compounds and their analogs. The molecular systems containing double IraHBs are scarcely studied for sensing of cations and anions. Therefore, the motivation of this thesis was to gain theoretical insight into the ESIPT phenomenon in different molecular architecture. Developing symmetrical as well as asymmetrical systems containing single or double intramolecular hydrogen bonding and evaluating their photophysical properties through mechanistic pathways of ESIPT/ESIDPT phenomena. Further, evaluating the sensing properties of these molecular systems.

Chapter 2

Materials and methods

The details of chemicals, reagents, and solvents used for the present work are provided. The methodology used for experiments, theoretical calculation, and data analysis were also described briefly. In addition, this chapter covers the details of the instruments used during the course.

2.1 Materials

The details of chemicals and solvents used for work were listed below

2.1.1 Chemicals

- 4-amino benzophenone (Sigma Aldrich)
- Salicylaldehyde (Spectrochem, India)
- 4-(diethylamine)salicylaldehyde (Sigma Aldrich)
- 4-Nitrosalicylaldehde (Sigma Aldrich)
- 2-Aminopyrazine (Sigma Aldrich)
- *N*-bromosuccinimide (Sigma Aldrich)
- Chloroacetaldehyde (Avra Synthesis, India)
- 2-hydroxyphenyl boronic acid (Alfa Aesar)
- 7-hydroxyquinoline (Alfa Aesar)
- *o*-phenylenediamine (Spectrochem)
- Nitrobenzene (AR grade, Loba Chemie, India)
- Sulphuric acid (AR grade, Loba Chemie, India)
- Sodium hydroxide (Spectrochem, India)
- Silica gel (60-120, 120-240) (Merk India)
- Silica gel GF-256 (Spectrochem, India)
- Potassium carbonate (Spectrochem, India)

2.1.2 Metal ions

- Sodium perchlorate monohydrate, $NaClO_4.H_2O$; (Sigma Aldrich),
- Potassium perchlorate, $KClO_4$; (Sigma Aldrich),
- Magnesium perchlorate hexahydrate, $Mg(ClO_4)_2.6H_2O$; (Sigma Aldrich),
- Calcium perchlorate tetrahydrate $Ca(ClO_4)_2.4H_2O$; (Sigma Aldrich),

- Barium perchlorate, $Ba(ClO_4)_2$; (Sigma Aldrich),
- Aluminum perchlorate nonahydrate, $Al(ClO_4)_3.9H2O$; (Sigma Aldrich),
- Lead perchlorate hydrate $Pb(ClO_4)_3.\ xH_2O$; (Sigma Aldrich),
- Iron perchlorate hydrate $Fe(ClO_4)_3.xH_2O$; (Sigma Aldrich),
- Cobalt perchlorate hexahydrate $Co(ClO_4)_3.6H_2O$; (Sigma Aldrich),
- Nickel perchlorate hexahydrate $Ni(ClO_4)_3.6H_2O$; (Sigma Aldrich),
- Copper perchlorate hexahydrate $Cu(ClO_4)_3.6H_2O$; (Sigma Aldrich),
- Zinc perchlorate hexahydrate $Zn(ClO_4)_3.6H_2O$; (Sigma Aldrich),
- Mercury perchlorate hydrate $Hg(ClO_4)_3.xH_2O$; (Sigma Aldrich),
- Silver perchlorate $Ag(ClO_4)_3$; (Sigma Aldrich)

2.1.3 Anions

- Tetrabutylammonium chloride $(n\text{-}Bu)_4NCl$; (Sigma Aldrich),
- Tetrabutylammonium bromide $(n\text{-}Bu)_4NBr$; (Sigma Aldrich),
- Tetrabutylammonium iodide $(n\text{-}Bu)_4NI$; (Sigma Aldrich),
- Tetrabutylammonium cyanide $(n\text{-}Bu)_4NCN$; (Sigma Aldrich),
- Tetrabutylammonium thiocyanate $(n\text{-}Bu)_4NSCN$; (Sigma Aldrich),
- Tetrabutylammonium fluoride $(n\text{-}Bu)_4NF$; (Sigma Aldrich),
- Tetrabutylammonium hydrogen sulfate $(n\text{-}Bu)_4NHSO_4$; (Sigma Aldrich),
- Tetrabutylammonium acetate $(n\text{-}Bu)_4NCH_3COO$; (Sigma Aldrich),
- Tris(tetrabutylammonium) hydrogen pyrophosphate
- $[(n\text{-}Bu)_4N]_3[O=P(O^-)_2OP(=O)(O^-)OH]$; (Sigma Aldrich)

2.1.4 Solvents

- 1, 4-dioxane (HPLC grade, Spectrochem India),
- 2-propanol (HPLC grade, Spectrochem India),
- Acetonitrile (HPLC grade, Spectrochem India),
- Cyclohexane (HPLC grade, Spectrochem India),
- Chloroform (HPLC grade, Spectrochem India),
- Dimethylformamide (HPLC grade, Spectrochem India),
- Dimethylsulfoxide (HPLC grade, Spectrochem India),
- Diethyl ether (HPLC grade, Spectrochem India),
- Ethanol (HPLC grade, Spectrochem India),
- Ethyl acetate (HPLC grade, Spectrochem India),

- Glycerol (AR grade, Rankem India),
- Methanol (HPLC grade, Spectrochem India),
- Tetrahydrofuran (HPLC grade, Spectrochem India),
- Toluene (HPLC grade, Spectrochem India),
- Water (Millipore).

The solvents were clear and transparent in the spectral region and therefore, used as received.

2.2 Experimental study

2.2.1 General procedure for the synthesis

All the reactions were carried out in clean and dry vessels. The reaction progress was monitored by thin-layer chromatography (TLC) analysis, performed on the glass-coated silica gel GF256. On the complete consumption of starting materials, the reaction was quenched, and desired products were collected either by either filtration or extraction through aqueous-organic solvent mixtures.

2.2.2 Preparation of stock solutions

All the compounds were soluble in acetonitrile, DMSO. Therefore, a stock solution was prepared to have the strength of 10^{-3} M. Further; required concentration solution was prepared in the different solvent medium by dilution method. The stock solution of above-mentioned metal ions and anions were prepared in CH_3CN, except for Al^{3+} ions. The Al^{3+} stock was prepared in H_2O. The strength of the stock solution was 10^{-1} M. The stock solutions were further diluted to the desired strength with the respective solvent. For pH titration, amount of H_2SO_4/NaOH solution was added to obtain the desired pH.

2.2.3 DNA binding studies

The stock solution of ct-DNA was prepared by dissolving DNA in phosphate buffer (10 mM, pH 7.0). The concentration was estimated from its absorbance intensity at 260 nm with a known molar absorption coefficient value of 6600 $dm^3M^{-1}cm^{-1}$. The purity of DNA was established from the ratio of absorbance intensity at 260 nm and at 280 nm. The titration experiments were performed by varying the concentration of ct-DNA and keeping the compound concentration constant (20 μM). All the UV spectra were recorded after equilibration of solution for 5 min.

2.2.4 Absorption/emission spectra measurements

The diluted solutions with strength range of μM were used further for the measurement of photophysical properties in several solvents. The spectra were measured in quartz cuvettes of 1 cm in path length, thermostated at 25.0 ± 0.1°C. The absorption spectra were recorded on SHIMADZU-2600 spectrophotometer by using slit width of 1.0 nm, and emission spectra were performed on a Varian Carey Eclipse fluorescence spectrophotometer at stated excitations. All the absorption and emission spectra were saved as ASCII files and further, analyzed with the help of Microsoft excel.

2.2.5 DLS sample preparation

The stock solution of compounds was prepared and filtered through 0.02 μM filter to remove suspended particles. Further, solutions of strength 20 μM were prepared for DLS analysis. The solutions were treated with detected analytes, and therefore, difference in size was measured at 25°C.

2.2.6 NMR/Mass measurements

^{1}H NMR and ^{13}C NMR spectra were recorded on JEOL ECS-400 MHz spectrometer at ambient temperature in $CDCl_3$ or/and DMSO-d_6 with TMS as an internal reference. All chemical shifts were reported in ppm relative to tetramethylsilane (TMS) as an internal reference and coupling constant *J* in Hz, multiplicity (s = singlet, d = doublet, t =triplet, q = quartet, dd = doublet of doublet, m= multiplets). Further, for ^{1}HNMR titration of compounds with their restively detected analytes were measured in the respective medium of detection. The NMR spectra of compounds were measured in the presence of analytes, which were also repeated after 24 h. The mass spectrum of the synthesized compound was recorded at Water Micromass-Q-T of Micro.

2.2.7 FTIR measurement

The FTIR measurements were made on the powder samples. The solid sample was mixed and grinded with potassium bromide (KBr), and pallet was formed. The pallet was placed on the FTIR substrate and analyzed by passing IR beam of the spectrometer. The samples were analyzed on Agilent-Cary 660 machine.

2.2.8 FESEM measurement

The effect of aggregation was studied by changes in size and surface morphology and thus, measured by FESEM imaging. The metal-template aggregation was studied by FESEM imaging. The solution of compounds was placed on copper grid and dried for 24 h. The dried samples were then plated using gold spray and analyzed for the FESEM. The samples were analyzed at Sprint testing solution, Mumbai, India.

2.2.9 Stoichiometry, binding constant and detection limit

In order to determine the stoichiometries of complexes, a series of solutions containing compounds and analytes were prepared with variations of mole fractions (X) of analytes from 0.1 to 1.0. The absorption/emission spectra were measured. Further, a plot was analyzed between the intensity was plotted against the molar fraction of the analyte solution, according to the Job plot method. Based on the Job plot, the complexation ratios of analyte and compounds were determined.

The binding constants of compounds for the different analyte are determined using the following Benesi-Hildebrand equation

$$\frac{1}{I - I_0} = \frac{1}{K_a(I_{max} - I_0)[C]^n} + \frac{1}{I_{max} - I_0}$$

Where I_0, I, and I_{max} are the absorption/emission intensities of the compound in the absence of an analyte, at an intermediate analyte concentration, and at a concentration of complete interaction with analyte respectively. K_a is the binding constant, C is the concentration of the analyte, and n is the number of analytes bound per compound molecule. In order to determine the S/N ratio, the emission intensity of the compounds was measured thrice, and the standard deviation of blank measurements was determined. The detection limit (DL) was determined from the following equation:

$$DL = \frac{3 \times Standard\ deviation\ of\ the\ blank\ solution}{slope\ of\ calibration\ curve}$$

2.3 Theoretical calculation

In order to get conclusive remarks on the experimental results for compounds, the geometrical optimization, and prediction of all photophysical properties have been carried out. The theoretical results at S_0 state were calculated on density functional theory (DFT) using different functional such as B3LYP/cam-B3LYP/ωb97-XD and 6-31+G(d,p)

level of basis set.[103-107] All the optimized structures were verified through the absence of imaginary frequency. The calculations were extended to excited state (S_n) geometry optimizations using TDDFT methods.

2.3.1 Solvent Effect

In order to integrate the real space environments in our results, the solvent effect was included using the integral equation of formalism polarized continuum model (IEFPCM) for all tautomeric forms and transition states in S_0, and S_n states.

2.3.2 Electronic spectra and NMR Prediction

Further, three Frank-Condon vertical excitation were predicted on the S_0 geometry using time dependent DFT (TDDFT). Among these, the excitation with highest oscillation strength was analyzed for frontier molecular orbitals. The nature of electronic excitation was quantitatively evaluated using hole-electron concept. The NMR shielding tensors were calculated using GAIO method.

2.3.3 Establishment of hydrogen bonding

Here, we were interested in exploring the nature of excited state intramolecular proton transfer. Therefore, the prerequisite condition of intramolecular hydrogen bonding was preliminary investigated through geometrical parameters and established through AIM, FTIR spectra at S_0 and S_n states.

2.3.4 Tautomeric preference

The free energy change ($\Delta G=G(S)-G(K)$; where S and K are the standard enol and keto tautomeric forms) was used to predict the tautomeric conversion in S_0 and S_1 states. The positive ΔG value depicted the more stabilization of standard enol form and tautomeric conversion through PT was not permissible. However, the negative ΔG value inferred the stabilization of keto tautomeric form and thus, suggests the tautomeric conversion through PT mechanism, and thus, envisage rise of emission.

The systematic theoretical study involved the following steps:

1. Structural optimization and geometrical analysis at S_0 and S_n states
2. Electronic spectra and charge distribution to the determined contributing excited state
3. Structural optimization and geometrical analysis at S_n states
4. FTIR spectra and AIM analysis for the establishment of IraHB
5. Energy profile of PT pathways

2.3.5 AIM Analysis

Further, the prerequisite condition of IraHB existing within key conformer, for the presence of ESIPT was established *via* established Popelier criteria using Bader's quantum theory of atoms in molecules (QTAIM).[108-110] The existence of hydrogen bonding was examined based on Popelier criteria, which are described as

1. The occurrence of the critical point (CP) between two neighboring atoms,

2. The electron density [$\rho(r_c)$] must be in the range of 0.002-0.034 au

3. The Laplacian of electron density [$\nabla^2\rho(r_c)$] must be in the range of 0.024-0.139 au at a critical point.

The topological properties of the bond critical points (BCP) for IraHBs were examined for stability and strength of the interactions. The degree of covalency and strength of the IraHB interactions were characterized according to Rozas' rules:

(i) $\nabla^2\rho(r_c) < 0$ and $H(r) < 0$ for strong H-bond of covalent nature,

(ii) $\nabla^2\rho(r_c) > 0$ and $H(r) < 0$ for medium H-bond of partially covalent nature

(iii) $\nabla^2\rho(r_c) > 0$ and $H(r) > 0$ for weak H-bond of electrostatic character.

Moreover, the hydrogen bond energy was determined by Espinosa equation[111], which states that the interaction energy of H···X contact is defined as, $E_{HX} = V(r)/2$ at BCP, where V(r) is potential electron density at a bond critical point.

2.3.6 Software used

- Gaussian 03, 09 & 16 version: For Quantum Chemical Calculation[112-114]
- Gauss view & Chemcraft : To visualization the results[115, 116]
- MS Excel & Origin 8: For Plotting the results

Chapter 3

Theoretical investigation of photophysical properties of symmetrical bis(diphenylmethylene)hydrazine-based Schiff bases

The molecular system containing azine functionality and appended hydroxyl unit through IraHB have been demonstrated for ESIPT phenomenon. Such compounds have been utilized as a potential candidate as fluorescent markers, OLEDs materials, chemical, and biological sensors etc.[17, 18, 50, 64, 117-121] However, literature limits the systematic theoretical insight of origin of their photophysical behavior of molecular structures containing the functionality of azine, imine, and hydroxyl units. In this Chapter, a detailed theoretical study was performed on bis(diphenylmethylene)hydrazine (BPAz) based Schiff base compounds for the establishment of intramolecular hydrogen bonding (IraHB) and investigation of the excited state intramolecular proton transfer. Herein, we report the study of the photophysical behavior of BpAz based Schiff bases through systematized experimental and theoretical methods. The objective of understating the effect of substitution was accomplished by introducing functional groups of electron-withdrawing and donating capacity to the model BpAz Schiff base structure. The designed compounds (**2-4**) established dual IraHBs through the acidic phenolic unit and basic imine unit (Figure 3.1). The study involved the calculation of origin of absorption and emission properties through different mechanistic photophysical processes.

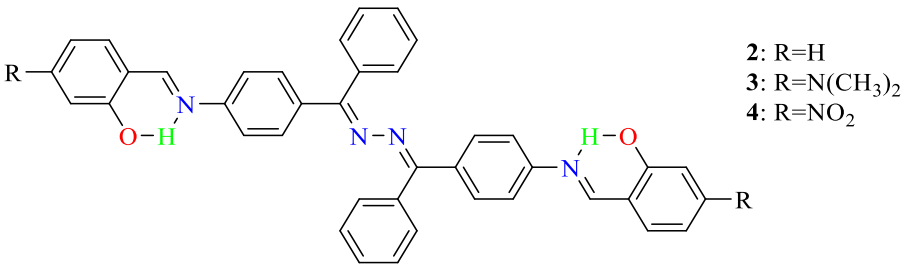

Figure 3.1 The different derivative of model BpAz Schiff base compounds

The experimental data analysis revealed that the substitution has altered the photophysical properties and tuned excited states processes. Further, the substitution-based studies have been summarized in the following three section

3.1. Excited state intramolecular proton transfer mechanism for dual emission of symmetrical bis(diphenylmethylene)hydrazine-based Schiff base

3.2. Effect of electron-withdrawing $-NO_2$ group on excited state intramolecular proton transfer of symmetrical bis(diphenylmethylene)hydrazine-based Schiff base

3.3. The supremacy of charge transfer over proton transfer in symmetrical bis(diphenylmethylene)hydrazine based Schiff base

3.1

Excited state intramolecular proton transfer mechanism for dual emission of symmetrical bis(diphenylmethylene)hydrazine-based Schiff base

3.1.1 Abstract

In this study, bis(diphenylmethylene)hydrazine based Schiff base (**2**), undergoing excited intramolecular proton transfer (ESIPT) was studied through theoretical methods. The compound **2** has dual intramolecular hydrogen bonding (IraHB) suited in C_2 symmetry and thus, consisted of two ESIPT sites. Therefore, the established IraHB and ESIPT process could rise three tautomeric forms as standard dienol form (**2.NN**), mono-keto form (**2.NK**) resulted from the single proton transfer, where the molecular structure has enolic form at one end while a proton transferred keto form at another end and di-keto form (**2.KK**) resulted from the double proton transfer. The computed free energy change (ΔG) was used to predict the preference for **2.NN**, **2.NK**, **2.KK** forms and thus, the defined origin of emission peaks based on the energy barrier of ESIPT process. Indeed, dual emission of compound **2** in CH_3CN clearly indicated the presence of ESIPT phenomenon. The calculations based on long-range hybrid functional (CAM-B3LYP) time-dependent density functional theory coupled integral equation formalism polarization continuum model (IEFPCM) imitated the mechanistic insight of proton transfer (PT). The AIM, FTIR established the prerequisite condition of existence of intramolecular HB. The redshift in vibrational frequency on photoexcitation indicated the strengthening of IraHBs at S_1 and S_2 states, and therefore prompting the ESIPT process. Moreover, the predicted absorption spectra and the electron density distribution on FMOs depicted the facilitation of ESIPT at S_2 state. The ESIPT process was explored through concerted PT (Path I) and sequential PT (Path II) mechanism. The energy barriers for forward PT were Path I (13.45 $kcalmol^{-1}$) and Path II (7.21 $kcalmol^{-1}$, 7.24 $kcalmol^{-1}$), while for reverse PT was Path I (3.47 $kcalmol^{-1}$) and Path II (1.96 $kcalmol^{-1}$, 1.95 $kcalmol^{-1}$), which indicated that the PT was not allowed through concerted mechanism nor sequential mechanism at S_1 state. Further, the energy barriers calculated at S_2 state for the forward PT were Path I (8.30 $kcalmol^{-1}$) and Path II (5.23 $kcalmol^{-1}$, 7.04 $kcalmol^{-1}$) while for reverse PT were Path I (20.84 $kcalmol^{-1}$) and Path II (22.47 $kcalmol^{-1}$, 1.74 $kcalmol^{-1}$). Moreover, the energy relationship of tautomeric forms (**2.NN**, **2.NK**, **2.KK**) was **2.NK**

< **2.KK** < **2.NN** in the S_2 state. Therefore, the ESIPT could take place through the single PT at S_2 state.

3.1.2 Experimental section

3.1.2.1 Synthesis of compound 1

Scheme 3.1 represented the synthesis of compound **1** and **2**. To (4-aminophenyl)(phenyl)methanone (0.985 g, 5 mmol) dissolved in 10 mL ethanol and hydrazine hydrate (121 µL, 2.5 mmol) was added. The resulted reaction mixture was heated at 80 °C for **6** h. The reaction was monitored by TLC. After completion of the reaction, the reaction mixture was cooled to room temperature, and the resulted light-yellow color solid was filtered off and washed with ethanol to get pure compound **1** in 75% yield; m.pt. 210°C.

^{1}H NMR spectrum of compound **1** displayed a resonating signals at δ 7.52 ppm as doublet of 3Ar-H, δ 7.38-7.23 ppm as multiplet of 8 ArH, δ 7.11 ppm as doublet of 3H (Ar), δ 6.58 ppm as doublet of 4 ArH and δ 4.86 ppm as singlet of 4H (NH_2) and ^{13}C NMR spectrum displayed resonating signals at δ 149.1 due to —C═N, 148.8 due to ArC—NH_2, 131.6, 131.2, 129.3, 128.6, 127.5, 127.4, 127.3, 122.2, 113.1, 112.6, 112.5 (Ar-H). ESI-MS (m/z) = 391.2 (M^++1) (close to calculated m/z (390.2)). Thus, spectroscopic and spectrometric data confirmed the formation of compound **1**.

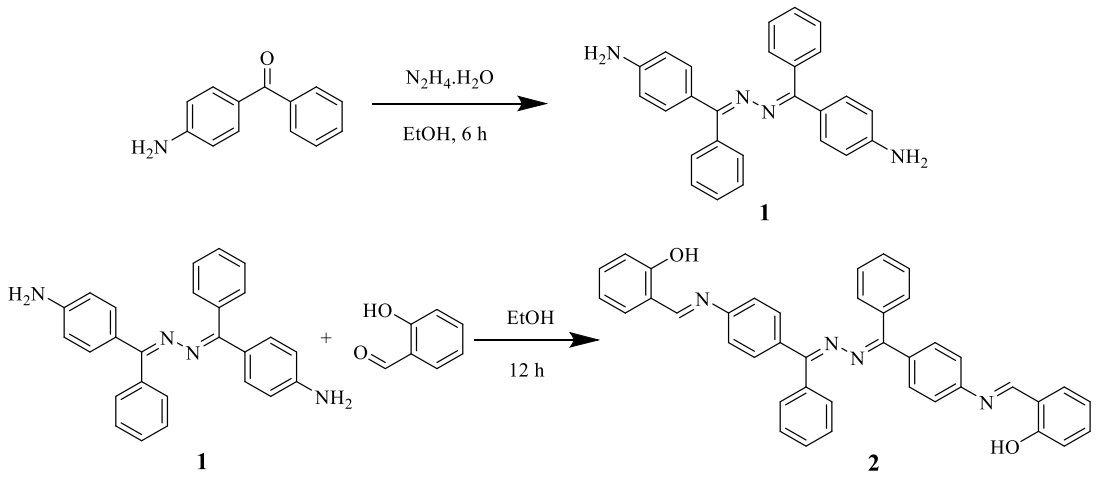

Scheme 3.1 Synthesis of compound **2**

3.1.2.2 Synthesis of compound 2

The compound **1** (390 mg, 1 mmol) and salicylaldehyde (244 mg, 2 mmol) were dissolved

in ethanol and heated at 80-85 °C. The progress of the reaction was monitored by TLC. The yellow-colored compound was formed after 12 h, which was further filtered off and washed with ethanol to get pure compound **2** in 70 % yield; m.pt. 243°C

The ^{1}H NMR spectrum displayed new resonating signals as singlet at δ 13.18 and 13.15 ppm of 2H (—OH), δ 8.69 and 8.63 ppm as singlet of —CH═N , δ 7.51-7.32 ppm as multiplet of 17 ArH, δ 7.25-7.05 ppm as multiplet of 5 ArH, δ 6.98-6.93 ppm as multiplet of 4 ArH and ^{13}C NMR spectrum displayed resonating signals at δ 163.1, 162.8, 160.8, 158.9, 149.3, 148.4, 137.8, 136.4, 134.9, 133.6, 133.2, 132.3, 130.7, 129.6, 128.5, 127.7, 120.7, 120.5, 119.1, 118.9, 116.9 of Ar-C. ESI-MS (m/z) = 599.2 (M^{+}+1) (close agreement to calculated m/z (598.2)). Thus, spectroscopic and spectrometric data confirmed the formation of compound **2.**

3.1.3 Results and discussion

3.1.3.1 ESIPT characteristics of Compound 2

Photophysical properties of compound **2** were studied through absorption and emission spectroscopic techniques. The absorption spectrum of compound **2** (20 µM, CH_3CN) displayed an absorption peak at 355 nm. Upon excitation, compound **2** (20 µM, CH_3CN) displayed dual emission peaks at 455 and 545 nm, which were accomplished with Stokes` shift of 100 and 190 nm, respectively (Figure 3.2).

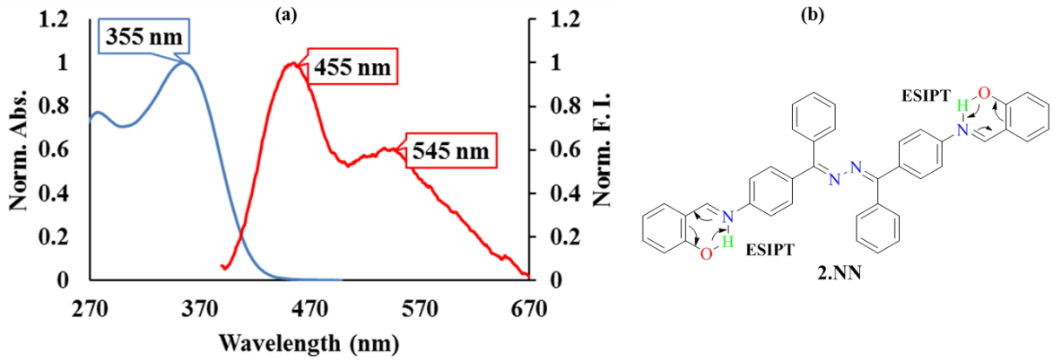

Figure 3.2 (a) Normalized absorption and fluorescence spectra of compound **2** (20 µM, CH_3CN); (b) Structure of compound **2** representing characteristics ESIPT process.

The characteristic dual emission of compound **2** indicates the ESIPT phenomenon. The emission peak at 455 nm could be ascribed as standard enol emission. The emission band at 545 nm, with large Stokes` shift (>100 nm, although weak in nature) is due to excited state intramolecular proton transfer (ESIPT). The ESIPT in compound **2** is due to proton

transfer from the phenolic group (acidic in nature, and thus, acting as proton donor) to imine nitrogen (basic in nature and thus, acting as proton acceptor) in an excited state.

3.1.3.2 Electronic spectra and charge distribution

The compound **2** was optimized at S_0 state using the DFT method using cam-B3LYP/6-31+g(d,p). In order to determine the electronic spectra of compound **2,** TDDFT method was used at the same level of theory. First three Frank-Condon (FC) excitations were calculated on the S_0 optimized structure to determine the contributing vertical excitation. The results were summarized as electronic transition, symmetry, the oscillation strength, and involved FMOs in Table 3.1 and the produced spectroscopic data depicted that the used method was efficient enough.

Table 3.1 The electronic excitation wavelength (λ/ nm), oscillator strengths (f) and compositions of the low-lying singlet excited states (MOs contribution) of the compound **2**

$S_0 \rightarrow Sn$	**Symmetry**	**λ_{calc}**	**λ_{exp}**	**f**	**MO contribution (%)**	
$S_0 \rightarrow S_1$	Singlet-A	360.9		0.0027	H-3→L	34
					H-1→L	26
$S_0 \rightarrow S_2$	Singlet-A	345.7	355	2.1651	H→L	77
$S_0 \rightarrow S_3$	Singlet-A	308.8		0.0117	H→L+1	34
					H-1→L	24

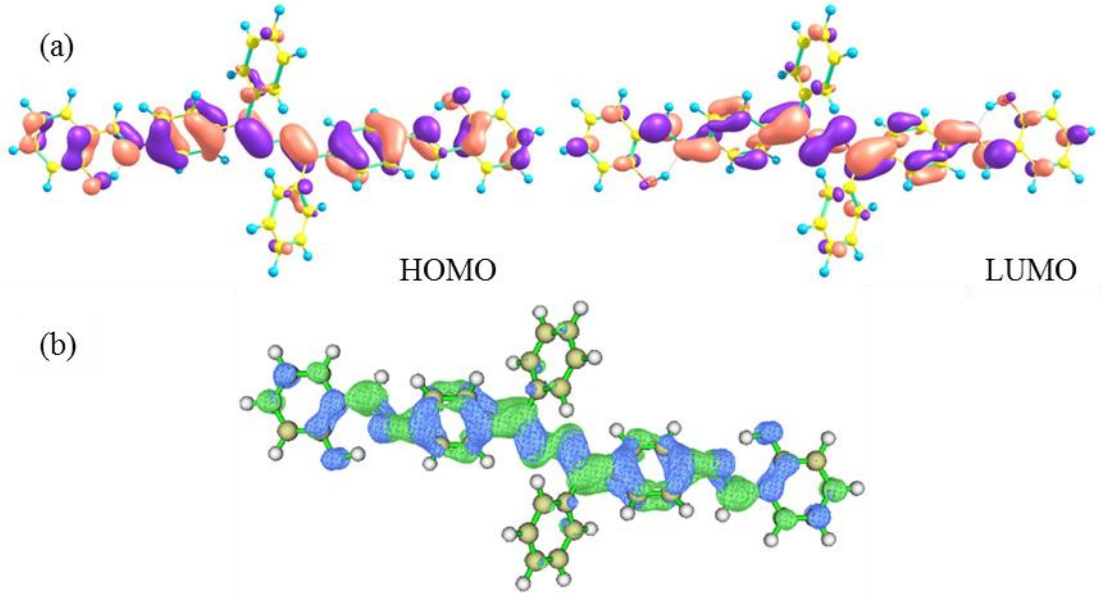

Figure 3.3. (a) FMOs of compound **2** and (b) hole-electron distribution for $S_0 \rightarrow S_2$.

The first FC transition ($S_0 \rightarrow S_1$) was calculated at 360 nm, with oscillation strength of 0.0027, and resulted from the HOMO-3→LUMO and HOMO-1→LUMO transition. The

$S_0 \rightarrow S_2$ transition was calculated at 345 nm, with highest oscillation strength of 2.1651 and originated from the HOMO→LUMO. Next, $S_0 \rightarrow S_3$ was calculated at 308 nm, with oscillation strength of 0.0017 and caused from H→L+1, and H-1→LUMO transition. Among these excitations, only $S_0 \rightarrow S_2$ excitation was found to be significant with the highest oscillation strength and also in close to experimentally observed absorption peak at 355 nm. Therefore, the representative FMOs were considered and shown in Figure 3.3. The HOMO and LUMO have an electronic distribution over the benzophenone skeleton and extended up to Schiff base linkage. Therefore, electronic distribution clearly depicted the π and π*-character of HOMO and LUMO, respectively and thus, $S_0 \rightarrow S_2$ transition could be assigned as the character of π→π* transition. Further, the quantitative nature of excitations was measured through hole-electron distribution, the distance between the centroid of hole and electron center was found to be 0.0042 Å, while the overlap integral was 0.474. The overlap integral value with little spatial separation of hole-electron distribution revealed the transition as the local excitation transition. Next, the $S_0 \rightarrow S_1$ transition has smaller oscillation strength (<0.01) and therefore could be considered as a dark state, while $S_0 \rightarrow S_2$ could be considered as golden state with significant oscillation strength. Moreover, this signified that the S_2 state must also be evaluated for the emission phenomenon.

3.1.3.3 Geometrical parameters

The compound **2** has double O─H···N IraHBs, which were categorized as I and II and shown in Figure 3.4. Further, the proton transfer could rise three tautomeric forms **2.NN**, **2.NK**, **2.KK** and therefore, tautomeric forms **2.NN**, **2.NK**, **2.KK** were optimized at S_0, S_1 and S_2 states using DFT and TDDFT methods with cam-B3LYP/6-31+g(d,p). The optimized structures were validated for the local minima through the absence of imaginary frequency. The optimized structures of tautomeric forms were presented in Figure 3.4. The compound **2** attained C_2 symmetry, and thus own the similar geometrical parameters such as bond lengths for proton donors $O_{71}H_{72}/O_{73}H_{74}$, IraHB distances for $H_{72}\cdots N_{47}/H_{74}\cdots N_{48}$ and bond angles for $O_{71}H_{72}\cdots N_{47}$ (I) and (II) values in S_0, S_1, and S_2 states. The bond lengths for O_{71}—H_{72} and O_{73}—H_{74} were increased by ~0.0027 Å from 0.9933 at S_0 state to ~0.9960 Å at S_1 state. Further, these bond lengths were increased by ~0.0051 Å to 0.9984 Å at S_2 state. On the other hand, the H_{72}—N_{47} and H_{74}—N_{48} bond lengths decreased by 0.0168 Å from 1.7547 Å at S_0 state to 1.7485 Å at S_1 state, which

further decreased by 0.0318 Å to 1.7197 Å at S_2 state. Meanwhile, the bond angles for interactions ($O_{71}H_{72}\cdots N_{47}$ (I) and $O_{73}H_{74}\cdots N_{48}$ (II)) were slightly enlarged for $S_0 \rightarrow S_1$ from 146.64° to 147.28°, which was further increased to 147.88° for $S_0 \rightarrow S_2$ excitation. Thus, the small interacting distance indicated six-membered intramolecular hydrogen bonding

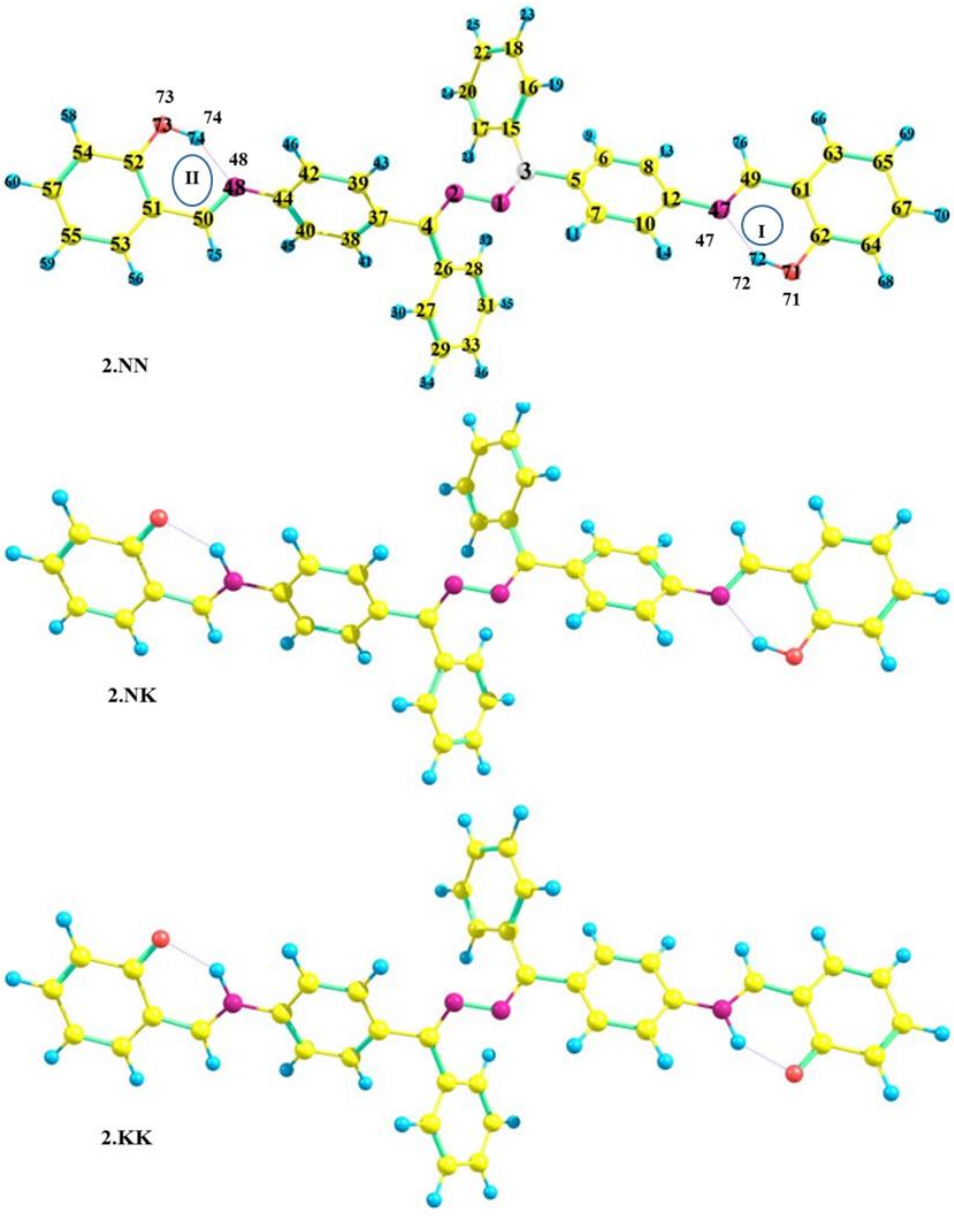

Figure 3.4. Optimized structure of **2** in three tautomeric forms at S_0 state

(IraHB) in S_0, S_1 and S_2 states. However, the decreased $O_{71}H_{72}\cdots N_{47}$ (I) and $O_{73}H_{74}\cdots N_{48}$ (II) bond lengths, and increased interacting bond angles imply that the IraHB strengthened in S_1 and S_2 states relative to S_0 state. The IraHBs also exist in tautomeric forms, and therefore, substantial geometrical parameters for IraHBs, such as bond lengths and bond angles, were noted and summarized in Table 3.2.

Table 3.2. The essential bond lengths (Å) and bond angles (∠OHN/°) of the compound **2** in **NN**, **NK**, and **KK** forms at S_0 S_1 and S_2 states, respectively

	2.NN			**2.NK**			**2.KK**		
	S_0	**S_1**	**S_2**	**S_0**	**S_1**	**S_2**	**S_0**	**S_1**	**S_2**
$O_{71}H_{72}$	0.9933	0.9960	0.9984	1.6952	1.6853	1.6786	1.6949	1.6851	1.6736
$H_{72}N_{47}$	1.7515	1.7347	1.7197	1.0409	1.0425	1.0458	1.0409	1.0424	1.0442
$O_{73}H_{74}$	0.9933	0.9960	0.9984	0.9932	0.9936	0.9941	1.6949	1.6851	1.6736
$H_{74}N_{48}$	1.7515	1.7347	1.7197	1.7519	1.7491	1.7460	1.0409	1.0424	1.0442
∠(I)	146.64	147.28	147.88	139.92	140.38	141.55	139.94	140.38	140.90
∠(II)	146.64	147.28	147.88	146.62	146.83	147.04	139.94	140.38	140.90

3.1.3.4 Frequency analysis

All the optimized structures have been confirmed through the frequency calculations. No tautomeric forms were found with imaginary frequency. Moreover, the FTIR signals are rightly related to IraHBs strength, and therefore, the spectral shifts to the characteristics of functional groups provided a closer eye on the nature of hydrogen bonding. Therefore, the simulated FTIR spectra in S_0, S_1, and S_2 states have been presented in Figure 3.5, which was further enlarged as an inset for O—H signals of compound **2**. The O–H stretching vibrational frequency was located at 3282 cm^{-1} at S_0 state, however, on photoexcitation to S_1 and S_2 states it was found at 3108 cm^{-1} and 3060 cm^{-1}, respectively. The relatively large red-shift in FTIR signal for $S_0 \rightarrow S_2$ (222 cm^{-1}) to $S_0 \rightarrow S_1$ (174 cm^{-1}) transition, implies that the IraHBs (OH···N (I) and OH···N (II)) was relatively more strengthened in the S_2 state compared to S_1 state.

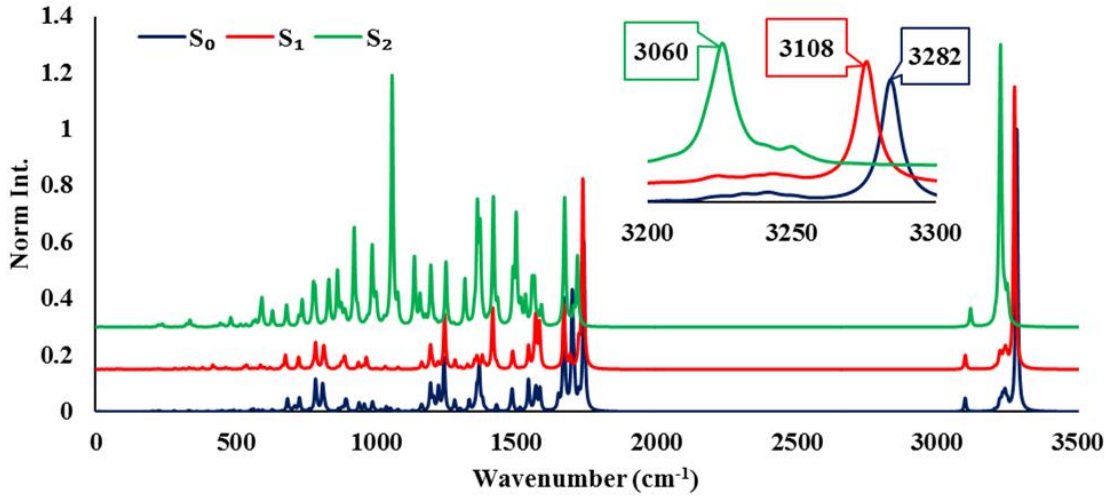

Figure 3.5. FTIR spectra of compound **2** at S_0, S_1, and S_2 states

3.1.3.5 AIM Analysis

Further, the prerequisite condition of IraHB existing within key conformer, for the presence of ESIPT was established *via* an effective and established Popelier criteria using Bader's quantum theory of atoms in molecules (QTAIM).[122] The determined topological parameters were within the limit of criteria and thus, established two IraHBs at S_0, S_1 and S_2 states for the primary structure of compound **2** (Table 3.3) and the type of BCPs was (3,-1). The positive value of Laplacian of electron density [$\nabla^2\rho(r_c)$] for the standard enol form of **2.NN** depicted electrostatic close shell interaction at S_0, S_1, and S_2 states. It was noted that the Laplacian of electron density for O—H···N interactions increased at S_1 and S_2 states relative to S_0 state, which signified the strengthening of IraHB. The degree of covalency and strength of the IraHB interactions were characterized according to Rozas' rules. All the listed BCPs has been ascertained as medium-range interactions with the partial covalent character at S_0, S_1 and S_2 states (Table 3.3**)**.[123] Moreover, the hydrogen bond energy was determined by Espinosa equation[111], which states that the interaction energy of H···X contact is defined as, $E_{HX} = V(r)/2$ at BCP, where V(r) is potential electron density at a bond critical point. The interaction energies for OH···N (I) and OH···N (II) were determined to be -12.49 kcalmol^{-1} at S_0 state. However, on photoexcitation, IraHBs were strengthened to -13.08 kcalmol^{-1}, and -13.67 kcalmol^{-1} for S_1 and S_2 states respectively.

Table 3.3. Topology parameters electron density(ρ), Laplacian electron density ($\nabla^2\rho$), potential energy density [V(r)], total energy density [H(r)], hydrogen bonding energy [E_{HB}(kcalmol^{-1})] at bond critical point of non-covalent interactions (D···HA) for standard enol form at S_0, S_1 and S_2 states of compound **2**

State	**Interaction**	**$\nabla^2\rho$**	**V(r)**	**G(r)**	**H(r)**	**E_{HB}**
S_0	$O_{71}H_2\cdots N_3$ (I)	0.1303	-0.0398	0.0362	-0.0036	-12.49
	$O_4H_5\cdots N_6$ (II)	0.1303	-0.0398	0.0362	-0.0036	-12.49
S_1	$O_1H_2\cdots N_3$ (I)	0.1340	-0.0417	0.0376	-0.0041	-13.08
	$O_4H_5\cdots N_6$ (II)	0.1340	-0.0417	0.0376	-0.0041	-13.08
S_2	$O_1H_2\cdots N_3$ (I)	0.1377	-0.0436	0.039	-0.0046	-13.67
	$O_4H_5\cdots N_6$ (II)	0.1377	-0.0436	0.039	-0.0046	-13.67

The molecular graphs of compound **2** for IraHBs were platted at S_0, S_1 and S_2 states and presented in Figure 3.6. The molecular graph for S_1 and S_2 state have the same nature, and therefore, the molecular graph of S_2 state was presented.

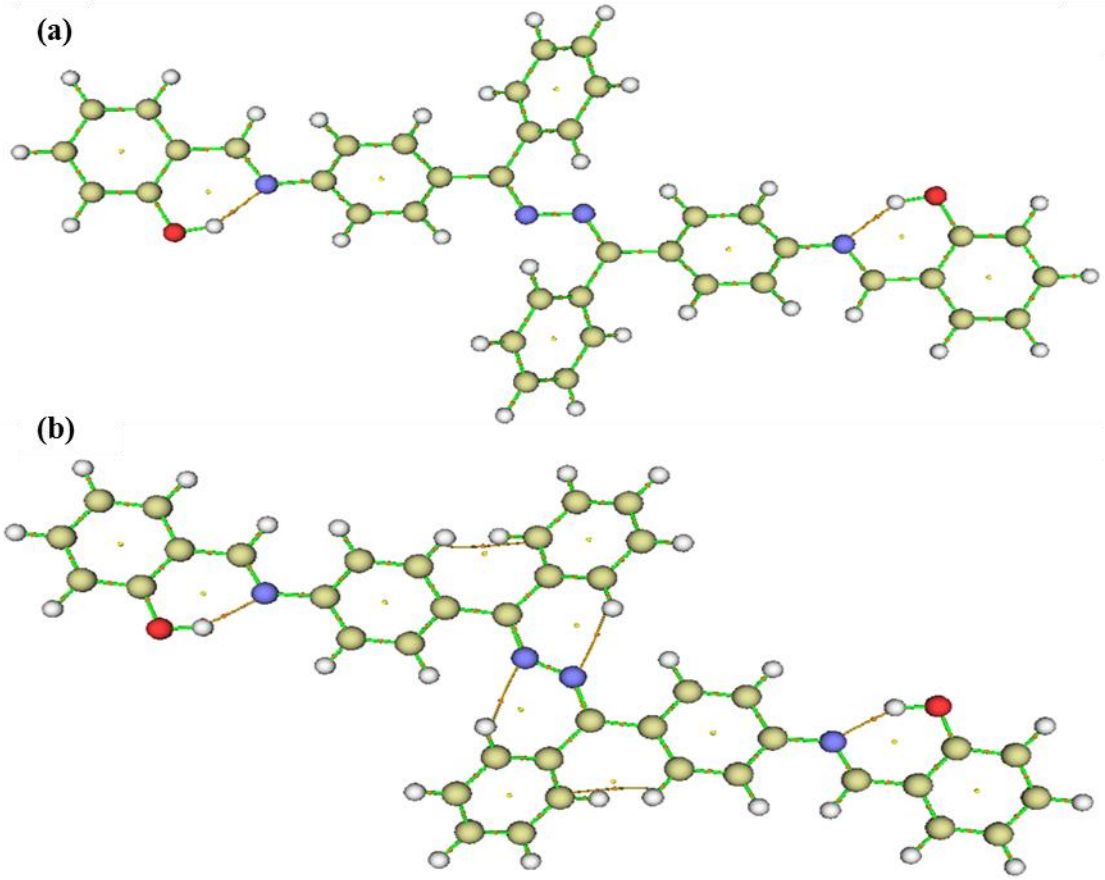

Figure 3.6. Molecular graph of compound **2** in (a) S_0 state (b) S_1 and S_2 states

3.1.3.6 Proton transfer mechanism

The compound **2** established two IraHBs and therefore, consisted of two sites for the ESIPT process. The intramolecular PT could take place through two pathways. The path I was the isomeric double proton transfer, where the H_{72} and H_{74} simultaneously moved from O_{71} and O_{73} towards the N_{47} and N_{48}, respectively. Path II was sequential proton transfer, where first H_{72} (or H_{74}) atoms transferred from the O_{71} (or O_{73}) to N_{47} (or N_{48}) to form **2.NK**, and then H_{74} (or H_{72}) atom transferred from O_{73} (or O_{71}) to N_{48} (or N_{47}) to form **2.KK**. Therefore, different possible tautomeric forms have been optimized at S_0, S_1 and S_2 states as per Scheme 3.2**.** Further, the free energy profile for all tautomeric forms (**2.NN, 2.NK, 2.KK**) stated a relationship as E(**2.NN**) < E(**2.NK)** < E(**2.KK**) for S_0 state, E(**2.NN**) < E(**2.NK)** < E(**2.KK**) for S_1 state and E(**2.NK**) < E(**2.KK)** < E(**2.NN**) for S_2 state (Table 3.6). The positive ΔG for **2.NN→2.NK, 2.NK→2.KK** and **2.NN→2.KK** in

S_0 and S_1 states depicted that intramolecular PT could not be allowed (where ΔG (**2.NN→2.NK)** = [G(**2.NK**)-G(**2.NN**)] and similarly calculated for other tautomeric conversions). On the other hand, the negative ΔG for **2.NN→2.NK** and **2.NN→2.KK** in S_2 state, indicated the possibility of ESIPT phenomenon.

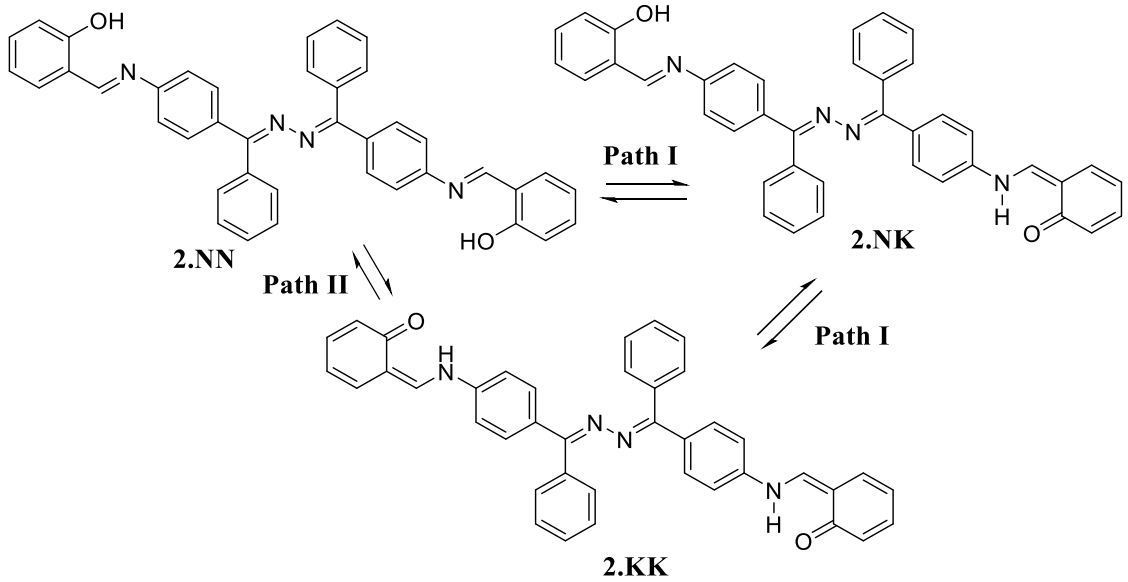

Scheme 3.2. Possible tautomeric forms of compound **2**.

Table 3.4. The relative free energy (ΔG/kcalmol^{-1}) of tautomers at S_0 S_1 and S_2 states based on the DFT and TDDFT methods, respectively

	2.NN			**2.NK**			**2.KK**		
	S_0	**S_1**	**S_2**	**S_0**	**S_1**	**S_2**	**S_0**	**S_1**	**S_2**
ΔG	0	49.89	72.39	5.15	73.96	55.14	10.33	60.43	60.43

The PECs were calculated for different tautomeric conversion as **2.NN→2.KK** (Path I) and **2.NN→2.NK; 2.NK→2.KK** (Path II) using constraints on interacting distances for OH···N (I) and OH···N (II) respectively in S_0, S_1 and S_2 states (Scheme 3.2). It was noted that the isomeric conversion with double PT in forwarding direction has energy barrier of 13.63 kcalmol^{-1}, 13.45 kcalmol^{-1} and 8.30 kcalmol^{-1}, while the reverse PT has a barrier of 3.81 kcalmol^{-1}, 3.47 kcalmol^{-1} and 20.84 kcalmol^{-1} in S_0, S_1 and S_2 states (Figure 3.7). The high energy barrier value for forwarding PT and low barrier value for reverse PT condemned the **2.NN→2.KK** tautomeric conversion for S_0 and S_1 states. On the other hand, the low energy barrier for forwarding PT and high value for reverse PT could possibly lead the ESIPT phenomenon. In addition, the sequential PT mechanism was also evaluated and presented in Figure 3.7. The energy barrier for forwarding ESIPT **(2.NN→2.NK; 2.NK→2.KK)** were determined to be 7.21 kcalmol^{-1} and 7.24 kcalmol^{-1},

respectively, while the calculated energy barrier for reverse ESIPT (**2.NK→2.NN; 2.KK→2.NK)** were determined to be 1.96 kcalmol^{-1} and 1.95 kcalmol^{-1} for S_1 state. The relatively high energy barrier for forwarding PT than reverse PT in S_1 state would not allow the sequential PT in S_1 state. Now, moving towards the S_2 state, the calculated energy barrier for the forward ESIPT (**2.NN→2.NK; 2.NK→2.KK)** were determined to be 5.24 kcalmol^{-1} and 7.04 kcalmol^{-1}, respectively while the reverse PT (**2.NK→2.NN; 2.KK→2.NK)** has a barrier of 22.47 kcalmol^{-1} and 1.74 kcalmol^{-1}, respectively. As the (**2.NN→2.NK)** tautomeric conversion has a low barrier for the forward PT reaction, while high barrier for reverse PT reaction, therefore, concluded as allowed tautomeric conversion in S_2 state. However, the (**2.NK→2.KK)** tautomeric conversion is not allowed for S_2 state due to the low barrier for the reverse PT than forwarding PT. Consequently, only a single proton transfer was allowed in S_2 states.

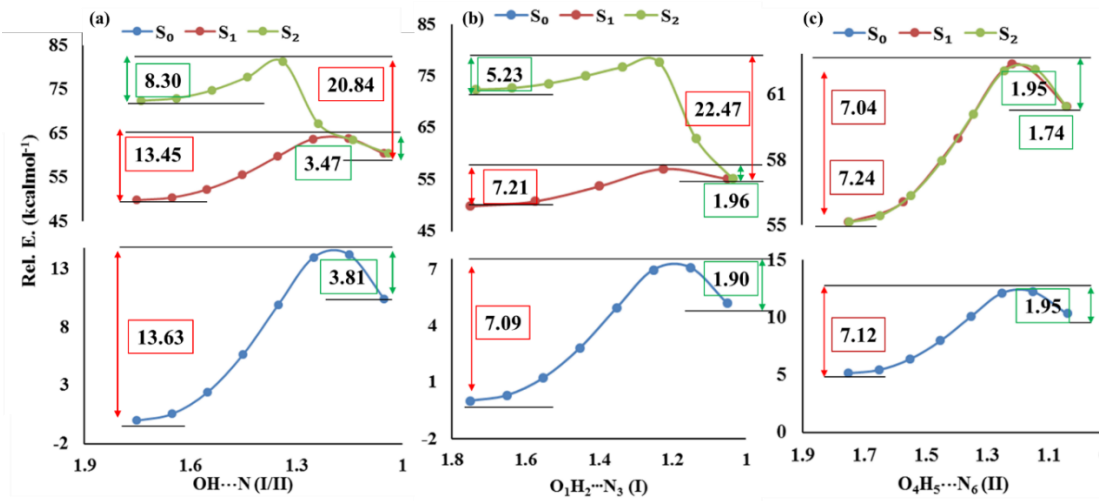

Figure 3.7. Energy profile of (a) **2.NN→2.KK;** (b) **2.NN→2.NK;** and (c) **2.NK→2.KK** tautomeric conversion at S_0, S_1 and S_2 states.

3.1.4 Conclusion

Herein, the dynamical ESIPT process of compound **2** was discussed theoretically using DFT and TDDFT method in details. Based on the calculations, the prerequisite condition of existence of intramolecular HB was established through AIM and FTIR. Furthermore, the geometrical parameters such as bond lengths, bond angles, and FTIR/AIM indicated that the HB strength increased in S_1 and S_2 states, which could prompt the ESIPT process. Moreover, the predicted absorption spectra and the electron density distribution on FMOs depicted the facilitation of ESIPT in the S_2 state. In order to study it thoroughly, the PECs were calculated as a function of constrained bond length of OH···N (I) and OH···N (II)

bond distances. The mechanism of PT was explored through two paths as concerted and sequential nature. The energy barrier for forward PT was Path I (13.45 $kcalmol^{-1}$) and Path II (7.21 $kcalmol^{-1}$, 7.24 $kcalmol^{-1}$), while for reverse PT was Path I (3.47 $kcalmol^{-1}$) and Path II (1.96 $kcalmol^{-1}$, 1.95 $kcalmol^{-1}$), which indicated that the PT was not allowed through concerted mechanism nor sequential mechanism. However, the energy barrier for the forward PT was Path I (8.30 $kcalmol^{-1}$) and Path II (5.23 $kcalmol^{-1}$, 7.04 $kcalmol^{-1}$), while for reverse PT was Path I (20.84 $kcalmol^{-1}$) and Path II (22.47 $kcalmol^{-1}$, 1.74 $kcalmol^{-1}$). Moreover, the energy relationship of tautomeric forms (**2.NN**, **2.NK**, **2.KK**) was **2.NK** < **2.KK** < **2.NN** at S_2 state. Therefore, the ESIPT could take place through the single PT in the S_2 state, which was schematically presented in Figure 3.8.

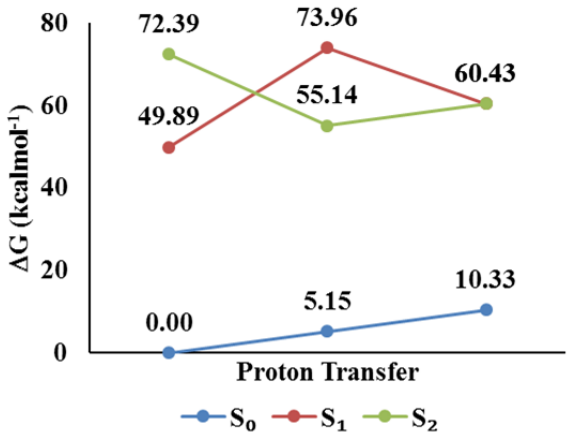

Figure 3.8. Possible mechanism of ESIPT for compound **2**

3.1.5 Experimental data

3.1.5.1 Synthesis of compound 1

To (4-aminophenyl)(phenyl)methanone (0.985 g, 5 mmol) dissolved in 10 mL ethanol and hydrazine hydrate (121 µL, 2.5 mmol) was added. The resulted reaction mixture was heated at 80 °C for **6** h. The reaction was monitored by TLC. After completion of reaction, reaction mixture was cooled to room temperature and the resulted light yellow colour solid was filtered off and washed with ethanol to get pure compound **1** in 75% yield.

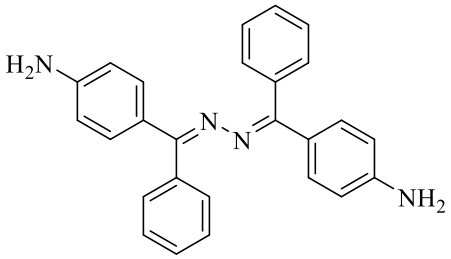

1

^{1}H NMR ($CDCl_3$ + DMSO-d_6, 400 MHz): δ (ppm) 7.52 (d, *J* = 7.60 Hz, 3H, ArH), 7.38-7.23 (m, 8H, ArH), 7.11 (d, *J* = 8.80 Hz, 3H, ArH), 6.58 (d, *J* = 8.40 Hz, 4H, ArH), 4.86 (s, 4H, NH_2); ^{13}C NMR ($CDCl_3$ + DMSO-d_6, 100 MHz): δ (ppm) 149.1, 148.8, 131.6, 131.2, 129.3, 128.6, 127.5, 127.4, 127.3, 122.2, 113.1, 112.6, 112.5; ESI-MS: m/e 391.2 (M^++1).

3.1.5.2 Synthesis of compound 2

The compound **1** (390 mg, 1 mmol) and salicylaldehyde (244 mg, 2 mmol) were dissolved in ethanol and heated at 80-85 °C. The progress of the reaction was monitored by TLC. The yellow-colored compound was formed after 12 h, which was further filtered off and washed with ethanol to get pure compound **2** in 70 % yield.

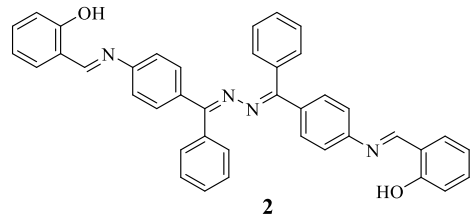

2

^{1}H NMR ($CDCl_3$, 400 MHz): δ (ppm) 13.18 (s, 1H, OH), 13.15 (s, 1H, OH), 8.69 (s, 1H, CH), 8.63 (s, 1H, CH) 7.51-7.32 (m, 17H, ArH), 7.25-7.05 (m, 5H, ArH), 6.98-6.93 (m, 4H, ArH); ^{13}C NMR ($CDCl_3$ + DMSO-d_6, 100 MHz): δ (ppm) 163.1, 162.8, 160.8, 158.9, 149.3, 148.4, 137.8, 136.4, 134.9, 133.6, 133.2, 132.3, 130.7, 129.6, 128.5, 127.7, 120.7, 120.5, 119.1, 118.9, 116.9. ESI-MS: m/e 599.2 (M^++1); Anal. Calcd. CHN for $C_{40}H_{30}N_4O_2$: C, 80.25; H, 5.05; N, 9.36, Found: C, 80.10; H, 5.41; N, 9.65.

3.2

Theoretical insight at the effect of electron-withdrawing –NO_2 group on excited state intramolecular proton transfer of symmetrical benzophenone azine based Schiff base

3.2.1 Abstract

In this study, the effect of –NO_2 as an electron-withdrawing group on photophysical properties of compound **3** was explored through experimental and theoretical methods. Likewise, compound **2**, compound **3** also exhibited dual emission due to the ESIPT phenomenon. Compound **3** has dual IraHBs suited at C_2 symmetry, and thus, possessed ESIPT process, which could rise three tautomeric forms as **3.NN**, **3.NK,** and **3.KK** for compound **3**. A very similar protocol was adopted to explain the ESIPT phenomenon as in the previous section 3.1. The computed free energy change (ΔG) for different tautomers established a relationship as E(**3.NN**) < E(**3.NK)** < E(**3.KK**) at S_0 state, and E(**3.NK)** < E(**3.KK**) < E(**3.NN**) at S_1 state. The negative ΔG (where ΔG(**3.NN→2.NK)** = [G(**3.NK**)-G(**3.NN**)) for **3.NN→3.NK** and **3.NN→3.KK** at S_1 state, indicated the possibility of ESIPT phenomenon, however higher energy barrier for **3.NN→3.KK** relative to **3.NN→3.NK** prompt ESIPT through single proton transfer mechanism.

3.2.2 Experimental section

3.2.2.1 Synthesis of compound 3

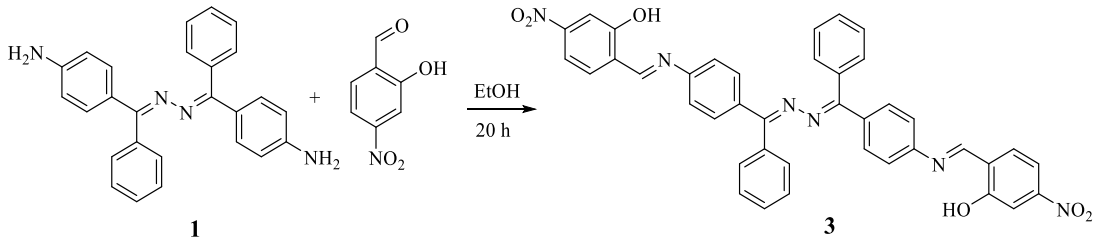

Scheme 3.3 Synthesis of compound **3**

Scheme 3.3 described the synthesis of compound **3**. The compound **1** (390 mg, 1 mmol) and 4-nitrosalicylaldehyde (334 mg, 2 mmol) were dissolved in ethanol and heated at 80-85 °C. The progress of the reaction was monitored by TLC. The yellow colored compound was formed after 24 h, which was further filtered off and washed with ethanol to get pure compound **3** in 65 % yield; m.pt. 267°C.

The ^{1}H NMR spectrum displayed resonating signals at δ 9.12 ppm as singlet due to 2H of —CH═, δ 8.70-8.64 ppm as multiplet for 16H of aromatic, δ 8.29-8.25 ppm as multiplet for 4H of aromatic, δ 7.42-7.14 ppm as multiplet for 2H aromatic, and ^{13}C NMR resonating signals at 163.5, 159.8, 149.6, 148.5, 143.8, 131.3, 132.8, 130.3, 130.1, 127.9, 127.7, 127.5, 126.6, 125.4, 124.8, 122.6, 116.6, 107.9 of aromatic carbons (ArCs). The ESI-MS (m/e) peak was observed at 689.7 (M^{+}+1), which was in close agreement to calculated m/z (688.7) and thus, confirm the formation of compound **3.**

3.2.3 Results and discussion

3.2.3.1 Photophysical properties

Photophysical properties of compound **3** were studied through absorption and emission spectroscopic techniques. The absorption spectrum of compound **3** (20 µM, CH_3CN) displayed an absorption peak at 350 nm. On excitation at 350 nm, compound **3** (20 µM, CH_3CN) displayed dual emission bands at 415 and 525 nm accomplished by Stokes` shift of 65 and 175 nm, respectively (Figure 3.9). The characteristic dual emission of compound **3** indicates the ESIPT phenomenon. The high energy emission peak at 415 nm was ascribed due to its standard enol emission, while the low energy emission was due to excited state intramolecular proton transfer (ESIPT). Compound **3** contained proton donor phenolic and proton acceptor imine nitrogen, and therefore, the proton transfer from the donor site to acceptor could raise the ESIPT phenomenon. The emission for compound **3** was observed to be stronger than compound **2**, which could be due to the strengthening of IraHBs.

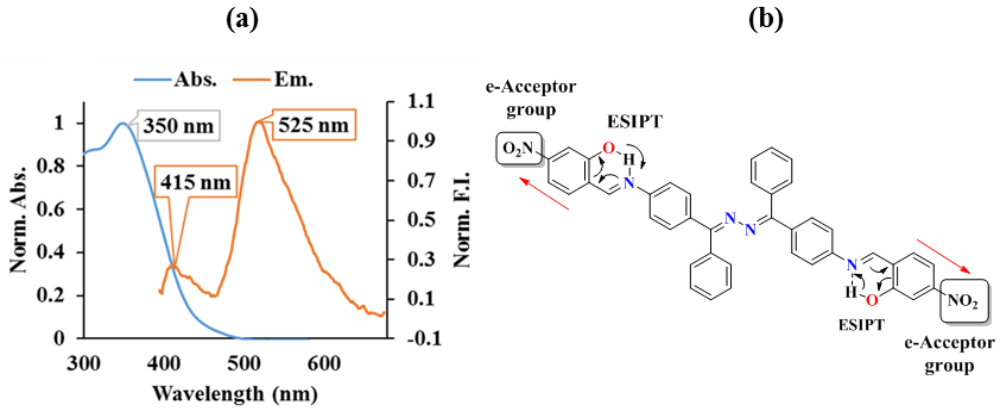

Figure 3.9 (a) Normalized absorption and fluorescence spectra of compound **3** (20 µM, CH_3CN); (b) ESIPT present in compound **3**

3.2.3.2 Electronic spectra and charge distribution

In order to complement the experimental results of absorption spectra and to determine the origin of spectra, the first three excitations were calculated for compound **3**. The compound **3** was optimized at S_0 state using the DFT method using cam-B3LYP/6-31+g(d,p) and excitations were calculated using TDDFT method was used at the same level of theory. First, three Frank-Condon (FC) excited states were calculated and has been presented along with predicted absorption peak, oscillation strength, symmetry and involved FMOs in Table 3.5.

Table 3.5. The electronic excitation wavelength (λ/nm), oscillator strengths (f) and compositions of the low-lying singlet excited states (contributing MOs) of the compound **3**

Transition	**λ_{calc}**	**λ_{exp}**	**Symmetry**	**f**	**Major MOs Contribution**	
$S_0 \rightarrow S_1$	360.42	350	Singlet-A	2.1744	H→L	44 %
$S_0 \rightarrow S_2$	348.50		Singlet-A	0.0215	H-1→L	35 %
$S_0 \rightarrow S_3$	338.28		Singlet-A	0.0017	H-3→L	24 %
					H-1→L+2	24 %

The first FC transition ($S_0 \rightarrow S_1$) was calculated at 360 nm, with highest oscillation strength of 2.1744, and the transition resulted majorly from the HOMO→LUMO transition. The $S_0 \rightarrow S_2$ and $S_0 \rightarrow S_3$ excitation were calculated at 348 nm, and 338 nm with oscillation strength of 0.0215 and 0.0017, respectively. The contributing MOs were displayed in Table 3.5. Further, the FMOs were graphically presented in Figure 3.10.

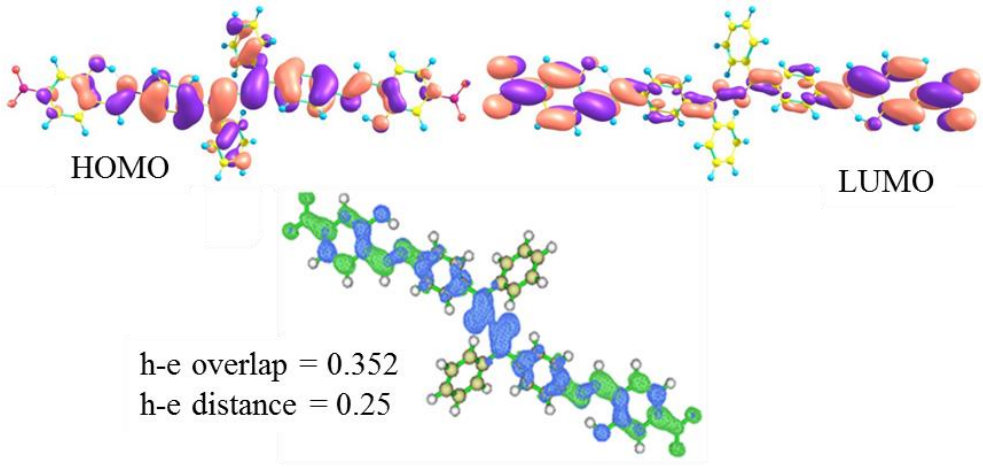

Figure 3.10. (a) FMOs of compound **3** contributing to electronic excitation and (b) hole-electron distribution for $S_0 \rightarrow S_1$.

Due to high oscillation strength for $S_0 \rightarrow S_1$ excitation, only HOMO and LUMO orbitals were considered. The HOMO was distributed over the benzophenone skeleton and

extended up to Schiff base linkage; on the other hand, LUMO has an electronic distribution over the benzophenone unit and extended up to ─NO_2 functional groups (Figure 3.10**)**. The electronic distribution clearly depicted that the π and π*-character of HOMO and LUMO, respectively and thus, the transition could be assigned as π→π* transition. Also, the partial charge transfer was also observed towards ─NO_2 from azine core. Further, the quantitative nature of excitations was measured through hole-electron distribution (Figure 3.10). The distance between the centroid of hole and electron center was found to be 0.258 Å, while the overlap integral was 0.352. The overlap integral value with little spatial separation of hole-electron distribution revealed the transition as the local excitation transition. The hole-electron distribution clearly depicted that the transition has an electron density shift from the azine unit to the ─NO_2 unit.

3.2.3.3 Geometrical parameters

Compound **3** was optimized in its three tautomeric forms **3.NN**, **3.NK**, **3.KK** at S_0, and S_1 states using the DFT and TDDFT methods. The optimized structures were validated for the local minima through the absence of imaginary frequency and have been presented in Figure 3.11. Compound **3** attained C_2 symmetry like compound **2**, and thus own the similar bond lengths for $O_{69}H_{70}$ and $H_{70}\cdots N_{47}$ as well as $O_{71}H_{72}$ and $H_{72}\cdots N_{48}$ and bond angles ($O_{69}H_{70}\cdots N_{47}$ and $O_{71}H_{72}\cdots N_{48}$) values at S_0, and S_1 states. For better understanding, the hydrogen donor and acceptor units were labeled, as shown in Figure 3.11, and the interactions were categorized as I and II. The important geometrical parameters related to IraHB were summarized in Table 3.6.

Table 3.6. The essential bond lengths (Å), bond angles (°) of compound **3** in **3.NN**, **3.NK**, and **3.KK** tautomeric structures at S_0 and S_1 states, respectively

	3.NN		**3.NK**		**3.KK**	
	S_0	**S_1**	**S_0**	**S_1**	**S_0**	**S_1**
O—H(I)	0.9982	0.9999	1.7156	1.7912	1.7162	1.7930
H—N(I)	1.7238	1.7132	1.0396	1.0345	1.0395	1.0344
O—H(II)	0.9982	0.9999	0.9982	0.9982	1.7162	1.7930
H—N(II)	1.7238	1.7132	1.7235	1.7235	1.0395	1.0344
∠(I)	146.95	147.49	139.49	137.99	139.48	137.92
∠(II)	146.95	147.49	146.95	146.94	139.48	137.92

As listed, the bond lengths for O_{69}—H_{70} and O_{71}—H_{72} were increased by ~0.0017 Å from 0.9882 at S_0 state to ~0.9999 Å at S_1 state. On the other hand, the H_{70}—N_{47} and H_{72}—N_{48}

bond lengths decreased by 0.0106 Å from 1.7238 Å at S_0 state to 1.7132 Å at S_1 state. Meanwhile, the bond angles for interactions were enlarged for $S_0 \rightarrow S_1$ from 146.95° to 147.49°. Thus, the small interacting distance indicated six-membered IraHB at S_0 and S_1 states. However, the decreased IraHB distances and increased interacting bond angles for OH···N (I/II), implied that the IraHBs strengthens at S_1 state relative to S_0 state.

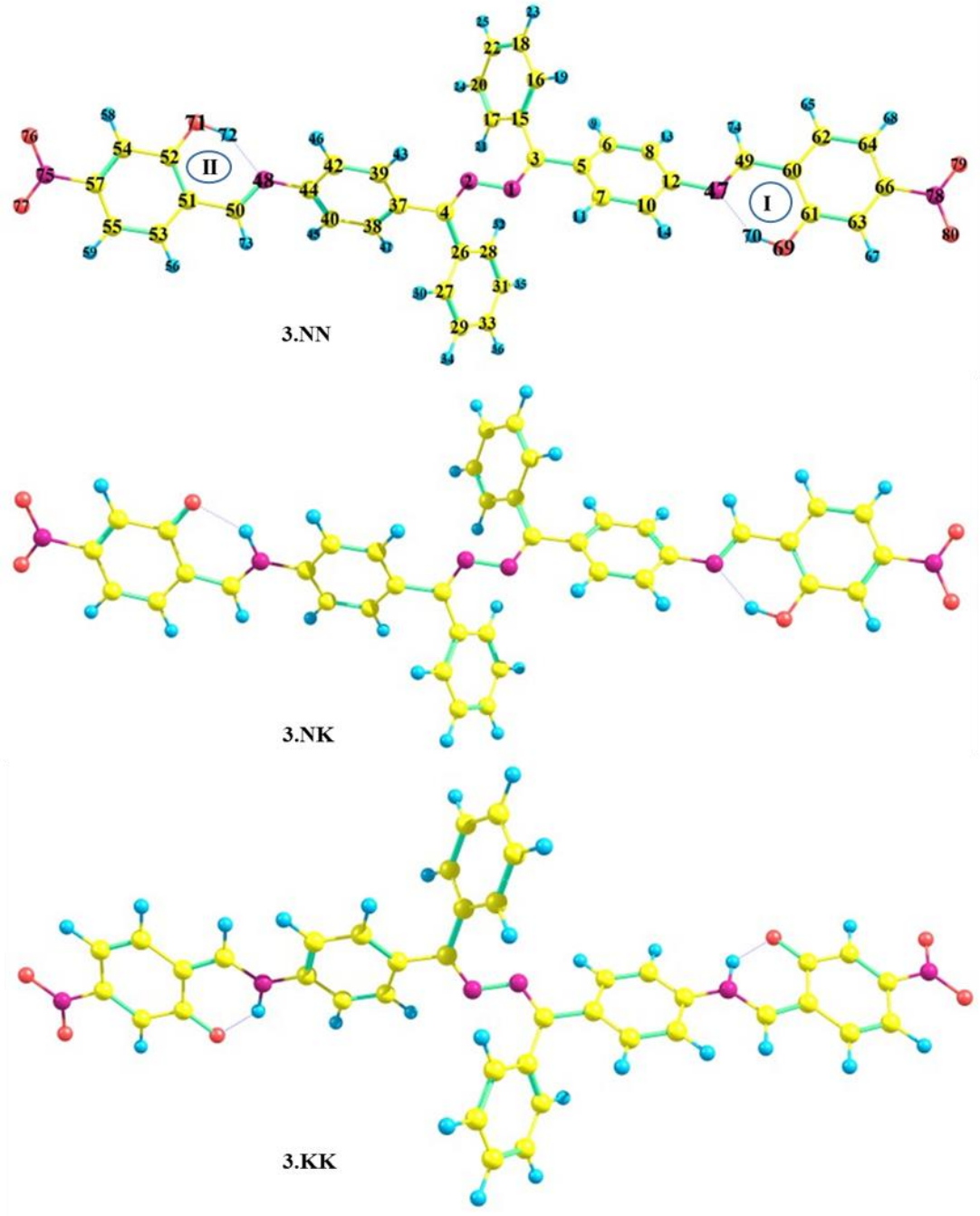

Figure 3.11. Optimized structure of **3** at S_0 states

3.2.3.4 Frequency analysis

The simulated FTIR spectra at S_0 and S_1 states have been presented in Figure 3.12, which was further enlarged as an inset for O—H signals of compound **3**. The O–H stretching vibrational frequency was located at 3181 cm^{-1} at S_0 state, which was calculated at 2974 cm^{-1} at S_1 state. Further, the red-shift in FTIR signal for $S_0 \rightarrow S_1$ (207 cm^{-1}) transition, implies that the IraHBs (OH···N (I) and OH···N (II)) was relatively more strengthened at the S_1 state relative to S_0 state.

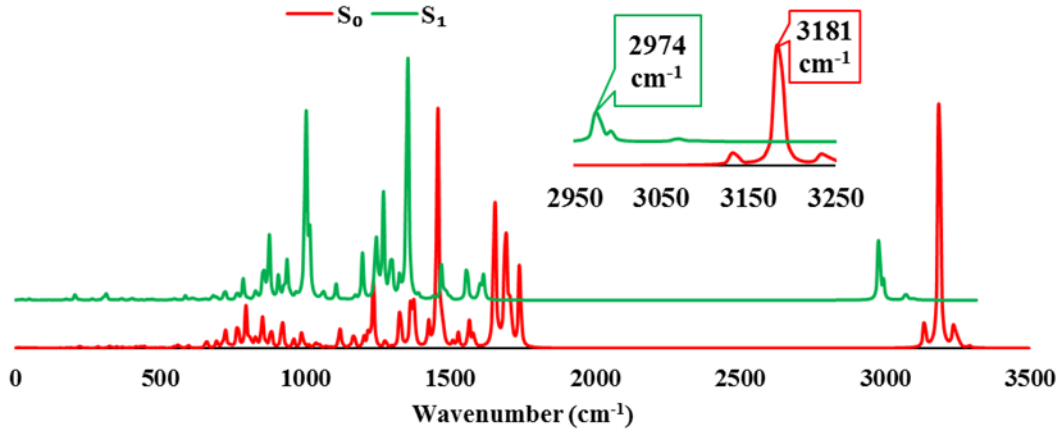

Figure 3.12. FTIR spectra of compound **3** at S_0, and S_1 states

3.2.3.5 AIM Analysis

Further, the existence of hydrogen bonding was examined based on Popelier criteria, and determined topological parameters were within the limit of criteria (Table 3.7), and the type of BCPs was (3,-1). The positive value of Laplacian of electron density [$\nabla^2\rho(r_c)$] for standard enol form of compound **3** depicted electrostatic close shell interaction at S_0, and S_1 states. The degree of covalency and strength of the IraHB interactions were characterized according to Rozas' rules, which established that the determined parameters for listed BCPs ascertained medium-range interactions with the partial covalent character ($\nabla^2\rho(r_c) > 0$ and $H(r) < 0$) at S_0, and S_1 states (Table 3.7**)**.[123] The interaction energies for OH···N (I) and OH···N (II) were determined to be -13.37 $kcalmol^{-1}$ at S_0 state. However, on photoexcitation, IraHBs were strengthened to -15.11 $kcalmol^{-1}$ at S_1 states.

Table 3.7. Topology parameters electron density(ρ), Laplacian electron density ($\nabla^2\rho$), potential energy density [V(r)], total energy density [H(r)], hydrogen bonding energy [E_{HB}(kcalmol^{-1})] at bond critical point of non-covalent interactions (D···HA) for standard enol form in S_0, and S_1 states of compound **3**

State	Interaction	$\nabla^2\rho$	V(r)	G(r)	H(r)	E_{HB}
S_0	$O_{69}H_{70}\cdots N_{47}$	0.1360	-0.0426	0.0383	-0.0043	-13.37
	$O_{71}H_{72}\cdots N_{48}$	0.1360	-0.0426	0.0383	-0.0043	-13.37
S_1	$O_{69}H_{70}\cdots N_{47}$	0.1444	-0.0482	0.0423	-0.0059	-15.11
	$O_{71}H_{72}\cdots N_{48}$	0.1444	-0.0482	0.0423	-0.0059	-15.11

The molecular graphs of compound **3** at S_0 and S_1 states were plotted for BCPs and bond paths (Figure 3.13)**.** Also, there was the rise of new IraHBs at S_1 state in the form of ArH···N; however, at present, only OH···N interactions were discussed.

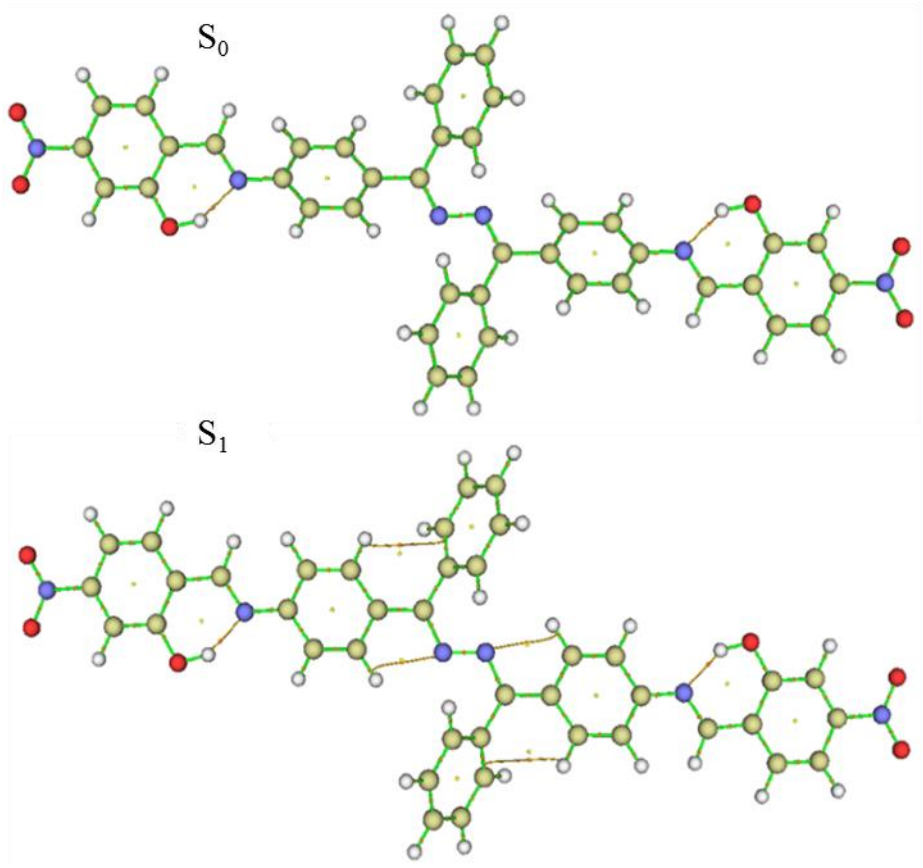

Figure 3.13. Molecular graph of compound **3** at S_0 and S_1 states

3.2.3.6 Proton transfer mechanism

The dual IraHB and proton transfer could raise three tautomeric forms (**3.NN**, **3.NK**, and **3.KK**) of compound **3,** which were displayed in Scheme 3.4. As previously discussed in

Section 3.1.3.6, the proton transfer mechanism in compound **3** could follow two pathways. The path I was the isomeric double proton transfer, while Path II was sequential proton transfer. Therefore, the free energy profile for all tautomeric forms (**3.NN, 3.NK, 3.KK**) were calculated at S_0 and S_1 states and stated a relationship as E(**3.NN**) < E(**3.NK)** < E(**3.KK**) at S_0 state, and E(**3.NK)** < E(**3.KK**) < E(**3.NN**) at S_1 state. The relative energy of tautomeric forms was presented in Table 3.8. The positive ΔG for **3.NN→3.NK, 3.NK→3.KK** and **3.NN→3.KK** at S_0 state depicted that intramolecular PT could not be allowed (where ΔG(**3.NN→3.NK)** = [G(**3.NK**)-G(**3.NN**)] and similarly calculated for other tautomeric conversions). On the other hand, the negative ΔG for **3.NN→3.NK** and **3.NN→3.KK** at S_1 state, indicated the possibility of intramolecular PT. However, the positive ΔG for **2.NK→2.KK** condemned the tautomeric conversion and hence, intramolecular PT. Therefore, free energy relationship stated that the preferential tautomer conversions at S_1 state were **3.NN→3.NK** and **3.NN→3.KK.**

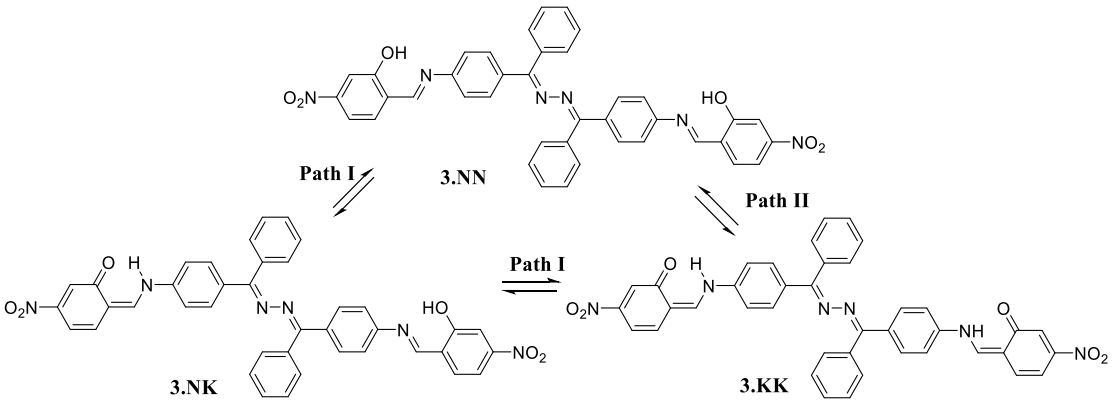

Scheme 3.4 Possible tautomeric forms of compound **3**

Table 3.8. The relative free energy ΔG (kcalmol^{-1}) of tautomeric forms at S_0 and S_1 states based on the DFT and TDDFT methods, respectively

	3.NN		**3.NK**		**3.KK**	
	S_0	**S_1**	**S_0**	**S_1**	**S_0**	**S_1**
ΔG	0	66.46	2.75	61.57	5.50	64.33

The **3.NN→3.NK** tautomeric conversion involved the transfer of H_{70} (or H_{71}) atoms from the O_{69} (or O_{72}) to N_{47} (or N_{48}), while **3.NN→3.KK** tautomeric conversion involved the isomeric proton transfer of H_{70} and H_{71}) atoms from the O_{69} and O_{72} to N_{47} and N_{48}, respectively. Therefore, potential energy curves were calculated using constraints on interacting distances for $O_{69}H_{70}\cdots N_{47}/O_{71}H_{72}\cdots N_{48}$ at S_0, and S_1 states. It was noted that PT in forwarding direction of ESIPT has an energy barrier of 2.15 kcalmol^{-1}, while

reverse PT has a barrier of 4.96 kcalmol^{-1} for **3.NN→3.NK** tautomeric conversion (Figure 3.14). On the other hand, **3.NN→3.KK** tautomeric conversion has a barrier of 5.22 kcalmol^{-1} and 7.34 kcalmol^{-1} for forward and reverse ESIPT. The low energy barrier for forwarding PT for **3.NN→3.NK** relative to **3.NN→3.KK** at S_1 state could lead the ESIPT phenomenon *via* single proton transfer mechanism.

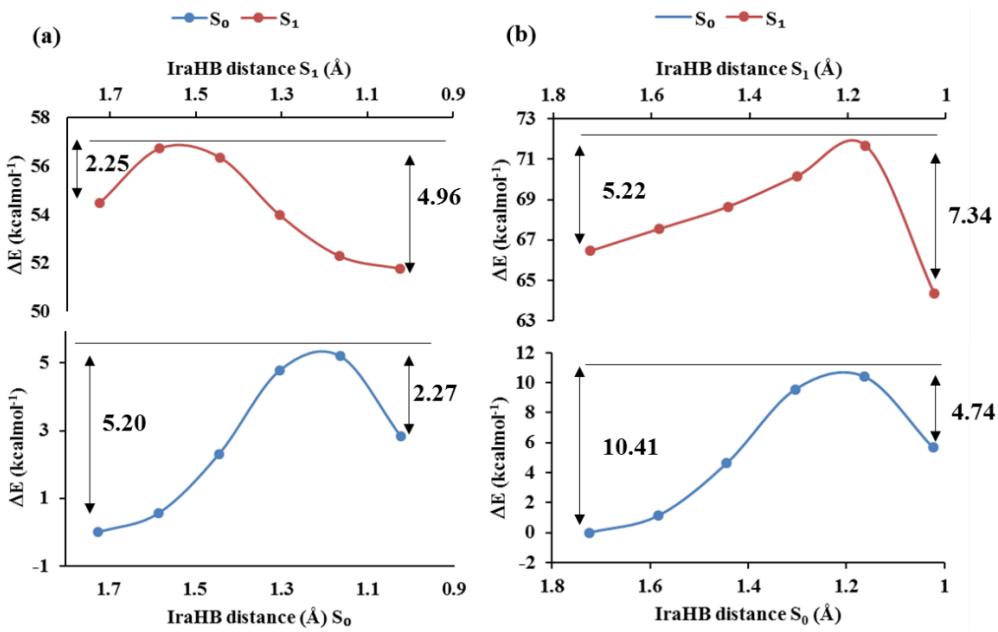

Figure 3.14. Energy profile of (a) **3.NN→3.NK**, (b) **3.NN→3.KK** tautomeric conversions at S_0, and S_1 states.

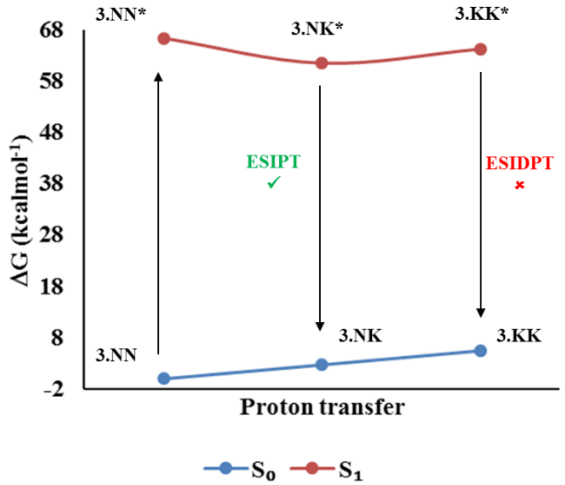

Figure 3.15. Possible mechanism of ESIPT for compound **3**

3.2.4 Conclusion

Herein, the dynamical ESIPT process of compound **3** was discussed experimentally and theoretically. Based on the calculations, the prerequisite condition of existence of IraHB was established through AIM, FTIR. Furthermore, the geometrical parameters such as

bond lengths, bond angles, and FTIR/AIM analysis indicated the strengthening of IraHB at S_1 state, which prompted the ESIPT process. Moreover, the predicted absorption spectra and the electron density distribution on FMOs depicted the facilitation of ESIPT phenomenon. The relative free energy and PECs favored the **3.NN→3.NK** tautomeric conversion at S_1 state. Therefore, the ESIPT could take place through the single PT at the S_1 state, which was schematically presented in Figure 3.15.

3.2.5 Experimental data

3.2.5.1 Synthesis of compound 3

The compound **1** (390 mg, 1 mmol) and 4-nitrosalicylaldehyde (334 mg, 2 mmol) were dissolved in ethanol and heated at 80-85 °C. The progress of the reaction was monitored by TLC. The yellow-colored compound was formed after 24 h, which was further filtered off and washed with ethanol to get pure compound **3** in 65 % yield; m.pt. 267°C.

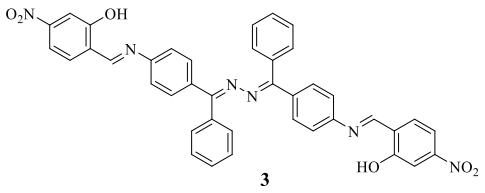

3

^{1}H NMR ($CDCl_3$ + DMSO-d_6, 400 MHz): δ (ppm) 9.12 ppm (s, 2H, ═CH═), 8.70-8.64 (m, 16H, ArH) 8.29-8.25 (m, 4H, ArH) 7.42-7.14 (m, 2H, ArH).^{13}C NMR ($CDCl_3$ + DMSO-d_6, 100 MHz): δ (ppm) 163.5, 159.8, 149.6, 148.5, 143.8, 131.3, 132.8, 130.3, 130.1, 127.9, 127.7, 127.5, 126.6, 125.4, 124.8, 122.6, 116.6, 107.9 (ArCs). ESI-MS (m/z) = 689.7 (M^++1); calculated m/z (688.7).

3.3

The supremacy of charge transfer over proton transfer in symmetrical bis(diphenylmethylene)hydrazine based Schiff base

3.3.1 Abstract

In this section, we study the effect of $–NEt_2$ as an electron-donating group on photophysical behavior of bis(diphenylmethylene)hydrazine-based Schiff base (**4**). Compound **4** displayed yellow absorption at 410 nm and an emission peak at 500 nm, which was accompanied by Stokes' shift of ~90 nm. The study involved an explanation for the origin of photophysical behavior. Like compound **2** and **3**, compound **4** too contained dual intramolecular hydrogen bonding (IraHB) suited at C_2 symmetry and thus, two ESIPT sites. Therefore, three tautomeric forms as **4.NN**, **4.NK,** and **4.KK** for compound **4** could be formed through PT, likely happened in compound **2** and **3**. However, the $–NEt_2$ group present in compound **4** have the tendency to push the electron density towards the electron loving center. Therefore, its presence will generate the intramolecular charge transfer (ICT). The presence of IraHBs and ICT constituents could tune the photophysical properties based on ESIPT or/and ESICT phenomenon. Further, the relative free energy change (ΔG) was calculated for tautomeric forms. It was depicted that the **4.NN** was the most stabilized form than **4.NK**, and **4.KK** at S_0 and S_1 states, and thus, exclude the chances of ESIPT phenomenon. All the calculations were based on long-range hybrid functional (cam-B3LYP) time-dependent density functional theory coupled integral equation formalism polarization continuum model (IEFPCM) imitated the mechanistic insight of photophysical response. The ESICT phenomenon was studied and established in the presence of acid and base. The introduction of acid to compound **4** preferentially protonated the imino center and resulted in the monocationic and dicationic protonated form. The monocationic form (**4_HSB**) displayed absorption and emission peak at 455 nm and 520 nm, respectively. The dicationic form (**4_2HSB**) displayed absorption peak at 455 nm, 335 nm and 260 nm, and emission peak at 490 nm. On the other hand, in case of addition of base to compound **4**, the absorption was increased at 415 nm, and emission was blue-shifted to 480 nm for monoanionic form (**4_O$^-$**). However, for dianionic form (**4_O$^-$O$^-$**), redshifted absorption peak and emission peak was observed at 435 nm and 620 nm, respectively. The FMOs analysis revealed the shifting of electron density and thus, endorsed the ESICT phenomenon.

3.3.2 Experimental section

Scheme 3.3 described the synthesis of compound **4**. The compound **1** (390 mg, 1 mmol) and 4-(diethylamino)-2-hydroxybenzaldehyde (386 mg, 2 mmol) were dissolved in ethanol and heated at 80-85 °C. The progress of the reaction was monitored by TLC. The yellow-colored compound was formed after 20 h, which was further filtered off and washed with ethanol to get pure compound **4** in 70 % yield; m.pt. 227°C.

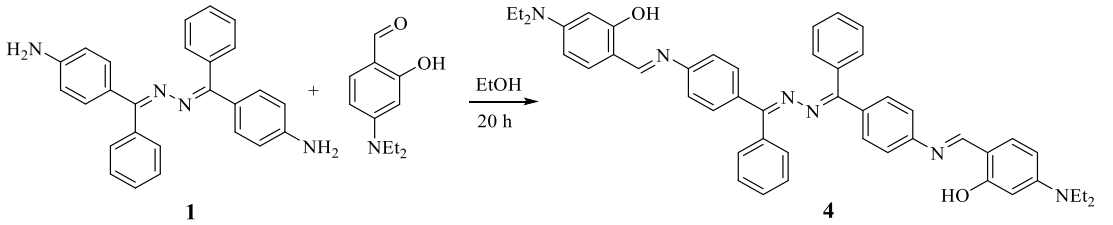

1 **4**

Scheme 3.5 Synthesis of compound **4**

The ^{1}H NMR displayed resonating signals at δ 13.79 ppm as singlet due to 2H of ―OH, δ 8.47 ppm as singlet due to 2H of ―CH═, δ 7.52-7.30 ppm as multiplet due to 16H of aromatic, δ 7.18-7.13 ppm as multiplet for 4H aromatic, δ 6.26-6.16 ppm as multiplet due to 2H of aromatic, 3.42-3.39 as quartet due to 8H of –CH_2, 1.23-1.18 as triplet for CH_3 and ^{13}C NMR resonating signals at δ 161.5, 158.8, 149.1, 146.5, 138.2, 132.8, 132.4, 129.2, 127.9, 127.2, 126.7, 124.8, 122.8, 122.1, 119.7, 118.9, 111.6, 110.9 due to aromatic carbons (ArCs) 47.9 due to CH_2, 15.9 due to CH_3. The ESI-MS (m/e) peak was observed at 741.9 (M^++1), which was in close agreement to calculated m/z (740.9) and thus, confirm the formation of compound **4.**

3.3.3 Results and discussion

3.3.3.1 Photophysical properties of compound 4

The measured steady-state absorption and emission spectrum of compound **4** (20 µM, CH_3CN) displayed peaks at 415 nm and 500 nm, respectively (Figure 3.16). The compound **4** contained double IraHBs, which could rise to ESIPT phenomenon, likely compound **2** and **3**, respectively. In addition, compound **4** contained –NEt_2 unit with a capacity of pushing electron density towards the hydrazine unit, which could raise the ESICT phenomenon. The possible phenomenon in the excited state was demonstrated in Figure 3.16**.** Therefore, the modest Stokes' shift of 85 nm could be tuned by the presence of ESICT or ESIPT suppressed ESICT.

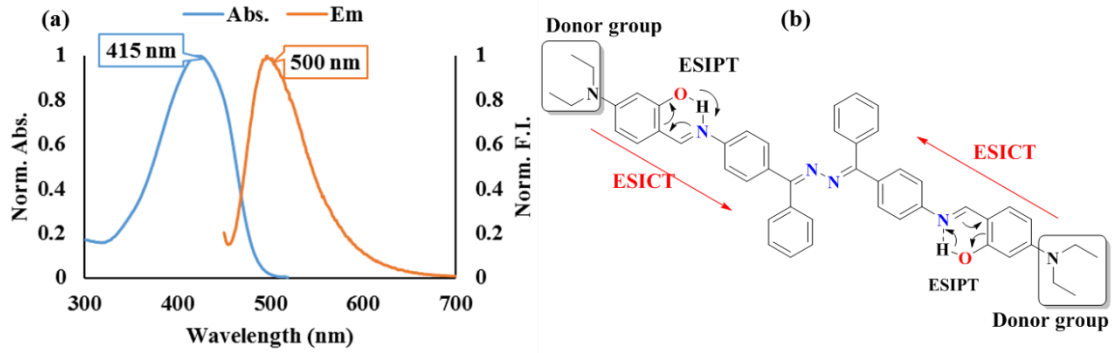

Figure 3.16. (a) Normalized absorption and fluorescence spectra of compound **4** (20 μM, CH_3CN); (b) The possible photophysical mechanism in compound **4**.

3.3.3.2 Absorption spectra and electronic distribution

The experimental results were complemented by predicting the Frank-Condon vertical excitation energies on S_0 optimized geometry of compound **4**, and corresponding symmetry, oscillation strength, and CI value of contributing molecular orbitals were summarized in Table 3.9. The nature of the electronically excited state, qualitative/quantitative charge distribution was discussed.

Table 3.9. The electronic excitation wavelength (nm), oscillator strengths (f) and compositions of the low-lying singlet excited states (contributing MOs) of the compound **4**

$S_0 \rightarrow S_n$	λ (nm)	Symmetry	f	Contributing MOs (%)	
$S_0 \rightarrow S_1$	364.19	Singlet-A	3.4615	H→L	55
$S_0 \rightarrow S_2$	345.59	Singlet-A	0.0157	H-1→L	30
				H-3→L	25
$S_0 \rightarrow S_3$	328.39	Singlet-A	0.0072	H→L+2	32

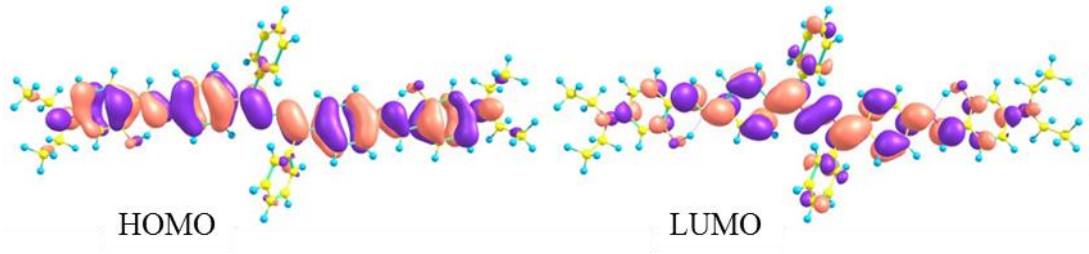

Figure 3.17. Frontier molecular orbitals of compound **4**

The first FC transition ($S_0 \rightarrow S_1$) was calculated at 364 nm, with highest oscillation strength of 3.4615, and the transition resulted majorly from the HOMO→LUMO transition. The $S_0 \rightarrow S_2$ excitation was calculated at 345 nm, with oscillation strength of 0.0157 and was resulted from the HOMO-1→LUMO, and HOMO-3→LUMO transition,

with a contributing factor of 30 %, and 25%, respectively. The $S_0 \rightarrow S_3$ excitation was calculated at 328 nm, with oscillation strength of 0.0072 and was resulted from the HOMO→LUMO+2 transition with a contributing factor of 32 %.

Due to high oscillation strength for $S_0 \rightarrow S_1$ excitation, only HOMO and LUMO orbitals were considered as contributing FMOs and therefore, presented in Figure 3.17. The HOMO was distributed over the diphenylmethylene hydrazine skeleton and extended up to Schiff base linkage; while, LUMO has an electronic distribution over the hydrazine unit and attached phenyl rings. The electronic distribution clearly depicted that the electron density was shifted from $–NEt_2$ unit to the hydrazine core unit, and therefore, $S_0 \rightarrow S_1$ excitation was assigned as intramolecular charge transfer (ICT) transition.

3.3.3.3 Geometrical parameters

In order to understand the possible phenomenon of PT along with ICT, compound **4** was optimized in possible tautomeric forms **4.NN**, **4.NK**, and **4.KK** at S_0 and S_1 states using DFT and TDDFT methods, respectively. The optimized structures were validated for the local minima through the absence of imaginary frequency and presented in Figure 3.18. Compound **4** attained C_2 symmetry like compound **2** and **3**, and thus, own the similar bond lengths ($O_{69}H_{70}$ and $H_{70}\cdots N_{47}$ as well as $O_{71}H_{72}$ and $H_{72}\cdots N_{48}$) and bond angles ($O_{69}H_{70}\cdots N_{47}$(I) and $O_{71}H_{72}\cdots N_{48}$(II)) values in S_0, and S_1 states. The bond lengths of atoms involved in IraHB were summarized in Table 3.10. As listed, the bond lengths and bond angles for interactions ($O_{67}H_{70}\cdots N_{47}$ and $O_{71}H_{72}\cdots N_{48}$) were not changed significantly on photoexcitation to S_1 state.

Table 3.10. The essential bond lengths (Å) and bond angles (°) of compound **4** in **4.NN**, **4.NK**, and **4.KK** tautomeric forms and their relative free energy ΔG ($kcalmol^{-1}$) at S_0 and S_1 states based on the DFT and TDDFT methods, respectively

	4.NN		**4.NK**		**4.KK**	
	S_0	**S_1**	**S_0**	**S_1**	**S_0**	**S_1**
O_{69}—H_{70}	1.002	1.002	1.7156	1.7912	1.7162	1.7930
H_{70}—N_{47}	1.705	1.705	1.0396	1.0345	1.0395	1.0344
O_{71}—H_{72}	1.002	1.002	0.9982	0.9982	1.7162	1.7930
H_{72}—N_{48}	1.705	1.705	1.7235	1.7235	1.0395	1.0344
$\angle O_{69}H_{70}N_{47}$	148.89	148.89	139.49	137.99	139.48	137.92
$\angle O_{71}H_{72}N_{48}$	148.89	148.89	146.95	146.94	139.48	137.92
ΔG	0	64.92	3.36	67.40	6.72	69.87

Further, the free energies were calculated for all tautomeric forms (**4.NN, 4.NK,** and **4.KK**) and established a relationship as G(**4.NN**) < G(**4.NK)** < G(**4.KK**) at S_0 and S_1 states (Table 3.10**)**. The positive ΔG for **4.NN→4.NK, 4.NK→4.KK,** and **4.NN→4.KK** at S_0 and S_1 states depicted that intramolecular PT could not be allowed.

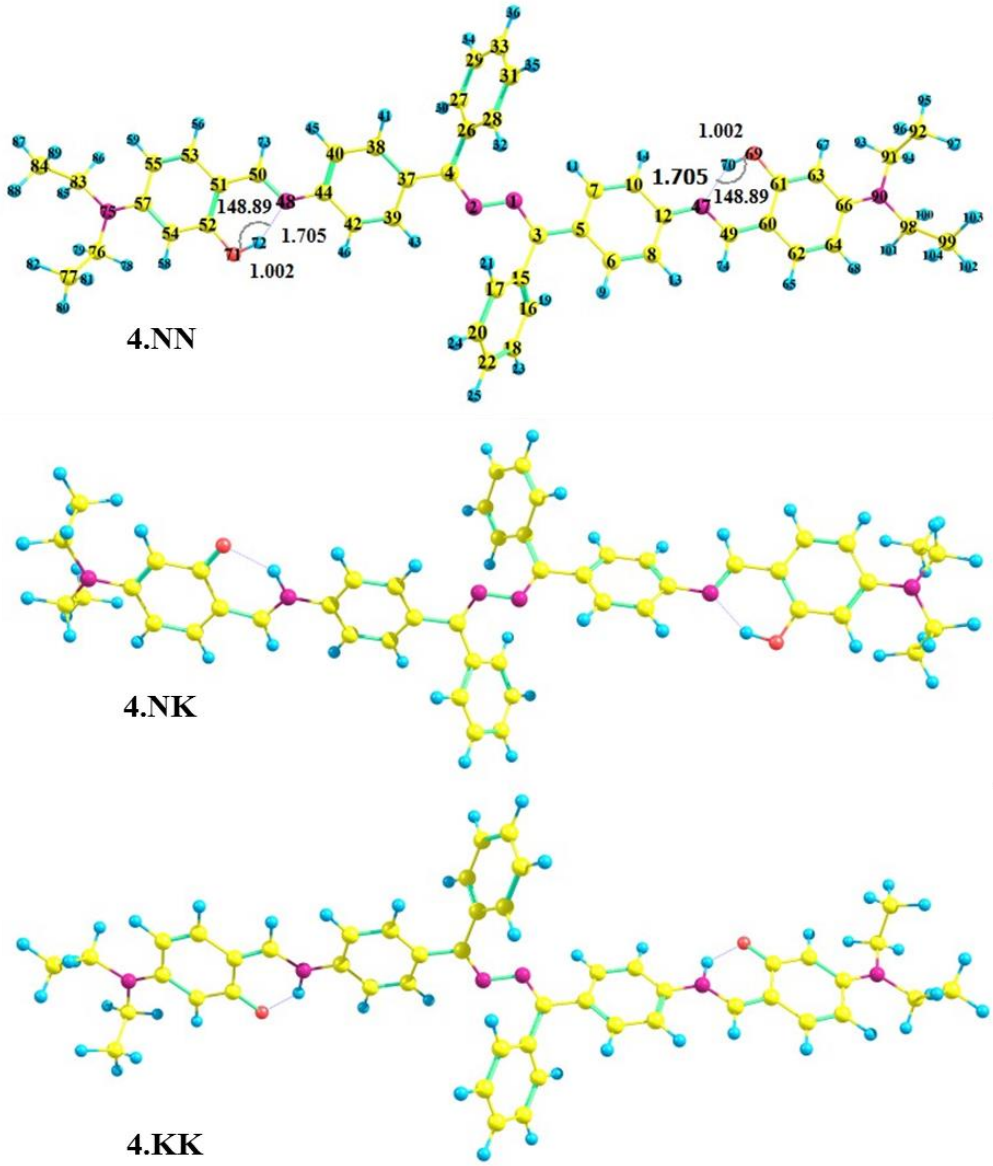

Figure 3.18 Optimized tautomeric forms of compound **4**

3.3.3.4 Effect of H^+ ions on Absorption and emission spectra of Compound 4

The FMOs of compound **4** clearly displayed the electron density shift from ─NEt_2 units towards core hydrazine unit. The ICT mechanism was further better understood by protonation/deprotonation of compound **4**. The compound **4** contained two imine units and two ─NEt_2 units, which were of basic character, and thus, abstract the introduced H^+

ions. The protonation could take place either at imino N center or at the –NEt_2 center and therefore, generate substitution isomeric monocationic and dicationic forms, which are denoted by **4_HSB**, **4_HN**, **4_2HSB**, and **4_2HN** (Scheme 3.6).

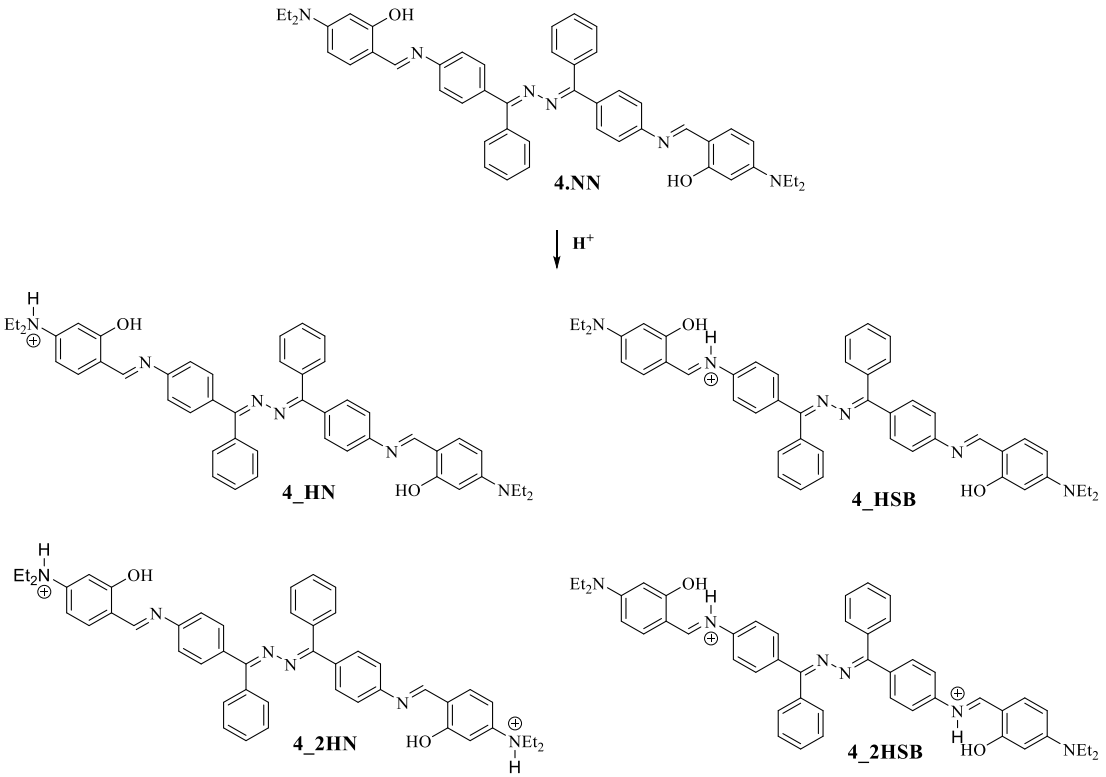

Scheme 3.6. Possible isomeric structures for the protonated form of compound **4.**

Herein, both possibilities were studied by optimizing isomeric monocationic and dicationic forms. It was noted that the protonated conformer **4_HSB** was found to be more stable by 12.64 $kcalmol^{-1}$ as compared to **4_HN**. Similarly, **4_2HSB** conformer was found to be more stable by 25.19 $kcalmol^{-1}$ compared to **4_2HN**. Thus, it could be concluded that the protonation preferentially take place at imino N center. Herein, **4_HSB** and **4_2HSB** forms were preferential and therefore, the optimized structures of **4_HSB** and **4_2HSB** were displayed along with topology of FMOs in Figure 3.19. The HOMO/LUMO electronic distribution displayed a shift of electron density from unprotonated imino center side to protonated imino center side, and thus, represented the increased ICT. On the other hand, for **4_2HSB**, the HOMO and LUMO were located over the whole molecule except the phenyl rings. However, it could be noted that the electron density at protonated imino center was increased, while it was decreased at ─NEt_2 center.

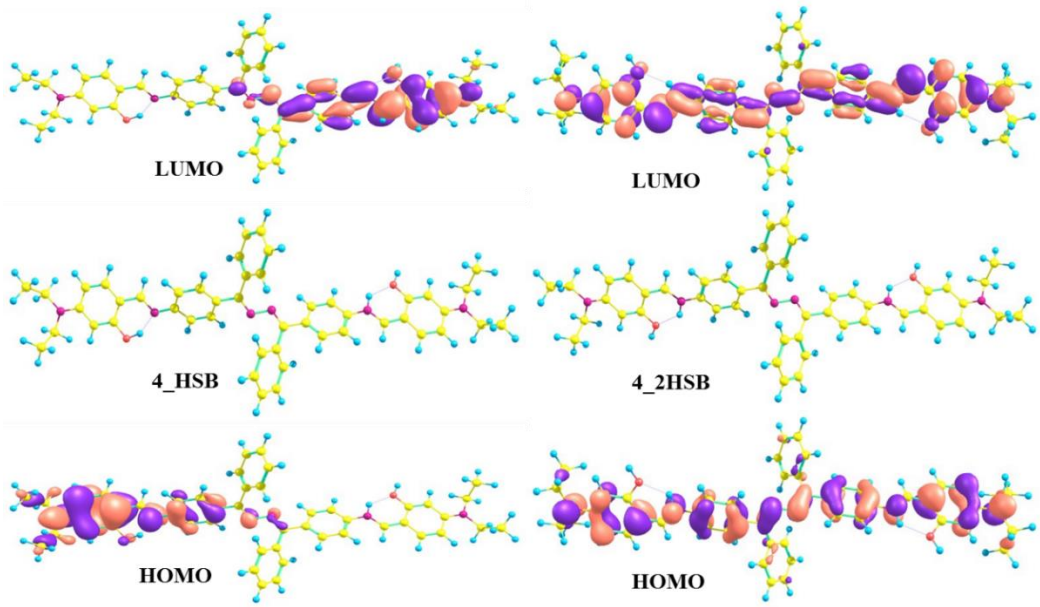

Figure 3.19 Optimized structures and FMOs for **4_HSB** and **4_2HSB** forms of compound **4**

Therefore, ─NEt_2 pushed the electron density towards the protonated imino center symmetrically (Figure 3.19). The protonation at hydrogen accepting imino nitrogen center would prevent PT, and therefore, a blue-shifted emission should be observed for the absence of ESIPT phenomenon, while, the redshifted in emission should be observed for ESICT phenomenon due to stabilization of the charge transfer state.

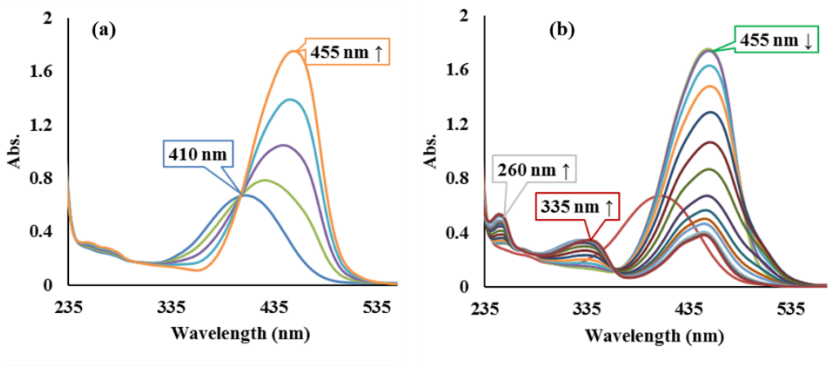

Figure 3.20 Effect of H^+ ions on the absorption spectra of compound **4** (a) 0-30 μM and (b) 30-400 μM concentration of H_2SO_4 in CH_3CN

The real-time addition of H^+ ions to compound **4**, displayed a redshifted absorption band at 455 nm with increased absorption intensity, suggesting the formation of monocationic form. Further, the addition of H^+ ions, decreased the absorption intensity at 455 nm with the concomitant rise of the new absorption peak at ~335 nm and ~260 nm, suggesting the protonation at another imino center and thus, the formation of dicationic form. The

stabilization energy and redshifted absorption spectra endorsed the calculated outcomes and led to the formation of **4_HSB** and **4_2HSB**.

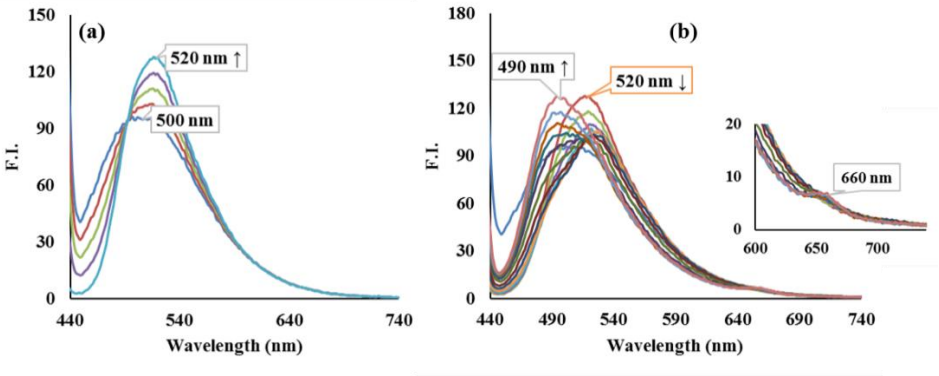

Figure 3.21 Effect of H^+ ions on the emission spectra of compound **4** with the addition of (a) 0-30 μM and (b) 30-50 μM H_2SO_4 in CH_3CN

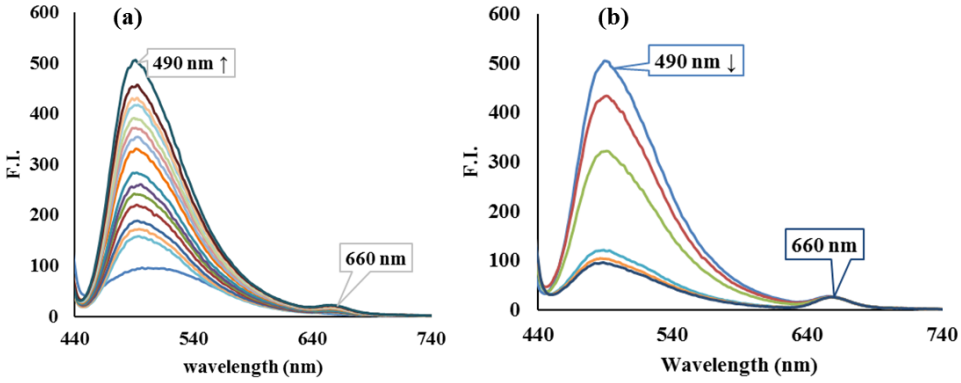

Figure 3.22 Effect of H^+ ions on the emission spectra of compound **4** (a) 50-300 μM and (b) 300-400 μM concentration of H_2SO_4 in CH_3CN

In case of emission spectra, the addition of H^+ ions (0-30 μM) to compound **4**, a red-shifted emission peak was observed from 500 nm to 520 nm, with a slight rise of emission intensity. The observed redshifted emission was due to stabilization of monocationic form **4_HSB** in an excited state. However, further addition of acid (30-50 μM), decreased the emission intensity at 520 nm, and the concomitant rise of a new peak at ~490 nm. Interestingly, the appearance of a new peak with lesser intensity at 660 nm was noted. The emission intensity at 490 nm continuously increased up to 300 μM concentration of H^+ ions. The blue-shifted emission at 490 nm was due to charge transfer in dicationic form **4_2HSB**, while emission at 660 nm was due to protonation at imino center. More addition of H^+ ions, quenched the emission intensity at 490 nm, while the emission intensity at 660 nm remains unaltered. It was due to protonation of ─NEt_2 center in the

presence of excess H^+ ions concentration, which further, decreased capacity of pushing the electron density towards imino center.

3.3.3.5 Effect of the base on absorption and emission spectra of compound 4

Further, the effect of the base was studied on the steady-state absorption and emission spectra of compound **4**. The compound **4** contained two acidic sites in the form of phenolic ─OH unit. Thus, the deportation of acidic hydrogen could monoanionic and dianionic forms, which are abbreviated as **4_O$^-$** and **4_O$^-$O$^-$**. Also, there was the possibility of rotational isomerism, at ―C=N― center, and thus, there could be two isomeric structures of monoanionic and dianionic forms (Scheme 3.7).

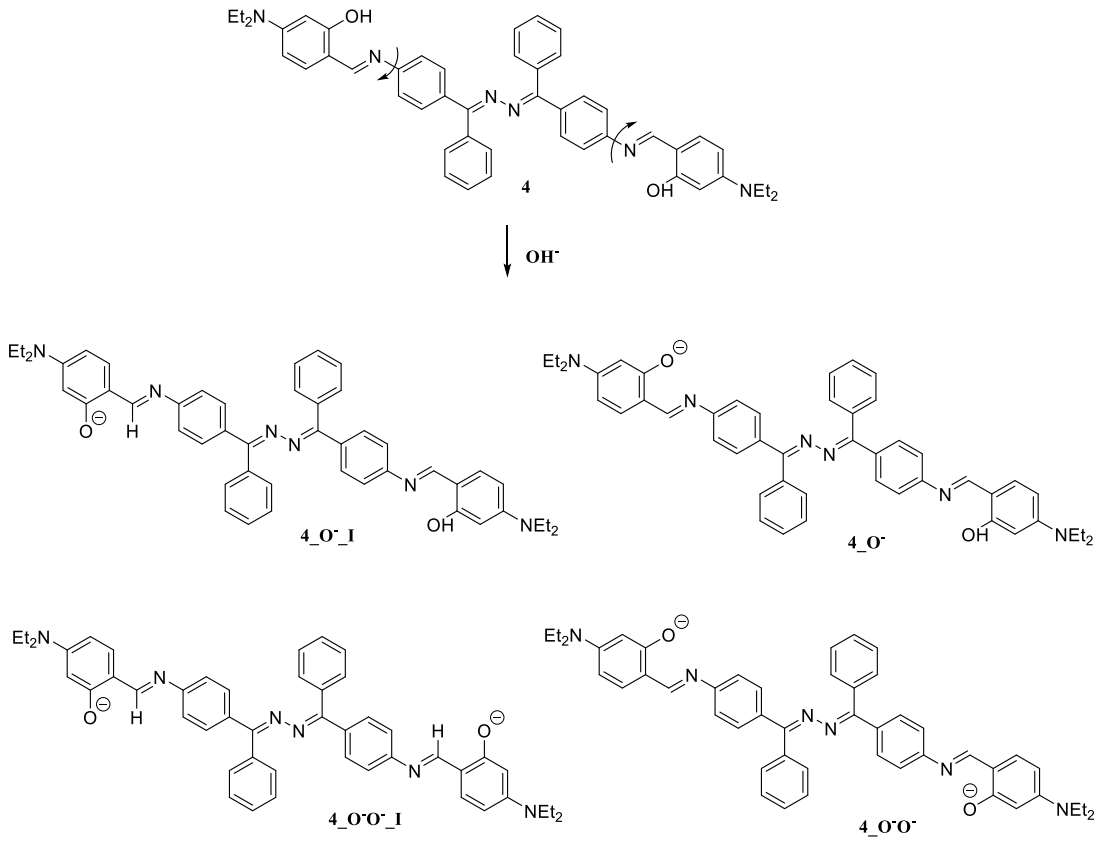

Scheme 3.7 Possible deprotonated forms of compound **4**

Therefore, both monoanionic and dianionic forms of Compound **4** were optimized and it was noted that the isomeric rotational structures (**4_O$^-$_I** and **4_O$^-$O$^-$_I**) were more stabilized by 4.19 kcalmol^{-1} and 8.45 kcalmol^{-1} for both monoanionic and dianionic forms, respectively. Further, the optimized structure and topology of FMOs of **4_O$^-$_I** and **4_O$^-$O$^-$_I** were discussed and displayed in Figure 3.23. The HOMO/LUMO electronic distribution depicted that the electron density shifted from the deprotonated

site towards another end, depicted asymmetric charge transition. However, in case of **4_O$^-$O$^-$_I**, the electron density was shifted from ─PhNEt$_2$ towards the center of molecule, and therefore, the transition was assigned as symmetrical charge transfer.

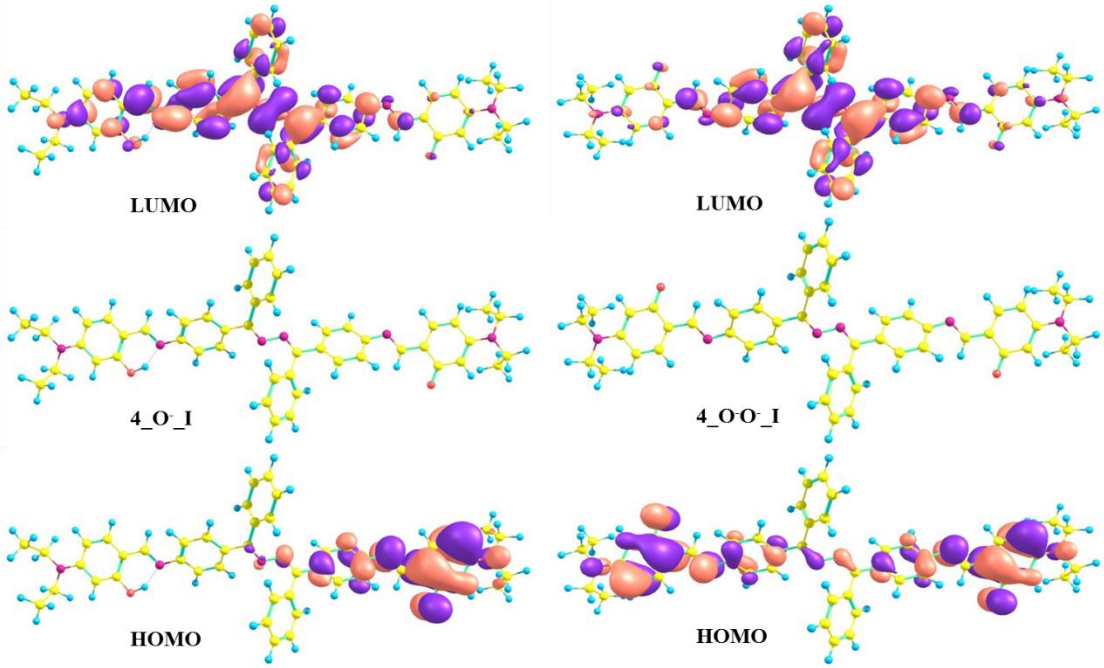

Figure 3.23 Optimized structure of monoanionic and dianionic forms **4_O$^-$_I** and **4_O$^-$O$^-$_I** along with their FMOs.

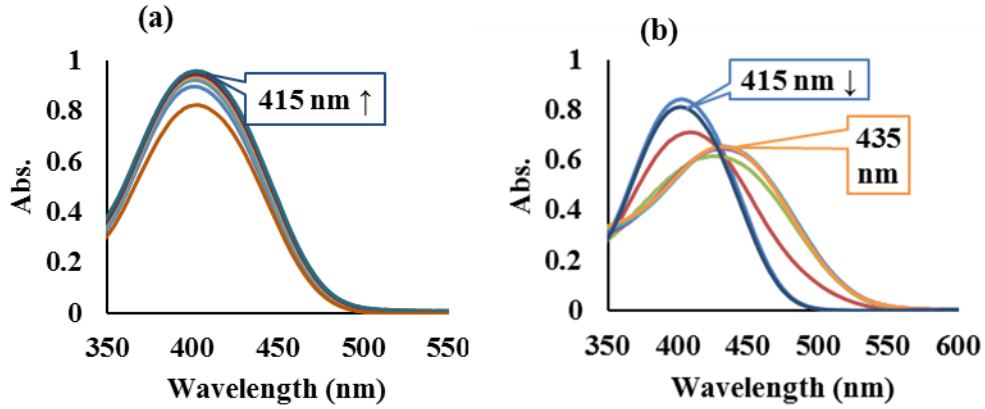

Figure 3.24 Absorption spectra of compound **4** (20 μM, CH_3CN) on addition of (a) 0-90 μM and (b) 90-320 μM concentration of NaOH.

The real-time addition of OH^- ions to compound **4**, increased the absorption intensity at its original band at 415 nm for monoanionic **4_O$^-$_I** form. Further, the addition of OH^- ions decreased the absorption intensity and concomitant redshift to 435 nm (Figure 3.24). On the other hand, the addition of OH^- ions (0-90 μM), first increased the emission intensity and concomitant blue shift from 510 nm to 480 nm for monoanionic form.

However, further addition of OH^- ions decreased the emission intensity at 480 nm and co-occurrence new peak emission peak at 620 nm (Figure 3.25).

The addition of OH^- ions at low concentration increased absorption intensity at 415 nm and blue-shifted emission at 480 nm, which was due to the formation of monoanionic form. However, at higher concentration of OH^- ions, the red-shifted absorption at 435 nm and emission at 620 nm was due to stabilization of dianions form and charge transfer towards the core of the molecular structure. The hydrazine core accepts the electron density from negatively charged phenolic oxygen and ─NEt_2 unit.

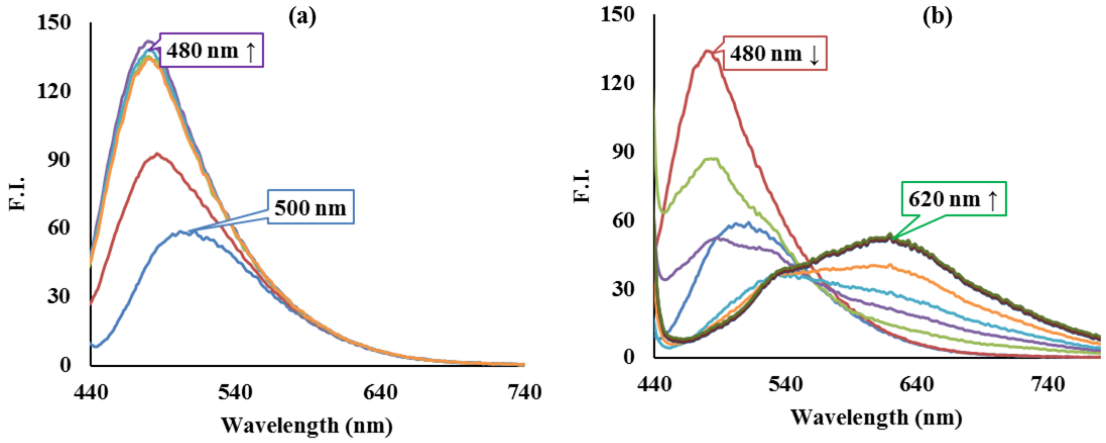

Figure 3.25 Emission spectra of compound **4** (20 μM, CH_3CN) on addition of (a) 0-90 μM and (b) 90-500 μM concentration of NaOH.

3.3.4 Conclusion

Herein, the effect of electron-donating –NEt_2 group was studied on photophysical behavior of compound **4**. Compound **4** displayed yellow absorption at 410 nm and an emission peak at 500 nm, which was accompanied by Stokes' shift of ~90 nm. The presence of –NEt_2 group in compound **4** pushed the electron density towards the electron loving hydrazine center and therefore, lead to intramolecular charge transfer (ICT). Also, the relative free energy change (ΔG) was calculated for tautomeric forms exclude the chances of ESIPT phenomenon. The introduction of acid to compound **4** preferentially protonated the imino center and therefore, increased the ICT character, which was supported by red-shifted absorption and emission peaks. Also, the interaction of base to compound **4**, the stabilized the anionic form and enhanced the charge transfer towards the core of the molecular structure. The FMOs analysis also revealed the shifting of electron density and thus, endorsed the ESICT phenomenon for modest Stokes' shift.

3.3.5 Experimental data

3.3.5.1 Synthesis of compound 4

The compound **1** (390 mg, 1 mmol) and 4-(diethylamino)-2-hydroxybenzaldehyde (386 mg, 2 mmol) were dissolved in ethanol and heated at 80-85 °C. The progress of the reaction was monitored by TLC. The yellow-colored compound was formed after 20 h, which was further filtered off and washed with ethanol to get pure compound **4** in 70 % yield; m.pt. 227°C.

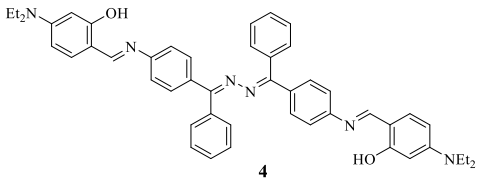

4

^{1}H NMR ($CDCl_3$ + DMSO-d_6, 400 MHz): δ (ppm) 13.79 (s, 2H, ―OH), 8.47 (s, 2H, ―CH═), 7.52-7.30 (m, 16H, ArH), 7.18-7.13 (m, 4H, ArH), 6.26-6.16 (m, 2H, ArH), 3.42-3.39 (q, J = 7.8 Hz, 8H, ―CH_2), 1.23-1.18 (t, J = 7.6 Hz, 12H, ―CH_3); ^{13}C NMR ($CDCl_3$ + DMSO-d_6, 400 MHz): δ (ppm) 161.5, 158.8, 149.1, 146.5, 138.2, 132.8, 132.4, 129.2, 127.9, 127.2, 126.7, 124.8, 122.8, 122.1, 119.7, 118.9, 111.6, 110.9 (ArCs) 47.9 (CH_2), 15.9 (CH_3). ESI-MS (m/z) = 741.9 (M^++1); calculated m/z (740.9).

Summary of Chapter 3

In summary, three symmetrical bis(diphenylmethylene)hydrazine based Schiff base (**2-4**) were synthesized and evaluated for their photophysical properties through experimental and theoretical calculations. All the three compounds have symmetrically suited double hydrogen donor (─OH) and hydrogen acceptor (─N=) sites at close proximity and therefore, established the intramolecular O─H···N hydrogen bonding. The substituents with a capacity of electron-withdrawing and donating were introduced at para position of hydrogen acceptor sites.

Among these three compounds, compound **2** and **3** displayed dual emission with broad Stokes' shifts, while compound **4** displayed a single emission peak with small stokes' shift. The compound **2** and **3** displayed ESIPT phenomena via single proton transfer at S_2 and S_1 state, respectively. The compound **2** has dominant standard enol emission; however, the introduced ─NO_2 unit in compound **3** pull the electron density and therefore, increased the acidity of ─OH unit. The increased acidity of the proton eases the proton transfer and therefore, has dominant keto emission.

On the other hand, the introduced ─NEt_2 unit in compound **4** pushed the electron density towards the core of the molecule. Also, the presence of electron-donating unit decreased the acidity of ─OH unit and therefore, condemned the ESIPT and permitted to rule ESICT phenomenon over ESIPT.

Chapter 4

Photophysical properties of bis(diphenylmethylene)hydrazine-based compounds exhibiting AIE phenomenon towards common metal ions

Designing a molecule with excellent selectivity and sensitivity towards metal ions as well as light-emitting ability in a polar medium such as water, methanol, etc. have appealing attention due to their application to a living system, daily life experiments.[124] Generally, organic luminophores were studied in dilute solutions, but some of these behave differently in the presence of a dual solvent system or in the presence of some analytes. At high concentration, the molecular system forms an aggregate, which may further lead to aggregation-caused quenching (ACQ) or aggregation-induced enhancement (AIE) phenomenon. The AIE can be attained by resisting intramolecular motion. The critical condition of resisting intramolecular rotation for AIE can be achieved by introducing bulky substitution, hindering the rotation by hydrogen bonding and metal chelation. In recent years, the AIE phenomenon has provided new scopes and functions to self-assembly and disassembly based on the detection of analytes. The organic luminophores with characteristics of AIE active have an advantage in a number of research areas such as OLEDs, bio-imaging, environmental protection, etc.[125-136]_ENREF_135

The organic compound derivatives based on tetraphenylethylene (TPE)[137, 138], silole[139], azine[56, 64, 140] are a novel class of material with properties of AIE and have been used as sensors in the range of samples such as chemicals, environment, and biology.[126-129, 133, 136, 141-145] On the other hand, compound exhibiting ESIPT have the advantage of a broad spectral window with large Stokes` shift, high quantum yield, and reducing the self-quenching of fluoro-sensor. Therefore, the molecular architecture design with properties of both AIE and ESIPT characteristics should have prominent Stokes` shift and do not require hydrophilic modification. Hence, they can find potential in chemical, environmental and biological sensing.[146-149]

Herein, a systematic study of AIE and ESIPT/ESICT, effects of different substitutions and their photophysical properties behavior towards common metal ions has been discussed. It has been predicted that substituents tuned the selectively and sensitivity towards detected metal ions. Therefore, depending upon the nature of substituents and their sensing behavior, this chapter has been divided into three sections:

4.1. Aggregation-induced emission and excited state intramolecular proton transfer-based "*off-on*" fluorescent sensor for Al^{3+} ions in liquid and solid-state

4.2. Aggregation-induced emission and excited-state intramolecular proton transfer based ratiometric and "*on-off*" sensor for Al^{3+} and Cu^{2+} ions

4.3. ESICT efficient sensor for discriminating Zn^{2+} and Cu^{2+} ions through the dual-channel

4.1

Aggregation-induced emission and excited state intramolecular proton transfer-based "*off-on*" fluorescent sensor for Al^{3+} ions in liquid and solid-state

4.1.1 Abstract

Bis(diphenylmethylene)azine based Schiff base (abbreviated as compound **2)** exhibiting AIE and ESIPT phenomenon has been synthesized and studied the photophysical behavior towards detection of Al^{3+} ions. The results showed that compound **2** exhibit aggregation-induced emission in >70% H_2O/CH_3CN. The significant hydrodynamic diameter change from 20 nm to 200 nm upon increasing the H_2O volume ratio in CH_3CN endorsed AIE phenomenon for compound **2**. Compound **2** showed colorimetric and "*off-on*" emission response for Al^{3+} ions, with a detection limit of 2.7×10^{-7} M in CH_3OH. The association of compound **2** to Al^{3+} also causes a restriction in intramolecular motion-induced emission. The hydrodynamic diameter of compound **2** increases from 335 nm to 625 nm in the presence of Al^{3+} ion in CH_3OH.

4.1.2 Results and discussion

4.1.2.1 Aggregation-induced emission (AIE) characteristic of compound 2

The compound **2** possesses the tetraphenylene moieties around the hydrazine, which likely to show the characteristics of tetraphenylethylene moiety, which is known to exhibit AIE phenomenon in a poor solvent. Thus, the AIE feature of compound **2** was studied by absorption and emission spectra in a suitable solvent (CH_3CN) with the incremental addition of poor solvent (H_2O) and presented in Figure 4.1. The solution of compound **2** (20 µM, CH_3CN) showed absorption maxima at 355 nm. Upon incremental addition of H_2O ratio to compound **2** (20 µM, CH_3CN), the absorption intensity at 355 nm decreased (up to 60% H_2O:CH_3CN; v/v) along with formation of new band at 400 nm (70-90% H_2O:CH_3CN; v/v) along with tail off absorption between 500-700 nm. The redshift in absorption maxima with increasing the water content in CH_3CN resulted in the formation of J-types of aggregates. The emission spectrum of compound **2** (20 µM, CH_3CN, λ_{ex} = 355 nm) showed weak emission at 455 and 545 nm. The compound **2** persisted low emission up to 60% H_2O:CH_3CN (v/v). Further, increasing the H_2O content to 70-90%, increased the emission intensity at 545 nm. The emission of compound **2**

decreased in pure water, comparative to 90% H_2O:CH_3CN (v/v). The increase in intensity at ESIPT band indicated the protection of hydrogen bonding in aggregate form and thus, available for the proton transfer. Therefore, the emission intensity increased at 545 nm in aggregated form due to restriction in intramolecular rotation around C─N, N─N, and C═N bonds and allowing proton transfer.

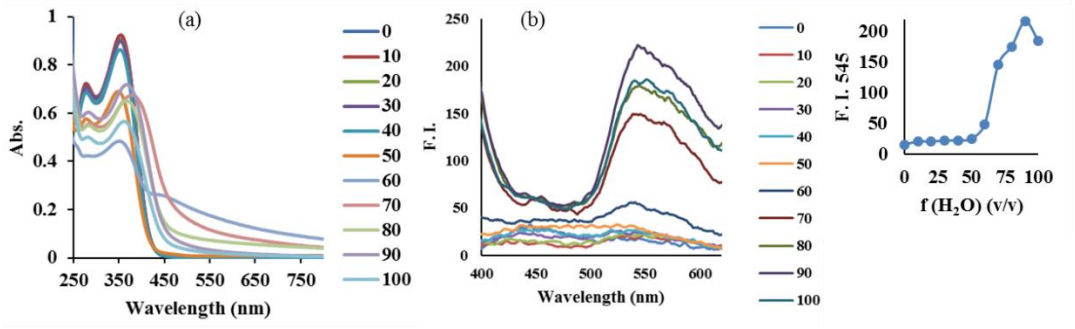

Figure 4.1 (a) Absorption and (b) emission spectra of compound **2** (20 µM) upon increasing the volume of H_2O in CH_3CN (λ_{ex} = 355 nm); Inset in (b) emission profile of compound **2** at 545 nm for a different fraction of H_2O in CH_3CN.

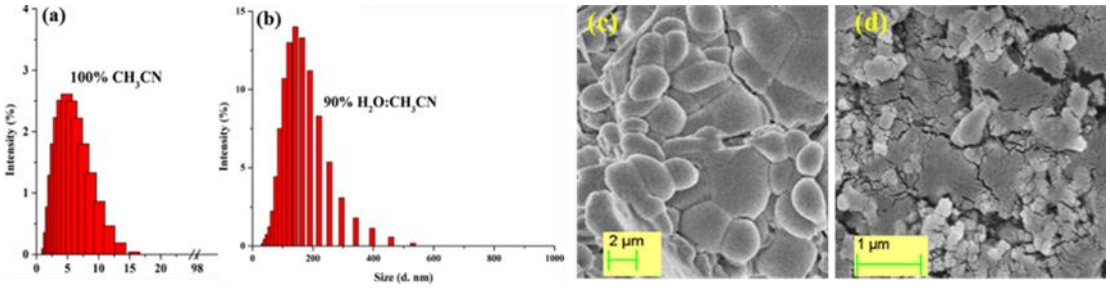

Figure 4.2 DLS bar graph of compound **2** in (a) CH_3CN, and (b) 90% H_2O/CH_3CN (v/v); FESEM images of compound **2** in (c) CH_3CN and (d) 90% H_2O/CH_3CN (v/v).

Further, the DLS measurements were also performed to support the aggregation behavior of compound **2** and determined the size of aggregates of compound **2** in the presence of different volume ratio of H_2O with CH_3CN. The DLS experiments revealed an average hydrodynamic diameter of 2-20 nm for compound **2** (20 µM, CH_3CN). However, increasing the H_2O volume ratio to 70-90% in CH_3CN, the increase in average hydrodynamic diameter was observed from 20 nm to 200 nm (Figure 4.2). FESEM micrographs were also studied for morphology and particle size. The FESEM micrographs showed the spherical morphology of compound **2** in pure CH_3CN, with a diameter of ~40 nm. However, increasing the H_2O content up to 90% v/v in CH_3CN, the formation of disordered aggregates were observed (Figure 4.2). The FESEM micrographs analysis were consistent with DLS experiment results.

4.1.2.2 Sensing properties of compound 2 towards various common metal ions

The interaction of compound **2** with various common metal ions such as Na^{+}, K^{+}, Mg^{2+}, Ca^{2+}, Ba^{2+}, Al^{3+}, Pb^{2+}, Fe^{3+}, Co^{2+}, Ni^{2+}, Cu^{2+}, Zn^{2+}, Hg^{2+}, and Ag^{+} was examined through UV-Vis absorption spectroscopy in polar protic solvent (CH_3OH) as shown in Figure 4.3. The position of absorption bands remained unchanged over the various metal ions except for Al^{3+} ions. The binding properties of compound **2** with Al^{3+} were studied by UV–Vis titration in CH_3OH solution. On gradual addition of Al^{3+} (0–140 µM), the absorption bands at 355 nm decreased, while the absorption band at 465 nm increased progressively with an isosbestic point at 390 nm (Figure 4.3). The presence of isosbestic point for compound **2** and Al^{3+} during absorption titrations indicate complex formation with Al^{3+} ion. The bathochromic shifts observed in the absorption spectrum inferring deprotonation of a phenolic proton, which enable complexation with Al^{3+} ions. The spectral changes were associated with visible color changes, as shown in Figure 4.3**.**

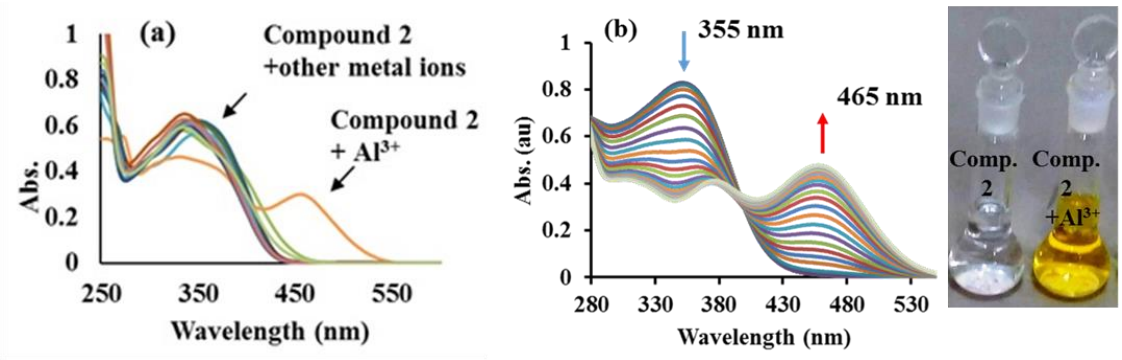

Figure 4.3 (a) Absorption spectra of compound **2** (20 µM, CH_3OH) in the absence and presence of different metal ions (1000 µM); (b) Effect of incremental addition of Al^{3+} ions (0-140 µM) to compound **2** and visible colour change for compound **2** on the addition Al^{3+} ions in CH_3OH

Further, the emission response of compound **2** was examined towards common metal ions (Na^{+}, K^{+}, Mg^{2+}, Ca^{2+}, Ba^{2+}, Al^{3+}, Pb^{2+}, Fe^{3+}, Co^{2+}, Ni^{2+}, Cu^{2+}, Zn^{2+}, Hg^{2+} and Ag^{+}) at 1000 µM in CH_3OH. Upon addition of 1000 µM of Al^{3+} ions, the fluorescent intensity of compound **2** showed remarkable enhancement, at the different emission wavelength. The fluorescence signal did not show any significant change in the presence of other metal ions, as shown in Figure 4.4**.**

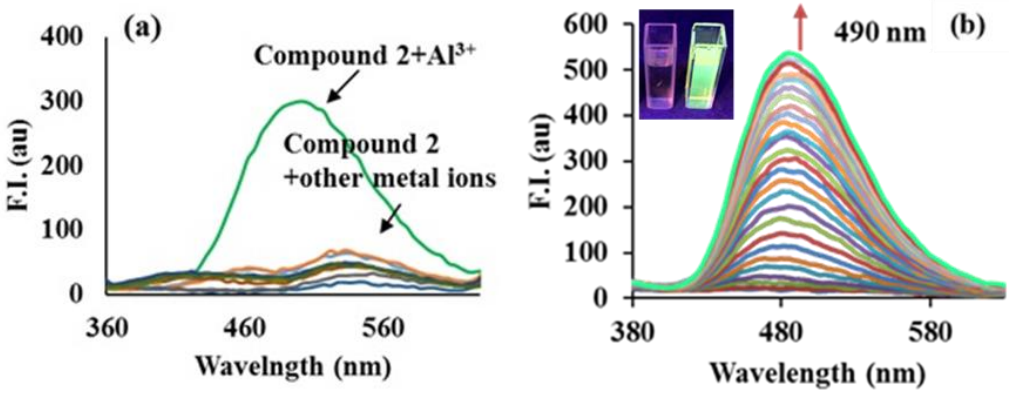

Figure 4.4 (a) Fluorescence spectra of compound **2** (20 µM, CH_3OH) before and after addition 1000 µM of metal ion; (b) Change of the emission intensity of compound **2** (20 µM) with increasing Al^{3+} concentration (0-180 µM) in CH_3OH, λ_{ex} = 355 nm, λ_{em} = 490 nm, Inset: fluorescence image of compound **2** in absence and presence of Al^{3+} ions.

The strong fluorescence 'turn-on' was associated with the formation of the complex between compound **2** and $Al^{3+,}$ which suppressed intramolecular rotation present in compound **2** and induced rigidity in the complexes. For quantitative analysis of Al^{3+}, the fluorescence signals of compound **2** were measured at various concentrations of Al^{3+} ion, and the results are shown in Figure 4.4. The solution of compound **2** and Al^{3+} showed green emission with maximum emission wavelength at 490 nm and having Stokes` shift of 155 nm. Based on the experimental results, it has been observed that compound **2** could be used to detect Al^{3+} selectively through emission response.

Furthermore, the complex formation was also confirmed by ESI-MS analysis where the mass of the mixture of compound **2** and $Al(ClO_4)_3.9H_2O$ in CH_3OH was taken. The m/z peak for compound **2** and its complex was observed at 599.27 and 641.16 (compound **2** + Al^{3+} + H_2O), respectively. The binding constant for the complexation of compound **2** with Al^{3+} has been found to be 1.6 x 10^4 M^{-1}. It has been observed that the intensity of the fluorescence signal increased almost linearly with the increasing Al^{3+} ions concentration up to 82 µM. Thus, the detection limit of compound **2** towards Al^{3+} ions was determined to be 2.7 × 10^{-7} M, which is low enough for any fluorescent probe to detect Al^{3+} in environmental and biological samples. The observed value is much lower than the permissible limit of 7.41 µM for Al^{3+} in drinking water, established by WHO.

4.1.2.3 Interference Study

In order to determine the sensitivity and selectivity of compound **2** towards Al^{3+} ions, the competitive emission responses were measured in the presence of other metal ions. Most

of the metal ions did not show any interference with the detection of Al^{3+} ions (Figure 4.5). However, Fe^{3+}, $Mg^{2+,}$ and Ni^{2+} partially reduced the emission intensity of the compound **2**.Al^{3+} complex, but clearly detectable. Therefore, "*turn-on*" fluorescence signal of compound **2** is a good indication for the prime presence of Al^{3+} ions.

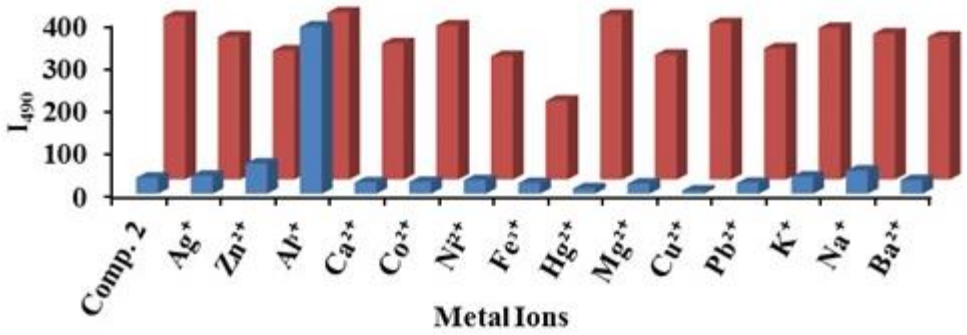

Figure 4.5 Relative emission intensity of compound **2** (20 μM) in CH_3OH (λ_{ex} = 335 nm) with different competing metal ions (1000 μM) in the absence (blue bars) and presence of Al^{3+} ions (red bars), at λ_{em} = 490 nm.

4.1.2.4 Theoretical studies

The geometry optimizations were carried out at DFT/B3LYP level of theories using 6-31+G(d) basis sets for C, H, N, O, and LANL2DZ for Al^{3+}. The frequency calculations were also performed on the obtained optimized structure at the same level of theory. In addition, absorption properties were analyzed by vertical excitation energy calculation using the time-dependent density functional theory (TD-DFT) method. The optimized structure of compound **2**.Al^{3+} has been shown in Figure 4.6. The calculated absorption spectra have been summarised in Table 4.1**.**

Table 4.1 The calculated absorption value**,** the symmetry, contributing molecular orbital and their % for compound **2.**Al^{3+}

Compound 2.Al^{3+}

λ_{Gas} (nm)	λ_{Exp} (nm)	Osc. Strength	Symmetry	% Major MOs	
529.45	465	0.1177	Singlet-A	H→L+1	86
445.35		0.3422	Singlet-A	H→L+2	77

The compound **2** displayed the coordination with Al^{3+} ions through the nitrogen of imine and phenolic oxygen and thus, indicated stable complexes formation. The calculated charges on the nitrogen of imine and phenolic oxygen were found to be -0.554 and -0.691, respectively, while aluminum has charge of +0.950 illustrated the dipolar interaction and

thus, showed the coordination. The absorption calculation showed that the experimentally observed absorption transition resulted from HOMO to LUMO+2 for compound **2.**Al^{3+}. The HOMO of complex (Compound **2.**Al^{3+}) has a contribution from phenyl ring with Schiff base linkage and hydrazine linkage of the molecule, while LUMO+2 was located at Al^{3+} only demonstrating charge transfer from compound **2** to Al^{3+} ions, further triggering the appearance of yellow color from colorless.

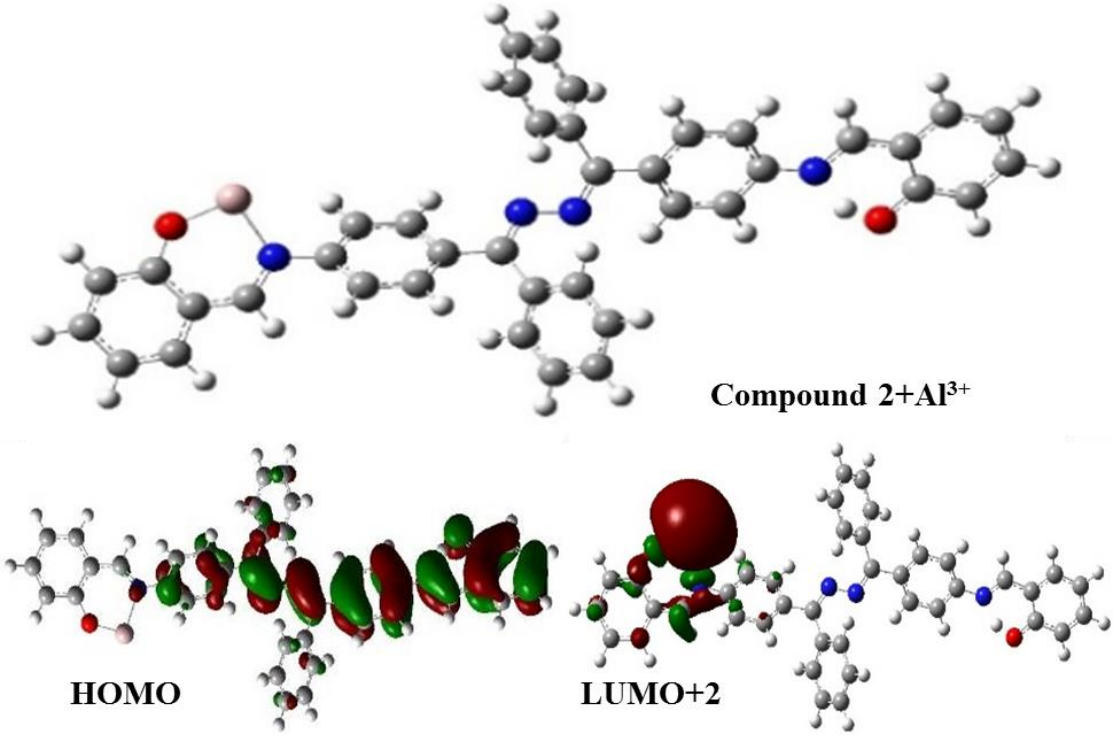

Figure 4.6 Optimized structures and frontier molecular orbitals of compound **2.**Al^{3+} (stoichiometry 1:1).

4.1.2.5 Mechanism

The compound **2 (**CH_3CN) displayed weak emission due to intramolecular rotations in dilute solution, which was found to be improved in an aggregated form (70-90% H_2O-CH_3CN). The DLS study revealed an increase in hydrodynamic diameter for compound **2** in 70-90% H_2O-CH_3CN and therefore, support the formation of aggregates. The aggregation ceased the molecular motions and hence, induced the enhancement in emission. The appearance of new absorption bands recognized as the coordination of Al^{3+} ions with the imine and phenolic oxygen of compound **2**. The binding of Al^{3+} to compound **2** also restricted the intramolecular rotation and caused enhancement in

emission. Also, the hydrodynamic diameter of compound **2** (20 µM, CH_3OH) increased from 335 nm to 625 nm on the addition of 200 µM of Al^{3+} ions (Figure 4.7).

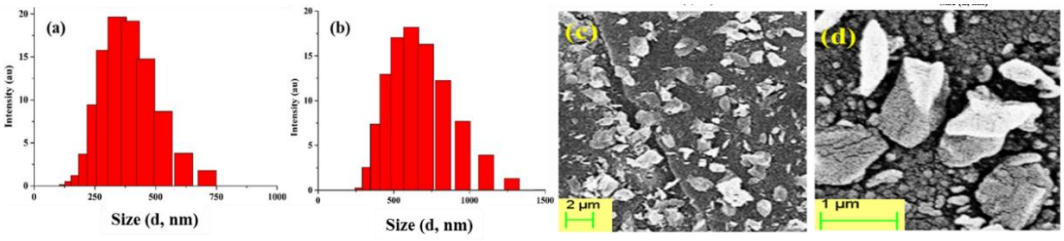

Figure 4.7 DLS profile for compound **2** (20 µM, CH_3OH) in (a) pure CH_3OH; (b) after the addition of 200 µM of $Al(ClO_4)_3$; FESEM micrographs of (c) compound **2** in CH_3OH and (d) after addition of Al^{3+} ions in CH_3OH.

FESEM micrographs displayed a change in morphology for compound **2** in the presence of Al^{3+} ions with an average size of 650 nm (Figure 4.7). The observed sizes from the DLS and FESEM were in good correlation and thus, supported the interaction with Al^{3+} ions. The increase in hydrodynamic diameter of a complex of compound **2**.Al^{3+} support formation of aggregates, which induced the enhanced emission for the complex.

The reversible nature of binding of compound **2** towards Al^{3+} ions was also examined with EDTA. The enhanced fluorescence was not reversed back to the state of the compound. The irreversible nature of detection could be due to the Al^{3+} ion template-based aggregation, which further, reduced the chances of direct interaction of EDTA to Al^{3+} ions.

Further, optimization of molecular structures has been performed at semi-empirical method PM6. It has been observed that compound **2** has head to head hydrogen bonding linkage. However, the introduction of Al^{3+} ions to compound **2** resulted in coordination through imine nitrogen and phenolic oxygen atoms (Figure 4.8). The binding behavior was also studied by mass spectrometry and Job plot, which suggests 1:1 stoichiometry of complex. The plausible binding can be according to Scheme 4.1**.**

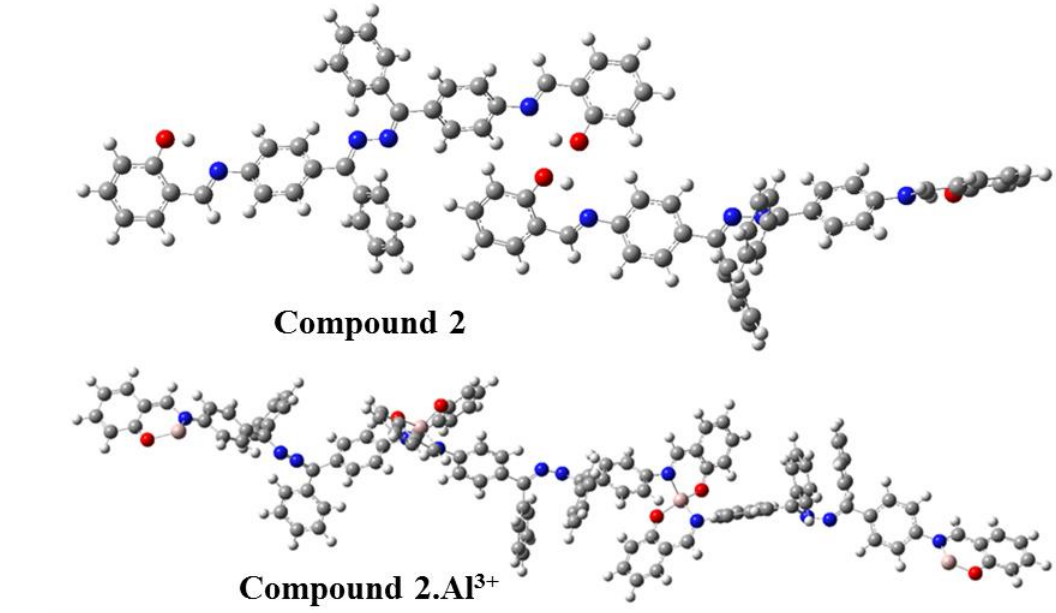

Figure 4.8 Optimized structure of compound **2** and compound **2**.Al^{3+}

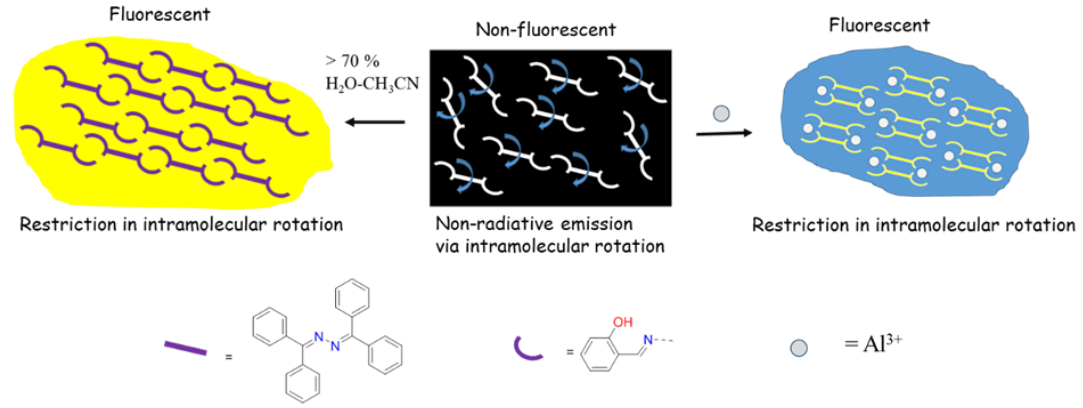

Scheme 4.1 Plausible binding mode of compound **2** with Al^{3+} ions in CH_3OH

4.1.2.6 Practical Applications

For on-site analysis, we developed paper-based fluorescent sensors for Al^{3+} detection. A series of 2.0 µL of 1.0 mM stock solution of compound **2** was dropped on to filter paper strips and then dried in air and was found to give blue fluorescence spots (Figure 4.9). Each spot was dropped with 2.0 µL containing 1.0 µM of various metal ions. Al^{3+} gave a fluorescent green emission while other examined metal ions did not show any significant change to spot. Interestingly, compound **2** could detect Al^{3+} in the solid-state *via* a color change from yellow to red color. The compound **2** is both AIE and ESIPT active and thus is expected to show enhanced solid-state emission in the presence of Al^{3+} ions. Keeping this in view, we explored the solid-state emission properties of compound **2**. The

compound **2** is non-fluorescent as observed under a UV lamp. The powder XRD studies showed sharp peaks, which confirmed the strong crystalline properties of compound **2**. The compound **2** in the presence of Al^{3+} ions in the solid-state showed bright yellow emission (Figure 4.9). The powder XRD studies of the compound **2**.Al^{3+} complex showed the weak peaks, which indicate the loss of crystallinity of this complex. We then explored the affinity of compound **2** towards Al^{3+} in the bulk sample. The addition of solid aluminum over stable compound **2** showed the yellow emission on gentle mixing for 5 min under the UV lamp. All the above studies proved the interaction of compound **2** towards Al^{3+} ions in solution as well as solid-state. Also, the biocompatibility of compound **2** has been checked at physiological pH. It has been observed that compound **2** was observed to be effective in the pH range of 4.2 – 10.2 and the compound 2.Al^{3+} was observed effectively in the pH range of 4.2 – 8.8.

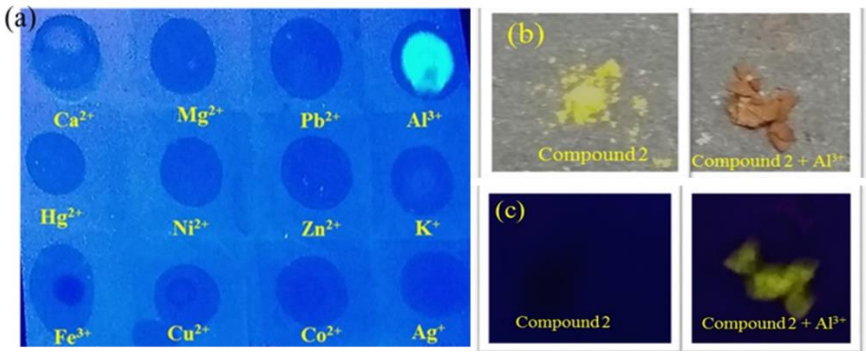

Figure 4.9 (a) Portable testing paper for compound **2** showing the emission changes in the presence of various metal ions under UV light; (b) Solid-state detection of Al^{3+} under visible light, (c) UV light.

4.1.3 Conclusion

In summary, we have synthesized the compound **2**, enclosing tetraphenyl rings containing Schiff bases, connected through hydrazine linkage. The hydrazine linked tetraphenyl rings are proficient of AIE phenomenon, and Schiff bases provided binding sites accomplished with ESIPT phenomenon. ESIPT-AIE active compound **2** has been successfully utilized for highly selective, fast responding ratiometric estimation of Al^{3+} in solution as well as solid-state. Moreover, the intense emission color of compound **2**.Al^{3+} complex in the solid-state offers its application in designing tunable organic luminescent materials.

4.2

Aggregation-induced emission and excited state intramolecular proton transfer based ratiometric and "*on-off*" sensor for Al^{3+} and Cu^{2+} ions

Likewise, compound **2**, compound **3,** also exhibited the AIE and ESIPT phenomenon. Also, compound **3** was found to be a novel sensor for Al^{3+} and Cu^{2+} ions in CH_3OH. Further, the effect of electron-withdrawing groups has been elaborated on the photophysical properties and sensing ability. Compound **3** displayed the absorption redshift of 120 nm and 25 nm towards Al^{3+} and Cu^{2+} ions, respectively. In the presence of Al^{3+} ions, compound **3** displayed blue-shifted ratiometric rise of new emission peak at 430 nm; however, the emission peak was decreased at 525 nm. The detection limit of compound **3** towards Al^{3+} and Cu^{2+} ions were determined to be 12 nM and 120 nM, respectively.

4.2.1 Results and discussion

4.2.1.1 Aggregation-induced emission (AIE) characteristic of compound 3

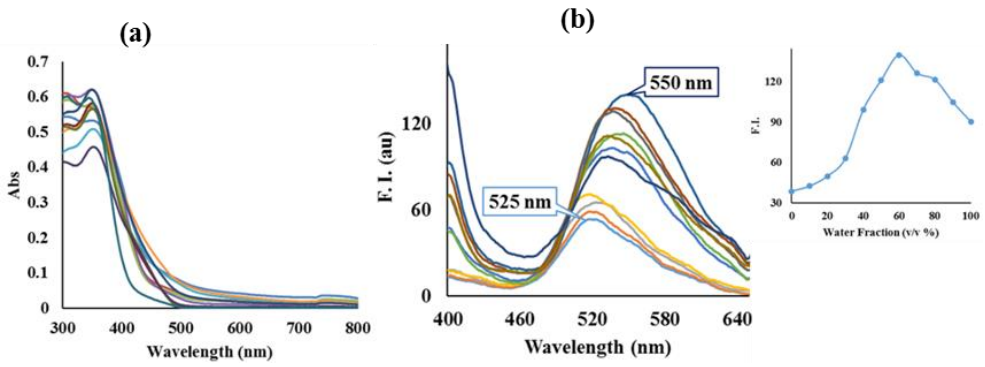

Figure 4.10 (a) Absorption and (b) emission spectra of compound **3** (20 µM) upon increasing the volume of H_2O in CH_3CN (λ_{ex} = 350 nm); Inset in (b) emission profile of compound **3** at 550 nm for a different fraction of H_2O in CH_3CN.

The AIE features of compound **3** were studied by absorption and emission spectroscopic techniques in CH_3CN/H_2O. The solution of compound **3** (20 µM, CH_3CN) showed absorption maxima at 350 nm. Upon incremental addition of H_2O ratio to compound **3** (20 µM, CH_3CN), the absorption intensity at 350 nm decreased (up to 70% H_2O:CH_3CN; v/v), and rise of shoulder peaks area (70-90% H_2O:CH_3CN; v/v) was observed. Also, a tail off absorption between 500-800 nm was observed (Figure 4.10).

The emission spectrum of compound **3** (20 µM, CH_3CN, λ_{ex} = 350 nm) displayed emission at 525 nm. On increasing the H_2O content in H_2O/CH_3CN, compound **3** displayed an increase in emission intensity at 525 nm and concomitant redshift to 550 nm up to 60% H_2O:CH_3CN (v/v). Further, increasing the H_2O content to 70-90%, slightly decreased the emission intensity than 60 % H_2O:CH_3CN (v/v); however, it was still higher than its initial state. The increase of emission intensity at ESIPT band along with redshift to 550 nm indicated the protection of IraHB and stabilization of excited state in aggregate forms. Therefore, the rise emission intensity at 525 nm in aggregated form would be due to restriction in intramolecular rotation around C─N, N─N, and C═N bonds and allowing proton transfer. The absorption spectra variation and with increased emission intensity at 525/550 nm indicated the formation of J-types of aggregates. The formation of aggregates was also endorsed by DLS measurements. The compound **3** displayed an average hydrodynamic size of ~45 nm in CH_3CN, which was determined to be ~220 nm and ~300 nm in 90 % H_2O/CH_3CN, respectively.

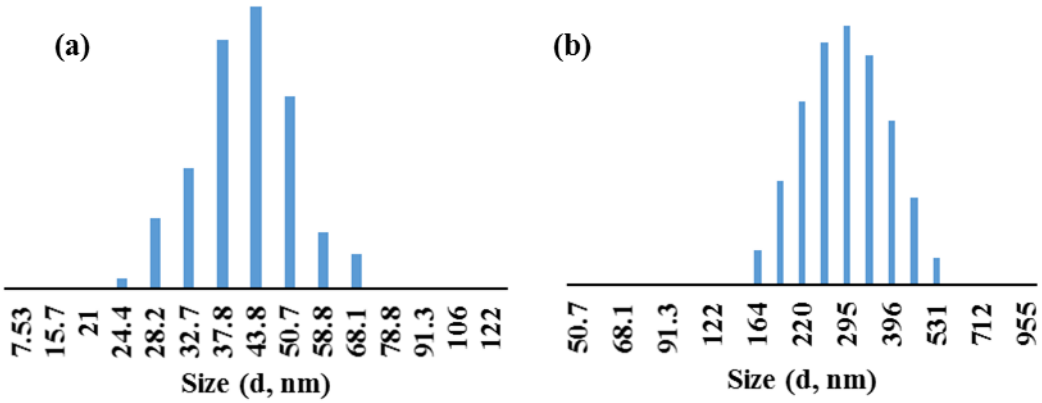

Figure 4.11 DLS bar graph of compound **3** in (a) pure CH_3CN; (b) 90% H_2O/CH_3CN (v/v) mixture.

4.2.1.2 Sensing properties of compound 3 towards metal ions

Compound **3** displayed an absorption peak at 350 nm and emission peak at 525 nm. The interaction of compound **3** with various metal ions such as Na^+, K^+, Mg^{2+}, Ca^{2+}, Ba^{2+}, Al^{3+}, Pb^{2+}, Fe^{3+}, Co^{2+}, Ni^{2+}, Cu^{2+}, Zn^{2+}, Hg^{2+}, and Ag^+ was examined through absorption and emission spectroscopy in polar protic solvent (CH_3OH). The absorption response of compound **3** remained unchanged over the various metal ions except for Al^{3+} and Cu^{2+} ions. In a similar way, the emission signal of compound **3** displayed variation in the

presence of Al^{3+} and Cu^{2+} ions only. No other ions significantly changed the emission response of compound **3** (Figure 4.12).

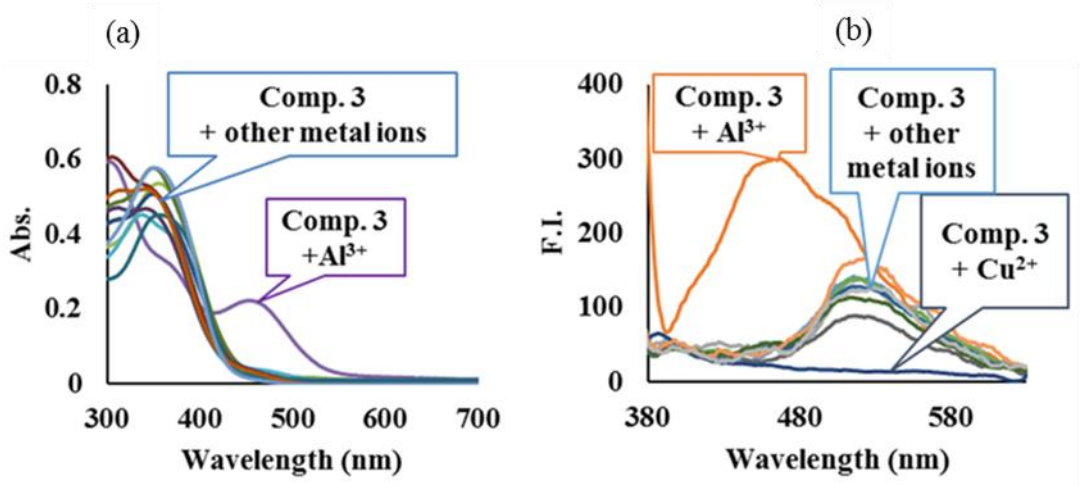

Figure 4.12. (a) Absorption and (b) emission response of compound **3** towards different metal ions.

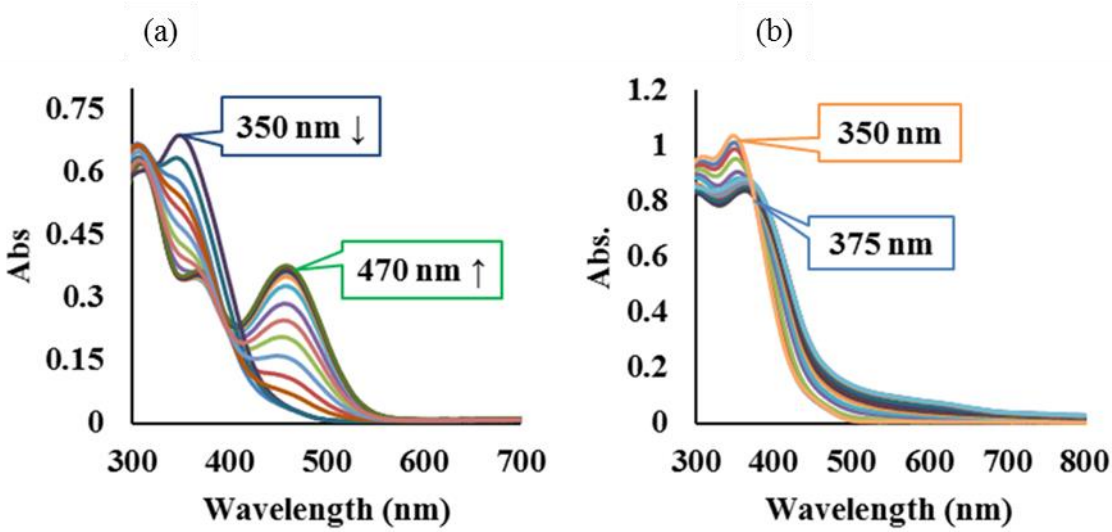

Figure 4.13. Absorption spectra of compound **3** (20 µM, CH_3OH) on incremental addition of (a) Al^{3+} and (b) Cu^{2+} ions.

Further, the quantitative estimation of Al^{3+} and Cu^{2+} ions were performed by titration experiments. The incremental addition of Al^{3+} ions, the absorption intensity was decreased at 350 nm and concomitantly increased at 470 nm ratiometrically with an isosbestic point at 400 nm. On the other hand, on the gradual addition of Cu^{2+} ions, the absorption peak was red-shifted to 375 nm with decreased in absorption intensity. The observed absorption bathochromic shift indicated the deprotonation of the phenolic unit, which will further assist the complexation with Al^{3+} and Cu^{2+} ions.

The titration experiment was further extended to emission spectroscopy. The quantitative addition of Al^{3+} ions to compound **3** displayed an emission ratiometric response. The incremental addition of Al^{3+} ions to compound **3**, decreased the emission intensity at 525 nm and the concomitant rise of emission peak at 430 nm. The emission intensity ratio at 430/525 nm was increased with increased concentration of Al^{3+} ions, and determined variation from 0.05 to 2.7 depicted the 55 fold ratiometric emission enhancement. On the other hand, the incremental addition of Cu^{2+} ions to compound **3** decreased the emission intensity at 525 nm. The emission intensity was decreased from 130 to 13, and thus, the emission quenched to 10 % to its initial state. Based on the experimental results, compound **3** was observed to be selective for Al^{3+} ions and Cu^{2+} ions.

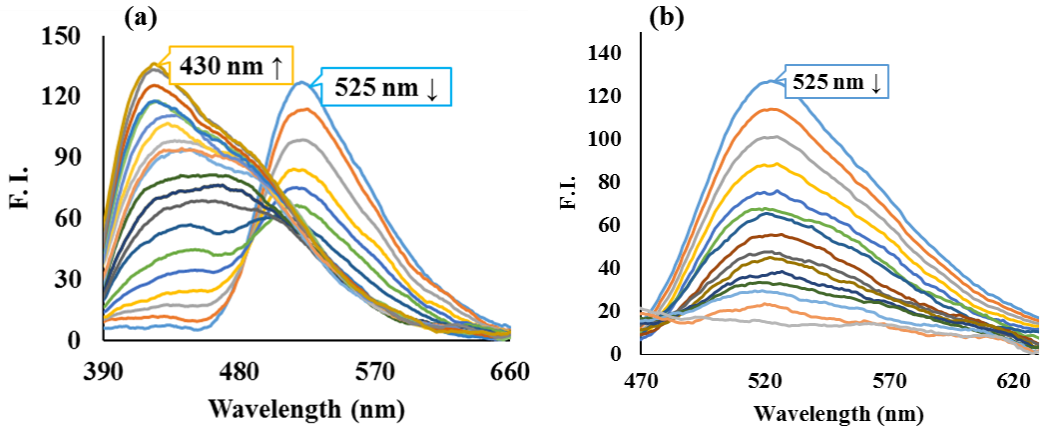

Figure 4.14 Emission response of compound **3** (20 μM, CH_3OH) on incremental addition of (a) Al^{3+} ions and (b) Cu^{2+} ions

Further, the stoichiometry of complexes was measured through Job plot and determined to be 1:1 for both Al^{3+} and Cu^{2+} ions. The binding constant for compound **3.**Al^{3+} and compound **3**.Cu^{2+} were calculated from the Benesi-Hildebrand equation and determined to be 4.5 x 10^4 M^{-1} and 1.4 x 10^4 M^{-1}, respectively. It was also observed that the emission intensity of compound **3** linearly dependant to concentration of Al^{3+} ions (5-40 μM) and Cu^{2+} ions (2-25 μM). Thus, the determined limit of detection for compound **4** towards Al^{3+} and Cu^{2+} ions has been found to be 12 nM, and 120 nM, respectively, which is low enough as a fluorescence probe to detect Al^{3+} and Cu^{2+} ions in environmental and biological samples.

Further, the interference of other metal ions in recognition of Al^{3+} ions and Cu^{2+} ions was measured by determining their emission response of compound **3** in the presence of other

metal ions in CH_3OH (Figure 4.15). The presence of other metal ions did not alter the emission signal of compound **3** towards Al^{3+} ions. Likewise, the emission signal of compound **3** remains unaltered towards Cu^{2+} in the company of other metal ions except for Al^{3+} ions. The emission response of compound **3**.Cu^{2+} was restored to compound **3**.Al^{3+}. Therefore, ratiometric emission enhancement and "*turn-off*" signal of compound **3** was a good indication for the prime presence of Al^{3+} ions and Cu^{2+} ions, respectively.

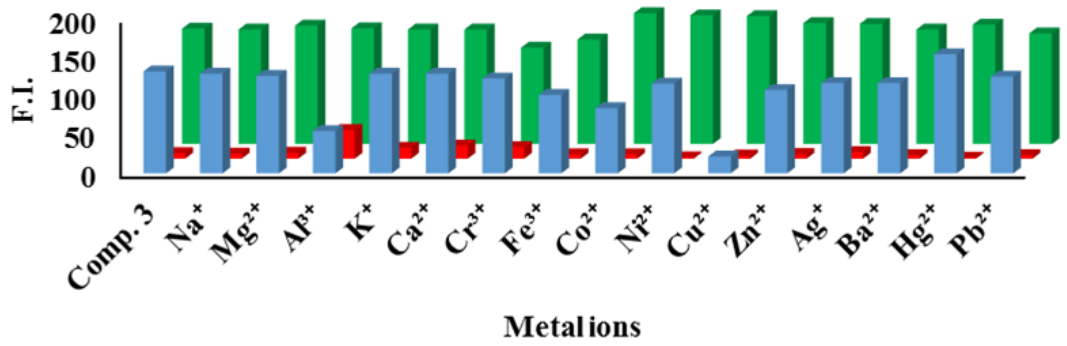

Figure 4.15 Emission intensity of compound **3** (blue bars), compound **3**.Al^{3+} (red bars) and Compound **3**.Cu^{2+} (green bars) in the presence of different competing metal ions.

4.2.1.3 Theoretical studies

The geometry optimizations for all molecules were carried out at DFT/B3LYP level of theories using 6-31+G(d,p) basis sets for C, H, N, O, and LANL2DZ for Al^{3+} and Cu^{2+}. Further, absorption properties were analyzed by vertical excitation energy calculation using the time-dependent density functional theory (TD-DFT) method. The calculated absorption spectra have been summarised in Table 4.2**.**

Table 4.2 The calculated absorption value for compound **3**, the symmetry of frontier orbital and % contributions of molecular orbitals

Compound **3**.Al^{3+}					
λ(nm)	**λ_{Exp} (nm)**	**Osc. Strength**	**Symmetry**	**Major Orbital**	
450	470	0.2247	Singlet-A	H→L+2	95
418		0.4360	Singlet-A	H-1→L+1	94
Compound **3.**Cu^{2+}					
476	375	0.4851	Singlet-A	H-1→L+1	70
358		0.4706	Singlet-A	H-1→L+3	81

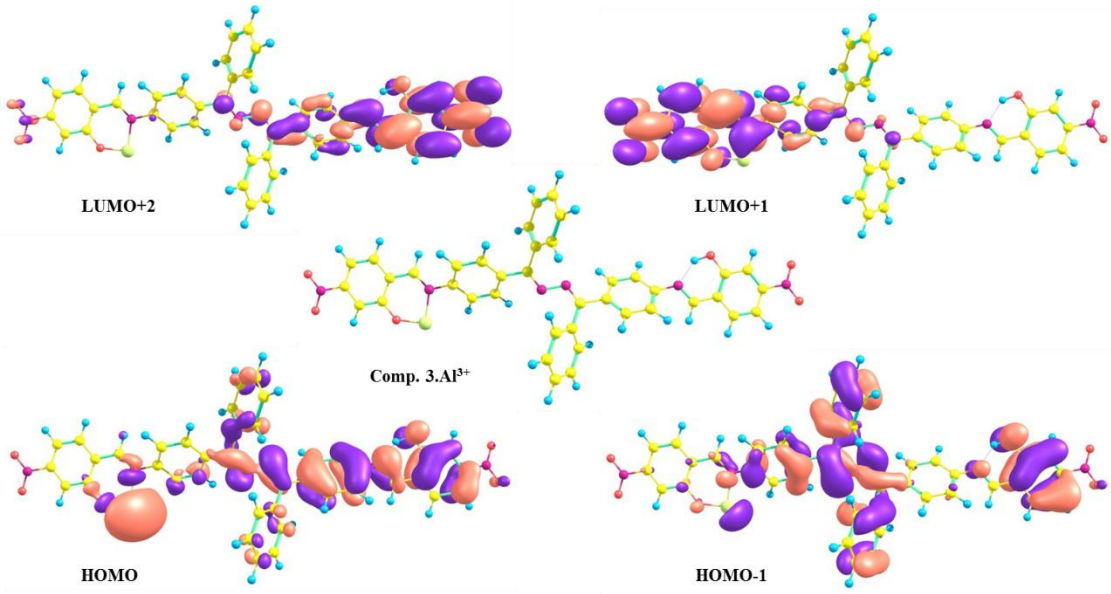

Figure 4.16. Optimized structures of compound **3.**Al^{3+} and their FMOs.

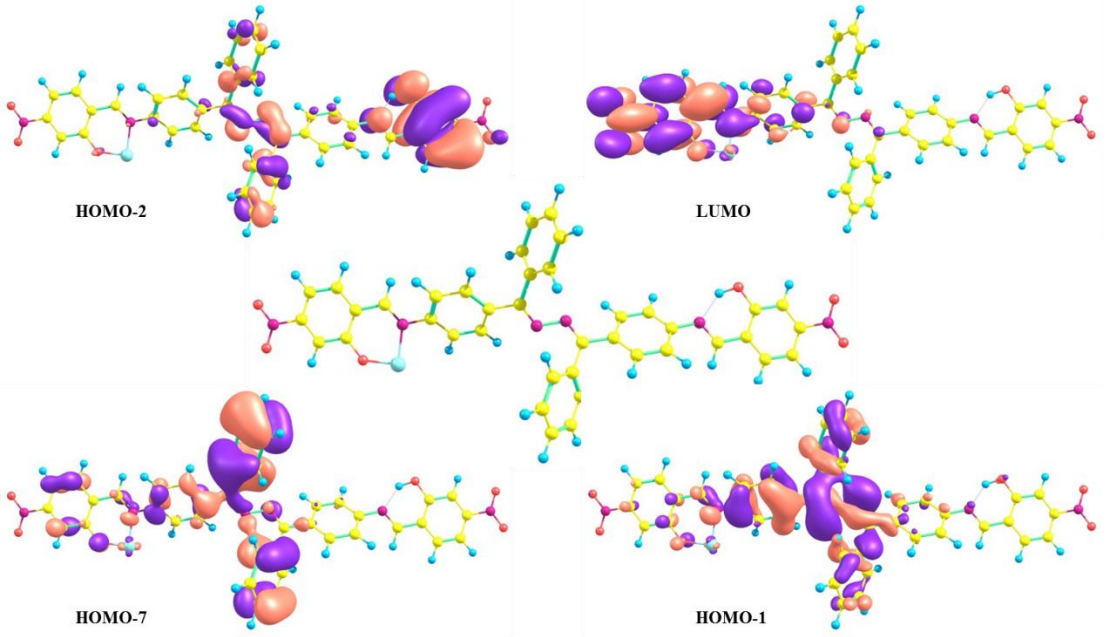

Figure 4.17 Optimized structures of compound **3**.Cu^{2+} and their FMOs.

The electronic excitation at 450 nm of compound **3**.Al^{3+} complex, displayed electron density shift from on half of the molecule to Al^{3+} ions and therefore, the excitation was assigned as LMCT transition. Another, excitation at 418 nm was originated from the electron density shift from azine linked phenyl rings to Al^{3+} coordinated sites and attached phenyl unit. On the other hand, the electronic excitations of compound **3**.Cu^{2+} complex were originated from the electron density shift from different parts of molecular

architecture to Cu^{2+} coordinated sites and attached phenyl unit. Therefore, the excitations involved the charge transfer.

4.2.1.4 Mechanism

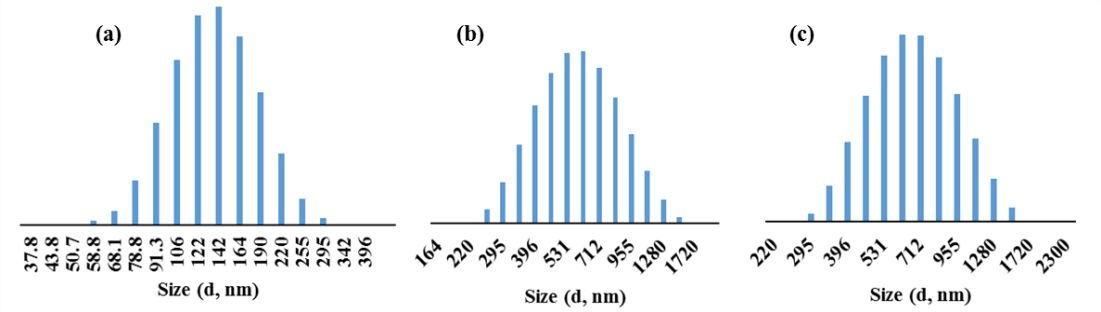

Figure 4.18 DLS profile for compound **3** (20 µM, CH_3OH) in (a) pure CH_3OH; (b) and (c) after the addition of 200 µM of Al^{3+} and Cu^{2+} ions, respectively.

The appearance of new absorption peaks and distinguished emission response of compound **3** recognized Al^{3+} and Cu^{2+} ions. The imine and phenolic oxygen are two coordinating sites for metal ions. The binding of Al^{3+} ions to compound **3** could restrict the intramolecular rotation and caused enhancement in emission. Likewise, the coordination of Cu^{2+} ions to compound **3** also restricted the intramolecular rotation and however, quenching of emission could be due to electron transfer from the compound **3** to Cu^{2+} ions. Further, the hydrodynamic diameters of compound **3** were measured in the presence of Al^{3+} and Cu^{2+} ions. The compound **3** (20 µM, CH_3OH) displayed a hydrodynamic diameter of 165 nm. However, upon introduction of 200 µM of Al^{3+} and Cu^{2+} ions to compound **3**, an increased in the hydrodynamic diameter was observed. The determined diameters were 590 nm, and 615 nm for Al^{3+} and Cu^{2+} ions, respectively. The increased diameter has supported the formation of aggregates for complexes. Supplementary, the emission response of compound **3**.Al^{3+} and compound **3**.Cu^{2+} were measured in the presence of EDTA. However, the emission responses were not affected by EDTA, which suggest that the formed aggregates were based on metal templates. The chances of direct interaction of EDTA to Al^{3+} and Cu^{2+} ions could not be possible due to metal-template aggregate formation.

Further, optimization of molecular structure of compound **3** and its complex were performed at semi-empirical method PM6. It has been observed that compound **3** has head to head hydrogen bonding linkage. However, the introduction of Al^{3+} and Cu^{2+} ions

to compound **3** resulted in coordination through imine nitrogen and phenolic oxygen atoms (Figure 4.19).

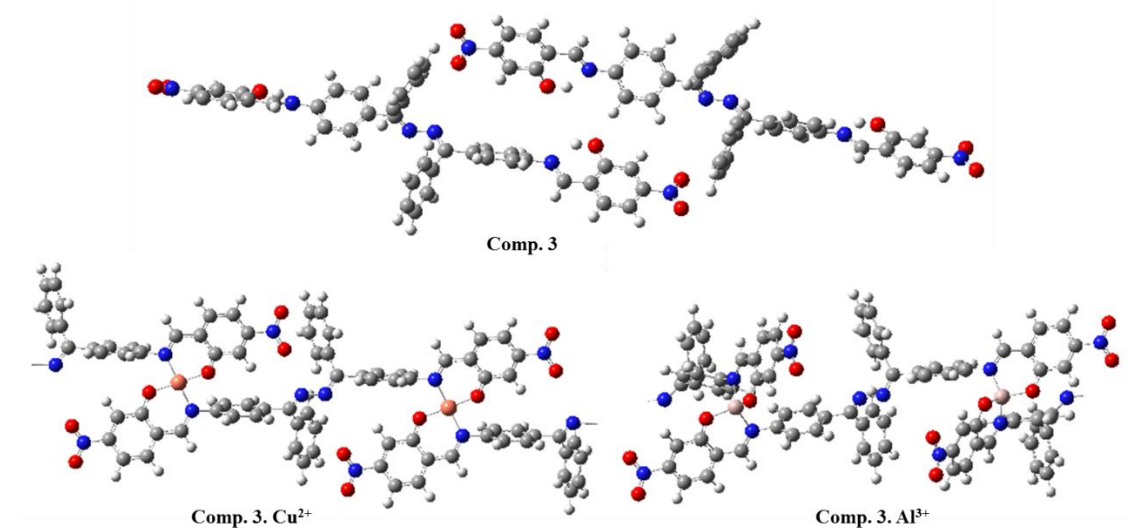

Figure 4.19 Optimized structure of compound **3** and its complex with Al^{3+} and Cu^{2+}.

4.2.2 Conclusion

Compound **3** was explored for aggregation-induced emission and sensing properties. It was noted that compound **3** exhibited the relatively stable AIE and ESIPT phenomenon in CH_3CN/H_2O than compound **2**. The increased DLS size in 70-90 % H_2O/CH_3CN medium supported the aggregation of compound **3.** Also, compound **3** was found to be a novel sensor for Al^{3+} and Cu^{2+} ions in CH_3OH. Compound **3** displayed absorption redshift of 120 nm and ratiometric blue-shifted emission response towards Al^{3+} ions, with detection limit of 12 nM. Also, compound **3** displayed the red absorption shift of 25 nm and emission quenching at 525 nm and thus, established as novel sensor for Cu^{2+} ions with detection limit of 120 nM.

4.3

ESICT efficient sensor for discriminating Zn^{2+} and Cu^{2+} ions through the dual-channel

4.3.1 Abstract

Compound **4** exhibited absorption and emission peak at 415 nm and 500 nm, respectively. Further, the AIE properties of compound **4** were studied in CH_3CN/H_2O, likely compound **2** and **3**. Compound **4** displayed a relatively weak AIE phenomenon due to presence of bulky ─NEt_2 group. Further, the effect of electron-donating groups has been elaborated on the photophysical properties towards metal ions. The compound **4** was established as a novel sensor towards Zn^{2+} and Cu^{2+} ions in CH_3OH/H_2O (9/1; v/v). Compound **4** displayed a red absorption shift of 40 nm towards Zn^{2+} ions, while a blue shift of 20 nm towards Cu^{2+} ions. In the presence of Zn^{2+} ions, compound **4** displayed slight blue-shifted emission enhancement at 490 nm; however, the emission intensity was decreased at 500 nm in the presence of Cu^{2+} ions. The detection limit of compound **4** towards Zn^{2+} and Cu^{2+} ions were determined to be 0.5 nM and 6.5 nM, respectively.

4.3.2 Results and discussion

4.3.2.1 Aggregation-induced emission (AIE) characteristic of compound 4

The compound **4** also possessed little flexibility through various single bonds likely compound **2** and **3**. Therefore, the AIE-characteristics of compound **4** was studied in CH_3CN/H_2O. The solution of compound **4** (20 µM, CH_3CN) showed absorption maxima at 415 nm. On increasing the H_2O content in CH_3CN/H_2O, the absorption intensity at 415 nm decreased (up to 50% H_2O/CH_3CN; v/v) and concomitant redshift to 430 nm (80 % H_2O/CH_3CN; v/v) along with tail off absorption between 500-700 nm (Figure 4.20). The redshift in absorption maxima with increasing the water content in CH_3CN resulted the formation of J-types of aggregates. The emission spectrum of compound **4** (20 µM, CH_3CN, λ_{ex} = 415 nm) displayed an emission at 500 nm, which increased concomitantly with slight redshift to 535 nm on increasing the H_2O content (up to 80 %) in CH_3CN/H_2O. Further, the aggregation behavior of compound **4** was supported by DLS measurements. The average hydrodynamic diameter of compound **4** (20 µM, CH_3CN) was determined to be ~50 nm, which increased to ~280 nm for 90 % H_2O/CH_3CN (v/v) and thus, endorsed the outcome of absorption and emission spectra. Therefore, the emission at 535 nm was

due to aggregated form. However, raised emission intensity was feeble compared to compound **2** and **3**. It was due to the presence of bulky ─NEt_2 group.

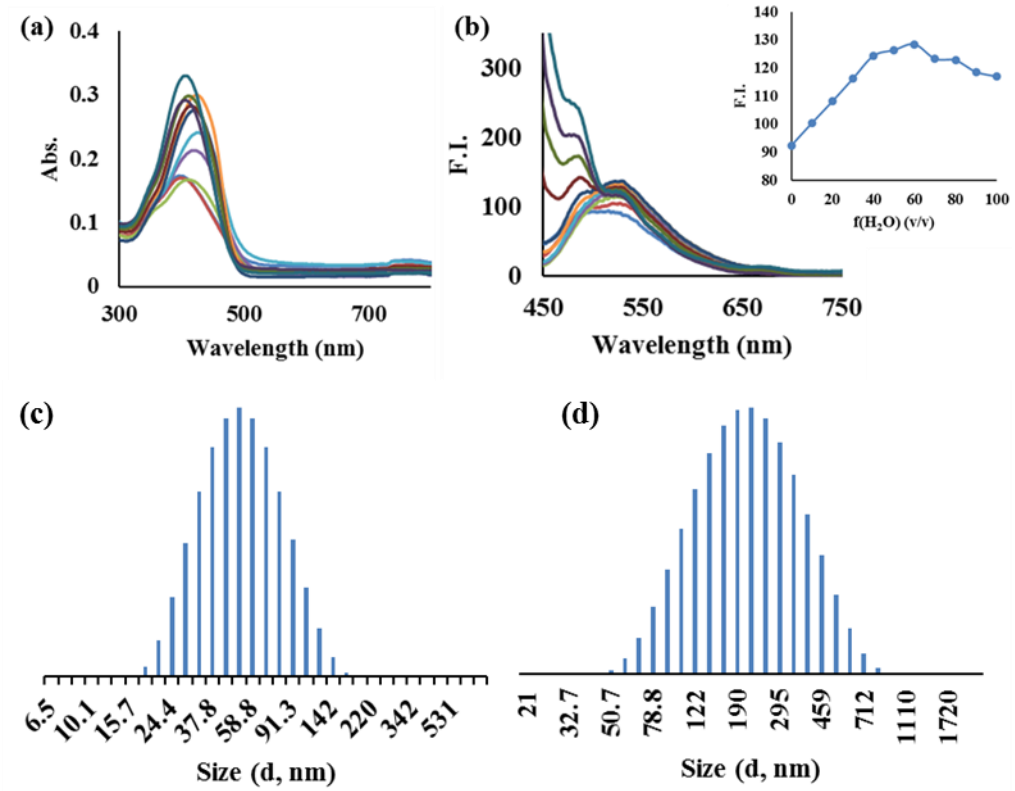

Figure 4.20 (a) Absorption and (b) emission spectra of compound **4** (20 µM) upon increasing the volume of H_2O in CH_3CN; Inset: increased emission intensity on increasing H_2O fraction; (c, d) DLS profile for compound **4** in CH_3CN and 90 % H_2O/CH_3CN; (v/v), respectively.

4.3.2.2 Sensing properties of compound 4 towards metal ions

The interaction of compound **4** with various metal ions such as Na^+, K^+, Mg^{2+}, Ca^{2+}, Ba^{2+}, Al^{3+}, Pb^{2+}, Fe^{3+}, Co^{2+}, Ni^{2+}, Cu^{2+}, Zn^{2+}, Hg^{2+} and Ag^+ was examined through absorption and emission spectroscopy in polar protic solvent (H_2O/CH_3OH; 1:9; v/v). It was noted that the absorption and emission response of compound **4** remained unchanged over the various metal ions except for Zn^{2+} and Cu^{2+} ions. The results were shown in Figure 4.21**.** The absorption peak of compound **4** at 415 nm shifted to 455 nm and 395 nm on the introduction of Zn^{2+} and Cu^{2+} ions, respectively. On the other hand, the presence of Zn^{2+} ions to compound **4** increased the emission intensity at 490 nm, while it was quenched at 500 nm in the presence of Cu^{2+} ions.

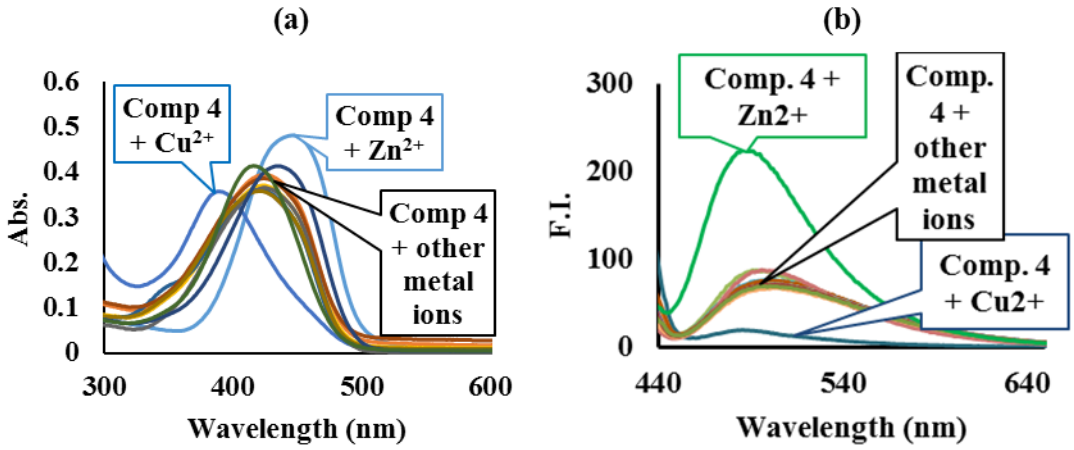

Figure 4.21 (a) Absorption spectra and (b) emission spectra of compound **4** (20 µM, H_2O/CH_3OH; 1:9; v/v) in the presence of different metal ions (1000 µM).

Further, the recognition of Zn^{2+} and Cu^{2+} ions were further studied quantitatively through the titration experiment. On gradual addition of Zn^{2+} ions, compound **4** displayed increased absorption peak at 455 nm with increased intensity (Figure 4.22). On the other hand, the addition of Cu^{2+} ions to compound **4**, decreased the absorption intensity to 395 nm (Figure 4.22). Also, it was noted that there are tailing off absorption intensity for compound **4**.Zn^{2+} and compound **4**.Cu^{2+} from 500-700 nm. These observations signified that the formation of aggregates for compound **4**.Zn^{2+} and compound **4**.Cu^{2+}.

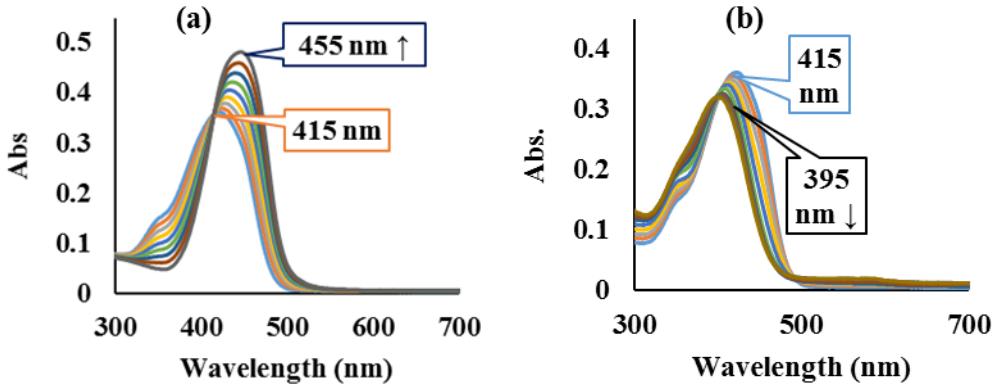

Figure 4.22. Absorption spectra of compound **4** (20 µM) on incremental addition of (a) Zn^{2+} ions and (b) Cu^{2+} ions.

Further, the quantitative recognition behavior of Zn^{2+} and Cu^{2+} ions were also studied through emission spectroscopy through titration experiment. On addition of Zn^{2+} ions, compound **4** displayed a remarkable emission enhancement at 490 nm with a small blue shift of 10 nm. The associated emission enhancement was due to the formation of compound **4.**Zn^{2+} complex was presented in Figure 4.23.

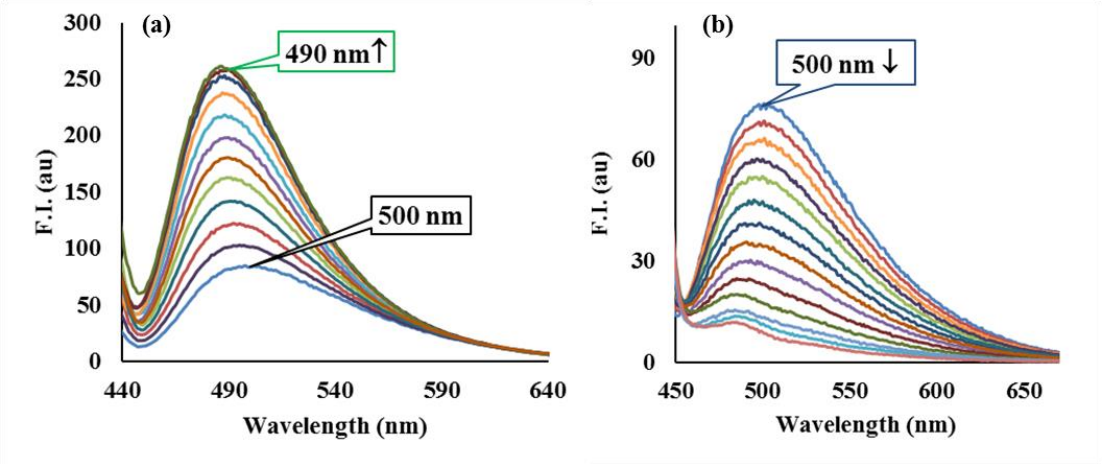

Figure 4.23. Change of the emission intensity of compound **4** with increasing concentration of (a) Zn^{2+} ions (0-30 μM) and (b) Cu^{2+} ions (0-75 μM).

On the other hand, the gradual addition of Cu^{2+} ions to compound **4** displayed a decrement in emission intensity at 500 nm (Figure 4.23). Based on the experimental results, it has been observed that the compound **4** efficiently detected Zn^{2+} and Cu^{2+} ions as a high selectivity probe through emission spectroscopy with emission enhancement and quenching mechanism, respectively.

Further, the stoichiometry of complexes was measured through Job plot and determined to be 1:2 for Zn^{2+} and Cu^{2+} ions. Furthermore, the complex formation was also confirmed by ESI-MS analysis where the mass of mixture of compound **4** and Zn^{2+}/Cu^{2+} perchlorate in CH_3OH/H_2O (9:1; v/v) was taken. The m/z peaks for compound **4.**Zn^{2+} and compound **4.**Cu^{2+} were 869.15 (compound **4** + 2.Zn^{2+}) and 865.05 (compound **4** + 2.Cu^{2+}), respectively. Furthermore, the binding constant for compound **4.**Zn^{2+} and compound **4**.Cu^{2+} was calculated from Benesi-Hildebrand equation and determined to be 1.9 x 10^4 M^{-1} and 2.6 x 10^3 M^{-1}. It was also observed that the emission intensity of compound **4** linearly dependent on the concentration of Zn^{2+} ions (1.25-10 μM) and Cu^{2+} ions (5-55 μM). Thus, the determined limit of detection for compound **4** towards Zn^{2+} and Cu^{2+} ions has been found to be 0.5 nM, and 6.5 nM, which is low enough for any fluorescent probe to detect Zn^{2+} and Cu^{2+} in environmental and biological samples.

4.3.2.3 Interference Study

In order to evaluate the probable interference of other metal ions in the detection of Zn^{2+} and Cu^{2+} ions, the emission responses of compound **4** towards Zn^{2+} and Cu^{2+} ions was observed in the presence of other metal ions. Most of the metal ions did not show any interference with the detection of Zn^{2+} and Cu^{2+} ions. However, Mg^{2+}, Al^{3+}, Fe^{3+} $Co^{2+,}$ and Pd^{2+} partially reduced the fluorescence intensity of the compound **4.**Zn^{2+} complex, but clearly detectable, while the emission response of Zn^{2+} ions was quenched in the presence of Cu^{2+} ions. The results were displayed in Figure 4.24.Therefore, enhancement and quenching of emission for compound **4** is a good indication for the prime presence of Zn^{2+} and Cu^{2+} ions.

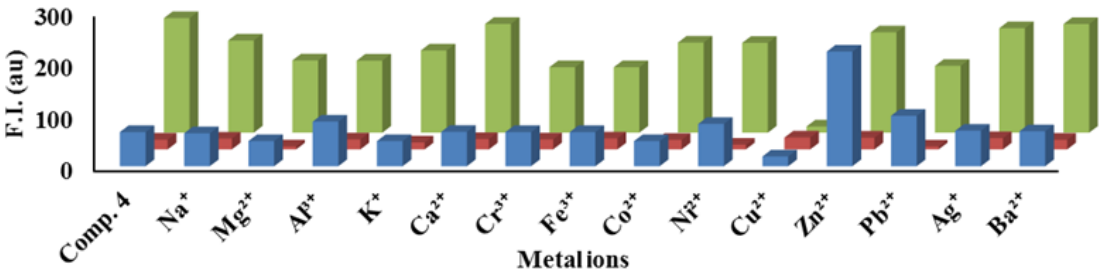

Figure 4.24. The emission intensity of compound **4** (blue bars, λ_{em} = 490 nm) compound **4**.Zn^{2+} (green bars, λ_{em} = 490 nm) and compound **4**.Cu^{2+} (red bars, λ_{em} = 500 nm) in CH_3OH/H_2O (9:1; v/v) (λ_{ex} = 415 nm) with different competing metal ions.

4.3.3 Theoretical studies

The geometry optimizations for compound **4**.Zn^{2+} and compound **4**.Cu^{2+} were carried out at DFT/B3LYP level of theories using 6-31+G(d,p) basis sets for C, H, N, O, and LANL2DZ for Al^{3+}. The frequency calculations were also performed on the obtained optimized structure at the same level of theory. In addition, absorption properties were analyzed by vertical excitation energy calculation using the time-dependent density functional theory (TD-DFT) method. The calculated absorption spectral values, symmetry, oscillation strength, and significant contributing FMOs have been summarised in Table 4.3**.** The optimized structures of compound **4**.Zn^{2+} and compound **4**.Cu^{2+} have been shown in Figure 4.25, along with their FMOs. The MOs distribution analysis of compound **4**.Zn^{2+} revealed that the electronic transitions were originated due to electron density shift from the Zn^{2+} center to compound **4**, and therefore, assigned as MLCT transition.

Table 4.3 The calculated absorption value for compound **4**, Osc. Strength (f) symmetry, and frontier orbital contributions of for electronic excitation

Complex	λ (nm)	λ_{Exp} (nm)	f	Symmetry	% MOs	
Compound **4.**Zn^{2+}	431	455	2.2309	Singlet-A	H-1→L	85
	366		0.3223	Singlet-A	H-2→L	68
Compound **4.**Cu^{2+}	405	395	0.9603	Singlet-A	H-1→L+1	33
					H→L+2	35
	364		0.4317	Singlet-A	H-2→L+2	35

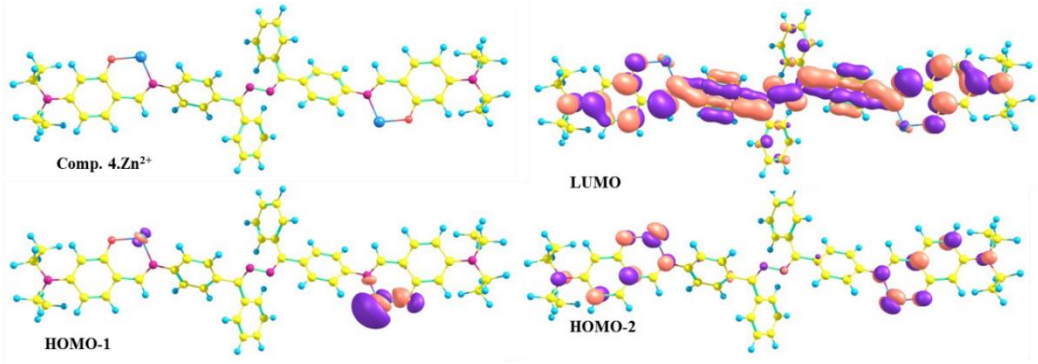

Figure 4.25 Optimized structure of compound **4.**Zn^{2+}, and it's molecular orbitals

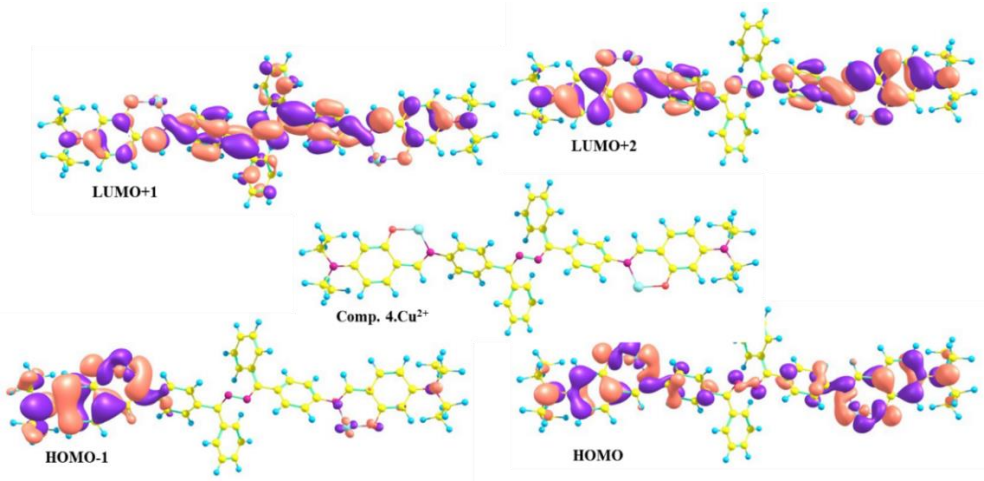

Figure 4.26 Optimized structure of compound **4.**Cu^{2+}, and it's frontier molecular orbitals

Likewise, MOs of compound **4.**Cu^{2+} complex were analyzed and found that the occupied MO have electron density distribution over compound **4** and Cu^{2+} center; however, the unoccupied MOs has shifted from compound **4**. Therefore, the electronic transitions were of MLCT nature; however, the paramagnetic effect of Cu^{2+} ions lead to emission quenching of compound **4**.

4.3.3.1 Mechanism

The appearance of new absorption peaks and distinguished emission response was recognized as the coordination of Zn^{2+} and Cu^{2+} ions with the imine and phenolic oxygen of compound **4**. The binding of Zn^{2+} ions to compound **4** also restricted the intramolecular rotation and caused enhancement in emission. The binding of Cu^{2+} ions to compound **4** also restricted the intramolecular rotation and however, quenching of emission was due to the paramagnetic effect of Cu^{2+} ions. Further, the hydrodynamic diameters of compound **4** were measured in the presence of Zn^{2+} and Cu^{2+} ions. The compound **4** (20 µM, H_2O/CH_3OH; 1:9; v/v) displayed a hydrodynamic diameter of 255 nm. However, upon introduction of 100 µM of Zn^{2+} and Cu^{2+}ions to compound **4**, the hydrodynamic diameter was increased to 530 nm, and 590 nm, respectively. The increased diameter has supported the formation of aggregates for complexes.

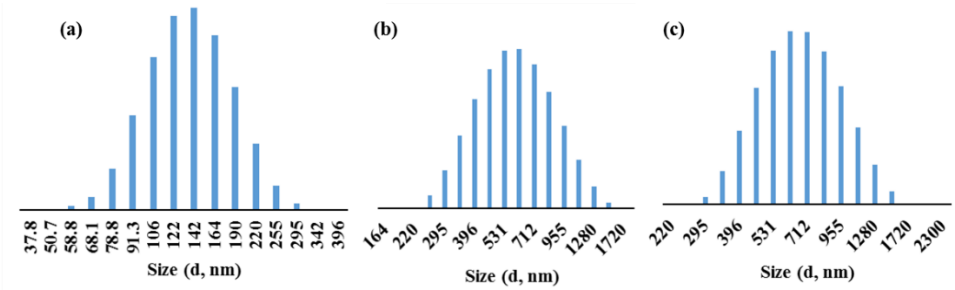

Figure 4.27 DLS profile for (a) compound **4** (20 µM, CH_3OH/H_2O; 9:1; v/v) and after the addition of 100 µM of (b) Zn^{2+} ions (c) Cu^{2+} ions.

4.3.4 Conclusion

Compound **4** exhibited absorption and emission peak at 415 nm and 500 nm, respectively. Further, the AIE properties of compound **4** were studied in CH_3CN/H_2O, likely compound **2** and **3**. Compound **4** displayed a relatively weak AIE phenomenon due to the presence of bulky ─NEt_2 group. Further, the effect of electron-donating groups has been elaborated on the photophysical properties towards metal ions. The compound **4** was established as a novel sensor towards Zn^{2+} and Cu^{2+} ions in CH_3OH/H_2O (9/1; v/v). Compound **4** displayed a red absorption shift of 40 nm towards Zn^{2+} ions, while a blue shift of 20 nm towards Cu^{2+} ions. In the presence of Zn^{2+} ions, compound **4** displayed slight blue-shifted emission enhancement at 490 nm; however, the emission intensity was decreased at 500 nm in the presence of Cu^{2+} ions. The detection limit of compound **4** towards Zn^{2+} and Cu^{2+} ions were determined to be 0.5 nM and 6.5 nM, respectively.

Summary of Chapter 4

The presence of single bonds and azine linkage in bis(diphenylmethylene)azine based Schiff base (abbreviated as compound **2-4)** encouraged the little flexibility and intramolecular motions and thus, lead to weak emission in the solution state. However, the molecular motions were restricted by inducing aggregation and introducing large groups. The measured absorption and emission spectra in CH_3CN/H_2O displayed that the aggregates were formed in >70% H_2O/CH_3CN. The significant hydrodynamic diameter changes were noted in support of aggregation. It was noted that compound **2** and **3** demonstrated strong AIE phenomenon relative to compound **4**. The weak AIE phenomenon for compound **4** was due to the presence of large ─NEt_2 groups. Further, compounds were elaborated for sensing properties towards metal ions.

Compound **2** displayed colorimetric and "*off-on*" emission response towards Al^{3+} ions, with a detection limit of 2.7×10^{-7} M in CH_3OH. The association of compound **2** to Al^{3+} also causes a restriction in intramolecular motion-induced emission. The hydrodynamic diameter of compound **2** increases from 335 nm to 625 nm in the presence of Al^{3+} ion in CH_3OH.

Further, the introduced $–NO_2$ group pulled the electron density towards the coordinating sites and therefore, compound **3** displayed ratiometric absorption and emission response towards Al^{3+} ions, with a detection limit of 12 nM. However, in the presence of Cu^{2+} ions, compound **3** displayed redshift to absorption spectra while emission quenching and thus established as a novel sensor towards Cu^{2+} ions with a detection limit of 120 nM.

For compound **4**, the $–NEt_2$ groups pushed the electron density towards azine center, and therefore, the compound **4** was established as a novel sensor towards Zn^{2+} and Cu^{2+} ions in CH_3OH/H_2O (9/1; v/v). Compound **4** displayed a red absorption shift of 40 nm towards Zn^{2+} ions, while a blue shift of 20 nm towards Cu^{2+} ions. In the presence of Zn^{2+} ions, compound **4** displayed slight blue-shifted emission enhancement at 490 nm; however, the emission intensity was decreased at 500 nm in the presence of Cu^{2+} ions. The detection limit of compound **4** towards Zn^{2+} and Cu^{2+} ions were determined to be 0.5 nM and 6.5 nM, respectively.

Chapter 5

Theoretical investigation of excited state intramolecular proton and charge transfer in naphthalimide-based Schiff bases

The naphthalimide unit is a potential candidate with versatile application in fluorescent markers, anticancer activity, chemical and biological sensors, photosensitizers, electron sinker etc.[69, 70, 72, 73, 150-158] The naphthalimide based compounds were used as potential candidates for chemo-sensing properties.[18, 159-164] Therefore, naphthalimide-based Schiff bases as compound **5** and **6** have been investigated for their photophysical properties by means of experimental and theoretical studies (Figure 5.1). Both compounds **5** and **6** contained the acidic ─OH group (phenolic unit) as hydrogen donor and basic ═N─ (imine unit) as hydrogen acceptor unit in close proximity to each other and therefore, established the intramolecular hydrogen bonding. Further, compound **6** contained electron-donating ─$N(Et)_2$ group at para to imine linkage, which has the tendency to push the electron density. On the other hand, naphthalimide unit has a tendency to attract electron density towards itself, and therefore, a push-pull mechanism could control the charge transfer along with proton transfer. The variation in photophysical behavior of compound **6** was studied. The study involved the calculation of origin of absorption and emission properties through different mechanistic photophysical processes. The analysis revealed that the substitution has altered the photophysical properties and tuned the PT mechanism in excited states.

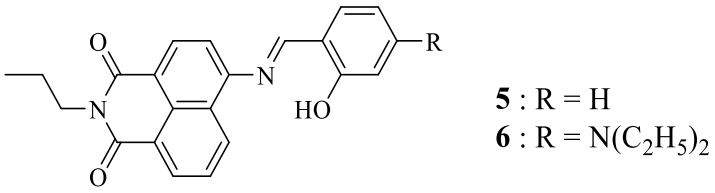

5 : R = H
6 : R = $N(C_2H_5)_2$

Figure 5.1 The different derivative naphthalimide-based Schiff base

Further, the substitution and phenomenon-based studies were summarized in the following three section

5.1. Excited state intramolecular proton transfer mechanism for high Stokes' shifted emission of naphthalimide based Schiff base

5.2. Excited state intramolecular proton and twisted charge transfer mechanism for dual emission of naphthalimide based Schiff base

5.3. Triple signaling (CHEF-ESICT-ESIPT) mechanism for a chromo-fluorescent ratiometric response for Al^{3+} and F^- ions

5.1

Excited state intramolecular proton transfer mechanism for high Stokes' shifted emission of naphthalimide-based Schiff base

5.1.1 Abstract

The detection of Hg^{2+} ions and HSO_4^- ions is very crucial. In this respect, a fluorescent naphthalimide based compound **5**, was designed to detect the Hg^{2+} and HSO_4^- ions by our group and reported in Sensors and Actuators B: chemical, 2017, **246**, 776-782. The study described the detection mechanism based on the cleavage of compound **5** to its precursors in the presence of Hg^{2+} and HSO_4^- ions. However, the study lacks in the origin of absorption and emission behavior of compound **5**. Therefore, in this work, we gave an in-depth insight into the origin of the spectral behavior of compound **5** for the first time. The compound **5** displayed an emission peak at 530 nm with significant Stokes shift of ~130 nm. Indeed, the compound **5** contained excited state intramolecular proton transfer (ESIPT) site in the form of acidic ─OH (phenolic group) as hydrogen donor and basic ═N─ (imine group) as hydrogen acceptor units. The intramolecular hydrogen bonding (IraHB) was established at S_0 state, and its strengthening at S_1 state was demonstrated through geometrical parameters, FTIR, and AIM study. The proton transfer and isomeric torsional conversion were analyzed by potential energy curves (PECs).

5.1.2 Results and discussion

5.1.2.1 Photophysical properties of compound 5

Compound **5** (20 µM, CH_3OH) displayed an absorption peak at 380 nm. Upon photoexcitation, compound **5** (20 µM, CH_3CN, λ_{ex} = 380 nm) showed emission bands at 510 nm accompanied by Stokes` shift of 130 nm (Figure 5.2). Indeed, compound **5** contained the acidic ─OH group (phenolic unit) and basic ═N─ (imine unit) in close proximity, which could establish keto-enol tautomerism through proton transfer. In addition, the large Stokes' shift or dual emission are two characteristics signs of ESIPT phenomenon. Therefore, the photophysical behavior of compound **5** was studied for the ESIPT mechanism. In order to explore the phenomenon, the theoretical calculations have been carried out for compound **5** at S_0 and S_1 state at B3LYP/6-31+G(d,p) using DFT and TDDFT methods, respectively.

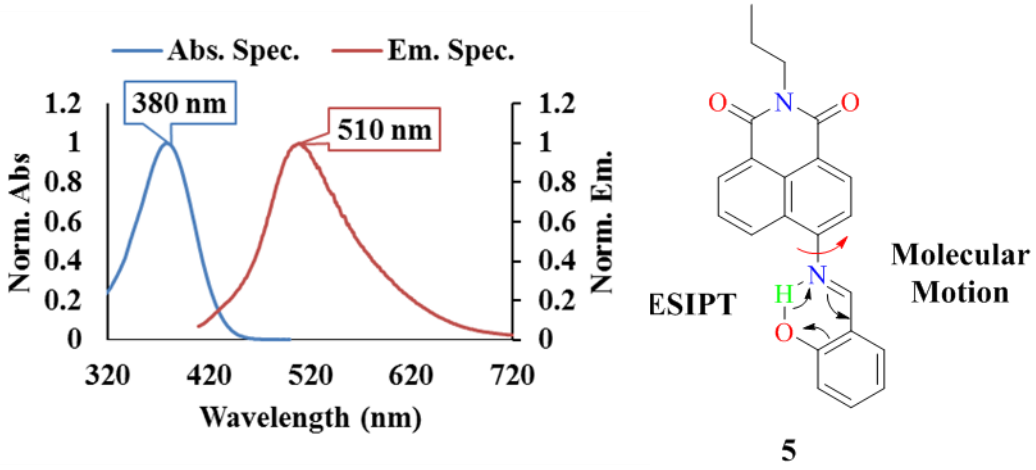

Figure 5.2. Normalized absorption and emission spectra of compound **5**

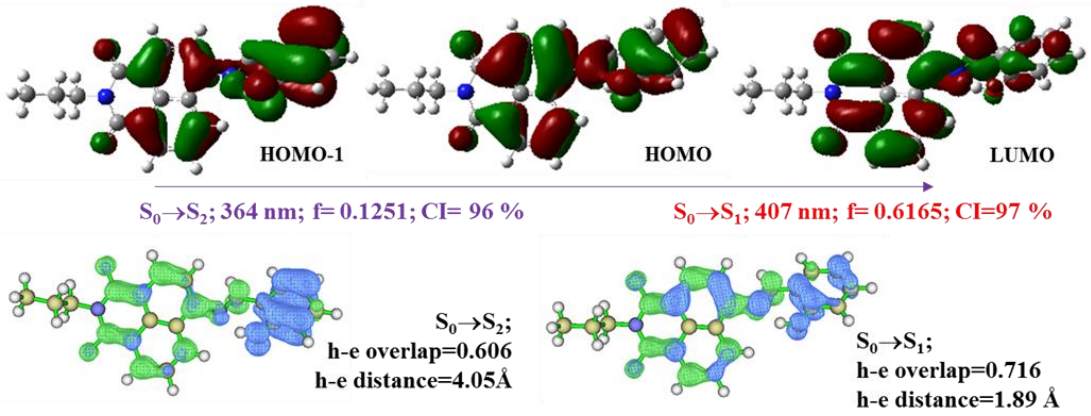

Figure 5.3. Calculated absorption peaks and contributing frontier molecular orbitals; and Hole-electron (h-e) distribution of compound **5**.

5.1.2.2 Electronic spectra and charge distribution

Further, the Frank-Condon (FC) excitations were calculated on the S_0 optimized structure to determine contributing vertical excitation, and the results have been summarized in Figure 5.3. In addition, electronic transition symmetry, the oscillation strength, and involved FMOs were summarized as an associated important parameter. The calculated absorption peak at 407 nm/3.05 eV was originated from the HOMO→LUMO transition, with the contribution of 97 % and oscillation strength of 0.6165, while another absorption peak at 364 nm/ 3.41 eV was originated from the HOMO-1→LUMO transition, with contribution factor of 96 % and oscillation strength of 0.1251. The FMOs analysis revealed that the HOMO and LUMO has electron density distribution over the whole molecular structure except the propyl chain. Further, the hole-electron plot was

constructed and used to determine the quantitative nature of the excitations (Figure 5.3). For $S_0 \rightarrow S_1$ hole-density was dispersed over the whole molecule (majorly over the phenyl unit and minor extension over the naphthalimide unit), while the electron density was located over the naphthalimide unit majorly. Also, the determined hole-electron spatial separation (1.89 Å) and their trivial overlap integral (0.716) indicated that the transition has the nature of local excitation. On the other hand, hole-electron density for $S_0 \rightarrow S_2$ transition was dispersed over the hydroxyphenyl unit and naphthalimide unit, respectively. The determined hole-electron spatial separation (4.05 Å), and their significant overlap integral (0.606) indicated the excitation as a charge-transfer transition. Also, it signified that the electron density shifted from hydroxyphenyl to the naphthalimide unit.

5.1.2.3 Geometrical parameters

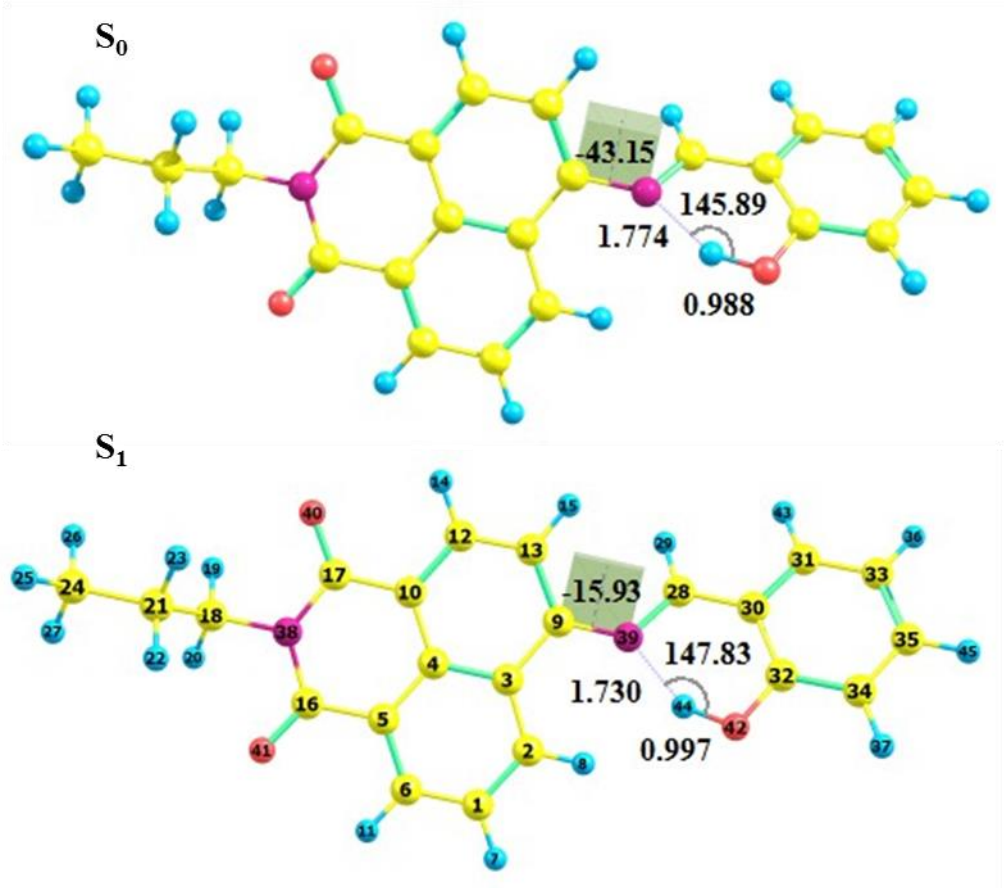

Figure 5.4. Optimized structure of compound **5** in S_0 and S_1 states.

The compound **5** was optimized at S_0 and S_1 states, with no imaginary frequency and found to be in the non-planar state. The optimized structures of compound **5** were

presented in Figure 5.4. The essential geometrical parameters of atoms involved in IraHB were discussed. The O_{42}–H_{44} bond distance was calculated to be 0.988 Å at S_0 state, which increased by 0.009 Å to 1.005 Å at S_1 state. In addition, the phenolic functional group (O_{42}–H_{44}) has a short contact distance of 1.774 Å with N_{39} at S_0 state. Further, on photoexcitation to S_1 state, the $O_{42}H_{44}\cdots N_{39}$ bond distance was decreased by ~0.044 Å to ~ 1.730 Å. Meanwhile, the bond angles for interactions $O_{42}H_{44}\cdots N_{39}$ was enlarged from 145.89° to 147.83° for $S_0 \rightarrow S_1$. Thus, the small interacting distance of $O_{42}H_{44}\cdots N_{39}$ indicated six-membered intramolecular hydrogen bonding (IraHB) in S_0 and S_1 states. However, the decreased $O_{42}H_{44}\cdots N_{39}$ bond lengths, and increased interacting bond angles imply that the IraHB strengthens in S_1 relative to S_0 state. In addition, it was noted that compound **5** tends to be more planar at S_1 state than S_0 state. The effective dihedral angle $\delta(C_{13}C_9N_{39}C_{28})$ was calculated to be -43.15° and -15.93° at S_0 and S_1 state, respectively.

5.1.2.4 Frequency analysis

The FTIR signals and the spectral shifts to the characteristics of functional groups involved in IraHBs provided information on the nature of IraHBs. Therefore, the simulated FTIR spectra at S_0 and S_1 states have been presented in Figure 5.5, which was further enlarged as an inset for O_{42}—H_{44} signals of compound **5**. The O_{42}–H_{44} vibrational stretching frequency was located at 3268 cm^{-1} at S_0 state, which was calculated at 3087 cm^{-1} at S_1 state. The relatively large red-shift of 181 cm^{-1} in FTIR signal for $S_0 \rightarrow S_1$ implied that the IraHBs ($O_{42}H_{44}\cdots N_{39}$) was relatively more strengthened at the S_1 state compared to S_0 state and thus, could promote the ESIPT.

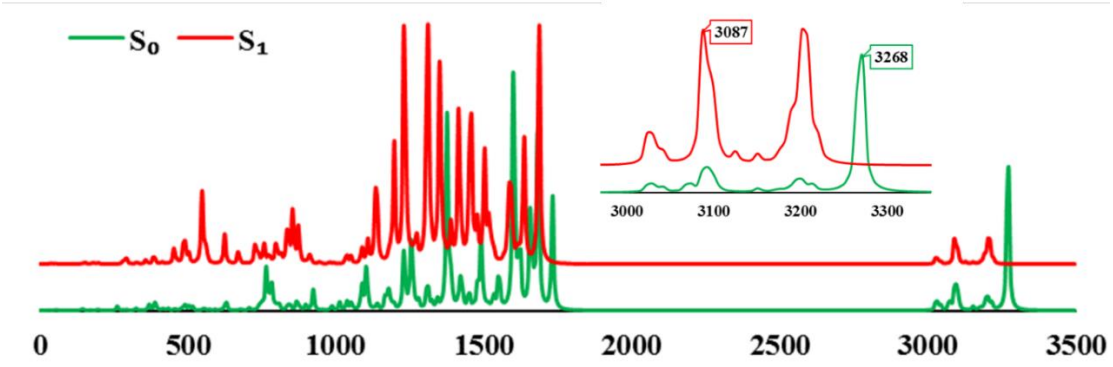

Figure 5.5. FTIR spectra of compound **5** at S_0 and S_1 state

5.1.2.5 AIM Analysis

Further, the prerequisite condition of IraHB was also established *via* an effective and established Popelier criteria using Bader's quantum theory of atoms in molecules (QTAIM).[122] The topological properties of the bond critical points (BCP) for IraHBs were within the limit of Popelier criteria (Table 5.1). The determined BCPs for IraHBs ($O_{42}H_{44}\cdots N_{39}$) were of type (3,-1) at S_0 and S_1 state. The positive value of Laplacian of electron density [$\nabla^2\rho(r_c)$] for the standard enol form of compound **5** depicted electrostatic close shell interaction in S_0, and S_1 states. Also, the Laplacian of electron density for $O_{42}H_{44}\cdots N_{39}$ interactions was increased for S_1 state relative to S_0 state, which signified the strengthening of IraHBs at S_1 state.

Table 5.1. Topology parameters electron density(ρ), Laplacian electron density ($\nabla^2\rho$), potential energy density [V(r)], total energy density [H(r)], hydrogen bonding energy [E_{HB}(kcalmol^{-1})] at bond critical point of non-covalent interactions (D···HA) for enol form in S_0, and S_1 states of compound **5**

State	Interaction	ρ	$\nabla^2\rho$	V(r)	G(r)	H(r)	E_{HB}
S_0	$O_{42}H_{44}\cdots N_{39}$	0.0011	0.1098	-0.0409	0.0342	-0.0067	-12.83
S_1	$O_{42}H_{44}\cdots N_{39}$	0.0021	0.1234	-0.0483	0.0396	-0.0087	-15.15

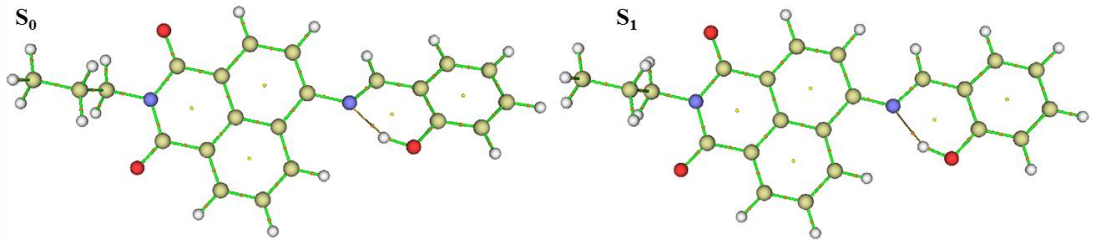

Figure 5.6. Molecular graph of compound **5** in S_0 and S_1 states

The degree of covalency and strength of the IraHB interactions were characterized according to Rozas' rules. The listed BCPs have $\nabla^2\rho(r_c) > 0$ and $H(r) < 0$ and thus, ascertained as medium-range interactions with the partial covalent character for S_0, and S_1 states (Table 5.1**)**.[123] Moreover, the interaction energies for $O_{42}H_{44}\cdots N_{39}$ was determined to be -12.83 kcalmol^{-1} and -15.15 kcalmol^{-1} at S_0 and S_1 state, respectively.[111] The increased IraHB strength at S_1 state also endorsed FTIR spectral red-shift. Further, the molecular graphs of compound **5** were plotted at S_0, and S_1 states and presented in Figure 5.6.

5.1.2.6 Proton transfer mechanism

Next, the ESIPT phenomenon was rationalized by optimizing the tautomeric forms of compound **5** (Scheme 5.1) in S_0 and S_1 states. The standard enolic tautomeric form (Compound **5**) was found to be stable relative to the keto-tautomeric form by 2.78 $kcalmol^{-1}$ at S_0 state. However, on photoexcitation to S_1 state, it was a keto-tautomeric form (**5.K**), which was relatively stabilized by 6.52 $kcalmol^{-1}$ than standard enol-tautomeric form (**5**). Therefore, the positive ΔG for **5→5.K** at S_0 state depicted that compound **5** has a preference for standard enol tautomeric form (Compound **5**), and intramolecular PT was not allowed at S_0 state (where ΔG (**5→5.K)** = [G (**5.K**)-G (**5**)]). On the other hand, the negative ΔG for **5→5.K** at S_1 state, indicated that the Compound **5.K** tautomeric form was more stabilized and thus, the intramolecular PT was permissible. In order to get the precise mechanism of dynamical PT process for compound **5**, PECs were calculated as a function of constrained IraHB bond distances ($O_{42}H_{44}\cdots N_{39}$), where the H_{44} was transferred to the N_{39} at S_0 and S_1 states.

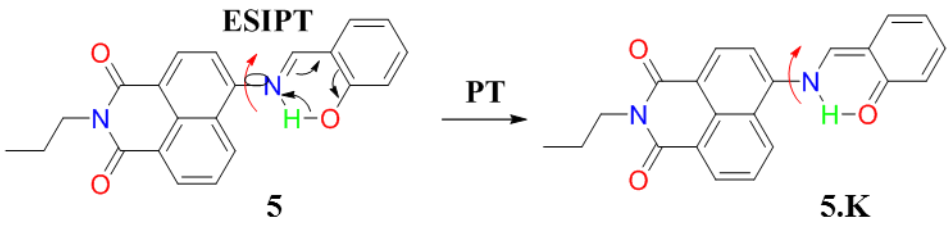

Scheme 5.1. Possible pathways of proton transfer for compound **5**.

It was noted that the PT in forwarding direction has an energy barrier of 6.39 $kcalmol^{-1}$, and 2.64 $kcalmol^{-1}$ at S_0 and S_1 states, respectively. While the reverse PT has a barrier of 3.61 $kcalmol^{-1}$, and 9.16 $kcalmol^{-1}$ at S_0, and S_1 states (Figure 3.7). Therefore, the low energy barrier value for forwarding PT and high barrier value for reverse PT support the **5→5.K** tautomeric conversions at S_1 state and thus, lead the ESIPT phenomenon.

On the other hand, the rotational flexibility about dihedral angle δ($C_{13}C_9N_{39}C_{28}$) for compound **5** was also studied at S_1 state for standard enolic and tautomeric forms **5** and **5.K**. No local minima were obtained for rotational isomeric configuration change and therefore, clearly indicated that rotational isomerism was not a feasible process.

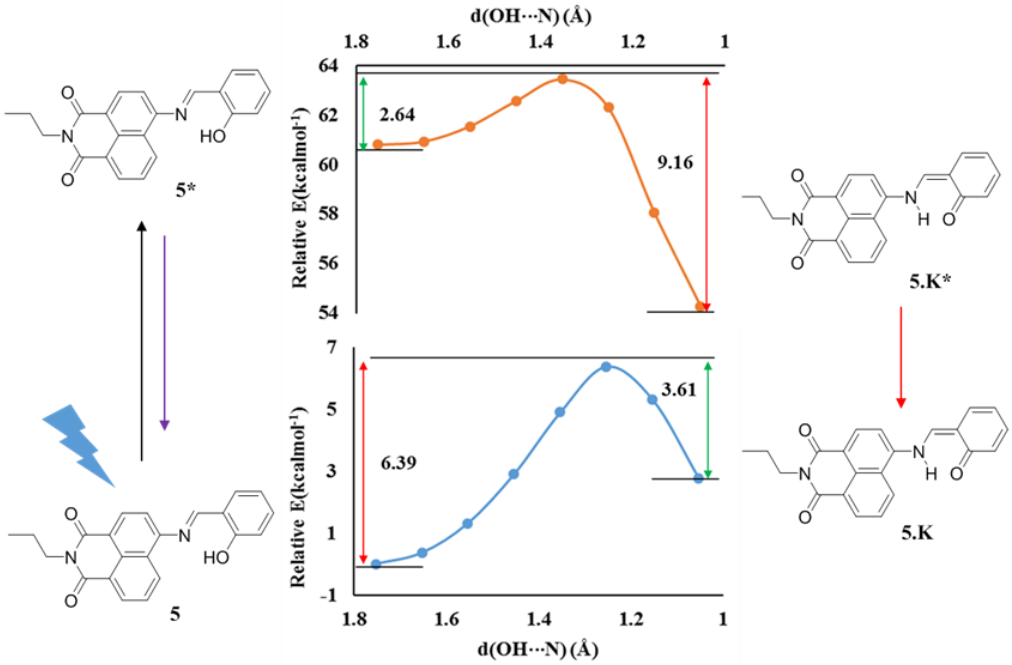

Figure 5.7. Energy profile of PEC of tautomeric conversion **5→5.K** at S_0, and S_1 states.

5.1.3 Conclusion

In this study, we investigated the ESIPT phenomenon and emission response of compound **5** through theoretical calculation approach. The computed absorption and emission peaks were in close agreement to the experimental outcomes. The prerequisite of IraHB was established using short-distance interaction, FTIR spectral signals, and calculated IraHB energy was 12.83 kcalmol^{-1} at S_0 state. The redshift of 181 cm^{-1} in FTIR spectral signal for —OH functional group verified the strengthening of IraHB, and calculated energy was found to be -15.15 kcalmol^{-1} at S_1 state. In addition, the tautomeric forms (**5.K**) was found to be more stable than its standard enol form (**5**) at S_1 state. The calculated energy barrier for forwarding ESIPT was 2.64 kcalmol^{-1}, which was determined to be lower than reverse PT (9.16 kcalmol^{-1}). Therefore, it could be concluded that the ESIPT phenomenon stimulates the emission with a significant Stokes' shift.

5.2

Excited state intramolecular proton and twisted charge transfer mechanism for dual emission of naphthalimide based Schiff base

5.2.1 Abstract

The designed compound **6** comprises of naphthalimide unit conjugated with the Schiff base linkage was synthesized and displayed excellent chromo-fluorescent properties. Compound **6** contained electron sinker naphthalimide unit and the introduced electron-donating $–NEt_2$ could push the electron density. This push-pull system could induce the intramolecular charge transfer and therefore tune the photophysical properties. The compound **6** exhibited two absorption peaks at 340 nm and 460 nm as local and charge-transfer excitation, respectively. On excitation at 460 nm, compound **6** displayed two emission bands at 510 nm and 610 nm, accompanied by Stokes` shift of 50 nm and 150 nm, respectively. In addition, on increasing the polarity of the medium, the compound **6** displayed a redshift of 20 nm and 80 nm in absorption and emission spectra, respectively. Indeed, the dual emissions are the characteristics sign of excited state intramolecular proton transfer (ESIPT). However, ESIPT could not explain the redshift in the absorption and emission peaks at high polarity. Therefore, in this work, in-depth insight was given into the ESIPT phenomenon and red-shifted absorption and emission spectra. The compound **6** contained short distance of 1.720 Å and 1.694 Å between basic imine group, (—N_{39}═) and acidic phenolic group (—$O_{42}H_{44}$) and thus, established intramolecular hydrogen bonding (IraHB) through AIM calculations at S_0 and S_1 states. The redshift of 224 cm^{-1} in FTIR spectral signals for $O_{42}H_{44}$ at S_0 and S_1 state depicted the strengthening of IraHB in S_1 state and could promote excited state intramolecular proton transfer (ESIPT). Further, the torsional isomeric form of compound **6** was found by calculating and analyzing the potential energy curves (PECs), which demonstrated the proton transfer at S_1 state. Further, the obtained torsional isomeric form at PECs displayed the relaxation at S_1 state, and the frontier molecular orbitals portrayed the charge distribution and thus, explained the spectral redshift originated from the twisted intramolecular charge transfer (TICT).

5.2.2 Experimental section

5.2.2.1 Synthesis of compound 6

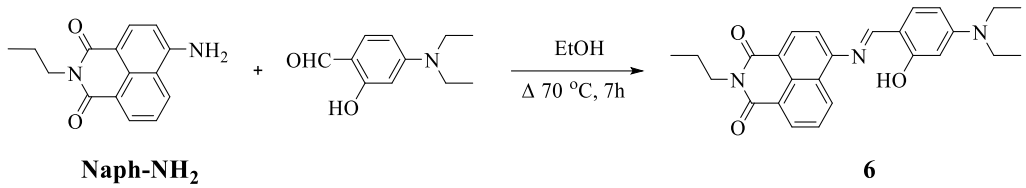

Scheme 5.1 Synthesis of compound **6**

The Naph-NH_2 has been synthesized using the reported procedure.[165] Further, Naph-NH_2 (100 mg, 0.39 mmol) was mixed with 4-diethyl amino salicylaldehyde (75 gm, 0.39 mmol) in ethanol (10 ml) at room temperature followed by refluxing (Scheme 5.1). The reaction progress was monitored using TLC. On the total consumption of reacting materials, an orange-colored solid was separated out. The solid was filtered out and washed with ethanol thrice. The filtered solid was dried over vacuum to give **2**60 mg (95%) of solid of compound **6**; m.pt. 238°C.

The ^{1}H NMR spectrum displayed resonating signals at δ 1.03 ppm as triplet due to 3H of propyl-CH_3, δ = 1.25 as triplet due to 6H of CH_3 (─NCH_2CH_3), δ 1.75-1.81 as multiplet due to 2H of propyl CH_2, δ 3.45 as quartet due to 4H of CH_2 (─NCH_2CH_3), δ 4.14 as triplet due to 2H of NCH_2, δ 6.25 as doublet due to 1H, ArH, δ 6.32-6.34 as doublet of doublet due to 1H, ArH, δ 7.26-7.28 as multiplet due to 1H, ArH, δ 7.36 as doublet due to 1H, ArH, δ 7.75 as triplet due to 1H, ArH, ppm as singlet s, 1H, ═CH—, δ 8.60 as doublet due to 1H, ArH, δ 8.63-8.66 as multiplet due to 2H, ArH; ^{13}C NMR resonating signals at δ 11.5 due to propyl CH_3, 12.7 for CH_3, 21.4 due to propyl CH_2, 41.8 due to NCH_2, 44.8 due to CH_2, 97.4, 104.6, 109.4, 114.5, 119.0, 122.5, 126.5, 126.8, 129.1, 130.1, 131.5, 132.4, 134.7, 152.5, 152.8, 162.8, 164.0 due to aromatic carbons (ArCs), 164.1 due to C=O, 164.5 due to C=O suggest the formation of compound **6**. The observed ESI-MS (m/z) 430.5 (M^{+}+1) was in close agreement with the calculated m/z =429.6 and thus, verified the formation of compound **6**.

5.2.3 Results and discussion

5.2.3.1 Photophysical properties of compound 6

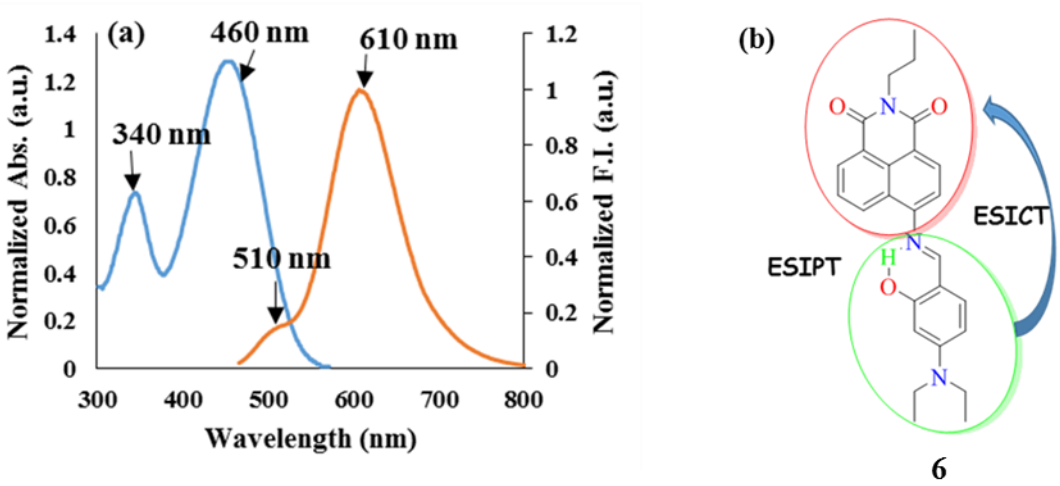

Figure 5.8. (a) Normalized absorption and emission spectra of compound **6** (20 µM, CH_3CN); (b) pictorial presentation of the possible photophysical phenomenon in compound **6**.

Photophysical properties of compound **6** were examined through absorption and emission spectroscopic techniques. Compound **6** (20 µM, CH_3CN) exhibited yellow and orange color absorption at 340 nm and 460 nm, respectively. Upon photoexcitation, compound **6** (20 µM, CH_3CN, λ_{ex} = 460 nm) showed dual emission bands at 510 nm and 610 nm accompanied with Stokes` shift of 50 and 250 nm, respectively (Figure 5.8). The dual emissions of compound **6** could be designated as characteristic ESIPT phenomenon. The emission band at 510 nm has been attributed to standard enol emission, while the emission band at 610 nm was due to excited state intramolecular proton transfer (ESIPT).

However, the presence of different functional groups/moiety of different capacity also permits different photophysical phenomenon for compound **6**. The presence of —NEt_2 unit with a capacity of electron-donating and naphthalimide core with a capacity of accepting electron density could induce ICT. Therefore, the dual emission could be tuned from a combination of the ICT or/and ESIPT (Figure 5.8). In order to understand this, the absorption and emission studies have been extended to different polarity system (Figure 5.9). The displayed redshift of 20 nm and 80 nm in absorption and emission spectra, respectively for compound **6** on increasing the polarity of system, demonstrated the presence of ESICT phenomenon along with ESIPT. In addition, the spectral changes were accompanied by several emission colors in different polarity system.

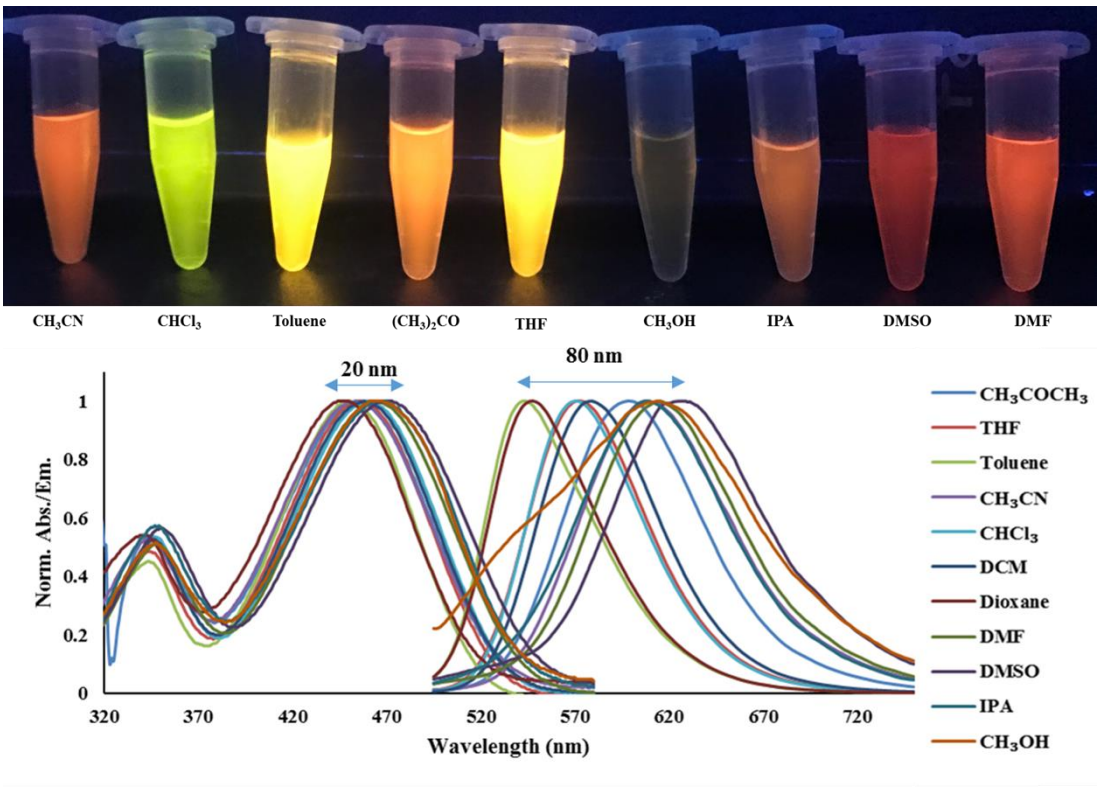

Figure 5.9. Normalized absorption and emission spectra of compound **6** in different solvents

5.2.3.2 Electronic spectra and charge distribution

First, compound **6** was optimized at S_0 state using DFT/B3LYP/6-31+g(d,p). Further, Frank-Condon (FC) excitations were calculated on the S_0 optimized structure to determine electronic excitation values using TDDFT method at the same level of theory. The determined contributing vertical excitation, and the results were summarized in Figure 5.10. In addition, electronic transition symmetry, the oscillation strength, and involved FMOs were summarized as an associated important parameter. The observed absorption peak at 460 nm was originated from the HOMO→LUMO transition, with the contribution of 99 % and oscillation strength of 0.7039, while another absorption peak at 340 nm was originated from the HOMO-1→LUMO transition, with contribution factor of 81 % and oscillation strength of 0.2039. The FMOs analysis revealed that the HOMO has significant electron density dispersal over —$PhNEt_2$ containing Schiff base unit, with a minor extension over the naphthalimide unit, however, LUMO has significant electron density dispersal over the naphthalimide unit, with a minor extension over —$PhNEt_2$ containing Schiff base unit.

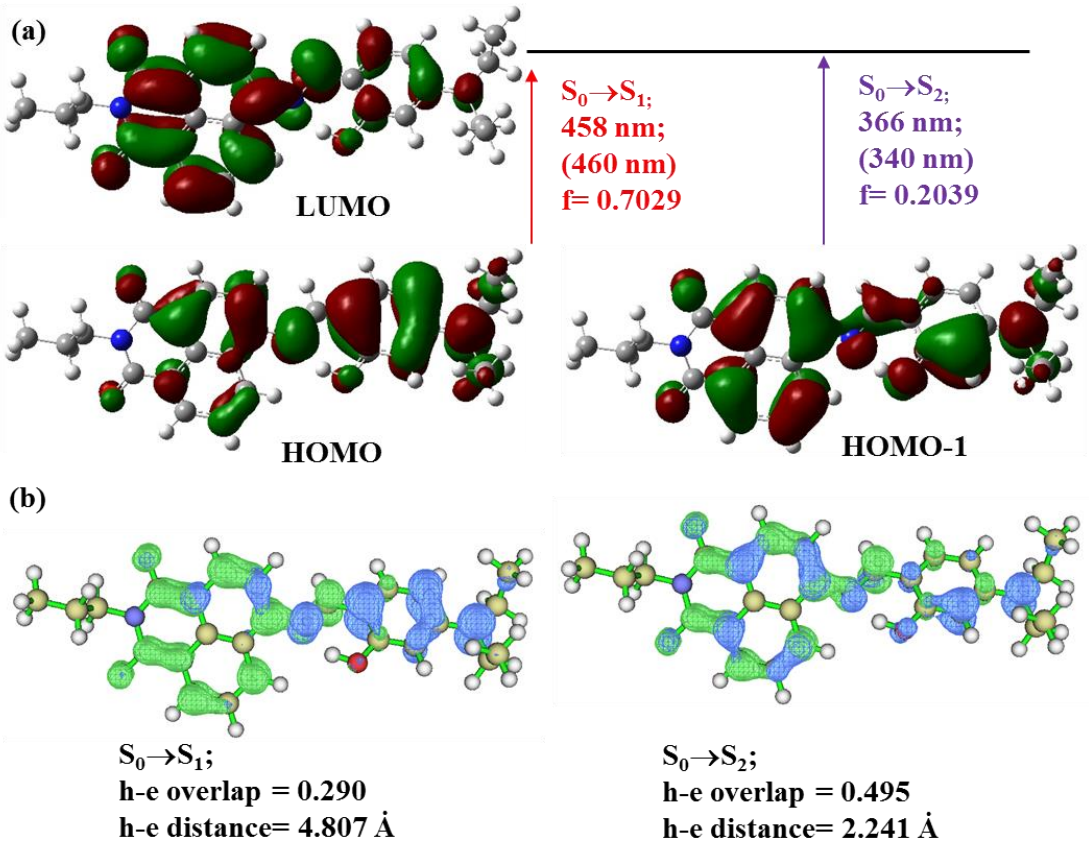

Figure 5.10. (a) Calculated absorption peaks and contributing frontier molecular orbitals; absorption values in parenthesis are the experimental values. (b) Hole-electron distribution of compound **6**

Further, the concept of hole-electron was used to determine the quantitative nature transition in Figure 5.10. For $S_0 \rightarrow S_1$ hole-density was dispersed over $-PhNEt_2$, while the electron density was located over the naphthalimide unit. This signified that the electron density shifted from $-PhNEt_2$ to naphthalimide unit. Also, the determined hole-electron spatial separation (4.807 Å) and their trivial overlap integral (0.290) indicated that the transition has the nature of charge transfer. On the other hand, hole-electron density for $S_0 \rightarrow S_2$ transition was dispersed over the whole molecular units, and the determined hole-electron spatial separation (2.241 Å), and their significant overlap integral (0.495) indicated the transition as local excitation.

5.2.3.3 Geometrical parameters

The compound **6** was found to be in a non-planar structure in the S_0 and S_1 states, with no imaginary frequency. The optimized structure of compound **6** has been presented in Figure 5.11. The essential geometrical parameters of atoms involved in IraHB were

discussed. The O_{42}─H_{44} bond distance was calculated to be 1.000 Å at S_0 state, which increased by 0.005 Å to 1.005 Å at S_1 state. In addition, the O_{42}─H_{44} unit has short contact distance of 1.720 Å with N_{39} at S_0 state. Further, on photoexcitation to S_1 state, the $O_{42}H_{44}\cdots N_{39}$ bond distance was decreased by ~0.026 Å to ~ 1.694 Å. Meanwhile, the bond angles for interactions $O_{42}H_{44}\cdots N_{39}$ was enlarged from 148.86° to 149.73° for $S_0 \rightarrow S_1$. The determined IraHB distances of compound **6** were smaller than compound **5** and bond angles were extended, which suggest that the IraHBs would be relatively stronger for compound **6**. Also, the small interacting distance of $O_{42}H_{44}\cdots N_{39}$ indicated six-membered intramolecular hydrogen bonding (IraHB) at S_0 and S_1 states. However, the decreased $O_{42}H_{44}\cdots N_{39}$ bond lengths, and increased interacting bond angles imply that the IraHB strengthens in S_1 relative to S_0 state.

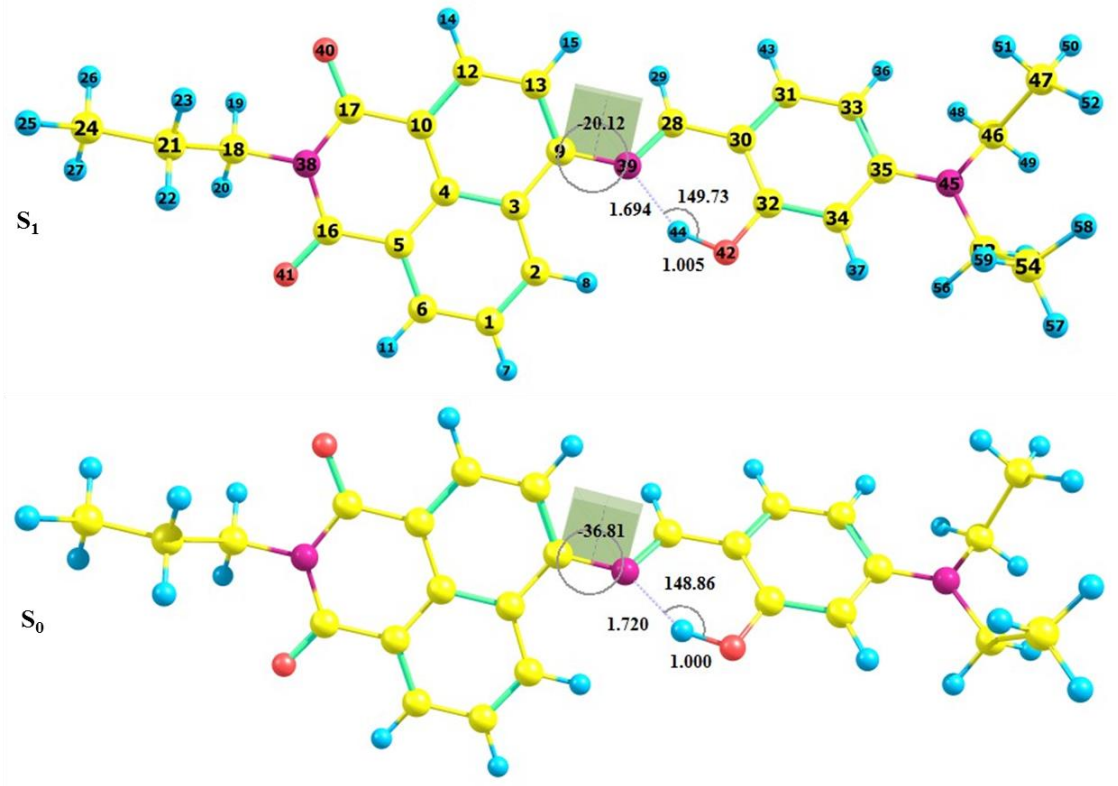

Figure 5.11. Optimized structure of compound **6** in S_0 and S_1 states.

5.2.3.4 Frequency analysis

The FTIR signals and characteristics of functional groups involved in IraHBs were simulated and noted at S_0 and S_1 states (Figure 5.12**)**, which was further enlarged as an inset for O_{42}—H_{44} signals of compound **6**. The O_{42}–H_{44} vibrational stretching frequency was located at 3199 cm^{-1} at S_0 state, which was calculated at 2975 cm^{-1} at S_1 state. The

relatively large red-shift of 224 cm^{-1} in FTIR signal for $S_0 \rightarrow S_1$ implied that the IraHBs ($O_{42}H_{44}\cdots N_{39}$) was relatively more strengthened in the S_1 state compared to S_0 state and thus, could promote the ESIPT.

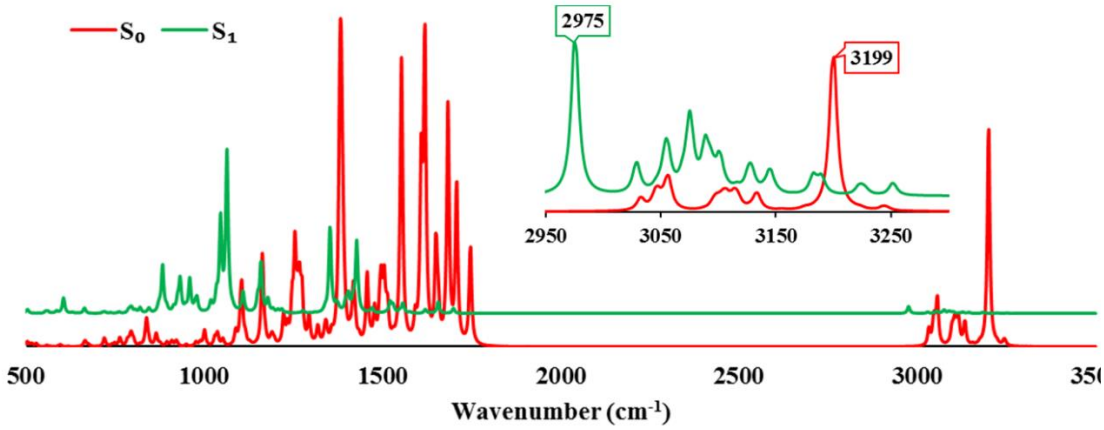

Figure 5.12. FTIR spectra of compound **6** at S_0 and S_1 state

5.2.3.5 AIM Analysis

Further, the prerequisite condition of IraHB and its energy profile was established *via* Popelier criteria using Bader's quantum theory of atoms in molecules (QTAIM).[122] The determined topological properties of the bond critical points (BCPs) for IraHBs were within the limit of criteria and thus, established IraHBs as $O_{42}H_{44}\cdots N_{39}$ at S_0, and S_1 states for compound **6** (Table 5.2). The determined BCPs for IraHBs ($O_{42}H_{44}\cdots N_{39}$) were of type (3,-1) at S_0 and S_1 state. The positive value of Laplacian of electron density [$\nabla^2\rho(r_c)$] for the standard enol form of compound **6** depicted electrostatic close shell interaction in S_0, and S_1 states. Also, the Laplacian of electron density for $O_{42}H_{44}\cdots N_{39}$ interactions was increased at S_1 state relative to S_0 state, which signified the strengthening of IraHBs at S_1 state. All the listed BCPs have $\nabla^2\rho(r_c) > 0$ and $H(r) < 0$ and thus, ascertained as medium-range interactions with the partial covalent character for S_0, and S_1 states (Table 5.2**)**.[123] Moreover, the interaction energies for $O_{42}H_{44}\cdots N_{39}$ were determined to be -11.99 $kcalmol^{-1}$ and -13.27 $kcalmol^{-1}$ at S_0 and S_1 state, respectively[111] and the increased IraHB strength endorsed the FTIR outcomes and preference for tautomeric conversion at S_1 state. Further, the molecular graphs of compound **6** were plotted at S_0, and S_1 states and presented in Figure 5.13.

Table 5.2. Topology parameters electron density(ρ), Laplacian electron density ($\nabla^2\rho$), potential energy density [V(r)], total energy density [H(r)], hydrogen bonding energy [E_{HB}(kcalmol^{-1})] at bond critical point of non-covalent interactions (D···HA) for standard enol form in S_0, and S_1 states of compound **6**

State	Interaction	ρ	$\nabla^2\rho$	V(r)	G(r)	H(r)	E_{HB}
S_0	$O_{42}H_{44}\cdots N_{39}$	0.0018	0.1142	-0.0382	0.0334	-0.0048	-11.99
S_1	$O_{42}H_{44}\cdots N_{39}$	0.0026	0.1168	-0.0423	0.0357	-0.0065	-13.27

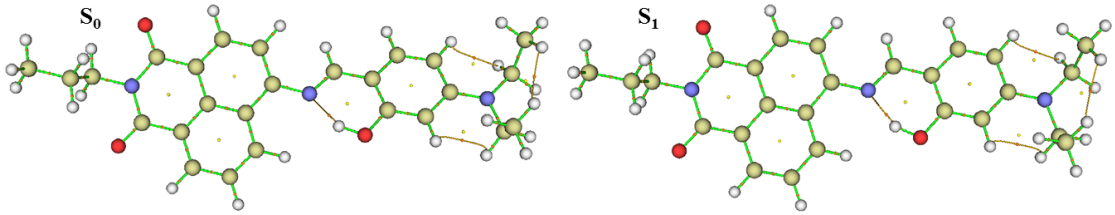

Figure 5.13. Molecular graph of compound **6** in S_0 and S_1 states

5.2.3.6 Proton transfer mechanism

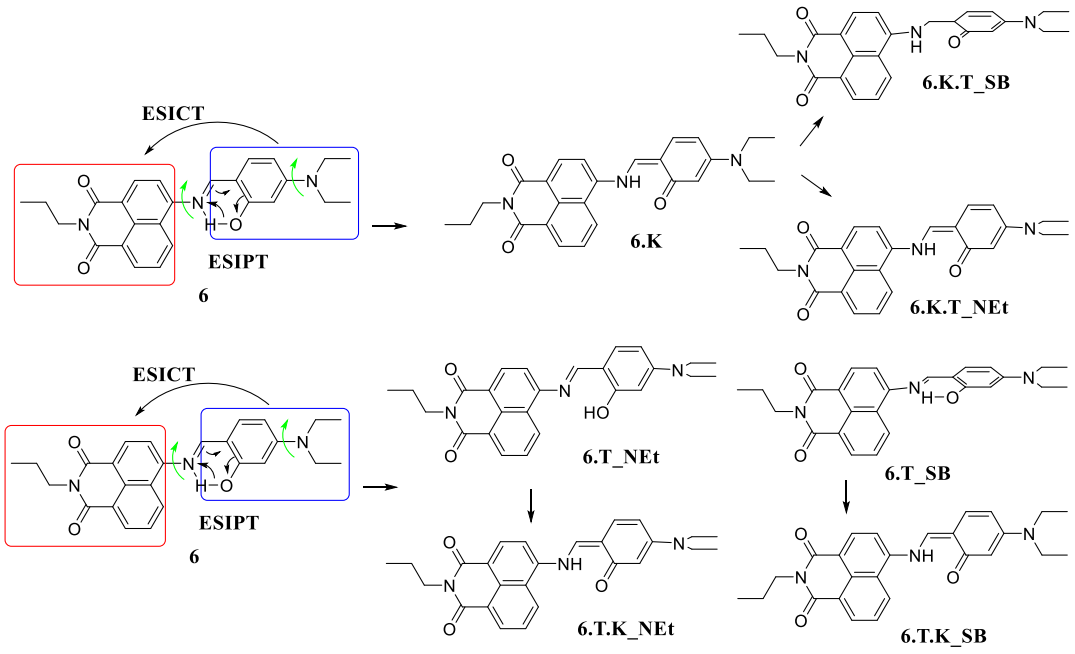

Scheme 5.2. Possible pathways of proton transfer for compound **6**.

In order to get the precise mechanism of emission spectra different possible pathways were investigated for compound **6** (i) dynamical PT process (**6→6.K**) followed by molecular rotation at (a) Schiff base linkage through C─N single bond, (**6→6.K.T_SB)** or at (b) amine centre through C─N single bond (**6→6.K.T_NEt**), Pathway I, and (ii) molecular rotation at (a) Schiff base linkage through C─N single bond, (**6→6.T_SB)** or

at (b) amine centre through C─N single bond (**6→6.T_NEt**) followed by dynamical PT process (**6→6.T.K_NEt** or **6→6.T.K_SB**), Pathway II (Scheme 5.2). Further, all the structures have been optimized using PECs approach at S_0, and S_1 states.

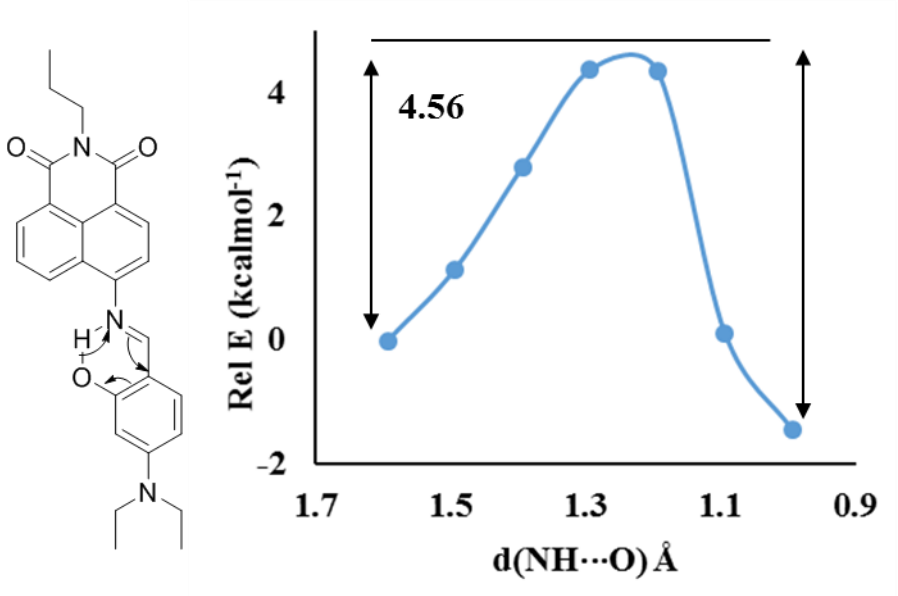

Figure 5.14. Energy profile of **6→6.K** tautomeric conversions at S_1 state.

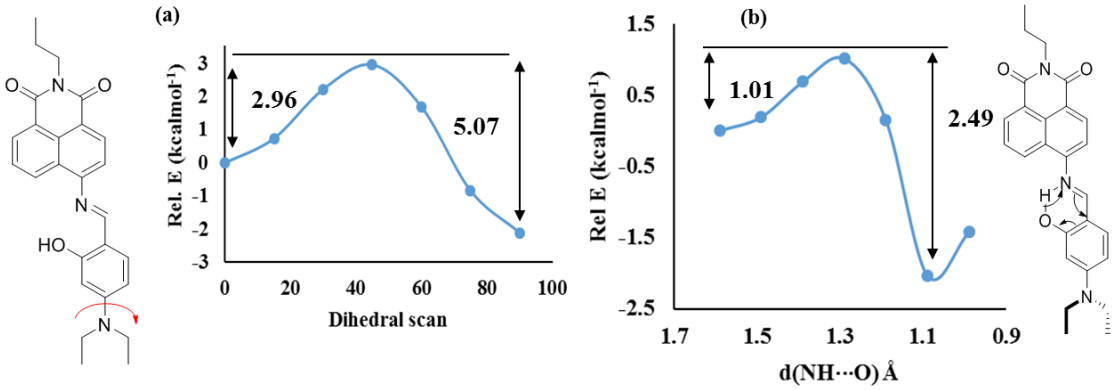

Figure 5.15. Energy profile of (a) **6→6.T_NEt** and (b) **6.T_NEt→6.T.K_NEt** tautomeric conversion at S_1 state

First, IraPT process was elaborated, and it was noted that the forwarding PT has energy barrier of 4.56 kcalmol^{-1} (**6→6.K**) and reverse PT has the barrier of 6.57 kcalmol^{-1} (**6.K→6**) (Figure 5.14). Further, the following molecular rotations were of high energy and therefore, low energy barrier for forwarding PT suggested the ESIPT process only through pathway I. On the other hand, the PECs of pathway II suggested that molecular rotation at amine center has energy barrier of 2.96 kcalmol^{-1} and followed forwarding PT process has energy barrier of 1.01 kcalmol^{-1} (Figure 5.15). The molecular rotation at

Schiff base center was of high energy and therefore, condemned the **6→6.T_SB→6.T.K_NEt** isomeric conversions. The total energy barrier of PT through pathway II was determined to be lower than PT of pathway I, and therefore, emission spectra were originated from **6→6.T_NEt→6.T.K_NEt** tautomeric conversions at S_1 states.

5.2.4 Conclusion

In this study, the origin of photophysical spectra of compound **6** was investigated through ESICT/ESIPT mechanism using theoretical calculation approach. The computed absorption and emission peaks were in close agreement to the experimental outcomes. The prerequisite of IraHB was established using short-distance interaction, FTIR spectral signals, and calculated IraHB energy was 11.99 $kcalmol^{-1}$ at S_0 state. The redshift of 224 cm^{-1} in FTIR spectral signal for ―OH functional group verified the strengthening of IraHB, and calculated energy was found to be -13.27 $kcalmol^{-1}$ at S_1 state. In addition, the isomeric conversion was elaborated through two pathways, where the molecular motion and tautomeric conversions were incorporated. The PT energy barrier was of 4.56 $kcalmol^{-1}$ for **6→6.K,** while it was calculated to be 6.57 $kcalmol^{-1}$ for **6.K→6** at S_1 state. Further, **6.K→6.K.T_NEt** and **6.K→6.K.T_SB** isomeric conversion were not favorable through pathway I. On the other hand, the **6→6.T_NEt** conversion has energy barrier of 2.96 $kcalmol^{-1}$, while it was calculated to be 5.07 kcalmol-1 for **6.T_NEt→6**. Further, the **6.T_NEt→6.T.K_NEt** has energy barrier of 1.01 $kcalmol^{-1,}$ and it was 2.49 $kcalmol^{-1}$ for **6.T.K_NEt→6.T_NEt**. However, **6→6.T_SB→6.T.K_SB** was not favorable. In addition, the total energy barrier for ESIPT (Pathway I) was 4.56 kcalmol-1, while it was 3.97 $kcalmol^{-1}$ for ESICT/ESIPT (Pathway II). Therefore, it could be concluded that the ESICT/ESIPT process stimulates the emission with a significant Stokes' shift.

5.2.5 Experiential data

The Naph-NH_2 has been synthesized using the reported procedure.[165] Further, Naph-NH_2 (100 mg, 0.39 mmol) was mixed with 4-diethyl amino salicylaldehyde (75 gm, 0.39 mmol) in ethanol (10 ml) at room temperature followed by refluxing (Scheme 5.1). The reaction progress was monitored using TLC. On the total consumption of reacting materials, an orange coloured solid was separated out. The solid was filtered out and washed with ethanol thrice. The filtered solid was dried over vacuum to give **2**60 mg (95%) of solid of compound **6**; m.pt. 238°C.

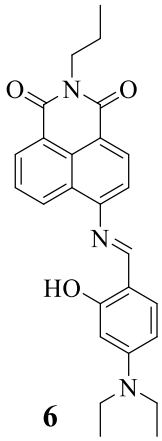

6

^{1}H NMR (CDCl3, 400 MHz): δ (ppm) 1.03 (t, *J* = 7.56 Hz, 3H, propyl-CH3), 1.25 (t, *J* = 7.10 Hz, 6H, C<u>*H*</u>$_3$), 1.75-1.81 (m, 2H, propyl C<u>*H*</u>$_2$), 3.45 (q, *J* = 7.17 Hz, 4H, C<u>*H*</u>$_2$), 4.14-4.18 (m, 2H, NC<u>*H*</u>$_2$), 6.25 (d, *J* = 2.28 Hz, 1H, ArH), 6.32-6.34 (dd, ^{2}J = 8.72 Hz, ^{3}J = 2.32 Hz, 1H, ArH), 7.26-7.28 (m, 1H, ArH), 7.36 (d, *J* = 8.24 Hz, 1H, ArH), 7.75 (t, *J* = 7.90 Hz, 1H, ArH), 8.57 (s, 1H, CH), 8.60 (d, *J* = 7.76 Hz, 1H, ArH), 8.63-8.66 (m, 2H, ArH); 13C NMR (CDCl3, 100 MHz): δ (ppm) 11.5 (propyl <u>*C*</u>H$_3$), 12.7 (<u>*C*</u>H$_3$), 21.4 (propyl <u>*C*</u>H$_2$), 41.8 (N<u>*C*</u>H$_2$), 44.8 (<u>*C*</u>H$_2$), 97.4, 104.6, 109.4, 114.5, 119.0, 122.5, 126.5, 126.8, 129.1, 130.1, 131.5, 132.4, 134.7, 152.5, 152.8, 162.8, 164.0 (ArC), 164.1 (C=O), 164.5 (C=O); MS (ESI): m/z 430.5 (M^{+}+1)

5.3

Triple signaling (CHEF-ESICT-ESIPT) mechanism for a chromo-fluorescent ratiometric response for Al^{3+} and F^- ions

5.3.1 Abstract

The designed compound **6** comprises of naphthalimide unit conjugated with the Schiff base linkage was synthesized and displayed excellent chromo-fluorescent selectivity toward Al^{3+} and F^- ions using conventional spectroscopic techniques. Upon addition of Al^{3+} ions, compound **6**'s absorption band at 460 nm was enhanced ratiometrically with respect to another absorption band at 340 nm, showing color change from orange to yellow. Likewise, compound **6**.Al^{3+} displayed ratiometric emission response at 530 nm with respect to compound **6**'s emission at 610 nm in H_2O/CH_3CN (1:9; v/v) and showing color change from yellow to blue-green emission. Therefore, the detection of Al^{3+} ions was followed up by inhibition of ESIPT band and exhibition of CHEF mechanism. On the other hand, on the addition of F^- ions, compound **6** showed a ratiometric absorption response with a new peak at 570 nm and accompanied by a color change from orange to purple. However, the emission responses of compound **6**.F^- were followed by a decrement in emission at 610 nm. The limit of detection of compound **6** towards Al^{3+} and F^- ions was measured to be 2×10^{-7} M and 7.5×10^{-7} M, respectively. The compound **6.**Al^{3+} complex was explored for the intercalation with calf thymus (ct)-DNA. The ethidium bromide displacement assay confirmed the intercalation.

5.3.2 Results and discussion

5.3.2.1 Sensing properties of compound 6

The recognition behavior of compound **6** towards various common metal ions and anions have been examined by absorption and emission spectroscopic techniques in H_2O/CH_3CN (1:9; v/v) and CH_3CN, respectively. The examined metal ions included Na^+, K^+, Mg^{2+}, Ca^{2+}, Ba^{2+}, Cr^{3+}, Al^{3+}, Co^{2+}, Ni^{2+}, Zn^{2+}, Cu^{2+}, Pb^{2+} and Ag^+ as their perchlorate salts, while the studied anions were Cl^-, Br^-, I^-, CN^-, SCN^-, F^-, HSO_4^-, NO_3^-, $H_2PO_4^-$, CH_3COO^- and PPi as their tetrabutylammonium salts. It has been observed that compound **6** selectively interacted to Al^{3+} in H_2O/CH_3CN (1:9; v/v) and F^- ions in CH_3CN through dual channel (colorimetric and fluorometric) response via ratiometric optical variations (Figure 5.16 and Figure 5.17).

5.3.2.1.1 Absorption responses of compound 6 towards Al^{3+} ions

Throughout the experiments, the compound **6** displayed a noticeable, and significant visible color change from orange to yellow in the presence of Al^{3+} ions specifically and quickly, as shown in Figure 5.16. In the presence of Al^{3+} ions to compound **6** (20 µM, H_2O/CH_3CN (1:9; v/v)) induced an absorption enhancement at 460 nm, however, absorption intensity receded at 340 nm (Figure 5.16). Further, the gradual addition of Al^{3+} ions (1-100 µM) to the solution of compound **6** also endorsed the preliminary examination, where the absorption intensity of the band at 340 nm was decreased with the simultaneous growth of absorption band at 460 nm with an isosbestic point at 390 nm (Figure 5.16). It was also determined that the absorption ratio for compound 6.Al^{3+} at 460 and 340 nm vary from 2.7 to 4.8, indicating ~3 fold ratiometric response. Therefore, these results demonstrated that compound **6** has high selectivity towards Al^{3+} ion over other metal ions and could serve as a "naked eye" sensor in H_2O/CH_3CN (1:9; v/v).

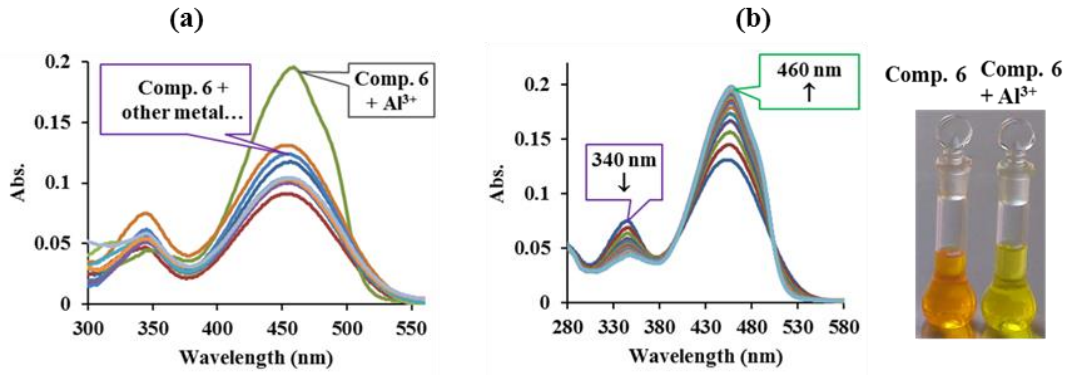

Figure 5.16. Absorption spectra of compound **6** (20 µM, H_2O/CH_3CN (1:9; v/v)) (a) in the presence of 50 equiv. of different metal ions; (b) with the incremental addition of Al^{3+} (1-100 µM); Inset: Visible color changes of compound **6** in the presence of 50 equiv. of Al^{3+} ions.

5.3.2.1.2 Emission response of compound 6 towards Al^{3+} ions

The compound **6** (20 µM, H_2O/CH_3CN (1:9; v/v)) on excitation at 460 nm showed two emission bands having weak emission at 510 nm and strong emission at 610 nm. On addition of different metal ions to the solution of compound **6**, no significant alteration was observed in the emission response of compound **6**. However, on the introduction of Al^{3+} ions, compound **6** exhibited a quick and noticeable emission color change from bright yellow to blue-green under UV light (Figure 5.17). In the presence of Al^{3+} ions, compound **6** showed a new emission peak at 530 nm ratiometrically with respect to emission at 610 nm. Further, the quantitative determination of Al^{3+} ions was performed

through a titration experiment. On gradual addition of Al^{3+} (1-250 µM) to compound **6**, the emission intensity at 610 nm was decreased with a simultaneous rise in intensity at 530 nm, with an isoemissive point at 560 nm (Figure 5.17). Also, it was determined that the emission intensity ratio at 530/610 nm showed a variation from 0.16 to 5.46 and thus, indicating ~ 34 fold ratiometric response. This enhancement in emission intensity at 530 nm might be due to the interaction of Al^{3+} ion with imine nitrogen and a hydroxyl group, which caused the chelation enhancement fluorescence (CHEF). A Job plot of the compound **6** (20 µM, H_2O/CH_3CN (1:9; v/v)) with Al^{3+} ion showed the maxima at a molar fraction of 0.5. This phenomenon indicated that the compound **6** bound to the Al^{3+} ions in a 1:1 ratio. The binding constant for compound **6**.Al^{3+} complex was determined by Benesi–Hildebrand equation and was found to be 5.4×10^4 M^{-1}. The compound **6** (20µM, H_2O/CH_3CN (1:9; v/v)) showed a linear response for Al^{3+} ion (3 - 37 µM) and the lowest detection limit was found to be 2×10^{-7} M.

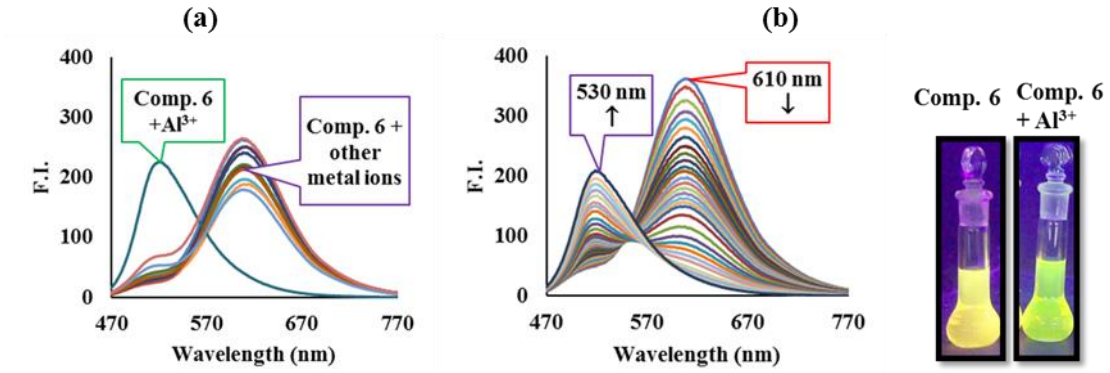

Figure 5.17. Emission spectra of compound **6** (20 µM, H_2O/CH_3CN (1:9; v/v)) (a) in the presence of 50 equiv. of different metal ions; (b) effect of the incremental addition of Al^{3+} ions to compound **6**; inset: Colour changes of compound **6** under UV light in the presence of Al^{3+} ions.

Further, the selectivity and sensitivity of compound **6** towards Al^{3+} ions were observed in the presence of other examined metal ions through emission response. The emission response of compound **6** and its complex with Al^{3+} was presented in Figure 5.18. The blue bars in Figure 5.18 represented the selectivity of compound **6** towards Al^{3+} ions over different metal ions, while red bars depicted the competitive selectivity and sensitivity of compound **6**.Al^{3+} complex in the presence of interfering metal ions. It could be noted that the emission response of compound 6.Al^{3+} complex was not altered and therefore showed excellent specificity towards Al^{3+} ions (Figure 5.18).

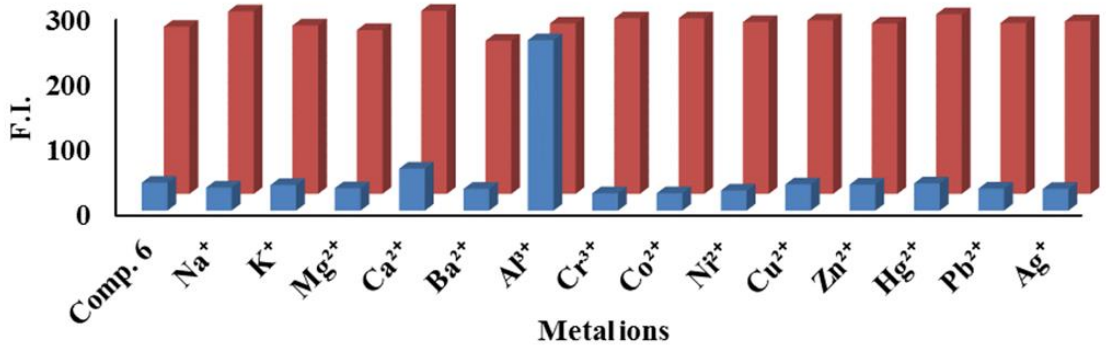

Figure 5.18. The relative emission intensity of compound **6** towards different metal ions in the absence and presence of Al^{3+} ions.

5.3.2.1.3 NMR studies

Further, the mode of interactions of compound **6** with Al^{3+} ions was studied through ^{1}H NMR titrations. The addition of 1.0 equiv. of Al^{3+} ions to compound **6**, resulted in shifting of imine proton (CH=N) of Schiff base present at δ 8.68 ppm and merged with aromatic protons at δ 8.60 ppm. The downfield shift of 0.3 ppm was observed with an aromatic proton from δ 7.50 to δ 7.80 while protons at δ 8.65 were shifted upfield by 0.2 ppm. Aromatic protons at δ 6.18 and 6.38 also shifted downfield to δ 6.30 and 6.58, respectively (Figure 5.19). Thus, the chelation of Al^{3+} ion with the nitrogen of imine bond, oxygen of the phenolic group was expected.

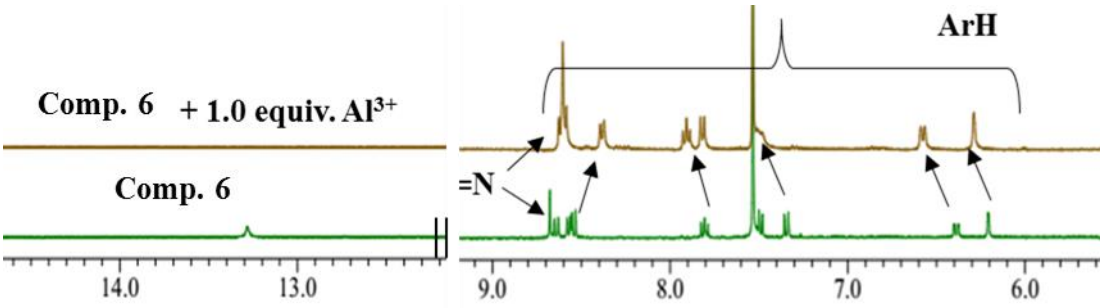

Figure 5.19. ^{1}H NMR titration spectra of compound **6** and compound **6** with 1.0 equiv. of Al^{3+} ions

5.3.2.1.4 Theoretical calculations

The experimental results have been complemented with the theoretical calculations. The compound **6**.Al^{3+} complex was optimized and shown in Figure 5.20, with precise coordination of Al^{3+} ion with phenolic O and imine N atom. The calculated absorption spectra for compound **6**.Al^{3+} was found to be in good agreement with observed absorption

value and summarised in Figure 5.20. The complex of compound **6**.Al^{3+} showed only enhancement and detraction at compound **6**'s absorption maxima experimentally, which could also be inferred from the oscillation strength values. From FMOs analysis, the observed absorption peak at 460 nm has been assigned as electron density transfer from N, N-diethyl, and propylamine to naphthalimide and Schiff base linkage, resulting in coordination with Al^{3+} ion. On the other hand, the transition at 340 nm, could be assigned as MLCT transition. Conclusively, the combinatorial analysis of experimental and theoretical results depicted that the compound **6** recognized the Al^{3+} ions in H_2O/CH_3CN (1:9; v/v) through inhibition of ESIPT/ESICT and exhibition of CHEF phenomenon.

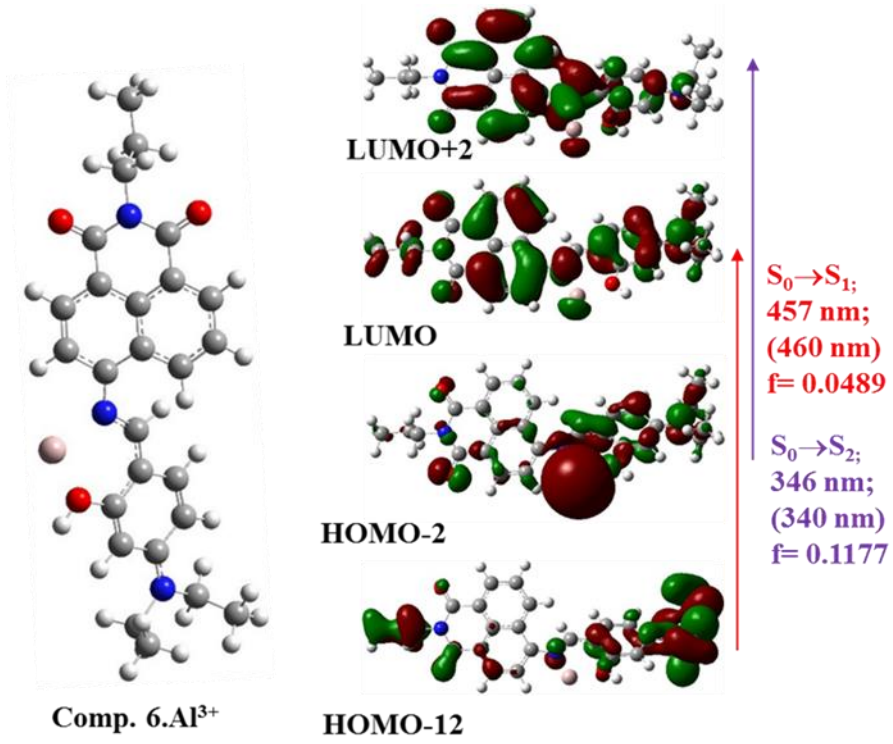

Figure 5.20. Optimized structures and frontier molecular orbitals of complex of compound **6**.Al^{3+}

5.3.2.1.5 Absorption response of compound 6 towards F^- ions

The recognition behavior of compound **6** towards various anions was studied in CH_3CN through absorption spectroscopy. Absorption spectra of compound **6** showed two absorption bands at 340 nm and 460 nm. Upon addition of 50 equiv. of tetrabutylammonium salts of various anions such as Cl^-, Br^-, I^-, CN^-, SCN^-, F^-, HSO_4^-, NO_3^-, $H_2PO_4^-$, CH_3COO^- and PPi to compound **6** (20 µM, CH_3CN), no significant change was observed in absorption spectrum except with F^- ions. A visible color change from

orange to purple with the naked eye was also observed on addition of 50 equiv. of F^- ion to 20 µM of compound **6** (Figure 5.21). On incremental addition of F^- ion (0.5-12.5 µM) to compound **6**, the absorption band at 460 nm was quenched followed by a redshift of band from 340 nm to 395 nm with the concomitant appearance of the new band at 570 nm with clear isosbestic points at 420 nm and 500 nm (Figure 5.21). The absorption ratio at 570 nm and 460 nm changes from 0.008 to 1.142 showed ~142 fold ratiometric response for F^- ions.

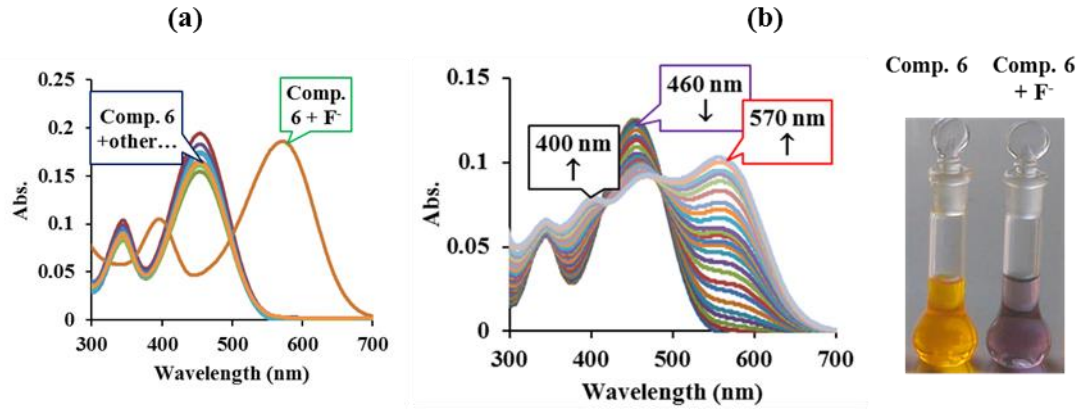

Figure 5.21 Absorption spectrum of compound **6** (20 µM, CH_3CN) (a) in the presence of 50 equiv. of different anions; (b) effect of the incremental addition of F^- (0.5-12.5 µM) to compound **6**; Inset: Visible color changes of compound **6** in the presence of various anions.

5.3.2.1.6 Emission response of compound 6 towards anions

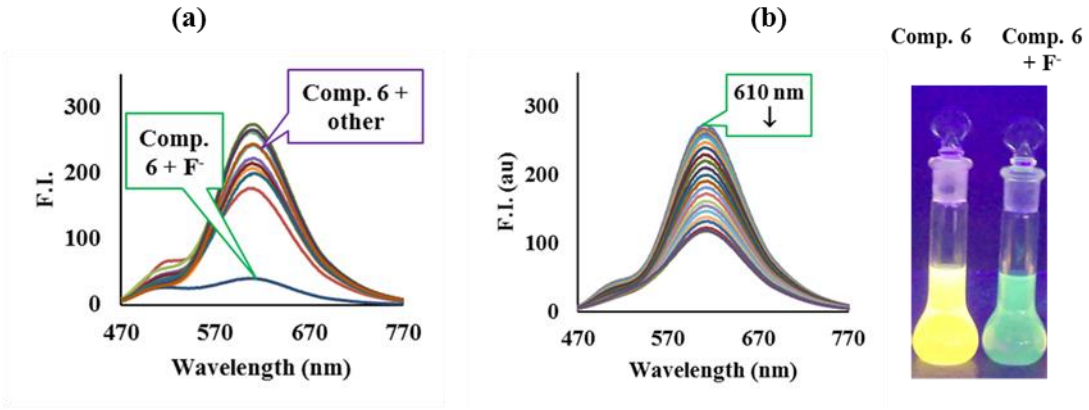

Figure 5.22. Emission spectra of compound **6** (20 µM, CH_3CN) (a) in the presence of different anions; (b) effect of incremental addition of F- (1-20 µM) to compound **6** (20 µM, CH_3CN); Inset: Color changes of compound **6** (20 µM, CH_3CN) in the presence of F^- ions.

Further, the interactions of compound **6** towards various anions were also studied through emission spectroscopy. As discussed earlier, compound **6** (20 µM, CH_3CN) showed the dual emission band at 510 nm and 610 nm. On addition of examined anions, no significant

change was observed in emission spectra except with F^- ions. A color change from yellow to green under UV light was also observed on addition of F^- ion to compound **6** (Figure 5.22). The incremental addition of F^- ions (2-20 μM) to compound **6**, resulted in a decrease in emission intensity at 510 nm and 610 nm. The equilibrium constant of compound **6** with F- ion has been determined with the Benesi-Hildebrand equation and found to be 2.2×10^4 M^{-1}. The compound **6** (20 μM, CH_3CN) showed a linear response for F- ion with the lowest detection limit of 7.5×10^{-7} M.

The selectivity of compound **6** with F^- ions was confirmed by carrying out the competitive anion experiment with 50 equiv. of F^- to compound **6** and various other anions such as Cl^-, Br^-, I^-, CN^-, SCN^-, HSO_4^-, NO_3^-, $H_2PO_4^-$, AcO^- and PPi. The addition of various competing anions to compound **6** in the presence of F^- ions did not affect the absorption spectra of compound **6** (Figure 5.23). Thus, compound **6** showed the selective and sensitive, detection of F^- ion in the presence of other anions as well.

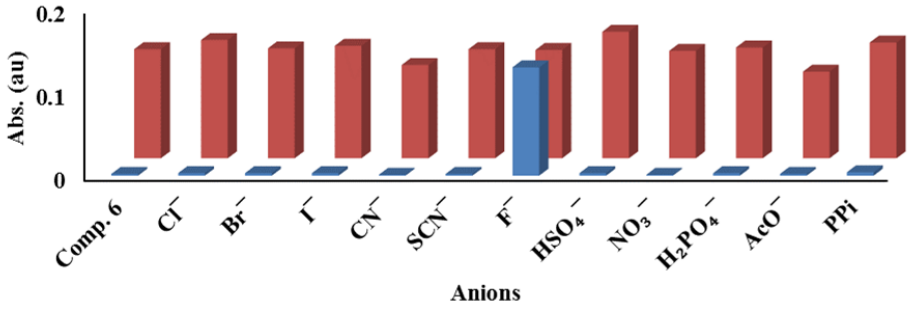

Figure 5.23. The relative emission intensity of compound **6** towards different metal ions in the absence and presence of F^- ions.

5.3.2.1.7 NMR Studies

Further, the ^1H NMR titration study was carried out to investigate the mode of interactions of compound **6** with F^- ions. On addition of 1.0 equiv. of F^- ions, the broad signal due to OH at δ 13.08 ppm disappeared, which suggesting hydrogen-bond interactions between compound **6** and F^- ions. The slight downfield shift of aromatic protons and deprotonation of OH proton in the presence of F^- ions suggested the interaction (Figure 5.24).

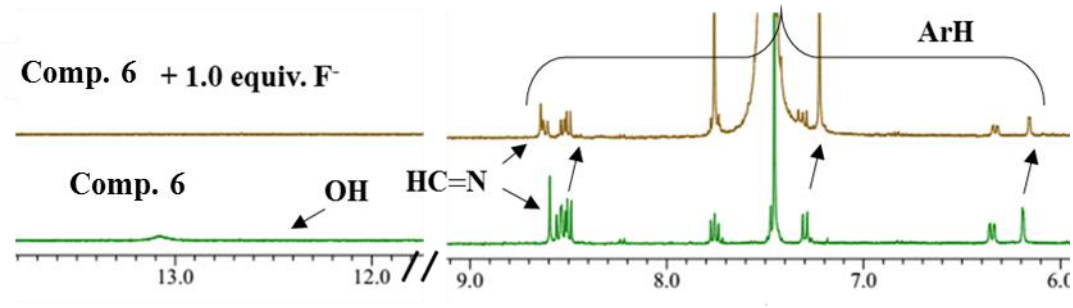

Figure 5.24. ^{1}H NMR titration spectra of compound **6** and compound **6** with 1.0 equiv. of F^- ions

5.3.2.1.8 Theoretical calculation

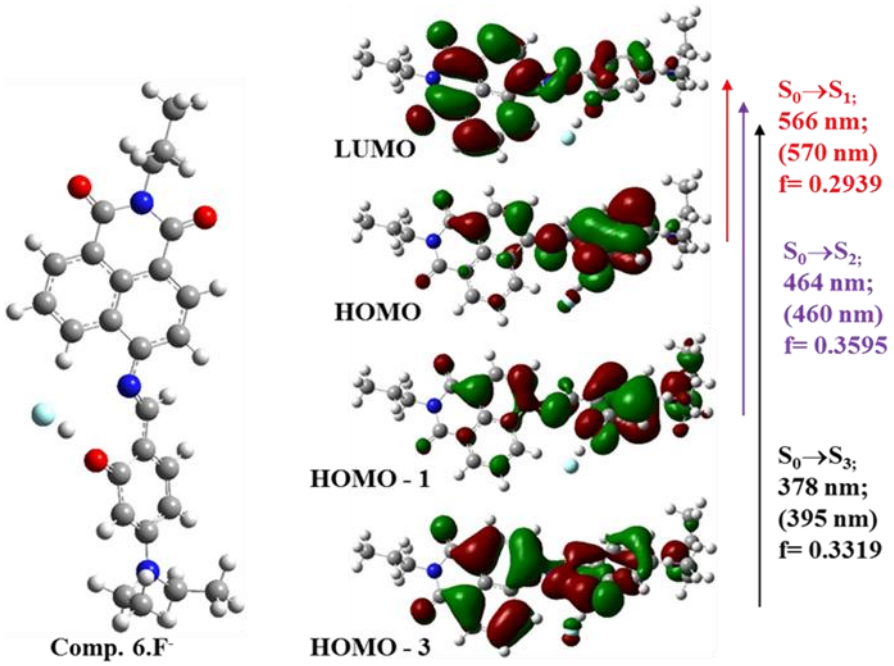

Figure 5.25. Optimized structures and frontier molecular orbitals of compound **6**.F^-.

Further, the experimental results have been supported with the theoretical calculation. The compound **6**.F^- was optimized and presented in Figure 5.25. The origin of absorption spectra was predicted on the optimized structure, and predicted absorption values were found to be in good agreement with experimental results. The observed absorption peaks of compound **6**.F^- was found to be due to HOMO→LUMO transition at 570 nm, HOMO-1→LUMO transition at 464 nm and HOMO-3→LUMO transition at 378 nm, respectively. The HOMO and HOMO-1 of Compound **6**.F^- were majorly distributed over the phenyl ring with Schiff base, while HOMO-3 and LUMO were majorly located at naphthalimide phenyl ring only. Therefore, the electronic transition at 570 nm, was

demonstrated as an intramolecular charge transfer transition, which further triggering the appearance of violet color from orange. On the other hand, the transition at 460 nm and 395 nm has a character of local excitation. Therefore, the experimental results have been endorsed by theoretical calculation, and the detection of F^- ions was followed by deprotonation of compound **6**.

5.3.2.2 DNA binding studies

The naphthalimide-derived molecules have fluorescent nature and found application for a biological activity like antiviral, anticancer activity, analgesic. Naphthalimide moiety is planar π-deficient heteroatom aromatic ring known for DNA intercalation.[150, 166-168] The complex of compound **6**.Al^{3+} could increase π-deficient properties, and thus, DNA base pair could interact more efficiently. The interaction of compound **6** with ct-DNA was studied by absorption and emission spectroscopies techniques. As discussed earlier, the compound **6**.Al^{3+} complex has characteristic absorption peaks at 340 nm and 460 nm. On consequent addition of ct-DNA (10-50 µM) to compound **6**.Al^{3+} complex, the absorption was gradually increased, indicating a hyperchromic effect at 340 nm and 460 nm (Figure 5.26). Hyperchromic effect of compound **6**.Al^{3+} complex with ct-DNA specifies strong intramolecular interaction. This is due to the overlapping of the electron cloud of naphthalimide with ct-DNA base pairs. Fluorescence experiments were also undertaken to investigate the interaction of compound **6**.Al^{3+} complex with ct-DNA. On excitation at 460 nm, compound **6**.Al^{3+} complex showed the strong band at 520 nm. On incremental addition of ct-DNA to compound **6**.Al^{3+} complex, the fluorescence intensity was subsequently increased while the maximum emission wavelength was slightly shifted from 520 nm to 530 nm. The binding constant for probe **1**.Al^{3+}.DNA was determined through Benesi-Hildebrand equation and determined to be 1.1×10^5 M^{-1}, with stoichiometry of 1:1.

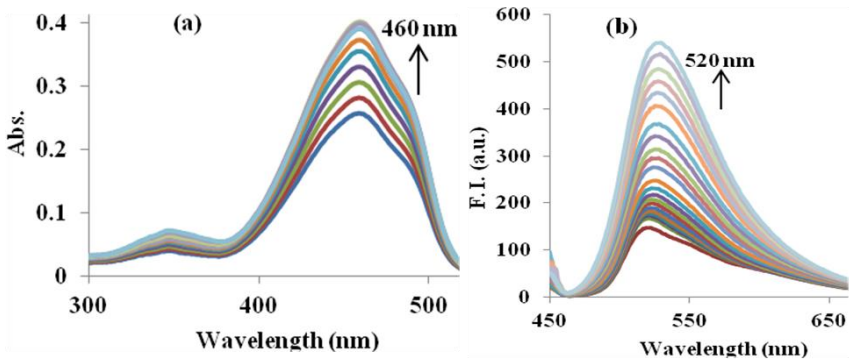

Figure 5.26. Effect of incremental addition of ct-DNA (10-50 µM) (a) on absorption spectra; (b) emission spectra of compound **6**.Al^{3+} complex

5.3.2.2.1 Ethidium bromide displacement study

In order to confirm the reversibility of compound **6**.Al^{3+} with DNA, the competitive ethidium bromide (EB) displacement study was performed, where ethidium bromide is one of a fluorescent dye, which binds to DNA via intercalation mode. The emission spectra of ethidium bromide bound to ct-DNA in absence and presence of each complex have been recorded at 10 µM of EB and 10 µM of DNA. The addition of 0-20 µM solution of compound **6**.Al^{3+} complex, the emission intensity of ct-DNA.EB at 615 nm underwent quenching with a blue shift at 600 nm and concomitant enhancement in emission intensity at 520 nm, indicating the displacement of DNA from EB.DNA complex. It is generally agreed that substantial emission enhancement accompanies intercalation of dye into double helix conformation of nucleic acids. There were significant changes in the emission intensity of EB.DNA complex, suggesting that compound **6**.Al^{3+} complex binds to DNA through intercalation mode (Figure 5.27).

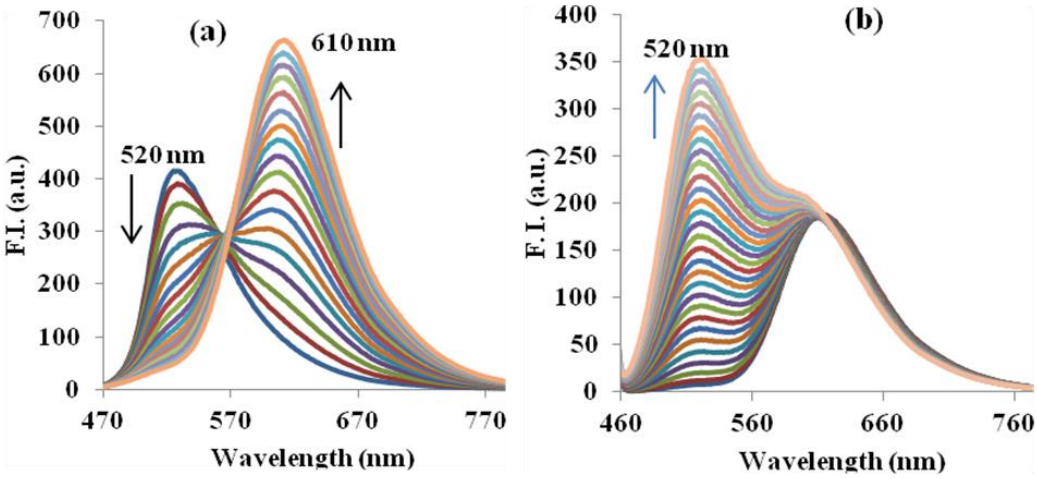

Figure 5.27 (a) Ethidium bromide displacement assay of compound 6.Al^{3+}.DNA complex; (b) Competitive ethidium bromide displacement assay of compound 6.Al^{3+}.DNA complex

Further, the competitive binding experiments were carried out to confirm the binding mode of compound 6.Al^{3+} complex with DNA.), The measured addition of compound 6.Al^{3+} (0-20 µM) to complex of EB.DNA (containing 20 µM of EB and DNA each) led a slight blue shift from 615 nm to 600 nm and the concomitant rise of emission intensity at 520 nm. This signified that EB displacement of DNA and thereby confirming the compound 6.Al^{3+} complex as a strong DNA intercalated (Figure 5.27).

5.3.3 Conclusion

In summary, a novel naphthalimide based compound **6** has been designed and synthesized. The compound **6** was efficiently used as a ratiometric chromo-fluorescent probe, for Al^{3+} and F^- ions selectively over other interfering metal ions and anions. The compound **6** showed rapid color changes for Al^{3+} and F^- ions from orange to yellow and orange to purple under visible light, respectively. Compound **6** also displayed blue-green and green emission under UV light for detection of Al^{3+} and F^- ions, respectively. The combinatorial results of absorption, emission, ^{1}HNMR spectroscopy, and theoretical calculation revealed that the detection followed up the inhibition of ESIPT/ESICT phenomenon. The recognition of Al^{3+} and F^- ions followed the CHEF and deprotonation mechanism, respectively. The detection limit was calculated to be as low as 2×10^{-7} M and 7.5×10^{-7} M for Al^{3+} and F^- ions, respectively. UV-vis and fluorescence studies predicted the possible binding capability of compound **6**.Al^{3+} complex with ct-DNA through intercalation mode; thus, find its applications as drug candidates.

Summary of Chapter 5

In summary, the ESIPT phenomenon and emission response of compound **5** and **6** were investigated through theoretical calculation approach. The computed absorption and emission peaks were in close agreement to the experimental outcomes. The prerequisite of IraHB was established using short-distance interaction, FTIR spectral signals, and AIM analysis at S_0 and S_1 state. For compound **5**, tautomeric forms (**5.K**) was more stabilized than its standard enol form (**5**) at S_1 state and calculated energy barrier for forwarding PT (2.64 kcalmol^{-1}) was lower than reverse PT (9.16 kcalmol^{-1}). Therefore, it could be concluded that the emission with a significant Stokes' shift was simulated through the ESIPT phenomenon. The isomeric conversion of compound **6** was elaborated ways, where the molecular motion and tautomeric conversions were incorporated. The PT has energy barrier of 4.56 kcalmol^{-1} for **6→6.K**, while rotameric isomeric conversions **6.K→6.K.T_NEt** and **6.K→6.K.T_SB** were determined to be high in energy and therefore, were not favorable. On the other hand, the **6→6.T_NEt** rotameric isomeric conversion has an energy barrier of 2.96 kcalmol$^{-1,}$ and following tautomeric conversion **6.T_NEt→6.T.K_NEt** has an energy barrier of 1.01 kcalmol^{-1}. However, **6→6.T_SB→6.T.K_SB** was not favorable. The total energy barrier for ESIPT/ESTICT (Pathway I) was 4.56 kcalmol^{-1} was higher than 3.97 kcalmol^{-1} for ESTICT/ESIPT (Pathway II) and thus, concluded that the ESICT/ESIPT process stimulates the emission with large Stokes' shift. The compound **6** was used as a ratiometric chromo-fluorescent sensor towards Al^{3+} and F^- ions selectively over other interfering metal ions and anions. The compound **6** showed rapid color changes for Al^{3+} and F^- ions from orange to yellow and orange to purple under visible light, respectively. Compound **6** also displayed blue-green and green emission under UV light for detection of Al^{3+} and F^- ions, respectively. The combinatorial results of absorption, emission, ^{1}HNMR spectroscopy, and theoretical calculation revealed that the detection followed up the inhibition of ESIPT/ESICT phenomenon. The recognition of Al^{3+} and F^- ions followed the CHEF and deprotonation mechanism, respectively. The detection limit was calculated to be as low as 2×10^{-7} M and 7.5×10^{-7} M for Al^{3+} and F^- ions, respectively. UV-vis and fluorescence studies predicted the possible binding capability of compound **6**.Al^{3+} complex with ct-DNA through intercalation mode; thus, find its applications as drug candidates.

Chapter 6

Appraisal of excited state intramolecular proton transfer in asymmetric systems containing double intramolecular hydrogen bonding

Excited state proton transfer (ESPT) is a very fundamental phenomenon and studied extensively in chemical, physical, and biological sciences.[90, 94, 96, 102, 169] The ESPT has been taken place with a capacity of double or multiple proton transfer such as DNA A-T, G-C base pairs, amino acid units, aligned H_2O etc.[89, 92, 93, 170-184] The multiple proton transfer could be assisted by self-assembly or/and solvent. Therefore, it has been studied extensively for various molecular architectures possessing symmetrical double inter/intramolecular hydrogen bonding through experimental and theoretical methods.[185] All the studied molecular systems have symmetrical double IraHBs in respect of interacting atoms such as OH···N/NH···N and their strength. However, literature still limits with reports of the asymmetrical structure containing asymmetrical double IraHBs. The contained asymmetrical double IraHBs could have different strength. The IraHB could be either distinguished by different interacting atoms such as OH···N/NH···N or by its ring size. Such molecular systems could have risen the competitive proton transfer, proton transfer triggering proton transfer or charge transfer coupled proton transfer mechanism.

In this chapter, asymmetrical molecular structures (Figure 6.1) containing asymmetrical double IraHBs were investigated for ESIPT process. Also, this chapter involved the study of structural analysis of rotamer stabilized distinguished IraHB and origin of photophysical properties.

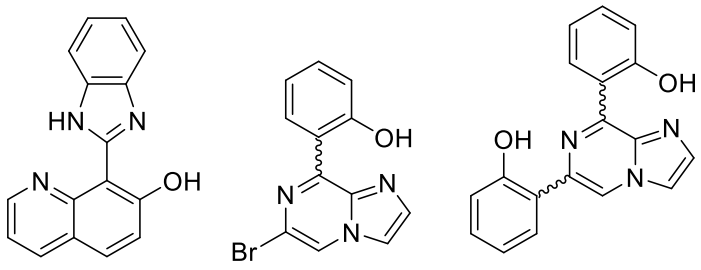

7 **8A, 8B** **9A, 9B**

Figure 6.1 The different asymmetrical compound containing intramolecular hydrogen bonding

Based on the study, this chapter was divided into three sections based on the study as following:

6.1. An asymmetric quinoline-benzimidazole system undergoing intramolecular charge-coupled double proton transfer in an excited state

6.2. Investigation of rotameric conformations of substituted imidazo-[1,2-a]pyrazine: Experimental and theoretical approaches

6.3. Investigation of excited state intramolecular double proton transfer in asymmetrical imidazo-[1,2-a]pyrazine compound: a theoretical study

6.1

An asymmetric quinoline-benzimidazole system undergoing intramolecular charge-coupled double proton transfer in an excited state

6.1.1 Abstract

8-(1*H*-benzo*[d]*imidazol-2-yl) quinolin-7-ol (compound **7**) has structural asymmetry and encloses two kinds of hydrogen bonds (HBs), which undergoes excited state intramolecular charge transfer and double proton transfer (ESICT/ESIDPT). On excitation at 360 nm, compound **7** resulted in dual emission at 420 nm and 570 nm, respectively. The FMOs analysis revealed the intramolecular charge transfer nature in the excited state. However, calculated hydrogen bond strength and FTIR analysis revealed that the emission was raised from the relaxation of intramolecular charge transfer excited state, followed by ESIDPT. The proton transfer (PT) pathways study showed that first proton transfer was barrierless followed by a small barrier for the ESIDPT and thus, favored the sequential PT mechanism. In this study, the photophysical properties of 8-(1*H*-benzo*[d]*imidazol-2-yl) quinolin-7-ol (compound **7**) system was systematically studied *via* experimental and theoretical techniques. The calculated results were used to evaluate the absorption and emission spectra, frontier molecular orbitals (FMOs), electron density difference map, hydrogen bond strength, and FTIR analysis. The compound **7** was optimized for possible tautomeric forms (**7**, SPT(NH), SPT(NH) and DPT) involved in proton transfer (PT) and established an energy relationship as SPT(OH)>DPT>SPT(NH)> **7** at S_0 state and **7**>SPT(OH)>DPT>SPT(NH) at S_1 state. The theoretical results revealed that the generation of ESIPT was attributed to ESICT owing to change in electron density on the frontier molecular orbitals (FMOs) and electron density difference map. The AIM calculation established the dual HBs for compound **7**. On $S_0 \rightarrow S_1$, compound **7** displayed a redshift of 212 cm^{-1} for N—H and blue shift of 121 cm^{-1} for O—H vibrational stretching. However, on tautomeric conversion **7**→SPT(NH)*, the O—H vibrational stretching displayed redshift of 178 cm^{-1}, which strengthen the intramolecular HBs and thus, promote the dual proton transfer in S_1 state. The proton transfer (PT) pathways study showed that first proton transfer was barrierless followed by a small barrier for the ESIDPT and thus, favors the sequential PT mechanism. Also, the predicted absorption and emission spectral value resembled experimental results.

6.1.2 Experimental Section

6.1.2.1 Synthesis of Compound 7

Compound **7** was synthesis by two-step reaction (Scheme 6.1). First, **7HQ-CHO** was synthesized using Riemer-Tiemann reaction. Further, **7HQ-CHO** was stirred and heated with o-phenylenediamine in the presence of 10 mL of nitrobenzene. The reaction was monitored by thin-layer chromatography. On successful consumption of reactant materials, diethyl ethyl ether was added to get the crude solid. The filtered solid was purified by column chromatography using $CHCl_3$ as an eluting solvent to get yellow-colored pure compound **7** in 60 % yield; m.pt. 277°C.

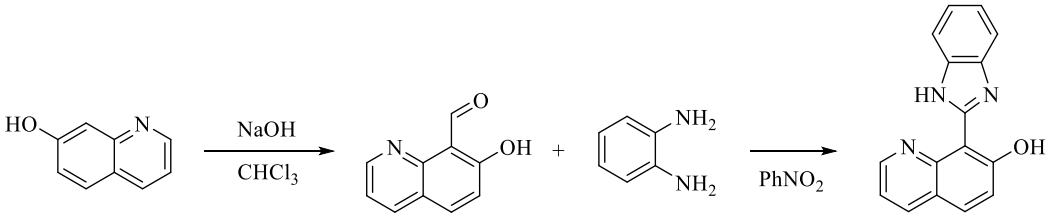

7HQ **7HQ-CHO** **7**

Scheme 6.1 Synthesis of compound **7**

The ^1H NMR spectrum displayed resonating signals at δ 8.95-8.93 ppm as doublet of doublet for 1H of ArH, δ 8.17-8.15 ppm as doublet of doublet for 1H of ArH, δ 7.80-7.76 ppm as multiplet for 2H of ArH, δ 7.66-7.63 ppm as multiplet for 1H of ArH, δ 7.42 ppm as doublet for 1H of ArH, δ 7.37-7.32 ppm as multiplet for 3H of ArH, and ^{13}C NMR signals resonate at δ 103.9, 111.4, 117.7, 118.4, 121.4, 122.5, 123.4, 130.9, 131.8, 136.9, 139.4, 147.4, 149.3, 152.7, and 163.6 for aromatic carbons (ArCs) suggest the formation of compound **7**. The observed ESI-MS (m/z) 262.1 (M^++1) was in close agreement with the calculated m/z =261.09 and thus, verified the formation of compound **7**.

6.1.3 Results and discussion

6.1.3.1 Photophysical properties

Figure 6.2 depicted the steady-state absorption and emission spectra of compound **7**. The compound **7** exhibited the absorption peak at 360 nm, 315 nm, and 305 nm in CH_3CN. Further, on excitation at 360 nm, compound **7** showed the dual emissions in CH_3CN at 420 nm and 570 nm with a Stokes shift of 60 nm and 210 nm respectively. The dual emission for compound **7** could be inferred from the ESIPT phenomenon. The low

energy/high Stokes-shifted emission could be assigned as ESIPT emission from the keto tautomeric form, while high energy/low Stokes shifted emission could be from the standard enol form. In addition, the steady-state absorption and emission spectra were measured in different polarity systems (Figure 6.2). The absorption spectra displayed a rise of shoulder band at ~400 nm in high polarity system, while the emission spectra displayed a rise of emission intensity for the high energy emission, along with significant redshift of ~35 nm with an increase of polarity. This observation depicted the stabilization of the standard form in high polarity system, and thus, lead intramolecular charge transfer relaxation prior to the ESIPT phenomenon. Therefore, it could be implicated that the high energy/low Stokes' shifted emission resulted from the ESICT while low energy/high stoke shifted emission resulted from ESIPT.

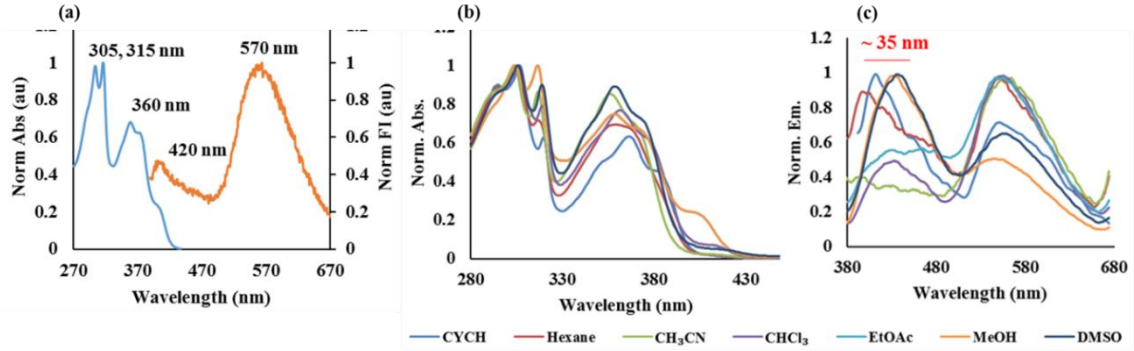

Figure 6.2. (a) Normalized absorption and emission spectra of compound **7** in CH_3CN; (b, c) absorption and emission spectra of compound **7** in different solvents.

6.1.3.2 Geometrical optimization

First, the stability of four tautomeric forms involved in the PT process (compound **7**, SPT(OH), SPT(NH), DPT) was confirmed through structural optimization in S_0 and S_1 state. All the local minima were supported *via* the absence of imaginary frequency. The optimized tautomers have been presented in Figure 6.3. The important geometrical parameters for tautomers have been summarized in Table 6.1 for S_0 and S_1 state. The calculated geometric parameters of compound **7** displayed alteration on photoexcitation ($S_0 \rightarrow S_1$). For better understanding, the atoms involved in HB were labeled in Figure 6.3 and interactions were assigned as I and II. The bond distance of O_1—H_2 (I), H_2···N_3 (I), N_4—H_5 (II) and H_5···N_6 (II) were determined to be 1.0104 Å, 1.6403 Å, 1.0192 Å and 2.0119 Å, respectively at S_0 state. However, on photoexcitation, the O_1—H_2 (I) bond

distance was decreased by 0.0070 Å to 1.0034 Å, while the interacting distance for $H_2\cdots N_3$ (I) was increased by 0.04 Å to 1.6803 Å in S_1 state.

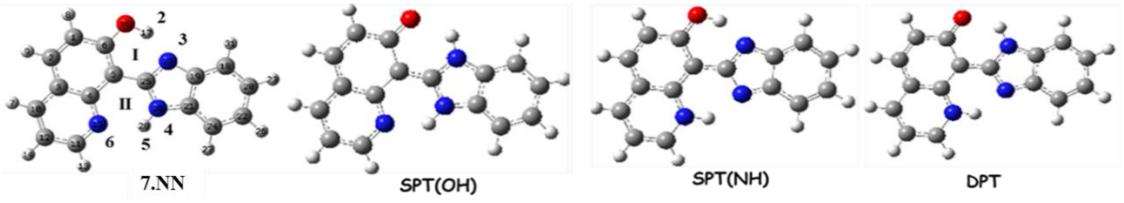

Figure 6.3 Optimized structure of tautomeric forms of compound **7**

Table 6.1. Calculated bond distances (Å) and bond angles (°) for different tautomeric forms of compound **7** at S_0 and S_1 state.

	7		**SPT (OH)**		**SPT (NH)**		**DPT**	
	S_0	**S_1**	**S_0**	**S_1**	**S_0**	**S_1**	**S_0**	**S_1**
O_1H_2	1.0104	1.0034	1.8175	1.9084	1.0301	1.0131	1.9032	1.8130
N_3H_2	1.6403	1.6803	1.0275	1.0215	1.5896	1.6148	1.0203	1.0252
N_4H_5	1.0192	1.0312	1.0232	1.0314	1.7456	1.8698	1.7844	1.8689
N_6H_5	2.0119	1.8702	1.9672	1.8747	1.0545	1.0217	1.0414	1.0230
$\angle O_1H_2N_3$	148.87	148.65	129.81	125.23	150.83	149.06	127.37	128.94
$\angle N_4H_5N_6$	124.52	128.83	125.86	129.03	141.13	136.73	139.22	136.81

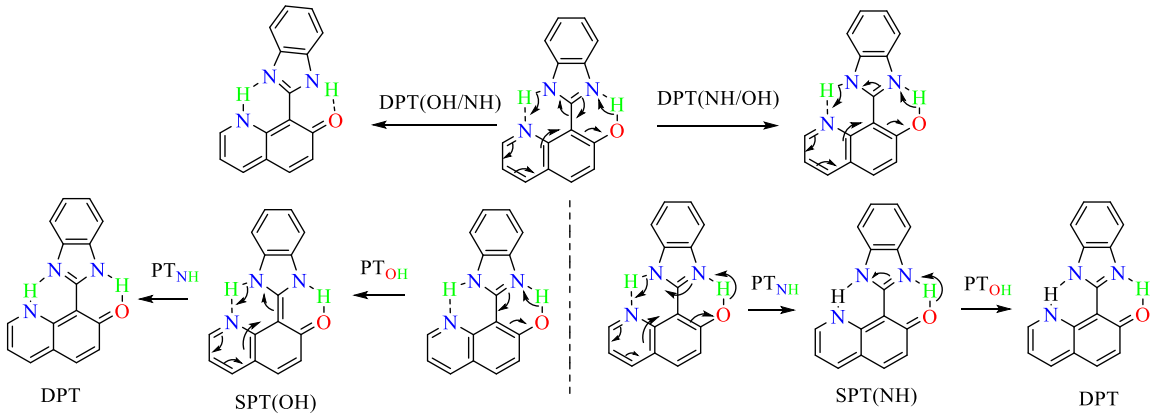

Scheme 6.2. Possible pathways of proton transfer in compound **7**

On the other hand, the bond distance for N_4—H_5 (II) was increased by 0.012 Å to 1.0312 Å, while the $H_5\cdots N_6$ (II) interacting distance was decreased by 0.1417 Å to 1.8702 Å in S_1 state. Meanwhile, the bond angle of $\angle O_1H_2N_3$ was decreased by 0.22° to 148.65°, while $\angle N_4H_5N_6$ was increased by 4.31° to 128.83° in S_1 state. These remarks indicated that $O_1H_2\cdots N_3$ HB was weakened, while $N_4H_5\cdots N_6$ HB was strengthened in S_1 state.

Therefore, the asymmetric structure of compound **7** has enclosed two types of HBs through different hydrogen donor and acceptor sites. Consequently, there could be the existence of single/double proton transfer phenomenon in the S_1 state (Scheme 6.2). Therefore, an attempt to answer the question of the origin of emission from intramolecular charge transfer and single/double proton transfer (SPT/DPT) was countered through structural optimization, FTIR calculations, AIM analysis, frontier molecular orbitals (FMOs) and different possible proton transfer pathways.

6.1.3.3 FTIR

Herein, the FTIR signals of O_1—H_2 and N_4—H_5 were analyzed to provide a closer eye on the strength of HBs at S_0 and S_1 state (Figure 6.4). The FTIR signals of OH and NH were observed at 2920 and 3486 cm^{-1} for compound **7** at S_0 state. However, on photoexcitation, the calculated FTIR spectra demonstrated a blue shift of 121 cm^{-1} for O_1—H_2 to 3041 cm^{-1} and a redshift of 212 cm^{-1} for N_4—H_5 to 3273 cm^{-1} for S_1 state. Therefore, it established that the $N_4H_5\cdots N_6$ IraHB was strengthened, while $O_1H_2\cdots N_3$, IraHB was weakened at the S_1 state for compound **7**.

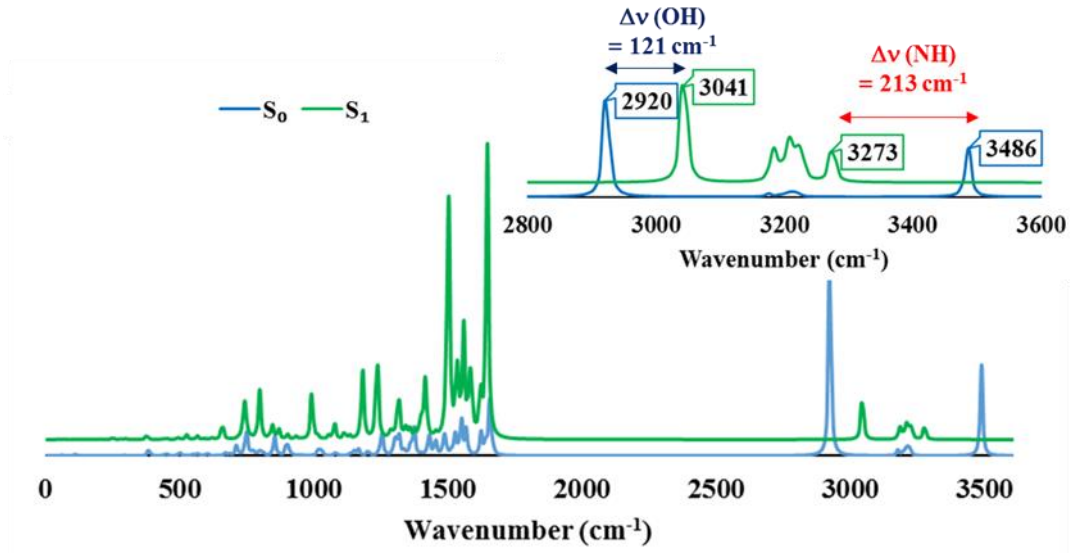

Figure 6.4. FTIR spectra of compound **7** at S_0 and S_1 state

6.1.3.4 AIM analysis

Further, the IraHBs was established *via* Popelier criteria using Bader's quantum theory of atoms in molecules (QTAIM).[122] The determined topological parameters were within the limit of criteria and thus, established two IraHBs as $O_1H_2\cdots N_3$ and $N_4H_5\cdots N_6$ at S_0 and S_1 states for the primary structure of compound **7** (Table 6.2). The positive value of

Laplacian of electron density [$\nabla^2\rho(r_c)$] with small electron density value for both the S_0 and S_1 state, depicted electrostatic close shell interaction. Further, according to Rozas' rules; all the BCPs listed in Table 6.2 has been ascertained as medium-range interaction with the partial covalent character ($\nabla^2\rho(r_c) > 0$ and $H(r) < 0$) for both the S_0 and S_1 state except for $N_{30}H_{28}\cdots N_{15}$ (in S_0 state), which has electrostatic nature.[123] Moreover, the interaction energies for $O_1H_2\cdots N_3$ and $N_4H_5\cdots N_6$ were determined to be -15.37 kcalmol^{-1}, and -6.28 kcalmol^{-1}, respectively at S_0 state. However, on photoexcitation to S_1 state, $O_{16}H_{17}\cdots N_{29}$ HB was weakened to -13.18 kcalmol^{-1}, while $N_{30}H_{28}\cdots N_{15}$ HB was strengthening to -8.79 kcalmol^{-1}.[111] Thus, these analyses clearly indicated that the HB strengthen for compound **7** at S_1 state.

Table 6.2. HB distances, bond angles & topology parameters electron density(ρ), Laplacian electron density ($\nabla^2\rho$), potential energy density [V(r)], total energy density [H(r)], hydrogen bonding energy [E_{HB}(kcalmol^{-1})] at bond critical pint of non-covalent interactions (D···HA) compound **7** at B3LYP/6-31++G**.

	Interaction	**ρ**	**$\nabla^2\rho$**	**G(r)**	**V(r)**	**H(r)**	**$\lvert E_{HB}\rvert$**
S_0	$O_{16}H_{17}\cdots N_{29}$	0.060	0.126	0.040	-0.049	-0.0089	15.37
	$N_{30}H_{28}\cdots N_{15}$	0.028	0.083	0.020	-0.020	0.21E-3	6.28
S_1	$O_{16}H_{17}\cdots N_{29}$	0.054	0.122	0.036	-0.042	-0.0060	13.18
	$N_{30}H_{28}\cdots N_{15}$	0.038	0.104	0.027	-0.028	-0.84E-3	8.79

6.1.3.5 Absorption/emission spectra and charge distribution

Further, first three low lying absorption peaks ($S_0\rightarrow S_1$, $S_0\rightarrow S_2$ and $S_0\rightarrow S_3$) were calculated for compound **7** and located at 366 nm, 313 nm and 303 nm, which were in close agreement with the observed absorption peaks 360 nm, 315 nm and 305 nm, shown in parenthesis (Figure 6.5). Further, qualitative/quantitative nature of the electronically excited state was discussed through charge distribution. The calculated $S_0\rightarrow S_1$ transition peak was at 633 nm with considerable oscillation strength of 0.3613 and composition of HOMO→LUMO (98 %).

The HOMO was localized all over the molecular structure while the LUMO was majorly localized over the quinoline moiety with partial contribution from the benzimidazole units. Next observed absorption peak at 315 nm was predicted at 313 nm with oscillation strength of 0.0147 and 97 % composition of HOMO-1 to LUMO. Likewise, the observed

absorption peak at 305 nm was predicted at 303 nm with oscillation strength of 0.0394 and 68 % composition of HOMO-2 to LUMO. Further, the quantitative nature of excitations was measured through hole-electron distribution; the distance between the hole and electron center. The smaller value of overlap integral with generous spatial separation of hole-electron distribution revealed these transitions as charge transfer excitation. The hole-electron distribution clearly depicted that all three transitions have an electron density shift from the benzimidazole unit to the quinoline.

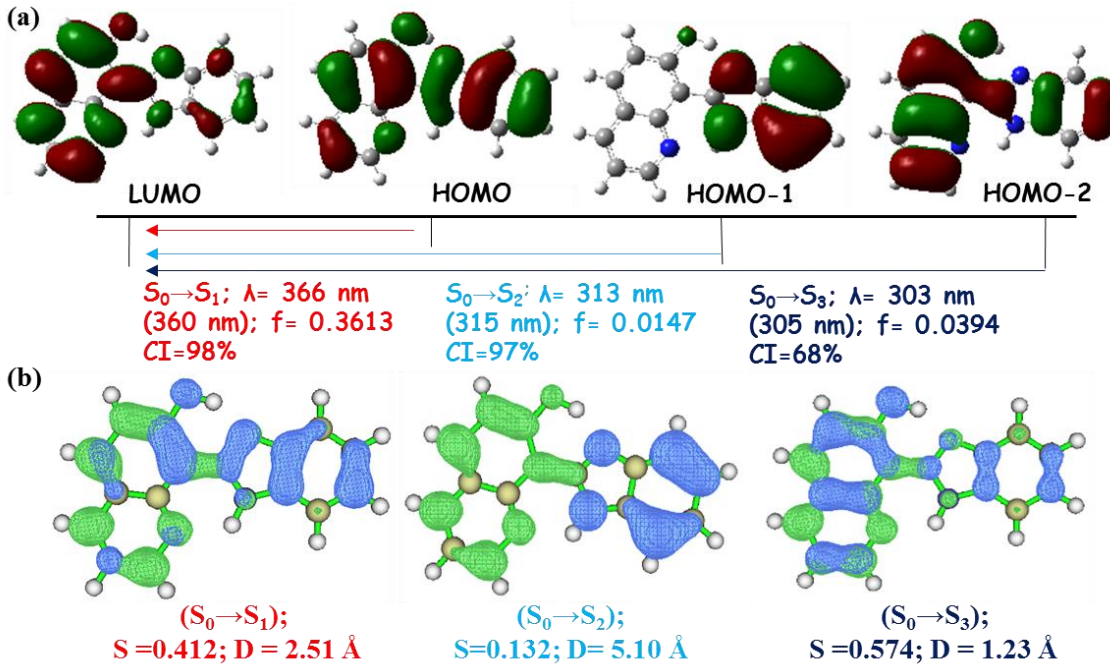

Figure 6.5. (a) Calculated absorption peaks for compound **7** and contributing frontier molecular orbitals in electronic transitions (value in parenthesis were experimental values; f= Oscillation strength; CI= % contributions of molecular orbitals); (b) The hole-electron distribution of compound **7** for the different observed excitation; color code: blue= hole, green = electron.

In order to get an insight into the properties of the S_1 state of compound **7**, SPT(OH), SPT(NH), and DPT tautomeric forms, a qualitative FMOs and emission energies were presented in Figure 6.6. The calculated emission energies were determined to be 454 nm, 445 nm, 656 nm, and 583 nm corresponding to 99.3 %, 98.5 %, 99.5 %, and 98.9 % composition of LUMO→HOMO for **7**, SPT(OH), SPT(NH), and DPT tautomeric forms, respectively. The calculated Stokes' shift for **7**, SPT(OH), SPT(NH) and DPT were determined to be 88 nm, 79 nm, 290 nm, and 217 nm, respectively. The emission energies of compound **7** and DPT were in good agreement with the experimental values (420 nm, and 570 nm) along with their Stokes' shift. Therefore, this analysis indicated that the used

method was reasonable and sufficient to predict the phenomenon. The emission energies of SPT(NH) was not observed experimentally. Also, the energy profile of FMOs of **7**, SPT(OH), SPT(NH) and DPT was presented in Figure 6.6. With respect to compound **7**, the FMOs energy gap decreased for SPT(NH), and DPT, however, it was increased for SPT(OH). Also, Figure 6.6 depicted that charge transfer state at 360 nm, emission was observed at 454 nm, on the relaxation of charge transfer state at S_1 state.

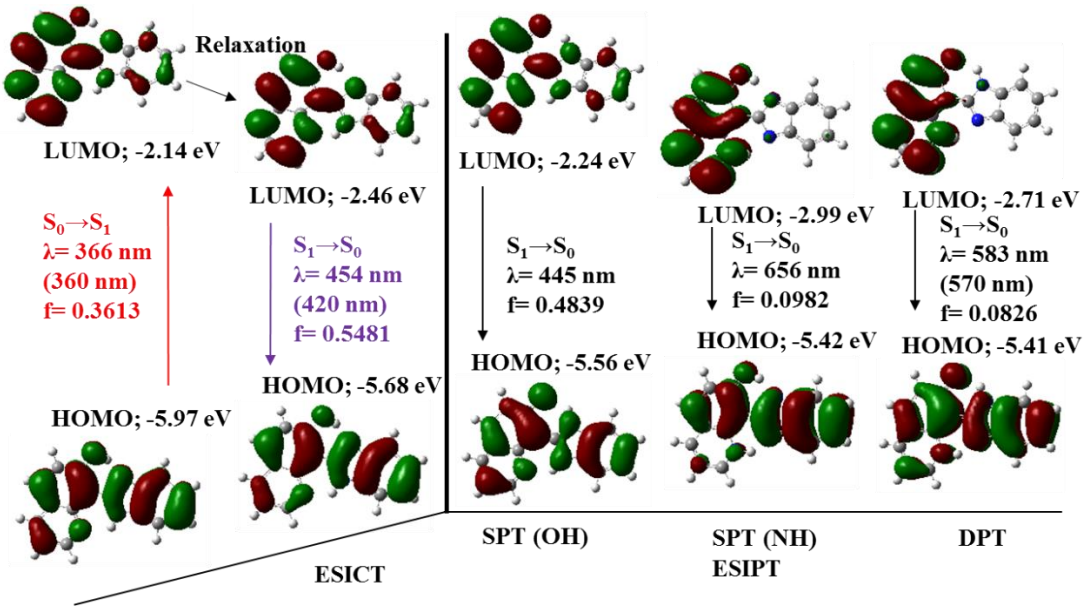

Figure 6.6. Schematic presentation of the photophysical phenomenon

6.1.3.6 Energy profile of proton transfer mechanism

Among the **7**, SPT (OH), SPT (NH), and DPT tautomeric forms, the **7** was found to be most stable at S_0 state, while it was DPT tautomeric form, which was most stable at S_1 state. The relative energy profile of tautomeric forms was presented in Figure 6.7. This energy profile indicated that the PT reaction likely to occur at S_1 state. Herein, two pathways of PT were presented as accessible in Scheme 6.2; Path I: PT for OH···N site followed by PT for site NH···N; Path II: PT for NH···N HB site followed by PT for OH···N site. The calculated energy barriers of forwarding ESIPT were determined to be 2.17 kcalmol^{-1} and 0.21 kcalmol^{-1} for **7**→SPT(OH) and SPT(OH)→DPT, respectively (in total 2.38 kcalmol^{-1} for Path I). However, the reverse ESIPT has a barrier of 2.86 kcalmol^{-1} and 10.84 kcalmol^{-1} for **7**←SPT(OH) and SPT(OH)←DPT, respectively (in total 13.69 kcalmol^{-1} for Path I).

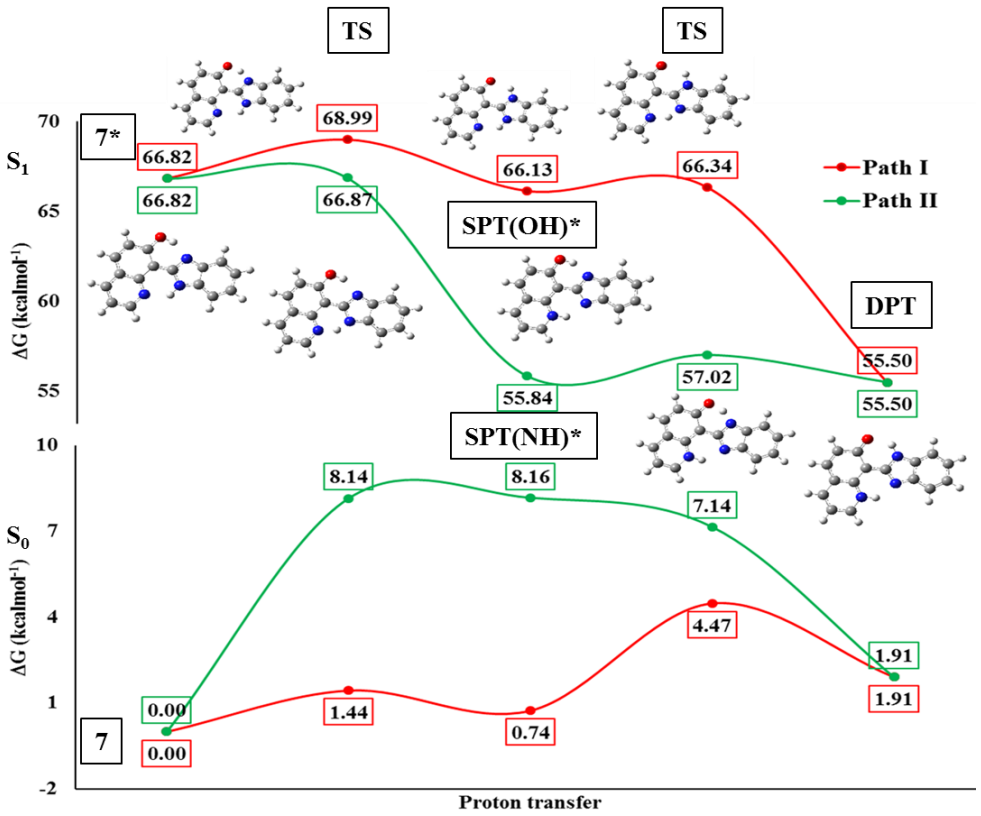

Figure 6.7. Energy diagram ESIPT mechanism of compound **7** at S_0 and S_1 state

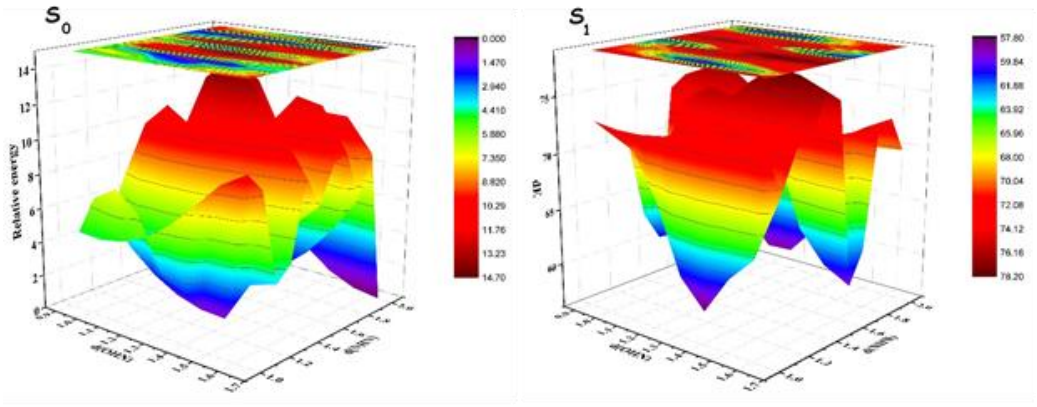

Figure 6.8 PECs of proton transfer of compound **7** at S_0 and S_1 state

Likewise, the calculated energy barriers of forwarding ESIPT were determined to be 0.05 eV and 1.18 eV for **7**→SPT(NH) and SPT(NH)→DPT, respectively (in total 1.23 kcalmol^{-1} for Path II), however, the reverse ESIPT has barriers of 11.02 kcalmol^{-1} and 1.52 kcalmol^{-1} for **7**←SPT(OH) and SPT(OH)←DPT, respectively (in total 12.54 kcalmol^{-1} for Path II). The total energy barrier of tautomeric conversion was nearly similar for Path I (**7**→SPT(H)→DPT) and Path II (**7**→SPT(NH)→DPT) and determined

to be very similar. Therefore, the tautomeric conversion pathways could not be concluded from the total energy barrier. The PECs of PT were presented in Figure 6.8

6.1.3.7 Emission mechanism

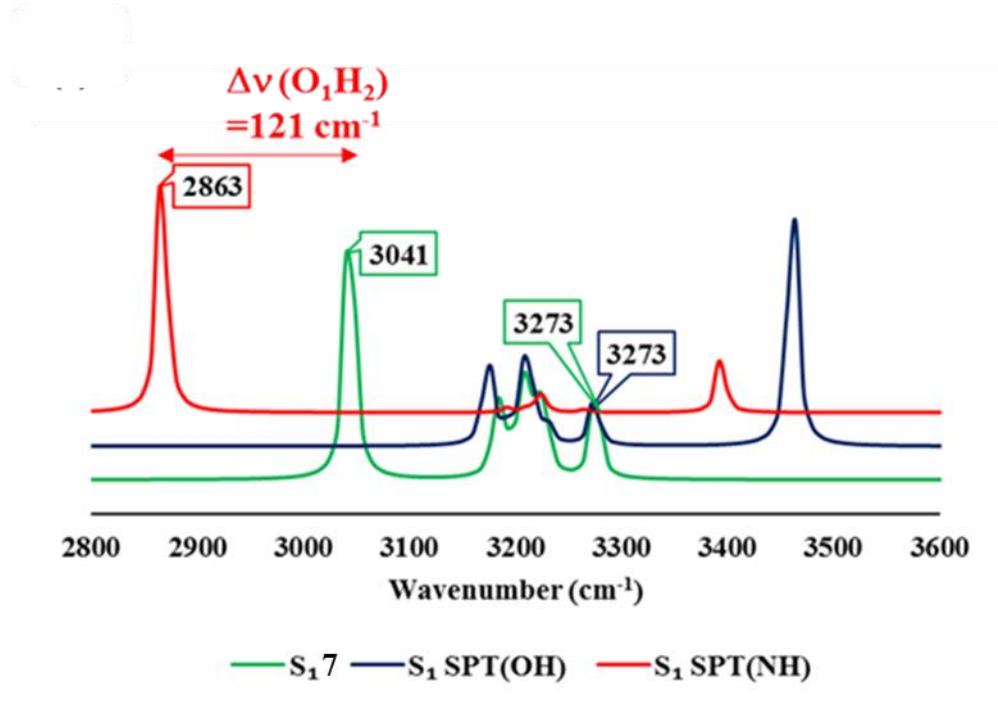

Figure 6.9 FTIR spectra of compound **7,** SPT(OH), and SPT(NH) at S_1 state.

Now, we discussed the emission mechanism of compound **7** and the driving forces for the ESIPT mechanism. It was noted that the forward and reverse ESIPT energy for **7**→SPT(OH) and **7**←SPT(OH) were similar and therefore, **7**→SPT(OH) conversion couldn't be feasible process through Path I. On the other hand, the **7**→SPT(NH) has low energy barrier than SPT(NH)→**7**, and hence, **7**→SPT(NH) conversion was allowed through Path II. The driving force for **7**→SPT(NH) conversion was increased strength of $N_4H_5\cdots N_6$ IraHB at S_1 state. Once the SPT(NH) tautomeric conversion was taken place the $O_1H_2\cdots N_3$ IraHB was strengthened, and consequently lead SPT(NH)→DPT tautomeric conversion. The increased strength of $O_1H_2\cdots N_3$ IraHB was shown by a redshift of 121 cm^{-1} to 2863 cm^{-1} from 3041 cm^{-1} for O─H vibrational frequency of SPT(NH) tautomer (Figure 6.9). The N─H vibrational frequency for SPT(OH) was found to be at 3273 cm^{-1} and hence displayed no change in the strength of $N_4H_5\cdots N_6$ IraHB. Thus, we make the conclusion on the consolidated results obtained from AIM, FTIR,

energy profile and calculated vertical emission values that the ESICT/ESIDPT process originated the dual emission and the ESIDPT was followed up by path II (Scheme 6.3).

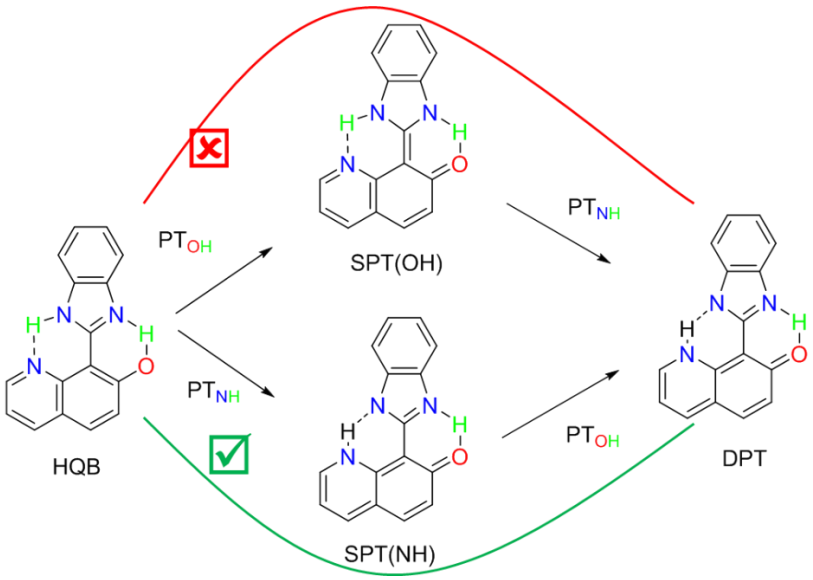

Scheme 6.3. Schematic pathway for the ESIDPT in compound **7.**

6.1.4 Conclusion

In Summary, a new compound enclosed dual hydrogen bonding was synthesized and studied for the photophysical properties. The compound **7** exhibited dual emission at 420 nm and 570 nm with Stokes' shifts of 60 nm and 210 nm, respectively. The dual emission with large Stokes' shifts and growth of absorption shoulder peak at ~400 nm in polarity system depicted the excited state intramolecular charge transfer (ESICT) coupled excited state intramolecular proton transfer (ESIPT). The theoretical results also revealed that the generation of ESIPT was attributed to ESICT owing to change in electron density on the frontier molecular orbitals (FMOs) and electron density difference map. The atoms in molecule (AIM) calculation established the dual HBs for compound **7**. On $S_0 \rightarrow S_1$, compound **7** displayed a redshift of 212 cm^{-1} for N—H and blue shift of 121 cm^{-1} for O—H vibrational stretching. However, on tautomeric conversion **7**→SPT(NH)*, the O—H vibrational stretching displayed redshift of 178 cm^{-1}, which strengthen the intramolecular HBs and thus, promote the dual proton transfer in S_1 state. The calculation established energy relationship as SPT(OH)> DPT > SPT(NH) > **7** for S_0 state and 7 >SPT(OH) > DPT > SPT(NH) for S1 state. The proton transfer (PT) pathways study showed that the sequential PT mechanism was followed with a small barrier for forwarding ESIPT.

6.1.5 Experimental data

6.1.5.1 Synthesis of Compound 7

First, **7HQ-CHO** was synthesized using Riemer-Tiemann reaction. Further, **7HQ-CHO** was stirred and heated with o-phenylenediamine in the presence of 10 mL of nitrobenzene. The reaction was monitored by thin-layer chromatography. On successful consumption of reactant materials, diethyl ethyl ether was added to get the crude solid. The filtered solid was purified by column chromatography using $CHCl_3$ as an eluting solvent to get yellow-coloured pure compound **7** in 60 % yield; m.pt. 277°C.

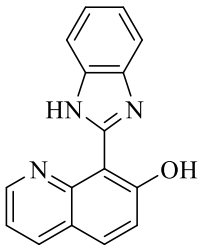

7

^{1}HNMR (400 MHz, $CDCl_3$): 8.95-8.93 (dd, 1H, J_2 = 2 Hz, J_3 = 4.4 Hz, ArH), 8.17-8.15 (dd, 1H, J_2 = 2 Hz, J_3 = 8.3 Hz, ArH), 7.80-7.76 (m, 2H, ArH), 7.66-7.63 (m, 1H, ArH), 7.42 (d, 1H, J = 9.2 Hz, ArH), 7.37-7.32 (m, 3H, ArH). ^{13}C NMR (400 MHz, $CDCl_3$): δ 103.9, 111.4, 117.7, 118.4, 121.4, 122.5, 123.4, 130.9, 131.8, 136.9, 139.4, 147.4, 149.3, 152.7, 163.6. ESI-MS (m/z) 262.1 (M^++1) [calculated m/z =261.09]. m.pt. = 277°C

6.2

Investigation of rotameric conformations of substituted imidazo-[1,2-*a*]pyrazine: Experimental and theoretical approaches

6.2.1 Abstract

The imidazo-[1,2-*a*]pyrazine based rotameric conformations were synthesized and characterized by the correlation of different experimental techniques such as NMR, FTIR, and absorption spectra and quantum chemical calculations. The different conformations were stabilized by intramolecular hydrogen bonding such as OH···N, ArH···N, and ArH···ArH. The ground state optimizations, potential energy curves (PECs) scanning profile displayed two stable rotameric forms for each molecule at density functional theory (DFT). The calculated absorption spectra and isotopic shielding constant were done by time-dependent density functional theory (TDDFT) and gauge-invariant atomic orbitals (GIAO)-DFT, respectively. The strength of hydrogen bond interactions resulted in different conformations was studied by quantum theory of atoms in molecules (AIM) theory. The conformation **8A** and **8B** were stabilized by six and seven-membered intramolecular hydrogen bonding respectively. Likewise conformation **9A** was stabilized by double six-membered O─H···N hydrogen bonding with shared site of interaction. However, the **9B** was stabilized by six-membered as well as seven-membered O─H···N double intramolecular hydrogen bonding.

6.2.2 Experimental section

6.2.2.1 Synthesis of rotamers

2-Aminopyrazine is used as the starting material, which was brominated with *N*-bromosuccinimide (NBS) in DMSO and H_2O at room temperature for **6** hours. The resultant 2-amino-3, 5- dibromopyrazine (**2-NH_2-Py-Br**)[186] was cyclized with chloroacetaldehyde in isopropyl alcohol to obtain 6, 8-dibromo-imidazo[1,2-*a*]pyrazine (**Imidazo-py-Br**).[187] Further, Suzuki–Miyaura cross-coupling reaction was performed with 6, 8-dibromo-imidazo[1,2-*a*]pyrazine and 2-hydroxyphenyl boronic acid in the presence of palladium catalyst afforded substituted mono-arylated products (**8A** and **8B**) and di-arylated products (**9A** and **9B**).[187]

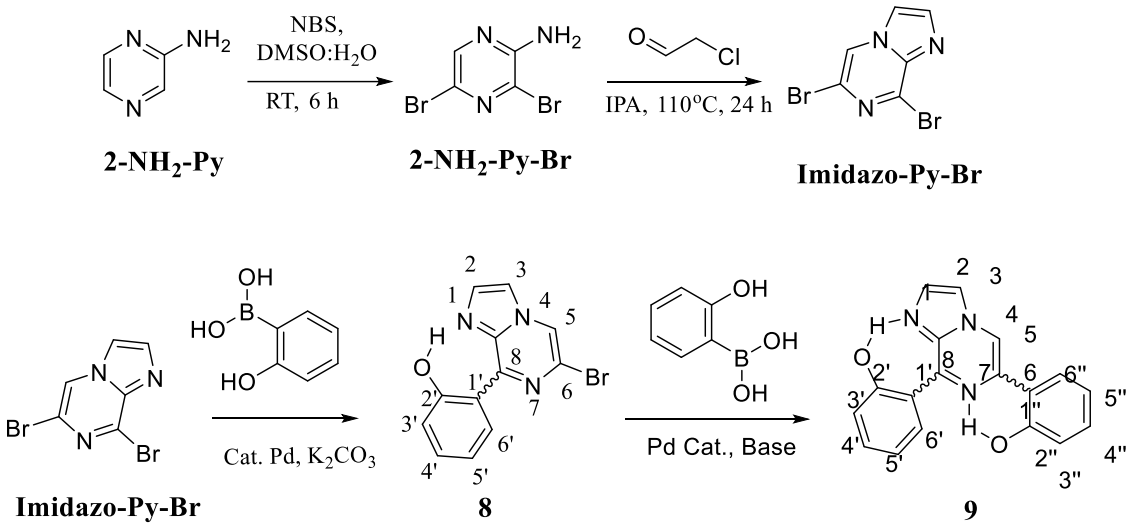

2-NH_2-Py **2-NH_2-Py-Br** **Imidazo-Py-Br**

Imidazo-Py-Br **8** **9**

Scheme 6.4 Synthesis of compound **8** and **9**

6.2.2.2 Synthesis of compound 8

A vial equipped with stirring bar was charged with 6,8-dibromo-imidazo[1,2-*a*]pyrazine (Imidazo-py-Br) (0.5 g, 1.8 mmol), Cs_2CO_3 (0.6 g, 1.8 mmol) and boronic acid (1.8 mmol), dissolved in CH_3CN:H_2O (9:1) at 100 ˚C under an inert atmosphere. Then, 5 mol% of $Pd(PPh_3)_4$ was added, and the vial was capped. The reaction mixture was refluxed for 7-12 h. After the completion of the reaction, (monitored by TLC), the reaction mixture was cooled and then extracted with water and chloroform. The organic layer was dried over Na_2SO_4, filtered and concentrated in vacuum to get crude product. The residue was purified by silica gel (60-120 mesh) column chromatography using hexane: ethyl acetate as eluents. Two different colored products were obtained in solid-state as compound **8A** and **8B** were obtained.

Compound 8A: Yellow solid; Yield: 30%; mp 232-234˚C; ^{1}H NMR spectrum displayed signals resonating at δ 7.05-7.09 ppm as multiplet due to 2H of ArH, δ 7.42-7.47 ppm as multiplet due to 1H of ArH, δ 7.74 ppm as doublet due to 1H of C_2H, δ 7.90 ppm as doublet due to 1H of C_3H, δ 8.23 ppm as singlet due to 1H of C_5H, δ 9.54-9.56 ppm as multiplet of 1H of ArH, δ 13.03 ppm as singlet due to OH; ^{13}C NMR ($CDCl_3$, 100 MHz): δ 114.7, 117.2, 117.9, 118.5, 118.9, 119.4, 132.4, 133.7, 135.8, 137.4, 150.0, and 160.8 ppm for aromatic carbons (ArCs), suggest the formation of compound **8A**. The observed MS (EI): m/z = 292 (M^++1) was in close agreement with calculated m/z = 291 and thus, confirmed the formation of compound **8B**.

Compound 8B: White solid; Yield: 30%; mp 232-234˚C; ^{1}H NMR spectrum displayed signals at δ 7.29-7.34 ppm as multiplet due to 2H of ArH, δ 7.43-7.47 ppm as multiplet due to 2H of ArH, δ 7.68 ppm as doublet due to 1H of C_2H, δ 7.77 ppm as doublet due to 1H of C_3H, δ 7.99 ppm as singlet due to 1H of C_5H; ^{13}C NMR ($CDCl_3$, 100 MHz): δ 115.3, 115.5, 119.3, 121.8, 125.9, 129.6, 132.6, 135.2, 152.1, and 152.1 for aromatic carbons (ArCs) suggested the formation of compound **8B**. Further, the observed MS (EI): m/z = 291 was in close agreement with calculated m/z = 291 and thus, confirmed the formation of compound **8B**.

6.2.2.3 Synthesis of compound 9

A vial equipped with stirring bar was charged with 6-bromo-8-substituted-imidazo[1,2-*a*]pyrazine (**8**) (0.1 g, 0.323 mmol), Cs_2CO_3 (0.105 g, 0.323 mmol) and 2-hydroxyphenylboronic acid (0.323 mmol), dissolved in CH_3CN:H_2O (9:1) at 100 ˚C under inert atmosphere. Then, 5 mol% of $Pd(PPh_3)_4$ was added, the vial was capped and refluxed for 6-12 h. After the completion of the reaction, (monitored by TLC), the reaction mixture was cooled, and then extracted the reaction mixture with water and chloroform. The organic layer was dried over Na_2SO_4, filtered, and concentrated in vacuum to get crude product. The residue was purified by silica gel (100-200 mesh) column chromatography using hexane: ethyl acetate as eluent. Two new different compounds as **9A** and **9B** were obtained with respect to their starting reactants as **8A** and **8B**.

Compound 9A: Yellow solid; Yield: 65%; mp 240-241 ^{0}C; ^{1}H NMR ($CDCl_3$, 400 MHz) spectrum displayed resonating signals at δ = 6.97 ppm as triplet due to 1H of ArH, δ 7.05 ppm as doublet due to 1H of ArH, δ 7.10 ppm as triplet due to 1H of ArH, δ 7.17 ppm as doublet due to 1H of ArH, δ 7.31-7.35 ppm as multiplet due to 1H of ArH, δ 7.46-7.50 ppm as multiplet due to 1H of ArH, δ 7.65 ppm as doublet due to 1H of ArH, δ 7.87 ppm as singlet due to 1H of C_2H, δ 7.88 ppm as singlet due to 1H of C_3H), δ 8.27-8.30 ppm as multiplet due to 1H of ArH, δ 8.59 ppm as singlet due to 1H of C_5H; ^{13}C NMR ($CDCl_3$, 100 MHz): δ 113.3, 115.2, 117.8, 118.6, 119.9, 120.8, 121.4, 125.7, 130.9, 131.2, 133.6, 133.7, 137.6, 139.8, 147.9, 157.6, and 158.0 for aromatic carbons (ArCs) suggested the formation of compound **9A**. Further, the observed MS (EI): m/z 303 was in close agreement with calculated m/z=303 and thus, confirmed the formation of compound **9A**.

Compound 9B: White solid; Yield: 70%; mp 244-246˚C; ^{1}H NMR ($CDCl_3$, 400 MHz) spectrum displayed resonating signals at δ = 6.82-6.86 ppm as multiplet due to 2H of

ArH, δ = 7.18 ppm as triplet due to 1H of ArH, δ = 7.29-7.31 ppm as multiplet due to 2H of ArH, δ = 7.39 ppm as triplet due to 1H of ArH, δ = 7.50-7.55 ppm as multiplet due to 2H of ArH, δ = 7.80 ppm as singlet due to 1H of C_2H), δ = 7.84 ppm as singlet due to 1H of C_3H), δ = 8.28 ppm as singlet due to 1H, C_5H, δ = 10.70 ppm as singlet due to 1H of OH; ^{13}C NMR ($CDCl_3$, 100 MHz): δ 110.5, 116.2, 117.1, 118.9, 119.6, 122.1, 124.9, 126.8, 130.3, 130.9, 131.7, 135.6, 136.5, 151.9, 152.6, 157.4 for aromatic resonating carbons (ArCs) suggested the formation of compound **9B**. Further, the observed MS (EI): m/z 304 (M^++1) was in close agreement with calculated m/z = 303 and thus, confirm the formation of compound **9B**.

Interestingly, the molecular mass from ESI-MS was found to be the same for compound **8A** and **8B.** However, both compounds possessed different NMR signals, different absorption maxima, and characteristics FTIR signals. Likewise, the **9A** and **9B** possessed the same molecular mass but distinguishable spectral signals. This depicted that the obtained compounds **8A** and **8B** would be isomeric forms of each other and likewise **9A** and **9B**. The obtained compounds have rigid architecture except for rotation around single bond connecting phenyl ring to imidazo-[1,2-*a*]pyrazine moiety. Therefore, the only possibility for the isomeric form to be rotameric conformations. Thus, in order to find the accurate structures of the possible conformers of compounds **8** and **9,** theoretical calculations were performed on the Gaussian 03 program .[27]

6.2.3 Results and discussion

6.2.3.1 Geometry optimizations and reactivity of compound Imidazo-py-Br

The Imidazo-py-Br was optimized and was further, treated for Fukui indices analysis, which is widely used to predict the reactivity indices in order to observe the reactive sites (electrophilic and nucleophilic sites) present on the molecule.[188] Fukui functions are the partial derivatives of electron density with respect to the number of electrons present.

$$f(r) = \left[\frac{\partial \rho(r)}{\partial N}\right]$$

Where ρ(r) denotes the electron density, N is the number of electrons present in the molecular system. Generally, the indices calculated for HOMO and LUMO, which further represents nucleophilicity and electrophilicity index, respectively. Reactive sites in the

molecular system have a more considerable value of Fukui indices (Figure 6.10) The molecular graph with Fukui indices suggested the C_6 as a reactive site. Therefore, followed reactions were taken place at C_6.

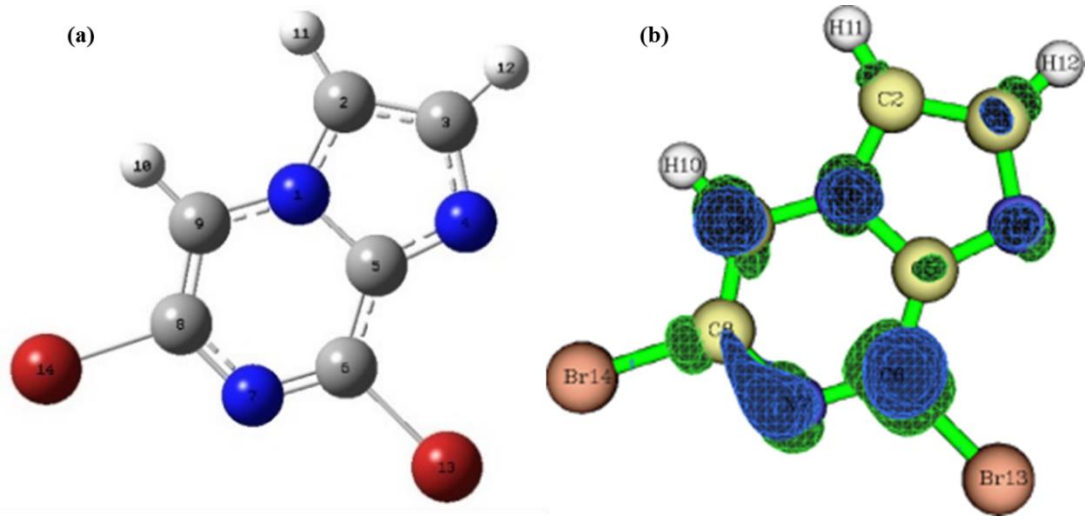

Figure 6.10 Optimized structure of precursor molecule (Imidazo-py-Br) (left) and the Fukui function mapping (right) (isosurface = 0.05), green and blue region denote the positive and negative electron density respectively

6.2.3.2 Conformational analysis of compound 8

The aim of finding the most stable conformational search has been fulfilled with a simple general strategy.

1. Compound **8** has rotational flexibility with respect to single bond joining the phenolic ring and rigid imidazo-[1,2-*a*]pyrazine ring. Therefore, the conformational search was carried out by rotational potential energy surface (PES) using DFT at B3LYP/6-31+G* level. All possible conformations of compound **8** at local minima have been shown in Figure 6.11.

2. The obtained structure at local minima was analyzed for relative Boltzmann contribution. From the principle of Boltzmann contribution, the conformers having free energy within the range of 5 kcalmol^{-1} can have some contribution to the Boltzmann population at room temperature (RT). Thus, the contributing conformers have been further optimized and confirmed by no imaginary frequency using DFT at B3LYP/ 6-31++G(d,p).

3. The absorption spectra and NMR chemical shifts were computed for each optimized conformers using TDDFT and GIAO methods.

4. The experimental and calculated data for absorption spectra, FTIR signals, and NMR shielding tensors were compared and evaluated to determine the structure of the compounds.

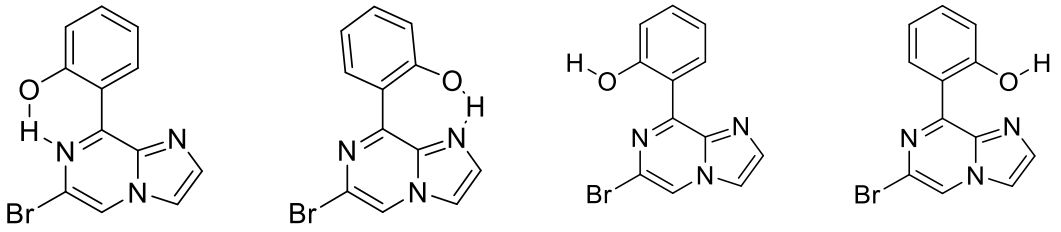

8A **8B** **8C** **8D**

Figure 6.11. Possible conformers of Compound **8**

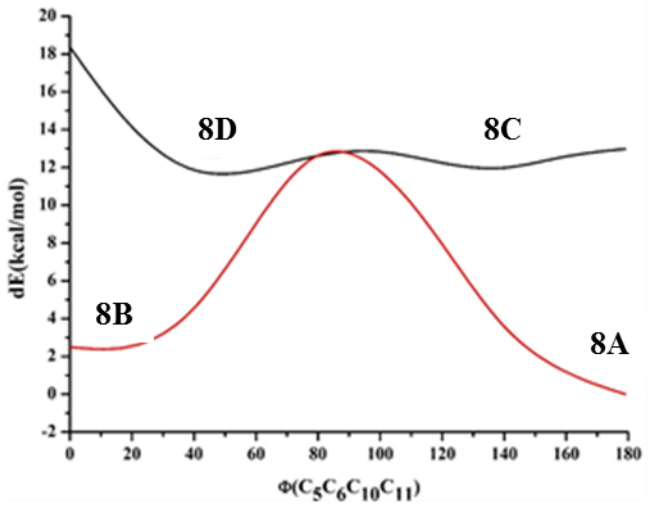

Figure 6.12 Energy variation (in kcalmol^{-1}) of different conformations for compound **8** with the dihedral angle between imidazole moiety and a phenolic moiety in the ground state.

6.2.3.3 Structure analysis of compound 8

At first, compound **8** was optimized in the form represented by **8A.** Further, the potential energy surface (PES) of dihedral angle for single bond rotation connecting phenyl ring and imidazo-[1,2-*a*]pyrazine moiety was performed for compound **8**. The PEC resulted in new local minima, with conformation represented by **8B**. Both the conformer were found to be stabilized by hydrogen bonding primarily examined by a bond distance of OH and NH, and it is found that the conformer at local minima **8B** has energy closer to **8A.** On the other hand, compound **8** was also optimized in conformer **8C** to know the impact of hydrogen bonding in the stabilization of conformer **8A** and **8B**. Also, the dihedral angle PES was performed to check other local minima. The new local minima

observed was assigned as conformer **8D**. The relative energy diagram for all conformation has been shown in Figure 6.12**.** It is found that both **8C** and **8D** have high energy relative to **8A** and **8B**. The relative free energy of optimized conformations along with Boltzmann distributions have been summarized in Table 6.3**.**

Table 6.3 The relative free energy of optimized conformations along with Boltzmann distributions for compound **8**

Conformers	**8A**	**8B**	**8C**	**8D**
ΔE (kcalmol^{-1})	0.000	1.488	9.948	23.845
Boltzmann Distribution (%)	92.5	7.5	0	0

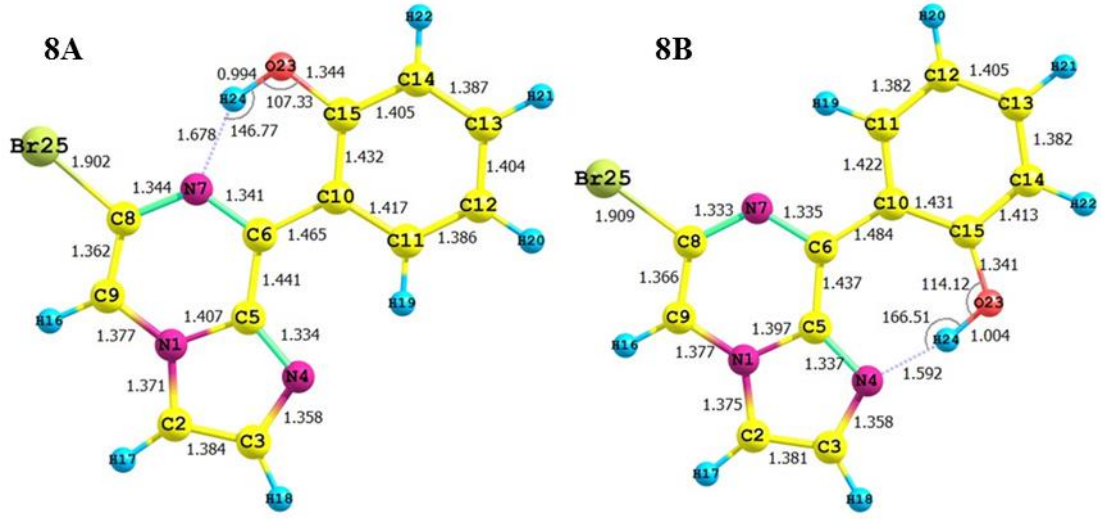

Figure 6.13 Optimized structures of stable conformers for compound **8** along with their structural parameters

From the principle of Boltzmann distribution, the conformers having free energy within the range of 5 kcalmol^{-1} can have some contribution to the Boltzmann population at room temperature (RT). Further, conformer **8A** and **8B** have been optimized at B3LYP/ 6-31++G(d,p). Both the conformer **8A** and **8B** found to be planar geometry and stabilized by six-membered and seven-membered hydrogen bonding, respectively. The conformer **8A** exists majorly about ~92.5% while **8B**, which is close in the energy of the configuration **8B** has relatively low (~7.5%) contribution. No other configurations have a significant contribution. The optimized structures of rotamers were shown in Figure 6.13**,** along with critical structural parameters such as bond lengths, and bond angles. The stabilization of conformers was discussed below:

6.2.3.3.1 Conformer 8A

According to Boltzmann distribution and optimized geometry, the conformer **8A** was critical conformation in the gas phase. The stability of conformation can be explained by the relative charges and hydrogen bonding distances. The calculated charges on H24 [0.505 (Mulliken); 0.505 (NBO)], N7 [0.074 (Mulliken); -0.571 (NBO)] and O23 [-0.320 (Mulliken); -0.677 (NBO)] atoms establishes the intramolecular dipolar interaction between phenolic hydrogen (O23─H24) and pyrazine nitrogen (N7) of imidazole moiety. The calculated non-bonded distance between the N7 and H24 bonded to O23 [d (N7···H24) = 1.678 Å), is less than the sum of the van der Waals radii of hydrogen and nitrogen. The smaller distance and dipolar interaction with opposite charges on H24, N7 support the six-membered intramolecular hydrogen bonding.

6.2.3.3.2 Conformer 8B

The other probable conformer **8B** have relatively low Boltzmann contribution in spite of its planar geometry. The calculated charges on H24 [+0.581 (Mulliken); +0.520 (NBO)], N4 [-0.28B8 (Mulliken); -0.538B (NBO)] and O23 [-0.560 (Mulliken); -0.712 (NBO)] atoms establishes the intramolecular dipolar interaction between phenolic hydrogen (O23-H24) and pyrrole nitrogen (N4). The non-bonded distance between phenolic hydrogen and pyrrole nitrogen [d (H24···N4) = 1.58B2 Å], which is less than the sum of the van der Waals radii of hydrogen and nitrogen support the hydrogen bonding. The smaller distance and dipolar interaction with opposite charges on H24, N4 confirmed the seven-membered intramolecular hydrogen bonding. In addition to N···H—O hydrogen bonding interaction in conformer **8A** and **8B**, there is (ArH···N) interaction where the aromatic hydrogen of phenolic moiety showed interaction to the nitrogen of pyrrole for conformer **8A** and imidazole nitrogen for conformer **8B**. These interactions are weak in nature, as confirmed by interacting distances and topological parameters. Additionally, both the conformers **8A** and **8B** were free from inter-electronic repulsion, which is present in conformer **8C** and **8D**. Further, the hydrogen bonding interaction is also estimated by QTAIM calculations (Table 6.4).

6.2.3.3.3 Topology parameters

In order to determine the nature of the intramolecular hydrogen bonds (HB) existing within key conformers, were studied by means of the Bader's quantum theory of atoms in molecules (QTAIM) using multiwfn 3.3.7. The existence of hydrogen bonding was

examined based on Popelier criteria.[122] The determined BCPs were off (3,-1) type. The positive value of $\nabla^2\rho(r_c)$ for both the conformers **8A** and **8B**, depicted electrostatic close shell interaction and the value found to be within Popelier's hydrogen bonding criteria. The Laplacian of electron density for N···HO hydrogen bonding in conformer **8A** is more than **8B** (Table 6.4). On the other hand, ArH···N has more Laplacian electron density in conformer **8B**. Further, the degree of covalency and strength of the interactions were characterized according to Rozas' rules.[30] All the bond critical points have ($\nabla^2\rho(r_c) > 0$, and $H(r) < 0$) are designated as medium-range interaction with the partial covalent character for both the conformers. Moreover, the hydrogen bond energy is determined by Espinosa equation.[111] The conformer **8A** manifested by two interactions N···HO and ArH···N, contributed -14.18 and -4.11 kcalmol^{-1} stabilization. On the other hand, the conformer **8B** also manifested by N···HO, and ArH···N interaction contributed, -18.22 and -4.39 kcalmol^{-1} stabilization, respectively. The ArH···N interaction has a nearly the same contribution for both conformers **8A** and **8B**, while the N···HO hydrogen bond found to be weaker in conformers **8A** than **8B**. This is due to the presence of electron withdrawing bromine atom which attracts the electron density and therefore, weakens the hydrogen bonding. On the other hand, lone pair on nitrogen atom could easily interact to a polarized hydrogen atom in conformer **8B,** forming strong hydrogen bonding. The bond critical point and bond paths of forms **8A** and **8B** were shown in Figure 6.14**.**

Table 6.4 Topology parameters electron density(ρ), Laplacian electron density ($\nabla^2\rho$), potential energy density [V(r)], total energy density [H(r)], hydrogen bonding energy [E_{HB}(kcalmol^{-1})] at bond critical pint of non-covalent interactions (D···HA) for conformer **8A** and **8B** at B3LYP/6-31++G**.

Compounds	**Interactions**	**$\nabla^2\rho$**	**V(r)**	**G(r)**	**H(r)**	**E_{HB}**
8A	N···HO	0.1303	-0.0452	0.0419	-0.0063	-14.18
	ArH···N	0.0637	-0.0131	0.0145	-0.0014	-4.11
8B	N···HO	0.1295	-0.0581	0.0453	-0.0129	-18.22
	ArH···N	0.0812	-0.0137	0.0170	-0.0033	-4.39

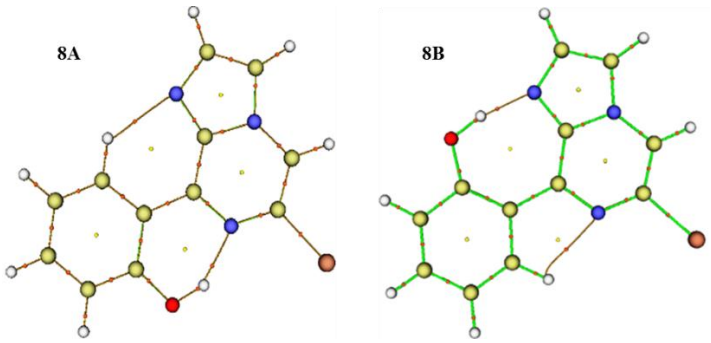

Figure 6.14 Molecular graphs for conformer **8A** (left) and **8B** (right); red dot denote BCP along with the bond path.

6.2.3.3.4 MBO and LBO analysis for compound 8A and 8B

Further, the Laplacian bond order (LBO), Mayer bond order (MBO) were analyzed for stable conformers **8A** and **8B**. LBO has a direct correlation to bond polarity and vibrational frequency. The bonds with bond order value smaller than 1.0 are polarized in nature and lower value, more is polarization. Mayer bond order and Laplacian bond order were summarized in Table 6.5**.** The MBO for C15-O23 in form **8A** is slightly lower than form **8B**. On the other hand, a smaller value of MBO and LBO for O23-H24 reflects more bond polarity for form **8B** than form **8A**. The polarization in OH bond causes a difference in bond strength, which results in the shift in vibrational frequency in two different conformations and validates the intramolecular hydrogen bonding.

Table 6.5 Affected bond order for conformer **8A** and **8B**

Bond	**MBO at 6-31G****		**LBO at 6-31++G****	
	8A	**8B**	**8A**	**8B**
N4─H24	--	0.1867	--	0.0011
N7─H24	0.1497	--	0.0006	--
C15─O23	1.0574	1.0746	0.5981	0.5917
O23─H24	0.7432	0.7011	0.5103	0.4638

6.2.3.3.5 Frequency analysis

FTIR is an excellent tool for functional group analysis. The FTIR signals of functional groups OH, C=N, C=C, etc. were observed for both conformers **8A** and **8B**. All computed band positions are in good agreement with the experimental values for both conformers. But, the OH stretching vibrations which are usually environmental dependent,

suggestively distinguish both conformations. The free O−H stretching vibration occurs between 3500-3700 cm^{-1} and hydrogen-bonded O−H stretching vibration usually observed in the range of 3200-3600 cm^{-1}.[189, 190] The computed frequency result showed the O−H stretching band at 3230.25 cm^{-1} in FTIR for conformer **8A**. Experimentally a broad O−H stretching band is observed at 3158 cm^{-1} for form **8A** (Figure 6.15). The computed and experimental values of FTIR for conformer **8B** were at 2999.47 cm^{-1} and 3069 $cm^{-1,}$ respectively (Figure 6.15). The broadness in the band also confirmed the presence of intramolecular hydrogen bonding. The difference in values of FTIR O−H bands for **8A** and **8B** revealed that OH bond found to be slightly weak in conformer **8A** relative to **8B.** As discussed earlier, the more polarized nature of the O−H bond through LBO bond order analysis and strong hydrogen bonding through QTAIM analysis for conformer **8B** which further weaken the O**─**H bond strength for **8B**. Therefore, FTIR values endorsed the observations from topology analysis, hydrogen bond strength, and LBOs.

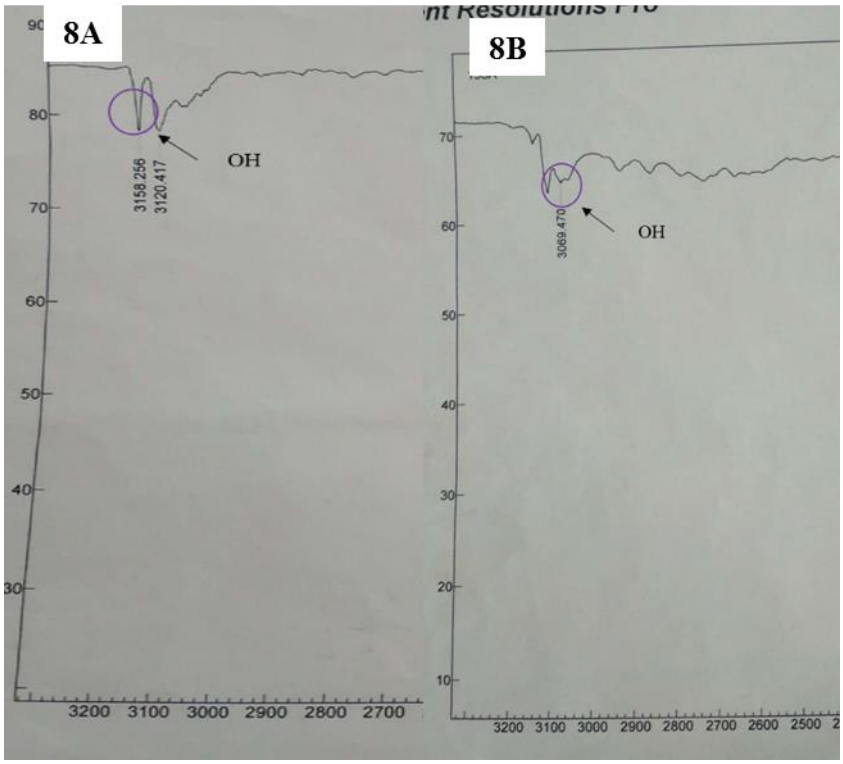

Figure 6.15 FTIR spectra of compound **8A** and **8B** for IraHB

6.2.3.3.6 NMR analysis

The ^{1}H and ^{13}CNMR shielding tensors were calculated using the GIAO method on the optimized structure, and the effect of solvent is included using the IEFPCM model. The

experimental chemical shifts of ^{1}H NMR and ^{13}C NMR have located between δ = 7.07 to 13.12 ppm and δ = 114.65 to 160.84 ppm, respectively. The comparison between the computed and experimental ^{1}H NMR and ^{13}C NMR results correlation value R^2=0.9888 and R^2=0.9331, respectively, for form **8A** (Figure 6.16). The deviation in an experimental chemical shift of C_{15} from the computed one is only due to the attachment of the hydroxy group to the phenyl ring. In a similar way, experimental NMR of conformer **8B** has been compared with calculated data. Although the correlation was not good, however, the combined information from FTIR and NMR could distinguish two conformers. The correlation of experimental and calculated NMR spectrum for conformer **8B** has been shown in Figure 6.16.

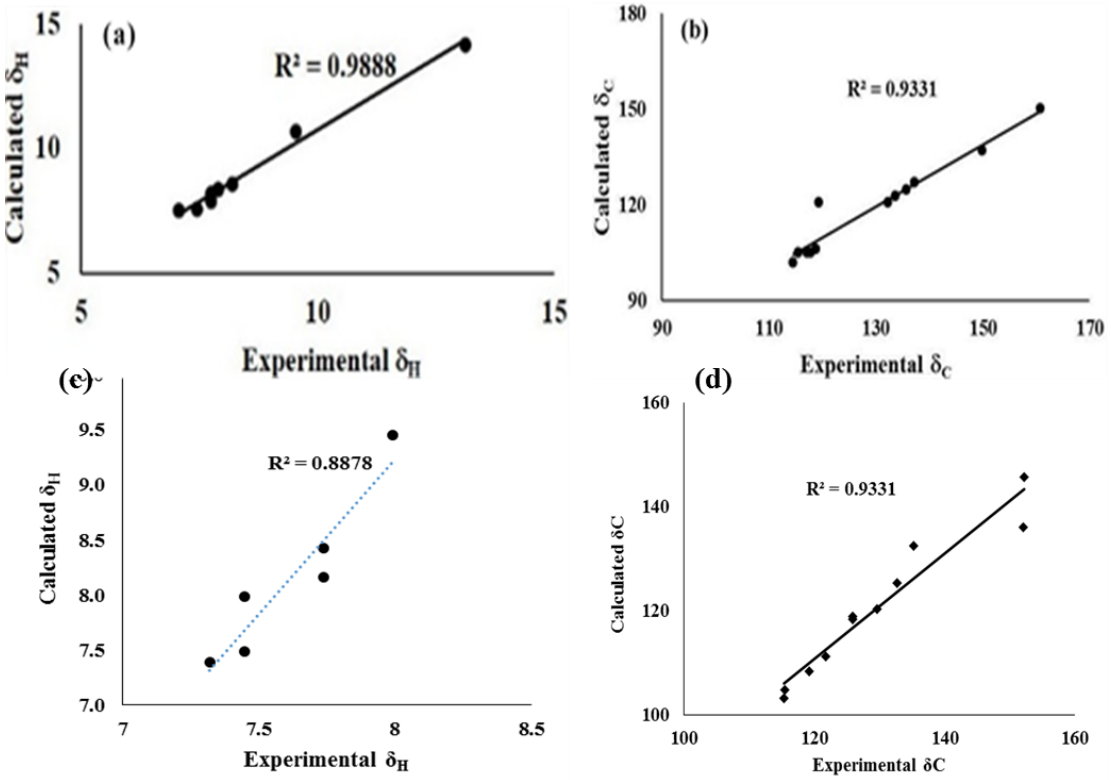

Figure 6.16 Experimental and theoretical correlation of ^{1}H and ^{13}C NMR for conformer (a, b) **8A** and (c, d) **8B**

6.2.3.3.7 Absorption analysis

The vertical excitations were calculated for conformers **8A** and **8B** on the optimized structure in gaseous and acetonitrile solution phase using TDDFT. The obtained absorption value for conformation **8A** at 380, 361, 318 nm has a contribution from the first three Franck-Condon excited states [(S_0-S_1), (S_0-S_2), (S_0-S_3)], respectively.

Table 6.6 The calculated absorption value (λ/nm) for conformer **8A** and **8B** in gas and CH_3CN solvent phase, the symmetry of frontier orbital and % contributions of Molecular orbitals

$S_0 \rightarrow S_n$	λ_{ACN}	λ_{Gas}	λ_{Exp}	f	Symmetry	MOs (%)	
			8A				
$S_0 \rightarrow S_1$	370.20	388.50	380	0.2567	Singlet-A	H→L	94
$S_0 \rightarrow S_2$	329.15	326.29	361	0.1214	Singlet-A	H-1→L	89
$S_0 \rightarrow S_3$	311.03	309.84	318	0.184	Singlet-A	H-2→L	86
			8B				
$S_0 \rightarrow S_1$	381.54	402.60	290	0.2699	Singlet-A	H→L	94
$S_0 \rightarrow S_2$	333.23	336.02		0.1178	Singlet-A	H-1→L	94
$S_0 \rightarrow S_3$	300.16	300.28		0.1204	Singlet-A	H-2→L	81

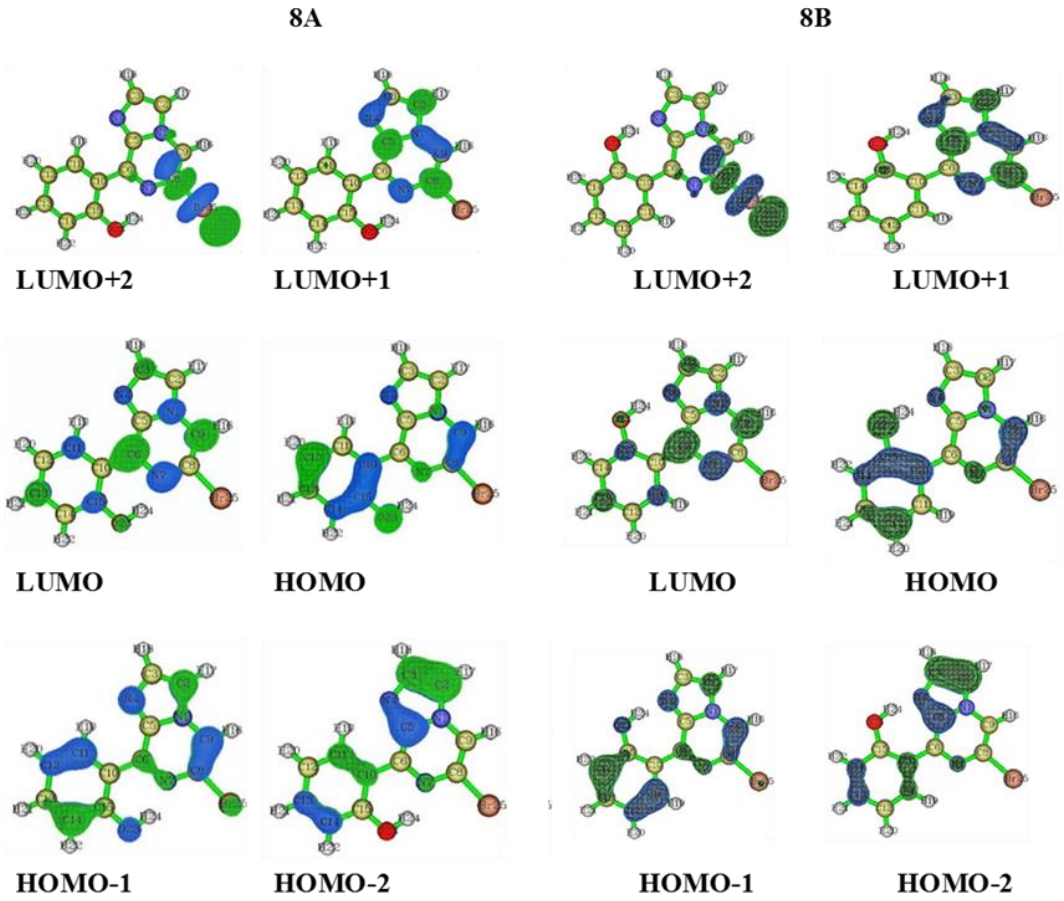

Figure 6.17 Frontier molecular orbital for conformer **8A** and **8B**

The first transition results from HOMO to LUMO majorly and has the nature of charge transfer from HOMO to LUMO (from phenolic moiety to imidazole moiety). While second and third transitions are kind of π—π^* nature and have a significant contribution from (HOMO-1) to LUMO and (HOMO-2) to LUMO respectively. On the other hand, the experimental absorption maxima value for conformer **8B** has been observed at 290 nm found due to the third Frank Condon transition. The transition resulted from (HOMO-2) to LUMO due to charge transition in the opposite direction. The calculated and experimental absorption values for conformers **8A** and **8B** are summarized in Table 6.6**.** The contributing frontier molecular orbitals have been shown in Figure 6.17. Thus, the synthesized conformers have been optimized in the form of **8A** and **8B**. Both the conformers **8A** and **8B** have planar geometry and found to be stabilized by six and seven-membered hydrogen bonding, respectively. The stability and strength of hydrogen bonding were established by QTAIM. The observed and calculated spectral data for NMR, FTIR found to be in good correlation for each form.

6.2.3.4 Structural analysis of compound 9

As discussed above, the isomeric forms of compound **8** found to have **8A** and **8B** geometry. Further, the separated isomers were reacted with another boronic acid and resulted in two new compounds. Therefore, the conformers resulted in the second substitution could have the possible structures, as shown in Figure 6.18.

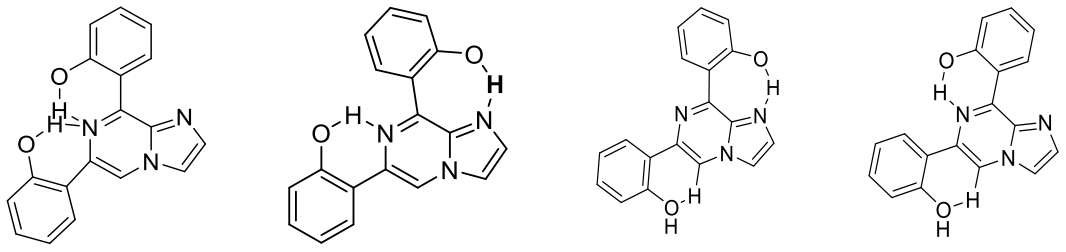

9A **9B** **9C** **9D**

Figure 6.18 Possible conformers of Compound **9**

The conformer **8A,** stabilized by six-membered hydrogen bonding could further result in either of **9A** or **9B** form. Therefore, compound **9** was first optimized for conformer **9A** using the same protocol as for compound **8**. The optimized geometry was confirmed by no imaginary frequency. Further, the optimized structure of form **9A** was analyzed

through potential energy surface for the dual dihedral scan of two phenolic moieties with imidazo-[1,2-*a*]pyrazine moiety with variation from 0^0 to 180^0 at a step size of 20 degrees.

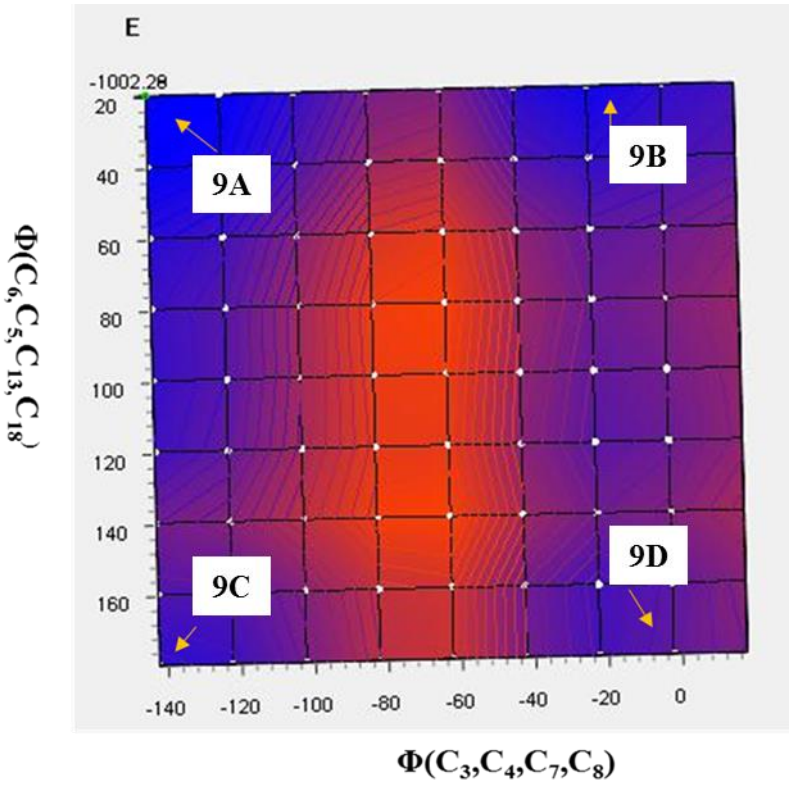

Figure 6.19 Energy variation (in kcalmol^{-1}) of different conformations for compound **9** with the dihedral angle between imidazole moiety and a phenolic moiety in the ground state.

Table 6.7 The relative free energy of optimized conformations along with Boltzmann distributions for compound 9

Conformers	**9A**	**9B**	**9C**	**9D**
ΔE (kcalmol^{-1})	1.530	0	8.508	2.627
Boltzmann Distribution (%)	6.96	91.91	0	1.09

For significant structures, the Boltzmann contribution at potential energy surface with relative energy of 5 kcalmol^{-1} was considered for further analysis. Four conformers represented by **9A**, **9B, 9C,** and **9D** found to be within Boltzmann energy limit for significant contribution (Figure 6.19).

The relative energy and Boltzmann distributions for all conformers at minima have been calculated in Table 6.7. All the conformers found to be stabilized by hydrogen bonding, established by interacting distance primarily. The conformer **9B** has been found to be most stable with the highest contribution of 91.9 %, followed by conformer **9A** with ~ 6.7 % contribution. On the other hand, **9C** and **9D** have negligible Boltzmann distribution.

The molecular structure with adequate Boltzmann distribution has been optimized and analyzed by frequency calculations. The optimized structures for conformers have been shown in Figure 6.20**,** along with their specific structural parameters such as bond length and bond angle. The stabilization of conformers has been discussed on the basis of hydrogen bonding.

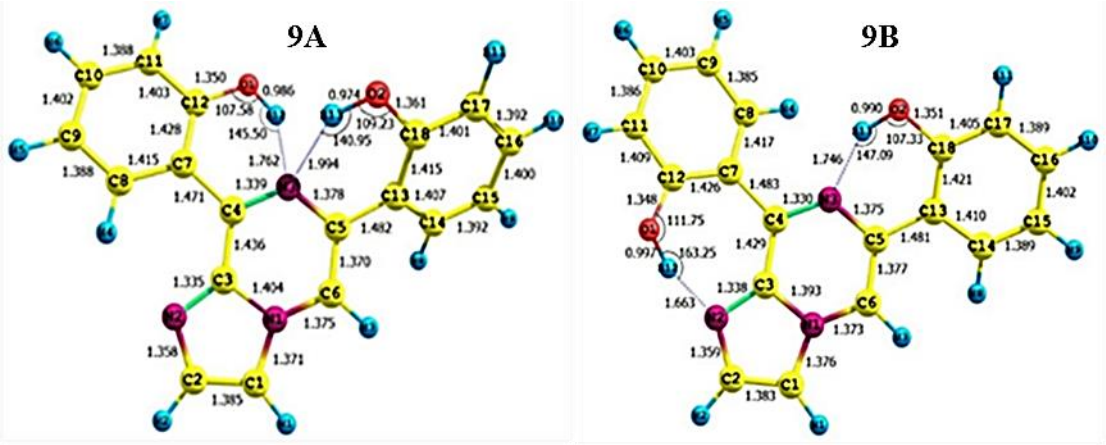

Figure 6.20 The optimized structure for compounds **9**

6.2.3.4.1 Conformer 9A

The conformer **9A** has ~ 7 % Boltzmann contribution, stabilized by two six-membered hydrogen bonding, which is further quantified by relative charges, and hydrogen bonding distances. The calculated charges on H12 [0.500 (Mulliken); 0.522 (NBO)], O1 [-0.488 (Mulliken); -0.699 (NBO)], H13 [0.446 (Mulliken); 0.519 (NBO)], O2 [-0.320(Mulliken); -0.677 (NBO)] and N3 [-0.355 (Mulliken); -0.567 (NBO)] atoms establishes the N···H─O intramolecular dipolar interactions between phenolic hydrogen and pyrazine nitrogen of imidazole moiety. The calculated non-bonded distance between phenolic hydrogen (H12, H13) and pyrazine nitrogen (N3) [d (N3···H12) = 1.762 Å), and d (N3···H13) = 1.994 Å] has been found to be less than the sum of the van der Waals radii of hydrogen and nitrogen. The smaller distance and dipolar interaction with opposite charges on H12, H13, and N3 supported the six-membered intramolecular hydrogen bonding.

6.2.3.4.2 Conformer 9B

The conformer **9B** has ~ 92 % Boltzmann contribution, stabilized by six-membered and seven-membered hydrogen bonding, which are further quantified by relative charges, and hydrogen bonding distances. The calculated charges on H12 [0.510 (Mulliken); 0.525

(NBO)], O1 [-0.549 (Mulliken); -0.710 (NBO)], N2 [-0.321 (Mulliken); -0.512 (NBO)], H13 [0.499 (Mulliken); 0.523 (NBO)], O2 [-0.498 (Mulliken); -0.722 (NBO)] and N1 [-0.198 (Mulliken); -0.540 (NBO)] atoms establishes the N···H─O intramolecular dipolar interactions between phenolic hydrogen and pyrazine/pyrrole nitrogen of imidazole moiety. The calculated non-bonded distance between phenolic hydrogen (H12, H13) and pyrazine/pyrrole nitrogen (N3/N2) [d (N2···H12) = 1.663 Å), and d (N3···H13) = 1.764 Å] were found to be less than the sum of the van der Waals radii of hydrogen and nitrogen. The smaller distance and dipolar interaction with opposite charges on H12, H13, and N3 support the six-membered intramolecular hydrogen bonding. Additionally, both the conformers **9A** and **9B** were free from inter-electronic repulsion.

6.2.3.4.3 Topology Analysis

The nature of the intramolecular hydrogen bonds existing within key conformers **9A** and **9B** were established by means of the Bader's QTAIM. Both the conformers were stabilized by intramolecular hydrogen bonding and recognized by Popelier's criteria of hydrogen bonding. The topological parameters for hydrogen bonding have been summarized in Table 6.8. It is found that the conformer **9A**, exhibiting N···H─O interactions of moderate strength with partial covalent character ($\nabla^2\rho(r_c) > 0$ and $H(r) < 0$) have largest stabilization contribution of -6.18 and -11.1 kcalmol^{-1}, while the weak electrostatic ArH···N interaction ($\nabla^2\rho(r_c) > 0$ and $H(r) > 0$) have stabilization contribution of -3.45 kcalmol^{-1}. On the other hand, the key conformer **9B**, demonstrated six-membered (6HB) and seven-membered (7HB) N···H─O and Ar─H···H─Ar interactions, it is ascertained that the N···H─O (6HB, 7HB) interactions have contributed major stabilization of -11.42, and -13.71 kcalmol^{-1}, while Ar─H···H─Ar interaction[191] has stabilization contribution of -1.76 kcalmol^{-1}. The N···H─O (6HB, 7HB) interactions ($\nabla^2\rho(r_c) > 0$ and $H(r) < 0$) have moderate strength with partial covalent character, while Ar─H···H─Ar interaction ($\nabla^2\rho(r_c) > 0$ and $H(r) > 0$) has weak electrostatic nature. The Laplacian of electron density $\nabla^2\rho(r_c)$ and stabilization energy for six-membered N···H─O hydrogen bonds have the nearly same value for both conformers **9A** and **9B**. However, the Laplacian of electron density $\nabla^2\rho(r_c)$ and stabilization energy for seven-membered N···H─O hydrogen bonds have significantly high value for conformer **9B** relative to six-membered N···H─O hydrogen bond for conformer **9A**, which ensured the large

Boltzmann contribution for conformer **9B**. The bond critical points and bond paths for both forms have been shown in Figure 6.21.

Table 6.8 Topology parameters electron density(ρ), Laplacian electron density ($\nabla^2\rho$), potential energy density [V(r)], total energy density [H(r)], hydrogen bonding energy [E_{HB}(kcalmol^{-1})] at bond critical point of non-covalent interactions (D···HA) for conformer **9A** and **9B** at B3LYP/6-31++G**.

Compounds	Interactions	$\nabla^2\rho$	V(r)	G(r)	H(r)	E_{HB}
9A	**N···HO**	0.0742	-0.0197	0.0191	-0.0006	-06.18
	N···HO	0.1151	-0.0354	0.0321	-0.0033	-11.10
	ArH···N	0.0577	-0.0110	0.0127	0.0017	-3.45
9B	**N···HO (7HB)**	0.1240	-0.0437	0.0374	-0.0064	-13.71
	N···HO (6HB)	0.1165	-0.0364	0.0327	-0.0036	-11.42
	ArH···HAr	0.0471	-0.0056	0.0087	0.0030	-1.76

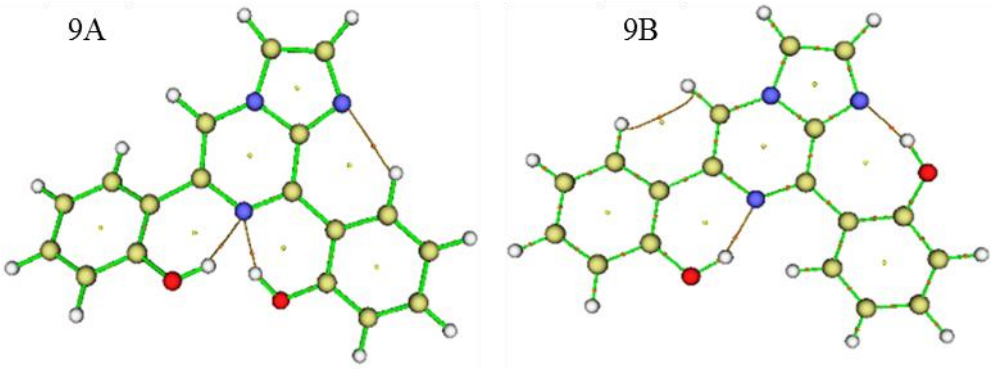

Figure 6.21 Molecular graphs for conformer **9A** and **9B**; red dot denotes BCP along with the bond path

6.2.3.4.4 MBO and LBO analysis for compound 9

Further, Mayer bond order (MBO) and Laplacian bond order (LBO) were analyzed for stable conformers **9A** and **9B** (Table 6.9). The MBO and LBO indexes for O─H bond have a value less than 1, clearly indicated the polarization of bond, which further allows hydrogen atom to interact with nitrogen atom through hydrogen bonding and validating the intramolecular hydrogen bonding. The low value of LBO and MBO indexes for conformer **9B** for O─H bonds ascertained the high bond polarization compared to

conformer **9A**. Additionally, both O─H bond polarization reasonably supported by almost same LBO and MBO indexes for conformer **9B**, while the difference in indexes for two O─H bonds for conformer **9A** depicted the difference in the strength of bonds as well.

Table 6.9 Affected Bond Order for conformer **9A** and **9B**

Bond	**MBO at 6-31G****		**LBO at 6-31++G****	
	9A	**9B**	**9A**	**9B**
N2-H12	─	0.1702	─	─
N3-H12	0.1268	─	─	─
N3-H13	0.0764	0.1317	─	─
C12-O1	1.0336	1.0451	0.5755	0.5775
C18-O2	0.9226	1.0342	0.5455	0.5775
O1-H12	0.7663	0.7261	0.5433	0.4993
O2-H13	0.8114	0.7565	0.6042	0.5364

6.2.3.4.5 Frequency analysis.

As discussed earlier, the free O−H stretching vibration occurs between 3500-3700 cm^{-1} and hydrogen-bonded O−H stretching vibration usually observed in the range of 3200-3600 cm^{-1}. The simulated FTIR spectrum for conformer **9A** has a broad signal for O─H bonds at 3695.05, and 3391.24 cm^{-1}, while conformer **9B** have O─H signals at 3159.33 and 3233.54 cm^{-1}. As discussed above, the conformer **9A** has two O─H bonds of different strength. Consequently, the calculated FTIR signals were found at higher wavenumber with a significant difference of ~ 300 cm^{-1}. The experimentally observed FTIR signals for conformer **9A** were found at 3100, and 3030 cm^{-1} (Figure 6.22). On the other hand, the conformer **9B** has O─H bonds of almost the same strength and high stabilization. Thus, the calculated FTIR signals were originated at lower wavenumber with a small difference of ~ 70 cm^{-1}. Likewise, the observed FTIR signals for conformer **9B** were at 3000, and 2930 cm^{-1} (Figure 6.22). The observed and calculated FTIR signals for O─H bonds in both conformers were in correlation with respect to their strength and polarization in bonds.

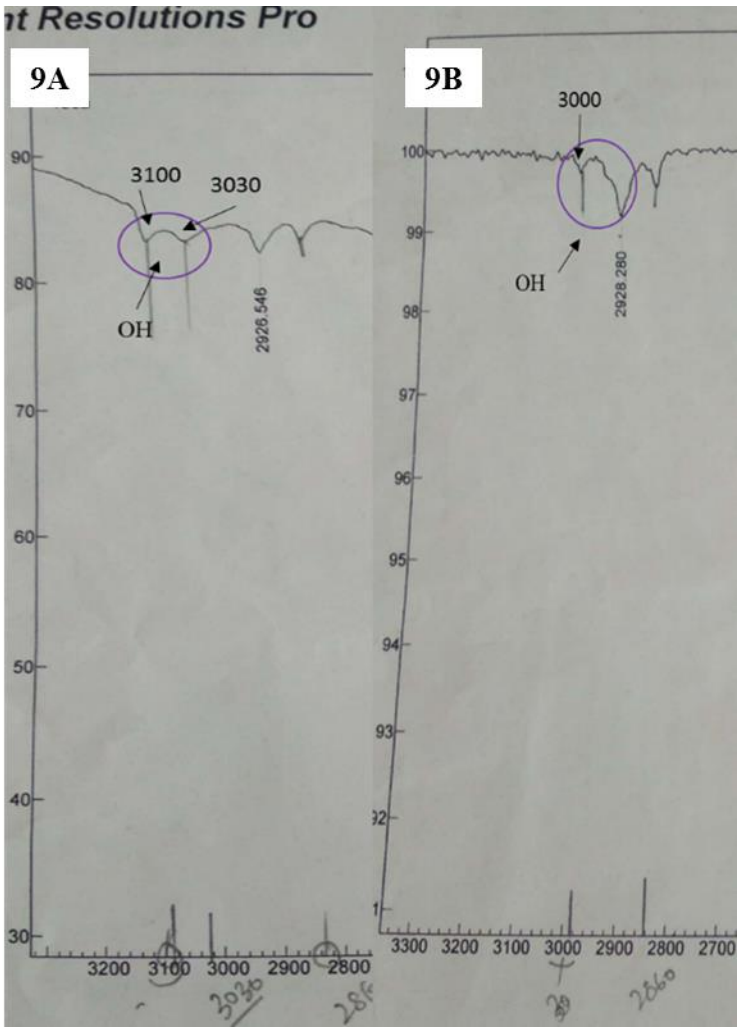

Figure 6.22 FTIR spectra of compound **9A** and **9B**

6.2.3.4.6 NMR

Likewise for **8A** and **8B**, the ^{1}H and ^{13}CNMR shielding tensors were calculated for conformers **9A** and **9B** using the GIAO method. The assessment of computed and experimental ^{13}CNMR results revealed good correlation for both conformers **9A** and **9B**. The correlation value for ^{13}CNMR found to be $R^2 = 0.97$, and 0.99 for conformer **9A** and **9B,** respectively. Furthermore, the correlation value of computed and experimental ^{1}HNMR results for conformer **9B** was $R^2 = 0.97$. However, the correlation of ^{1}HNMR for conformer **9A** was $R^2 = 0.90$. The weak correlation could be due to deviation in OH signals. The correlation of ^{1}HNMR and ^{13}CNMR for conformer **9A** and **9B** has been shown in Figure 6.23.

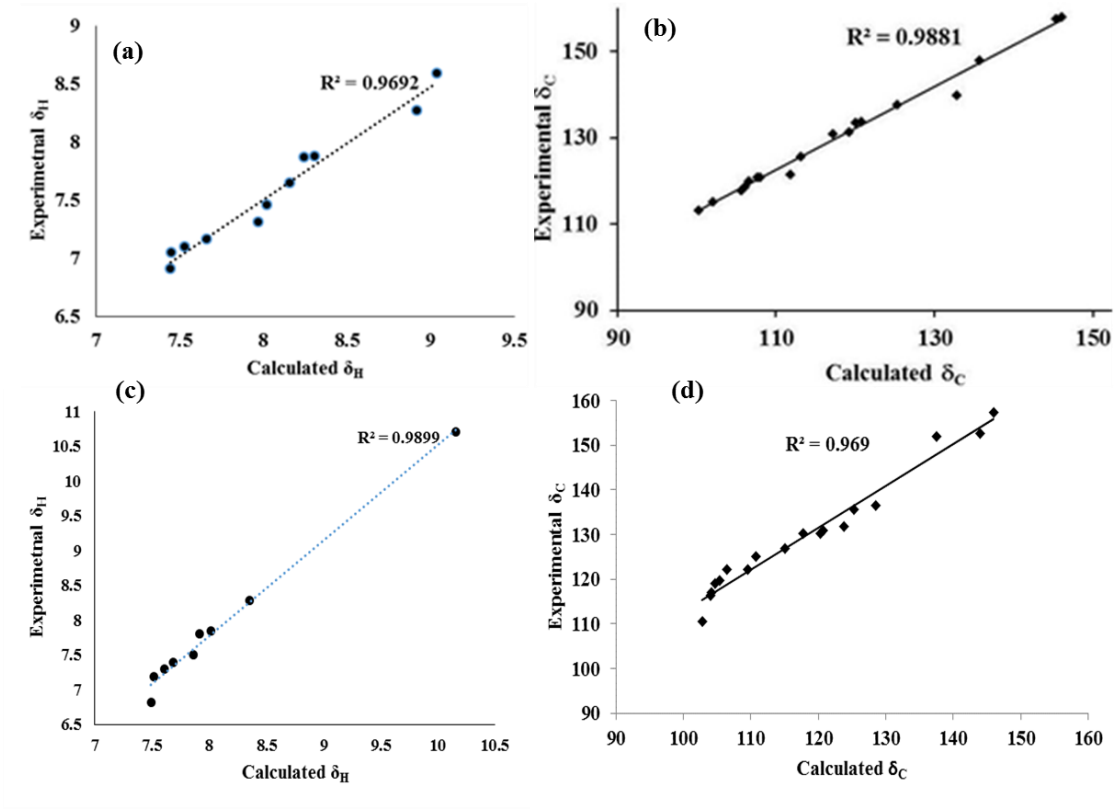

Figure 6.23 Experimental and theoretical ^{1}H NMR and ^{13}C NMR correlation for conformer (a, b) **9A** and (c, d) **9B,** respectively.

6.2.3.4.7 Absorption Properties

The vertical Frank Condon excitations were calculated for conformers **9A** and **9B** on their optimized structures, using TDDFT and further compared with experimental absorption spectra. The obtained absorption values for conformation **9A** at 380, 360, 265 nm has a significant contribution from three Franck-Condon excited states [(S_0-S_1), (S_0-S_5), (S_0-S_6)], respectively. On the other hand, the experimental absorption peak for conformer **9B** has been observed at 375, 315, 260 nm. The experimentally observed transitions were found due to [(S_0-S_1), (S_0-S_2), (S_0-S_6)] Frank Condon transition, respectively. The calculated and experimental absorption spectral data have been tabulated in Table 6.10. The different contributed molecular orbitals have been shown in Figure 6.24. Thus, the difference in signals for NMR, FTIR, and absorption peaks for two compounds and their correlation with theoretical calculations clearly predict the proper orientation of rotamers.

Table 6.10 The calculated absorption value (λ (nm)) for conformer **9A** and **9B** in gas and CH_3CN solvent phase at B3LYP/6-31++G** level of theory, the symmetry of frontier orbital and % contributions of Molecular orbitals

9A							
S_0-S_n	**λ_{Gas}**	**λ_{ACN}**	**λ_{Exp}**	**f**	**Symmetry**	**MOs contrib.**	
1	387.15	377.15	380	0.1640	Singlet-A	H→L	96%
2	375.78	357.40	360	0.0624	Singlet-A	H-1→L	98%
5	297.45	290.59	265	0.4008	Singlet-A	H→L+1	55%
6	292.17	286.91		0.2020	Singlet-A	H-4→L	81%
9B							
1	406.33	391.19	315	0.1003	Singlet-A	H→L	91%
2	389.98	362.46		0.1141	Singlet-A	H-1→L	93%
3	335.74	329.86	260	0.073	Singlet-A	H-2→L	93%
4	321.73	317.88		0.1328	Singlet-A	H→L+1	80%

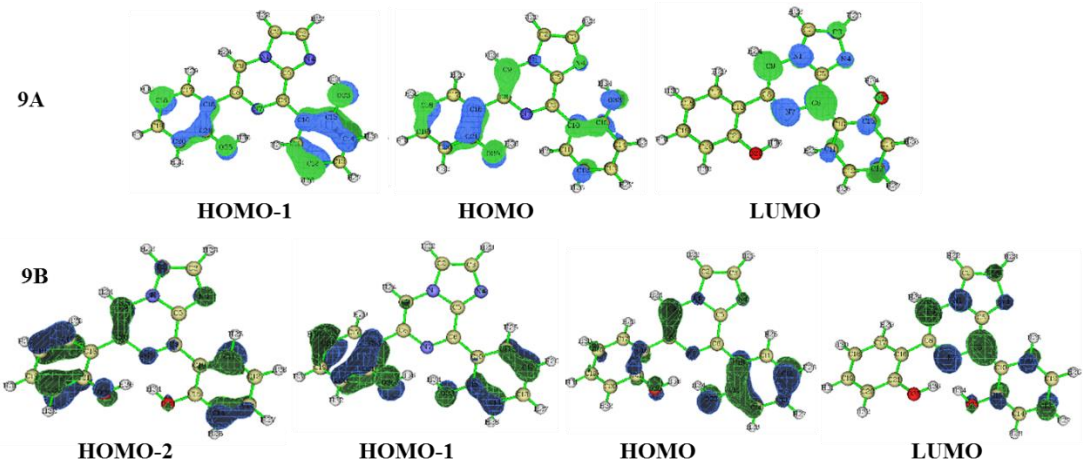

Figure 6.24 Frontier Molecular orbital of **9A** and **9B**

6.2.4 Conclusions

In summary, we have successfully synthesized and purified the rotameric conformations of mono/di-arylated substituted imidazo-[1,2-*a*]pyrazine. The PECs approach was used to investigate the fundamental structures of rotamers. The obtained rotameric forms were found to be stabilized by intramolecular hydrogen bond locking, which was further established and estimated by QTAIM analysis. The Laplacian and Mayer bond order

(LBO/MBO) analysis also revealed the difference in bond strength for different conformations and thus, distinction in vibrational frequency, NMR signals, assisted to recognize the fundamental structure for different conformations. The correlation between experimental and calculated results displayed directed us in the assignment of rotamers.

6.2.5 Experimental data

6.2.5.1 Synthesis of 2-amino-3,5-dibromopyrazine (2-NH_2-py-Br)[186]

N-Bromosuccinamide (14.95 g, 83.99 mmol) was added over 50 min to a mixture of 2-aminopyrazine (3.80 g, 40 mmol) in 80 ml DMSO and 2 ml H_2O below 15 ˚C. Mixture was then stirred for **6** h at room temperature. After completion of the reaction, the mixture was then extracted with water and ethyl acetate. Ethyl acetate layer was dried over Na_2SO_4 and concentrated in vacuum. The crude product was purified by column chromatography using hexane: ethyl acetate (9:1) as eluents. White solid; Yield: 90%; mp 115-116 ˚C.

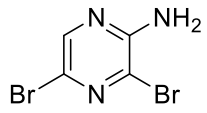

2-NH_2-Py-Br

^{1}H NMR ($CDCl_3$, 400 MHz): δ 5.12 (bs, 1H, NH_2), 8.04 (s, 1H, C6H); ^{13}C NMR ($CDCl_3$, 100 MHz): δ 123.5, 123.9, 143.1, 151.8; MS (EI): m/z 254 (M^+ +1).

6.2.5.2 Synthesis of 6,8-dibromo-imidazo[1,2-a]pyrazine (Imidazo-py-Br)[187]

To 2-amino-3,5-dibromopyrazine (5.0 g, 19.8 mmol) in 100 ml of isopropyl alcohol (IPA), 50% aqueous solution of chloroacetaldehyde (99 mmol) was added dropwise. The reaction mixture was refluxed at 110 ˚C for 24 h. After the completion of the reaction, cooled to room temperature and then extracted with water and chloroform. The chloroform layer was dried over sodium sulfate and concentrated in vacuum to get the crude product. The product was purified by column chromatography using hexane:ethyl acetate (6:4) as eluent to get pure compound as white solid. Yield: 80%; m.pt.: 165 ˚C;

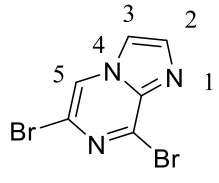

Imidazo-Py-Br

^{1}H NMR ($CDCl_3$, 400 MHz): δ 7.80 (d, *J* = 0.92 Hz, 1H, $C_2\underline{H}$), 7.86 (d, *J* = 1.36 Hz, 1H, $C_3\underline{H}$), 8.29 (s, 1H, $C_5\underline{H}$); ^{13}C NMR ($CDCl_3$, 100 MHz): δ 115.9, 119.3, 119.9, 137.0, 137.4, 142.5; MS (EI): m/z 278 (M^+ +1).

6.2.5.3 Synthesis of compound 8

A vial equipped with stirring bar was charged with 6,8-dibromo-imidazo[1,2-*a*]pyrazine (Imidazo-py-Br) (0.5 g, 1.8 mmol), Cs_2CO_3 (0.6 g, 1.8 mmol) and boronic acid (1.8 mmol), dissolved in CH_3CN:H_2O (9:1) at 100 ˚C under an inert atmosphere. Then, 5 mol% of $Pd(PPh_3)_4$ was added, and the vial was capped. The reaction mixture was refluxed for 7-12 h. After the completion of the reaction, (monitored by TLC), the reaction mixture was cooled and then extracted with water and chloroform. The organic layer was dried over Na_2SO_4, filtered, and concentrated in vacuum to get the crude product. The residue was purified by silica gel (60-120 mesh) column chromatography using hexane: ethyl acetate as eluents. Two different colored solids as products (**8A** and **8B)** were obtained.

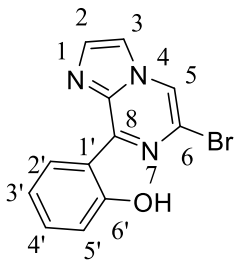

8A

Compound 8A: Yellow solid; Yield: 30%; m.pt. 232-234 ^{0}C; ^{1}H NMR ($CDCl_3$, 400 MHz): δ 7.05-7.09 (m, 2H, ArH), 7.42-7.47 (m, 1H, ArH), 7.74 (s, 1H, C2H), 7.90 (s, 1H, C3H), 8.23 (s, 1H. C5H), 9.54-9.56 (m, 1H, ArH), 13.03 (s, OH); ^{13}C NMR ($CDCl_3$, 100 MHz): δ 114.7, 117.2, 117.9, 118.5, 118.9, 119.4, 132.4, 133.7, 135.8, 137.4, 150.0, 160.8 (ArC); MS (EI): m/z 292 (M^++1).

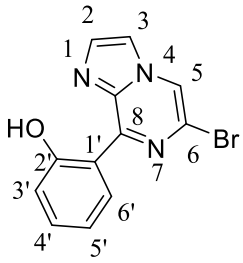

8B

Compound 8B: White solid; Yield: 30%; m.pt. 232-234 ^{0}C; ^{1}H NMR ($CDCl_3$, 400 MHz): δ 7.29-7.34 (m, 2H, ArH), 7.43-7.47 (m, 2H, ArH), 7.68 (d, *J* = 1.40 Hz, 1H, C2H), 7.77 (d, *J* = 0.92 Hz, 1H, C3H), 7.99 (s, 1H, C5H); ^{13}C NMR ($CDCl_3$, 100 MHz): δ 115.3, 115.5, 119.3, 121.8, 125.9, 129.6, 132.6, 135.2, 152.1, 152.1 (ArC); MS (EI): m/z 291 (M^+).

6.2.5.4 Synthesis of compound 9

A vial equipped with stirring bar was charged with 6-bromo-8-substituted-imidazo[1,2-*a*]pyrazine (**8**) (0.1 g, 0.323 mmol), Cs_2CO_3 (0.105 g, 0.323 mmol) and 2-hydroxyphenylboronic acid (0.323 mmol), dissolved in CH_3CN:H_2O (9:1) at 100 ˚C under inert atmosphere. Then, 5 mol% of $Pd(PPh_3)_4$ was added, the vial was capped and refluxed for 6-12 h. After the completion of the reaction, (monitored by TLC), the reaction mixture was cooled, and then extracted the reaction mixture with water and chloroform.

The organic layer was dried over Na_2SO_4, filtered and concentrated in vacuum to get the crude product. The residue was purified by silica gel (100-200 mesh) column chromatography using hexane: ethyl acetate as eluent. Two new different compounds as **9A** and **9B** were obtained with respect to their starting reactants as **8A** and **8B**.

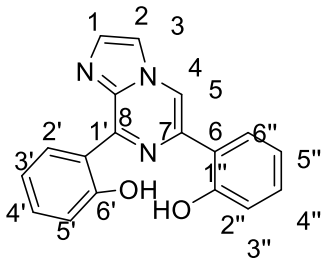

9A

Compound 9A: Yellow solid; Yield: 65%; m.pt. 240-241 ^{0}C; ^{1}H NMR ($CDCl_3$, 400 MHz): δ 6.97 (t, *J* = 7.48 Hz, 1H, ArH), 7.05 (d, *J* = 8.52 Hz, 1H, ArH), 7.10 (t, *J* = 7.48 Hz, 1H, ArH), 7.17 (d, *J* = 7.48 Hz, 1H, ArH), 7.31-7.35 (m, 1H, ArH), 7.46-7.50 (m, 1H, ArH), 7.65 (d, *J* = 6.52 Hz, 1H, ArH), 7.87 (s, 1H, C2H), 7.88 (s, 1H, C3H), 8.27-8.30 (m, 1H, ArH), 8.59 (s, 1H, C5H); ^{13}C NMR ($CDCl_3$, 100 MHz): δ 113.3, 115.2, 117.8, 118.6, 119.9, 120.8, 121.4, 125.7, 130.9, 131.2, 133.6, 133.7, 137.6, 139.8, 147.9, 157.6, 158.0 (ArC); MS (EI): m/z 303 .

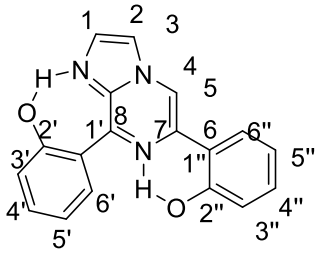

9B

Compound 9B: White solid; Yield: 70%; m.pt. 244-246 ^{0}C; ^{1}H NMR ($CDCl_3$, 400 MHz): δ 6.82-6.86 (m, 2H, ArH), 7.18 (t, *J* = 7.56 Hz, 1H, ArH), 7.29-7.31 (m, 2H, ArH), 7.39 (t, *J* = 7.34 Hz, 1H, ArH), 7.50-7.55 (m, 2H, ArH), 7.80 (s, 1H, C2H), 7.84 (s, 1H, C3H), 8.28 (s, 1H, C5H), 10.70 (s, 1H, OH); ^{13}C NMR ($CDCl_3$, 100 MHz): δ 110.5, 116.2, 117.1, 118.9, 119.6, 122.1, 124.9, 126.8, 130.3, 130.9, 131.7, 135.6, 136.5, 151.9, 152.6, 157.4 (ArC); MS (EI): m/z 304 (M^++1).

6.3

Investigation of excited state intramolecular double proton transfer in asymmetrical imidazo-[1,2-*a*]pyrazine compound: A theoretical study

6.3.1 Abstract

The compound **9A** and **9B** were stabilized by double intramolecular hydrogen bonding. The compound **9A** contained six-membered O─H···N hydrogen bonding with the shared site of interaction. On the other hand, compound **9B** contained six-membered as well as seven-membered O─H···N double intramolecular hydrogen bonding at different sites of interaction. Due to the presence of different mode of interactions, compound **9B** could rise the excited state intramolecular single/double proton transfer. Therefore, A novel compound **9B** enclosed double IraHB was studied for the photophysical properties. The compound exhibited dual emission at 430 nm and 570 nm with Stokes' shifts of 70 nm and 210 nm, respectively. The dual emission with large Stokes' shifts portrayed the excited state intramolecular proton transfer (ESIPT). Therefore, the prerequisite condition of IraHBs was established by atoms in molecules (AIM), and calculated IraHB energy showed that IraHBs were strengthened on photoexcitation $S_0 \rightarrow S_1$. The AIM results were endorsed through the redshifts in vibrational stretching of 879 cm^{-1} and 372 cm^{-1} for O_{34}—H_{36} and O_{22}—H_{35}, respectively. Therefore, there could be four tautomers as **9B**, **EK1**, **EK2,** and **KK**. The theoretical results also revealed the change in electron density on the frontier molecular orbitals (FMOs) and electron density difference map. Further, the ESIPT was estimated through the PECs as a function of IraHBs distances and corrected for the free energy of tautomeric forms. The relative free energy established stability order as **EK1**>**EK2**>**KK**>**9B** at S_1 state and thus, drive the ESIPT phenomenon. Also, the predicted emission for **9B** and **EK1** were in close agreement with observed emission.

6.3.2 Results and discussion

6.3.2.1 Photophysical properties

Compound **9B** (20μM, CH_3CN) displaced absorption peaks at 315 nm and 260 nm. Upon photoexcitation, at 315 nm, compound **9B** (20μM, CH_3CN) displayed dual emission at 430 nm and 570 nm with stokes' shift of 115 nm and 255 nm, respectively (Figure 6.25).

Indeed, compound **9B** contained double IraHBs and the presence of dual emission with broad stokes' shift clearly indicated the ESIPT phenomenon. The emission peak at 430 nm could be ascribed as standard enol emission. The emission band at 570 nm, with large Stokes` shift was due to excited state intramolecular proton transfer (ESIPT).

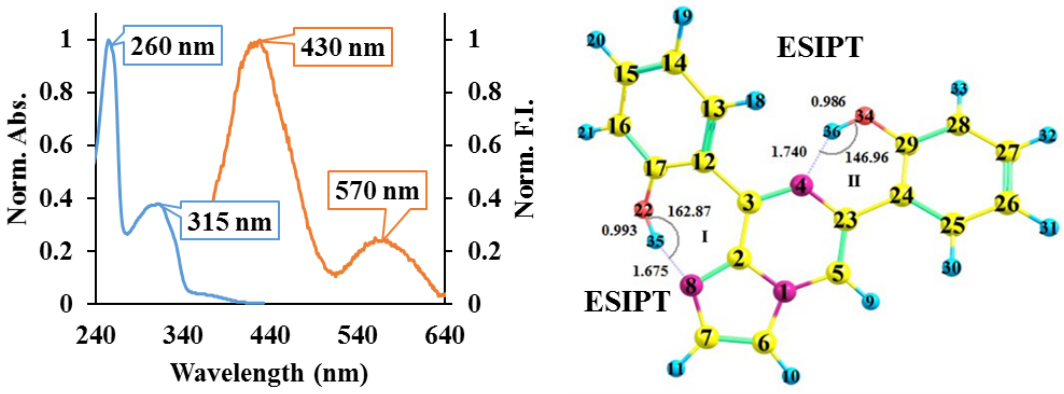

Figure 6.25 Normalize absorption and emission spectra of compound **9B**

6.3.2.2 Geometrical parameters

The compound **9B** was optimized at S_0 and S_1 states using DFT and TDDFT methods with ωb97-XD/6-31+g(d,p) and was validated for the local minima through the absence of imaginary frequency. The compound **9B** contained two ESIPT sites in the forms of two IraHBs. For better understanding, the interactions were labeled as I and II and shown in Figure 6.26. The geometrical parameters such as bond lengths, bond angles for IraHBs were also displayed.

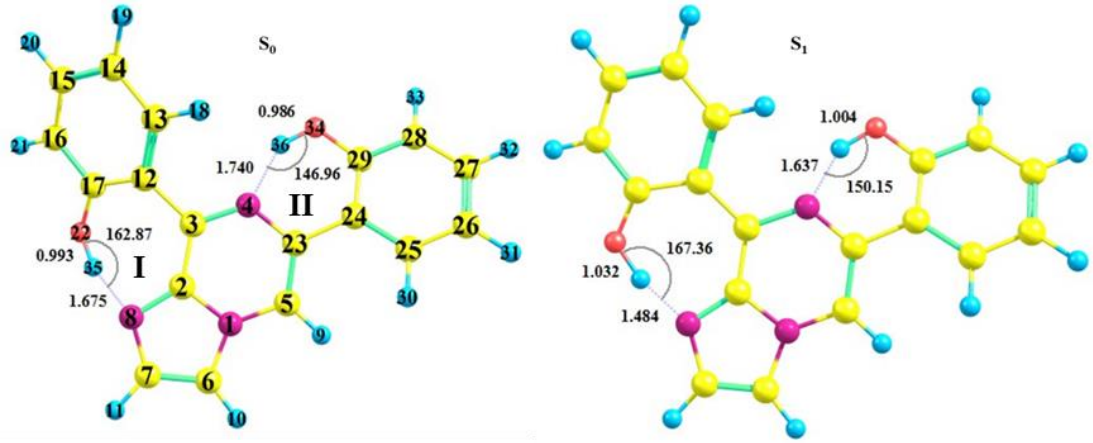

Figure 6.26. Optimized structure of compound **9B** in three tautomeric forms at S_0 and S_1 state

As displayed, for the interaction I, the bond lengths for O_{22}—H_{35} was increased by ~0.039 Å from 0.993 at S_0 state to 1.032 Å at S_1 state, while the H_{35}—N_8 bond length was decreased by 0.191 Å from 1.675 Å at S_0 state to 1.484 Å at S_1 state. On the other hand, the O_{34}—H_{36} bond distance was also increased by 0.018 Å, while the H_{36}—N_4 bond distance was decreased by 0.103 Å from 1.740 Å at S_0 state to 1.637 Å at S_1 state, for interaction II. Meanwhile, for $S_0 \rightarrow S_1$, the bond angles for interaction $O_{22}H_{35}\cdots N_8$ (I) was increased from 162.87° to 167.36°, likewise for $O_{34}H_{36}\cdots N_4$ (II) from 146.96° to 150.15°. Thus, the small interacting distances and angles indicated two kinds of intramolecular hydrogen bonding (IraHB) in S_0 and S_1 states. However, the decreased $O_{22}H_{35}\cdots N_8$ (I) and $O_{34}H_{36}\cdots N_4$ (II) bond lengths, and increased interacting bond angles imply that the IraHB strengthens in S_1 state relative to S_0 state.

6.3.2.3 Frequency analysis

The FTIR spectral signals are rightly related to IraHBs strength, and therefore, the spectral shifts to the characteristics of functional groups provided insight into the nature of IraHBs at S_1 state. Therefore, the simulated FTIR spectra at S_0 and S_1 states were presented in Figure 6.27, where the essential signals involved in the IraHBs were labeled. The O–H stretching vibrational frequency for O_{22}—H_{35} and O_{34}—H_{36} were located at 3392 cm^{-1} and 3222 cm^{-1}, respectively at S_0 state. On photoexcitation to S_1 state, the FTIR signal for O_{22}—H_{35} was displaced by redshifted of 372 cm^{-1} to 3020 cm^{-1}.

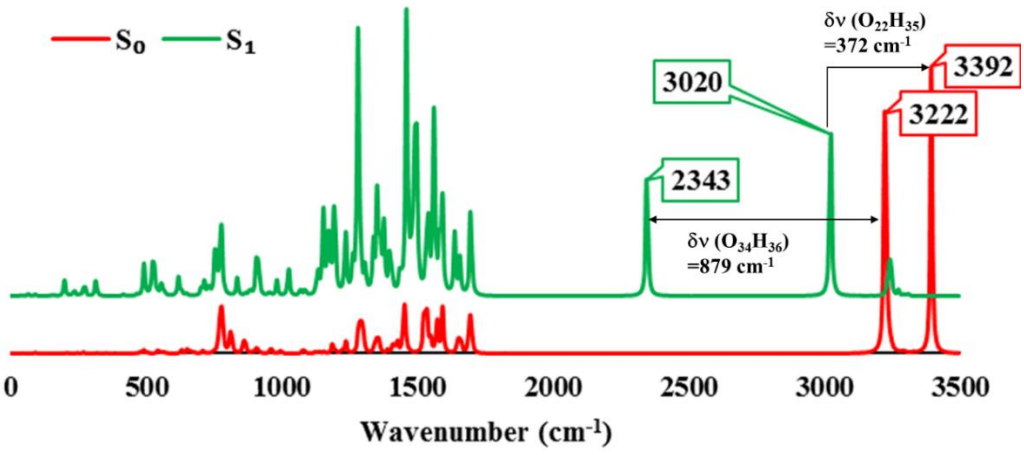

Figure 6.27 FTIR spectra of compound **9B** in S_0, and S_1 states

Likewise, the FTIR signal of O_{34}—H_{36} was determined with the redshift of 879 cm^{-1} to 2343 cm^{-1} at S_1 state. The relatively large red-shift in FTIR signals on photoexcitation

$S_0 \rightarrow S_1$ implied that the IraHBs (OH···N (I) and OH···N (II)) were more strengthened at S_1 state compared to S_0 state.

6.3.2.4 AIM analysis

Further, the prerequisite condition of IraHBs existing within key conformer, for the presence of ESIPT was also recognized *via* effective and well-established Popelier criteria using Bader's quantum theory of atoms in molecules (QTAIM).[122] The existence of hydrogen bonding was examined by critical bond points (BCPs) based on Popelier criteria. The topological properties of the BCPs for IraHBs were examined for stability and strength of the interactions. The determined topological parameters were within the limit of criteria and thus, established two IraHBs as $O_{22}H_{35}\cdots N_8$ (I) and $O_{34}H_{36}\cdots N_4$ (II) at S_0, and S_1 state for the primary structure of **9B** (Table 6.11). The determined BCPs were of (3,-1) types. The positive value of Laplacian of electron density [$\nabla^2\rho(r_c)$] for normal form of **9B** depicted electrostatic close shell interaction at S_0 and S_1 states. It was noted that the $\nabla^2\rho(r_c)$ for O—H···N (I/II) interactions was increased for S_1 state relative to S_0 state, which signified the strengthening of IraHBs. The degree of covalency and strength of the IraHBs interactions were characterized according to Rozas' rules. Therefore, all the listed BCPs has been ascertained as medium-range interactions with the partial covalent character at S_0, and S_1 states (Table 3.3**)**.[123] Moreover, the hydrogen bond energy was determined by Espinosa equation[111] and determined to be -11.58 kcalmol^{-1} and -13.08 kcalmol^{-1} for $O_{22}H_{35}\cdots N_8$ (I) and $O_{34}H_{36}\cdots N_4$ (II), respectively at S_0 state. However, on photoexcitation to S_1 state, the $O_{22}H_{35}\cdots N_8$ (I) and $O_{34}H_{36}\cdots N_4$ (II) IraHBs were strengthened to -16.22 kcalmol^{-1}, and -28.90 kcalmol$^{-1,}$ respectively. The molecular graph of **9B** was presented in along with BCPs (Figure 6.28).

Table 6.11 Topology parameters electron density(ρ), Laplacian electron density ($\nabla^2\rho$), potential energy density [V(r)], total energy density [H(r)], hydrogen bonding energy [E_{HB}(kcalmol^{-1})] at bond critical point of non-covalent interactions (D···HA) for conformer **9B** at ωb97-XD/6-31+G**

	Interaction	**$\nabla^2\rho$**	**V(r)**	**G(r)**	**H(r)**	**E_{HB}**
S_0	$O_{22}H_{35}\cdots N_8$ (I)	0.1206	-0.0369	0.0335	-0.0036	-11.58
	$O_{34}H_{36}\cdots N_4$ (II)	0.1246	-0.0417	0.0364	-0.0053	-13.08
S_1	$O_{22}H_{35}\cdots N_8$ (I)	0.1347	-0.0517	0.0427	-0.0090	-16.22
	$O_{34}H_{36}\cdots N_4$ (II)	0.1001	-0.0921	0.0585	-0.0034	-28.90

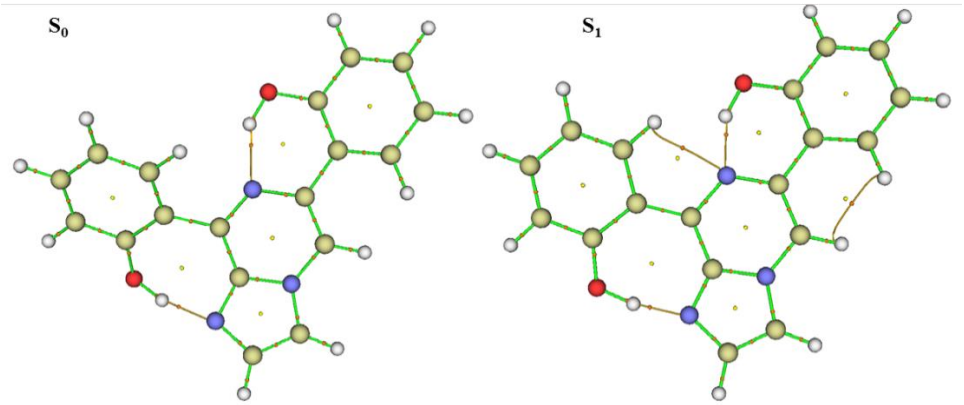

Figure 6.28 molecular graph of compound **9B**

6.3.2.5 Electronic Spectra and charge density difference

Further, the first six Frank-Condon (FC) excitations were calculated on the S_0 optimized structure to determine contributing vertical excitation, and the results were summarized in Table 6.12. In addition, electronic transition symmetry, the oscillation strength, and involved FMOs were summarized as an associated important parameter. The calculated spectroscopic data were in close agreement to experimental values. The electronic density distribution for the contributing molecular orbitals was discussed in the last section.

Table 6.12 The electronic excitation wavelength (nm/eV), oscillator strengths (f) and compositions of the low-lying singlet excited states of the compound **9B**

$S_0 \rightarrow S_n$	**Symmetry**	**λexp**	**λcalc**	**f**	**MOs (%)**	
$S_0 \rightarrow S_1$	Singlet-A	315/ 3.94	324.7/3.82	0.2955	H→L	85
$S_0 \rightarrow S_2$	Singlet-A		291.7/4.25	0.0592	H-1→L	58
$S_0 \rightarrow S_3$	Singlet-A		281.3/4.41	0.1322	H→L+1	62
$S_0 \rightarrow S_4$	Singlet-A	260/4.7 7	271.8/4.56	0.2995	H-3→L	30
					H-2→L	24
$S_0 \rightarrow S_5$	Singlet-A		256.7/4.83	0.1817	H-5→L	29

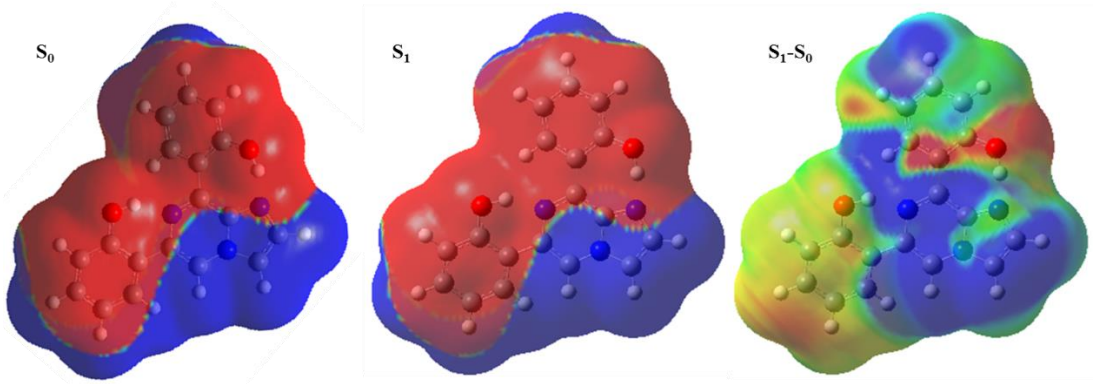

Figure 6.29. (a) The electrostatic potential of **9B** at S_0, S_1, and electron density difference map for (S_1-S_0).

However, the electrostatic potential (ESP) maps were plotted along with the difference in density at S_1 and S_0 state. The ESP maps displayed that the electron density shifted from phenyl units to the imidazo-pyrazine unit at S_0 and S_1 state. However, the difference in electron density map displayed that electron density on the hydrogen atoms decreased the shift of electron density at hydrogen donor atoms decreased, while it increased at hydrogen acceptor, and hence favor the ESIPT phenomenon.

6.3.2.6 Proton transfer mechanism

Further, the possible conversion of tautomeric forms was analyzed through PECs as a function of constrained bond lengths at ESIPT sites. As compound **9B** has two different kinds of IraHB sites, and which were strengthened at S_1 state. Therefore, the ESIPT phenomenon could take place through two sequential pathways. The path I involved the proton transfer, where the first H_{36} moved from O_{34} towards the N_4 to form EK1 and then H_{35} moved from O_{22} towards the N_8 to form KK. On the other hand, the path II followed the other way, where first H_{35} moved from O_{22} towards the N_8 to form EK2 and then H_{36} moved from O_{34} towards the N_4 to form KK.

The PECs were calculated for different tautomeric conversion as **9B→EK1→KK** (Path I) and **9B→EK2→KK** (Path II) using constraints on interacting distances for $O_{22}H_{35}\cdots N_8$ (I) and $O_{34}H_{36}\cdots N_4$ (II) respectively at S_0 and S_1 states. It was noted form PECs (Path I/II) calculated the high energy barrier for **9B→EK1, EK1→KK**, **9B→EK2, EK2→KK**, **9B→KK** at S_0 state (Figure 6.31, and Figure 6.32). However, the reverse tautomeric conversions **9B←EK1, EK1←KK**, **9B←EK2, EK2←KK**, **9B←KK** were barrier-less, and thus, no tautomeric form was converged to minima and their geometrical

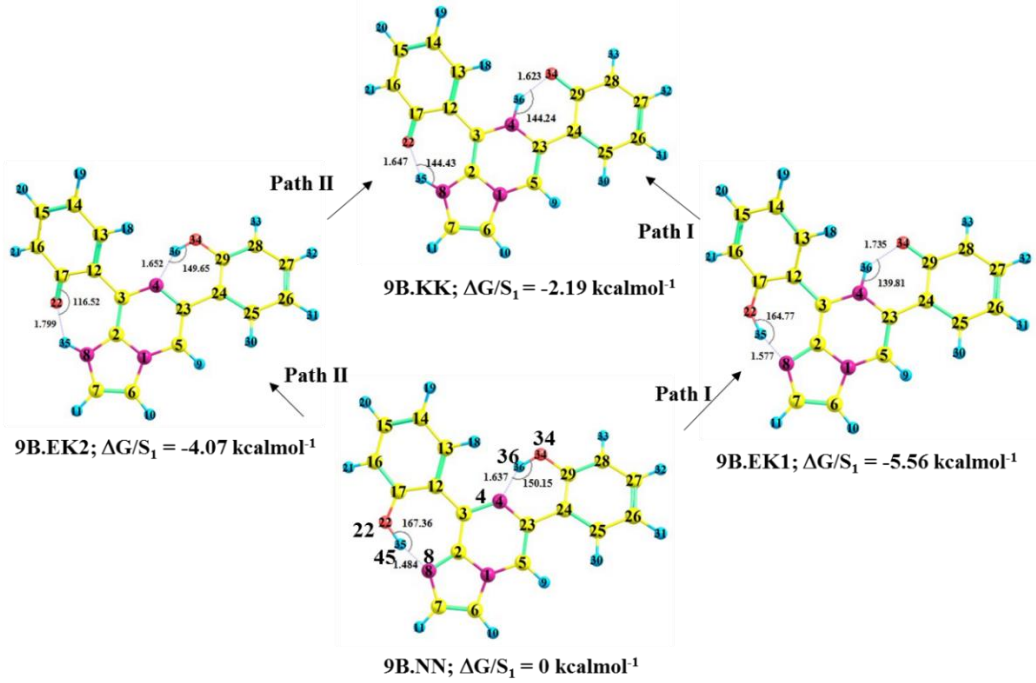

Figure 6.30 Pathways of proton transfer and tautomeric conversion of compound **9B**

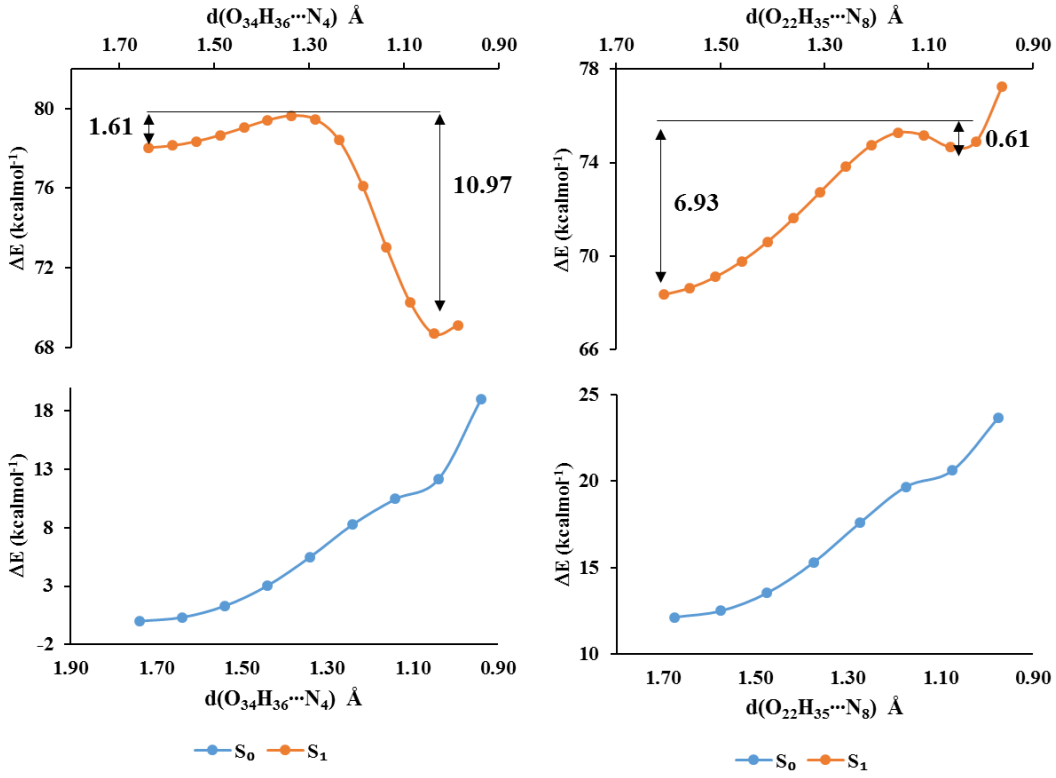

Figure 6.31 Energy profile of (**9B→EK1; EK1→KK)** tautomeric conversion at S_0, and S_1 states of compound **9B**

optimization lead to NN structure. Now moving towards S_1 state, the path I calculated the energy barrier of 1.61 kcalmol^{-1} and 6.93 kcalmol^{-1} for **9B→EK1** and **EK1→KK**

tautomeric conversion, respectively. While, **9B←EK1** and **EK1←KK** tautomeric conversion have an energy barrier of 10.97 kcalmol^{-1} and 0.61 kcalmol^{-1}, respectively (Figure 6.31). The low energy barrier for **9B→EK1** and **EK1←KK** depicted that only **9B→EK1** tautomeric conversion could be a feasible process through the path I.

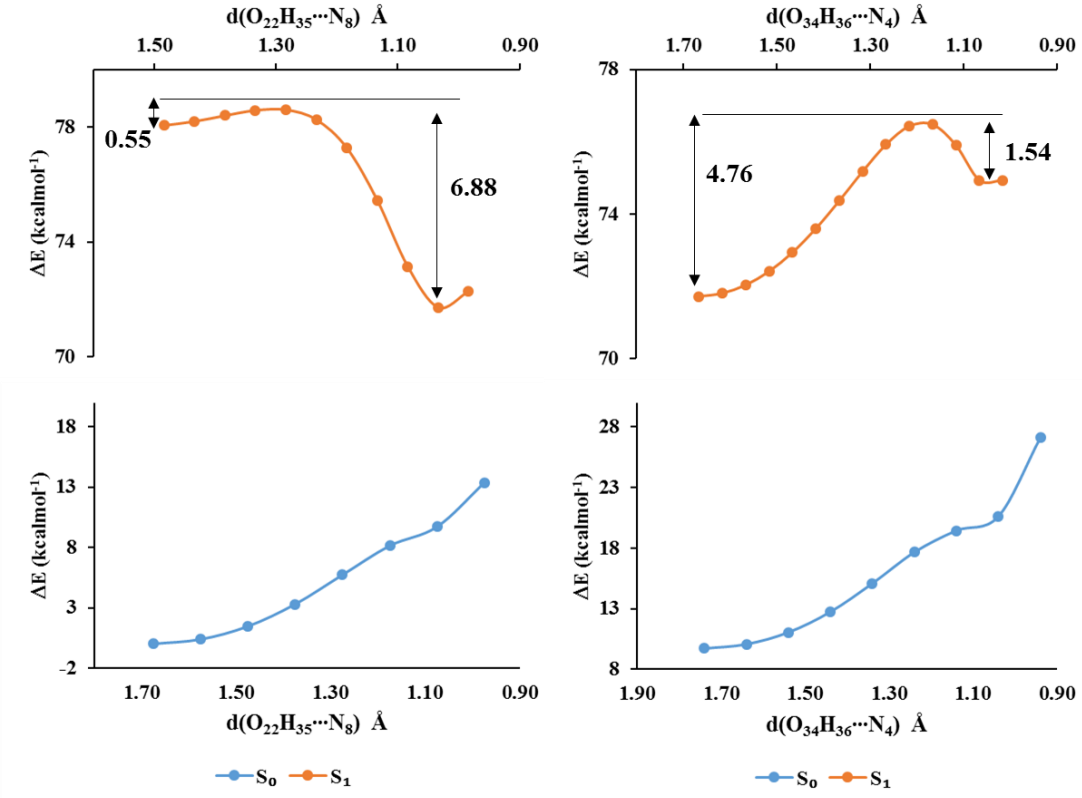

Figure 6.32 Energy profile of (**9B→EK2; EK2→KK)** tautomeric conversion at S_0, and S_1 states of compound **9B**

On the other hand, path II calculated the energy barrier of 0.55 kcalmol^{-1} and 6.88 kcalmol^{-1} for **9B→EK1** and **EK1→KK** tautomeric conversion, respectively. While, **9B←EK1** and **EK1←KK** tautomeric conversion have an energy barrier of 4.76 kcalmol^{-1} and 1.54 kcalmol^{-1}, respectively (Figure 6.32). The low energy barrier for **9B→EK2** and **EK2←KK** depicted that only **9B→EK2** tautomeric conversion could be a feasible process through path II. However, it could be noted that the **9B→EK1** and **9B→EK2** tautomeric conversion did not have considerable barrier difference. Therefore, the tautomeric forms **9B**, **EK1**, **EK2,** and **KK** were optimized for corrected free energy and determining the emission peaks. The relative free energy change (ΔG=G(S)-G (K); where S and K are the enol and keto tautomeric forms) predicted preference of the tautomeric conversion at S_1 state. The ΔG for **9B→KK**, **9B→EK1** and **9B→EK2** were determined

to be -2.20 kcalmol^{-1}, -5.56 kcalmol^{-1} and 4.07 kcalmol^{-1}, respectively. The calculated Boltzmann population depicted that the **EK1** would be more preferential tautomer at S_1 state. Also, the calculated vertical emission value ($S_1 \rightarrow S_0$) for **9B** and **EK1** were determined to be 418 nm, and 566 nm, respectively, which were in close agreement with the observed emission peak at 430 nm and 572 nm, respectively. On the other hand, the predicted emission peaks for **EK2** and **KK** were determined to be 510 nm, and 574 nm, respectively. Thus, it could be concluded that the **9B→EK1** tautomeric conversion is possible and results in dual emission.

6.3.3 Conclusion

In Summary, a novel compound enclosed double IraHB was studied for the origin of dual emission through ESIPT phenomenon. The compound exhibited dual emission at 420 nm and 570 nm with Stokes' shifts of 115 nm and 255 nm, respectively. The dual emission with large Stokes' shifts portrayed the excited state intramolecular proton transfer (ESIPT). The theoretical results also revealed the change in electron density on the frontier molecular orbitals (FMOs) and electron density difference map. The AIM calculation established the double IraHBs for **9B**, which strengthened on photoexcitation $S_0 \rightarrow S_1$. The results were endorsed through the redshifts in vibrational stretching of 879 cm^{-1} and 372 cm^{-1} for O_{34}—H_{36} and O_{22}—H_{35}, respectively. Further, the ESIPT was estimated through the PECs as a function of IraHBs distances and corrected for the free energy of tautomeric forms. The stabilization of **EK1** conformer at S_1 state drove the ESIPT. Also, the predicted emission of **9B** and **EK1** were in close agreement with the observed emission.

Summary of Chapter 6

In this chapter, asymmetrical systems containing intramolecular hydrogen bonding were studied. The first section involved the study of photophysical properties of quinoline based compound **7.** The compound **7** exhibited dual emission at 420 nm and 570 nm with Stokes' shifts of 60 nm and 210 nm, respectively. The dual emission with large Stokes' shifts and growth of absorption shoulder peak at ~400 nm in polarity system depicted the excited state intramolecular charge transfer (ESICT) coupled excited state intramolecular proton transfer (ESIPT). The theoretical results also revealed that the generation of ESIPT was attributed to ESICT owing to change in electron density on the frontier molecular orbitals (FMOs) and electron density difference map. Further, the ESIPT pathways study showed that the sequential proton transfer mechanism was followed with a small barrier for forwarding ESIPT.

The second section involved the study of synthesized and purified the rotameric conformations of mono/di-arylated substituted imidazo-[1,2-*a*]pyrazine. The PECs approach was used to investigate the fundamental structures of rotamers. The obtained rotameric forms were found to be stabilized by intramolecular hydrogen bond locking, which was further established and estimated by QTAIM analysis. The distinction in vibrational frequency, NMR signals, assisted to recognize the fundamental structure for different conformations.

The third section covered the photophysical properties of compound **9B**, which enclosed double IraHBs. The compound exhibited dual emission at 420 nm and 570 nm with Stokes' shifts of 115 nm and 255 nm, respectively. The theoretical results also revealed the change in electron density on the frontier molecular orbitals (FMOs) and electron density difference map. Further, the ESIPT was estimated through the PECs as a function of IraHBs distances and corrected for the free energy of tautomeric forms. The stabilization of **EK1** tautomer at S_1 state drove the ESIPT process.

Summary and scope of the thesis

Summary

In the present thesis, excited state intramolecular proton transfer phenomenon was explored along with other photophysical processes on different molecular architecture and results were summarized below;

1. Three symmetrical bis(diphenylmethylene)hydrazine-based Schiff bases as compound **2-4** have been synthesized and studied for ESIPT or ESICT phenomenon.
    i. Compound **2** and **3** displayed dual emission due to the ESIPT process.
    ii. The presence of electron-withdrawing ─NO_2 group in compound **3** ease the ESIPT process and thus, it displayed with dominant keto emission.
    iii. The presence of electron-donating ─NEt_2 group compound **4** ease the charge transfer over the proton transfer and thus, it displayed ESICT process.
2. The compound **2-4** have flexibility at azine linkage and single bonds, and therefore, these molecular systems raised the AIE effect
    i. Compound **2** and **3** strong AIE effect in 70-90% H_2O/CH_3CN solvent.
    ii. The presence of bulky ─NEt_2 group in compound **4** decreased the molecular motion, and therefore, compound 4 displayed weak AIE effect.
3. The heteroatoms of compound **2-4** provide the platform for coordination of the metal center and thus, resulted in tuned sensing of metal ions
    i. Compound **2** selectively detected Al^{3+} ions through ratiometric absorption and *turn-on* emission response in CH_3OH with a detection limit of 2.7×10^{-7} M.
    ii. Compound **3** detected Al^{3+} ions through ratiometric absorption and emission response in CH_3OH with a detection limit of 12 nM. Also, compound **3** displayed absorption and turn-off emission response towards Cu^{2+} ions with detection limit of 120 nM.
    iii. Compound **4** selectively detected Zn^{2+} and Cu^{2+} through emission *turn-on* and turn-off response, respectively. The detection limit towards Zn^{2+} and Cu^{2+} ion were 0.5 nM and 6.5 nM, respectively.

4. Two naphthalimide-based Schiff bases as compound **5** and **6** were studied for the origin of large Stokes' shifted emissions and chromo-fluorescent sensing properties

    i. Compound **5** exhibited large Stokes' shifted emission originated from the ESIPT process

    ii. Compound **6** exhibited dual emission and the presence of ─NEt_2 group displayed solvatochromism effect. The photophysical behavior was originated due to ESTICT/ESIPT process

    iii. Compound **6** displayed selective chromo-fluorescent response towards Al^{3+} and F^- ions with a detection limit of 2×10^{-7} M and 7.5×10^{-7} M, respectively.

5. Asymmetrical molecular systems were synthesized and studied for photophysical behavior

    i. Quinoline-benzimidazole based compound **7** displayed dual emission, and significant Stokes' shifts originated from the ESICT/ESIDPT process

    ii. The structures of rotameric conformations of asymmetrical mono-arylated imidazo-[1,2-*a*]pyrazine (**8A** and **8B**) and di-arylated imidazo-[1,2-*a*]pyrazine (**9A** and **9B**) were studied for structure elucidation through correlation of experimental and theoretical results

    iii. Di-arylated imidazo-[1,2-a]pyrazine **9B** containing asymmetrical double IraHB exhibited dual emission which was originated from the ESIPT process

Scope

In the present thesis, ESIPT or/and ESICT process were explored on different molecular architecture with diverse functionality. Symmetrical bis(diphenylmethylene)hydrazine-based Schiff bases were demonstrated for ESIPT/ESICT, AIE phenomenon, and sensing properties. Further, naphthalimide-based systems were established for ESICT/ ESIPT processes. Theoretical study of asymmetrical molecular systems depicted that the ESIPT phenomenon could be triggered another ESIPT phenomenon and lead broad Stokes' shifted emission.

Furthermore, incorporation of ESIPT phenomenon on AIE active moieties to have two phenomena on single platform displayed wise spectral window. Such systems have the advantage of high emission with large Stokes' shift even at higher concentration

Therefore, heterocyclic-based chromo-fluorophores based could be tuned for variable absorption and emission properties. The structural modification, structural constraints, optimization of conjugation, etc. could integrate the flow for charge transfer and thus, tuning of emission properties to visible region, have application in tissue imaging and OLEDs, etc. On the other hand, UV-light absorbing molecules with large Stokes' shifted emission could be used to design organo-electronic devices, where harmful UV-light could be converted to fruitful energy source. The incorporation of ESIPT mechanism over the core moiety with potential biological/drug application could be used for multi-task purposes such as live-cell imaging, biomarkers, etc. Theoretical insights may lead better insight into the phenomenon

REFERENCES

1. S. Park, J. E. Kwon and S. Y. Park, *Phys. Chem. Chem. Phys.*, 2012, **14**, 8878-8884.
2. D. R. Weinberg, C. J. Gagliardi, J. F. Hull, C. F. Murphy, C. A. Kent, B. C. Westlake, A. Paul, D. H. Ess, D. G. McCafferty and T. J. Meyer, *Chem. Rev.*, 2012, **112**, 4016-4093.
3. S. Hayashi, E. Tajkhorshid and K. Schulten, *Biophys. J.*, 2002, **83**, 1281-1297.
4. D. Jacquemin, J. Zuniga, A. Requena and J. P. Céron-Carrasco, *Acc. Chem. Res.*, 2014, **47**, 2467-2474.
5. P. J. Tonge and S. R. Meech, *J. Photochem. Photobiol., A*, 2009, **205**, 1-11.
6. P. Chou, D. McMorrow, T. Aartsma and M. Kasha, *J. Phys. Chem.*, 1984, **88**, 4596-4599.
7. J. Zhao, S. Ji, Y. Chen, H. Guo and P. Yang, *Phys. Chem. Chem. Phys.*, 2012, **14**, 8803-8817.
8. H.-W. Tseng, J.-Q. Liu, Y.-A. Chen, C.-M. Chao, K.-M. Liu, C.-L. Chen, T.-C. Lin, C.-H. Hung, Y.-L. Chou and T.-C. Lin, *J. Phys. Chem. Lett.*, 2015, **6**, 1477-1486.
9. J. E. Kwon and S. Y. Park, *Adv. Mater.*, 2011, **23**, 3615-3642.
10. C.-C. Hsieh, C.-M. Jiang and P.-T. Chou, *Acc. Chem. Res.*, 2010, **43**, 1364-1374.
11. A. P. Demchenko, K.-C. Tang and P.-T. Chou, *Chem. Soc. Rev.*, 2013, **42**, 1379-1408.
12. C. Azarias, Š. Budzák, A. D. Laurent, G. Ulrich and D. Jacquemin, *Chem. Sci.*, 2016, **7**, 3763-3774.
13. L. Cui, Y. Baek, S. Lee, N. Kwon and J. Yoon, *J. Mater. Chem. C*, 2016, **4**, 2909-2914.
14. L. Chen, D. Wu, J.-M. Kim and J. Yoon, *Anal. Chem.*, 2017, **89**, 12596-12601.
15. N. Suzuki, K. Suda, D. Yokogawa, H. Kitoh-Nishioka, S. Irle, A. Ando, L. M. Abegao, K. Kamada, A. Fukazawa and S. Yamaguchi, *Chem. Sci.*, 2018, **9**, 2666-2673.
16. J. Massue, D. Jacquemin and G. Ulrich, *Chem. Lett.*, 2018, **47**, 1083-1089.
17. A. C. Sedgwick, L. Wu, H.-H. Han, S. D. Bull, X.-P. He, T. D. James, J. L. Sessler, B. Z. Tang, H. Tian and J. Yoon, *Chem. Soc. Rev.*, 2018, **47**, 8842-8880.
18. M. H. Lee, J. S. Kim and J. L. Sessler, *Chem. Soc. Rev.*, 2015, **44**, 4185-4191.
19. L. Peng, S. Xu, X. Zheng, X. Cheng, R. Zhang, J. Liu, B. Liu and A. Tong, *Anal. Chem.*, 2017, **89**, 3162-3168.

20. V. S. Padalkar and S. Seki, *Chem. Soc. Rev.*, 2016, **45**, 169-202.

21. P. M. Vérité, C. A. Guido and D. Jacquemin, *Phys. Chem. Chem. Phys.*, 2019, **21**, 2307-2317.

22. K.-C. Tang, M.-J. Chang, T.-Y. Lin, H.-A. Pan, T.-C. Fang, K.-Y. Chen, W.-Y. Hung, Y.-H. Hsu and P.-T. Chou, *J. Am. Chem. Soc.*, 2011, **133**, 17738-17745.

23. C. Fang, R. R. Frontiera, R. Tran and R. A. Mathies, *Nature*, 2009, **462**, 200-204.

24. F. Han, W. Liu and C. Fang, *Chem. Phys.*, 2013, **422**, 204-219.

25. W. Liu, Y. Wang, L. Tang, B. G. Oscar, L. Zhu and C. Fang, *Chem. Sci.*, 2016, **7**, 5484-5494.

26. X. Peng, Y. Wu, J. Fan, M. Tian and K. Han, *J. Org. Chem.*, 2005, **70**, 10524-10531.

27. K.-S. Lee, H.-J. Kim, G.-H. Kim, I. Shin and J.-I. Hong, *Org. Lett.*, 2008, **10**, 49-51.

28. Y. Bao, B. Liu, H. Wang, J. Tian and R. Bai, *Chem. Commun.*, 2011, **47**, 3957-3959.

29. G.-J. Zhao and K.-L. Han, *Acc. Chem. Res.*, 2011, **45**, 404-413.

30. H.-W. Tseng, T.-C. Lin, C.-L. Chen, T.-C. Lin, Y.-A. Chen, J.-Q. Liu, C.-H. Hung, C.-M. Chao, K.-M. Liu and P.-T. Chou, *Chem. Commun.*, 2015, **51**, 16099-16102.

31. T. Mutai, H. Sawatani, T. Shida, H. Shono and K. Araki, *J. Org. Chem.*, 2013, **78**, 2482-2489.

32. C. Prommin, N. Kanlayakan, W. Chansen, R. Salaeh, K. Kerdpol, R. Daengngern and N. Kungwan, *J. Phys. Chem. A*, 2017, **121**, 5773-5784.

33. J. Zhao, X. Liu and Y. Zheng, *J. Phys. Chem. A*, 2017, **121**, 4002-4008.

34. A. J. Stasyuk, P. J. Cywiński and D. T. Gryko, *J. Photochem. Photobiol., C*, 2016, **28**, 116-137.

35. E. C. Gentry and R. R. Knowles, *Acc. Chem. Res.*, 2016, **49**, 1546-1556.

36. S. Hammes-Schiffer, *J. Am. Chem. Soc.*, 2015, **137**, 8860-8871.

37. Y. M. Cheng, S. C. Pu, C. J. Hsu, C. H. Lai and P. T. Chou, *ChemPhysChem*, 2006, **7**, 1372-1381.

38. M. Gutierrez, N. Alarcos, M. Liras, F. l. Sánchez and A. Douhal, *J. Phys. Chem. B*, 2015, **119**, 552-562.

39. W.-C. Lin, S.-K. Fang, J.-W. Hu, H.-Y. Tsai and K.-Y. Chen, *Anal. Chem.*, 2014, **86**, 4648-4652.

40. M. Savarese, É. Brémond, C. Adamo, N. Rega and I. Ciofini, *ChemPhysChem*, 2016, **17**, 1530-1538.

41. M. Kuss-Petermann, M. Orazietti, M. Neuburger, P. Hamm and O. S. Wenger, *J. Am. Chem. Soc.*, 2017, **139**, 5225-5232.

42. Y. Niu, R. Wang, P. Shao, Y. Wang and Y. Zhang, *Chem. - Eur. J.*, 2018, **24**, 16670-16676.

43. Q. Wang, L. Xu, Y. Niu, Y. Wang, M. S. Yuan and Y. Zhang, *Asian J. Chem.*, 2016, **11**, 3454-3464.

44. D. Yang, G. Yang, M. Jia, X. Song, Q. Zhang, T. Zhang and H. Gao, *RSC Adv.*, 2018, **8**, 29662-29669.

45. S. Mitra and N. Tamai, *Phys. Chem. Chem. Phys.*, 2003, **5**, 4647-4652.

46. J.-W. Hu, H.-Y. Tsai, S.-K. Fang, C.-W. Chang, L.-C. Wang and K.-Y. Chen, *Dyes Pigm.*, 2017, **145**, 493-504.

47. L. Gutiérrez-Arzaluz, F. Cortés-Guzmán, T. Rocha-Rinza and J. Peón, *Phys. Chem. Chem. Phys.*, 2015, **17**, 31608-31612.

48. P. Alam, V. Kachwal and I. R. Laskar, *Sens. Actuators, B*, 2016, **228**, 539-550.

49. L. Yan, T. Qing, R. Li, Z. Wang and Z. Qi, *RSC Adv.*, 2016, **6**, 63874-63879.

50. M. Ziółek, K. Filipczak and A. Maciejewski, *Chem. Phys. Lett.*, 2008, **464**, 181-186.

51. M. Ziółek, J. Kubicki, A. Maciejewski, R. Naskręcki and A. Grabowska, *Phys. Chem. Chem. Phys.*, 2004, **6**, 4682-4689.

52. X. Ma, J. Cheng, J. Liu, X. Zhou and H. Xiang, *New J. Chem.*, 2015, **39**, 492-500.

53. S. Jana, S. Dalapati and N. Guchhait, *J. Phys. Chem. A*, 2012, **116**, 10948-10958.

54. X. Chen, R. Wei, Y. Xiang, Z. Zhou, K. Li, P. Song and A. Tong, *J. Phys. Chem. C*, 2011, **115**, 14353-14359.

55. W. Tang, Y. Xiang and A. Tong, *J. Org. Chem.*, 2009, **74**, 2163-2166.

56. H. Liu, R. Wei, Y. Xiang and A. Tong, *Anal. Methods*, 2015, **7**, 753-758.

57. H. Zhou, B. Yang, G. Wen, X. Hu and B. Liu, *Talanta*, 2018, **184**, 394-403.

58. L. Peng, Z. Zhou, R. Wei, K. Li, P. Song and A. Tong, *Dyes Pigm.*, 2014, **108**, 24-31.

59. L. Peng, L. Xiao, Y. Ding, Y. Xiang and A. Tong, *J. Mater. Chem. B*, 2018, **6**, 3922-3926.

60. H. Song, Y. Zhou, H. Qu, C. Xu, X. Wang, X. Liu, Q. Zhang and X. Peng, *Ind. Eng. Chem. Res.*, 2018, **57**, 15216-15223.

61. X. Yao, J. X. Ru, C. Xu, Y. M. Liu, W. Dou, X. L. Tang, G. L. Zhang and W. S. Liu, *ChemistryOpen*, 2015, **4**, 478-482.

62. H. Xiao, K. Chen, D. Cui, N. Jiang, G. Yin, J. Wang and R. Wang, *New J. Chem.*, 2014, **38**, 2386-2393.

63. J. Hao and Y. Yang, *Org. Chem. Front.*, 2018, **5**, 1330-1341.

64. R. Wei, P. Song and A. Tong, *J. Phys. Chem. C*, 2013, **117**, 3467-3474.

65. L. Peng, R. Wei, K. Li, Z. Zhou, P. Song and A. Tong, *Analyst*, 2013, **138**, 2068-2072.

66. L. Peng, Z. Zhou, X. Wang, R. Wei, K. Li, Y. Xiang and A. Tong, *Anal. Chim. Acta*, 2014, **829**, 54-59.

67. Y. H. Zhao, Y. Luo, H. Wang, T. Guo, H. Zhou, H. Tan, Z. Zhou, Y. Long and Z. Tang, *ChemistrySelect*, 2018, **3**, 1521-1526.

68. J.-S. Ni, M. M. Lee, P. Zhang, C. Gui, Y. Chen, D. Wang, Z.-Q. Yu, R. T. Kwok, J. W. Lam and B. Z. Tang, *Anal. Chem.*, 2018, **91**, 2169-2176.

69. Y.-K. La, J.-A. Hong, Y.-J. Jeong and J. Lee, *RSC Adv.*, 2016, **6**, 84098-84105.

70. Y. Fu, C. Fan, G. Liu and S. Pu, *Sens. Actuators, B*, 2017, **239**, 295-303.

71. X. Yuan, C.-X. Zhao, Y.-X. Lu, Y.-J. Shen and C.-Y. Wang, *J. Photochem. Photobiol., A*, 2018, **361**, 41-47.

72. G. He, Q. Meng, X. Zhao, C. He, P. Zhou and C. Duan, *Inorg. Chem. Commun.*, 2016, **65**, 28-31.

73. N. Gupta, T. Kaur, V. Bhalla, R. D. Parihar, P. Ohri, G. Kaur and M. Kumar, *Chem. Commun.*, 2017, **53**, 12646-12649.

74. T. Mutai, T. Muramatsu, I. Yoshikawa, H. Houjou and M. Ogura, *Org. Lett.*, 2019, **21**, 2143-2146.

75. P. Wnuk, G. Burdziński, M. Sliwa, M. Kijak, A. Grabowska, J. Sepioł and J. Kubicki, *Phys. Chem. Chem. Phys.*, 2014, **16**, 2542-2552.

76. Y. Hao and Y. Chen, *Dyes Pigm.*, 2016, **129**, 186-190.

77. S. Park, J. E. Kwon and S. Y. Park, *Phys. Chem. Chem. Phys.*, 2012, **14**, 8878-8884.

78. G.-Y. Li and T. Chu, *Phys. Chem. Chem. Phys.*, 2011, **13**, 20766-20771.

79. A. J. Stasyuk, Y.-T. Chen, C.-L. Chen, P.-J. Wu and P.-T. Chou, *Phys. Chem. Chem. Phys.*, 2016, **18**, 24428-24436.

80. J. Seo, S. Kim and S. Y. Park, *J. Am. Chem. Soc.*, 2004, **126**, 11154-11155.

81. H. Singh, R. Sharma, G. Bhargava, S. Kumar and P. Singh, *New J. Chem.*, 2018, **42**, 12900-12907.

82. P. Singh, H. Singh, R. Sharma, G. Bhargava and S. Kumar, *J. Mater. Chem. C*, 2016, **4**, 11180-11189.

83. R. Ali, S. S. Razi, P. Srivastava and A. Misra, *Sens. Actuators, B*, 2015, **221**, 1236-1247.

84. N. Qiao, N.-N. Wei, J. Zhang and C. Hao, *New J. Chem.*, 2018, **42**, 11804-11810.

85. A. S. Gupta, K. Paul and V. Luxami, *Sens. Actuators, B*, 2017, **246**, 653-661.

86. A. S. Gupta, K. Paul and V. Luxami, *ChemistrySelect*, 2017, **2**, 800-804.

87. A. S. Gupta, A. Garg, K. Paul and V. Luxami, *J. Lumin.*, 2016, **173**, 165-170.

88. V. Luxami and S. Kumar, *RSC Adv.*, 2012, **2**, 8734.

89. Y. Zhang, K. de La Harpe, A. A. Beckstead, R. Improta and B. Kohler, *J. Am. Chem. Soc.*, 2015, **137**, 7059-7062.

90. J. Zhang, Q. Zhang, T. T. Vo, D. A. Parrish and J. n. M. Shreeve, *J. Am. Chem. Soc.*, 2015, **137**, 1697-1704.

91. C. Li, Y. Yang, D. Li and Y. Liu, *Phys. Chem. Chem. Phys.*, 2017, **19**, 4802-4808.

92. K. Röttger, H. J. Marroux, M. P. Grubb, P. M. Coulter, H. Böhnke, A. S. Henderson, M. C. Galan, F. Temps, A. J. Orr-Ewing and G. M. Roberts, *Angew. Chem. Int. Ed.*, 2015, **54**, 14719-14722.

93. H. Tachikawa and H. Kawabata, *J. Phys. Chem. A*, 2016, **120**, 1529-1535.

94. P. Yin, D. A. Parrish and J. n. M. Shreeve, *J. Am. Chem. Soc.*, 2015, **137**, 4778-4786.

95. A. S. Gupta, K. Paul and V. Luxami, *Spectrochim. Acta, Part A*, 2015, **138**, 67-72.

96. A. R. Fersht, J.-P. Shi, J. Knill-Jones, D. M. Lowe, A. J. Wilkinson, D. M. Blow, P. Brick, P. Carter, M. M. Waye and G. Winter, *Nature*, 1985, **314**, 235-238.

97. R. Rani, G. Kumar, K. Paul and V. Luxami, *New J. Chem.*, 2018, **42**, 12729-12736.

98. C. Niu, L. Zhao, T. Fang, X. Deng, H. Ma, J. Zhang, N. Na, J. Han and J. Ouyang, *Langmuir*, 2014, **30**, 2351-2359.

99. J. E. Kwon and S. Y. Park, *Adv. Mater.*, 2011, **23**, 3615-3642.

100. H. T. Feng and Y. S. Zheng, *Chemistry*, 2014, **20**, 195-201.

101. D. Wu, A. C. Sedgwick, T. Gunnlaugsson, E. U. Akkaya, J. Yoon and T. D. James, *Chem. Soc. Rev.*, 2017, **46**, 7105-7123.

102. J. L. Atwood, *Comprehensive Supramolecular Chemistry II*, Elsevier2017.

103. J. Tirado-Rives and W. L. Jorgensen, *J. Chem. Theory Comput.*, 2008, **4**, 297-306.

104. T. Yanai, D. P. Tew and N. C. Handy, *Chem. Phys. Lett.*, 2004, **393**, 51-57.

105. O. A. Vydrov and G. E. Scuseria, *J. Chem. Phys.*, 2006, **125**, 234109.

106. T. Schwabe and S. Grimme, *Phys. Chem. Chem. Phys.*, 2007, **9**, 3397-3406.

107. M. Dierksen and S. Grimme, *J. Chem. Phys.*, 2005, **122**, 244101-244109.

108. U. Koch and P. L. Popelier, *J. Phys. Chem.*, 1995, **99**, 9747-9754.

109. R. F. Bader, *Acc. Chem. Res.*, 1985, **18**, 9-15.

110. P. Popelier, F. Aicken and S. O'Brien, *Chemical Modelling: Applications and Theory*, 2000, **1**, 143-198.

111. E. Espinosa, E. Molins and C. Lecomte, *Chem. Phys. Lett.*, 1998, **285**, 170-173.

112. M. J. Frisch and A. B. Nielsen, *Gaussian 03 Programmer's Reference*, Gaussian2003.

113. M. J. Frisch, G. W. Trucks, H. B. Schlegel, G. E. Scuseria, M. A. Robb, J. R. Cheeseman, G. Scalmani, V. Barone, G. A. Petersson, H. Nakatsuji, X. Li, M. Caricato, A. V. Marenich, J. Bloino, B. G. Janesko, R. Gomperts, B. Mennucci, H. P. Hratchian, J. V. Ortiz, A. F. Izmaylov, J. L. Sonnenberg, Williams, F. Ding, F. Lipparini, F. Egidi, J. Goings, B. Peng, A. Petrone, T. Henderson, D. Ranasinghe, V. G. Zakrzewski, J. Gao, N. Rega, G. Zheng, W. Liang, M. Hada, M. Ehara, K. Toyota, R. Fukuda, J. Hasegawa, M. Ishida, T. Nakajima, Y. Honda, O. Kitao, H. Nakai, T. Vreven, K. Throssell, J. A. Montgomery Jr., J. E. Peralta, F. Ogliaro, M. J. Bearpark, J. J. Heyd, E. N. Brothers, K. N. Kudin, V. N. Staroverov, T. A. Keith, R. Kobayashi, J. Normand, K. Raghavachari, A. P. Rendell, J. C. Burant, S. S. Iyengar, J. Tomasi, M. Cossi, J. M. Millam, M. Klene, C. Adamo, R. Cammi, J. W. Ochterski, R. L. Martin, K. Morokuma, O. Farkas, J. B. Foresman and D. J. Fox, Wallingford, CT2016.

114. A. Frisch, *Wallingford, USA, 25p*, 2009.

115. G. Zhurko and D. Zhurko, *Lite version build*, 2005, **8**, 2005.

116. R. Dennington, T. Keith, J. Millam, K. Eppinnett, W. L. Hovell and R. Gilliland, Version2009.

117. M. Suresh, A. K. Mandal, S. Saha, E. Suresh, A. Mandoli, R. Di Liddo, P. P. Parnigotto and A. Das, *Org. Lett.*, 2010, **12**, 5406-5409.

118. S. Goswami, S. Das, K. Aich, B. Pakhira, S. Panja, S. K. Mukherjee and S. Sarkar, *Org. Lett.*, 2013, **15**, 5412-5415.

119. J. Shinar and R. Shinar, *J. Phys. D: Appl. Phys.*, 2008, **41**, 133001.

120. Y. Nagai, H. Sasabe, J. Takahashi, N. Onuma, T. Ito, S. Ohisa and J. Kido, *J. Mater. Chem. C*, 2017, **5**, 527-530.

121. S. K. Lanke and N. Sekar, *Dyes Pigm.*, 2016, **124**, 82-92.

122. U. Koch and P. Popelier, *The Journal of Physical Chemistry*, 1995, **99**, 9747-9754.

123. I. Rozas, I. Alkorta and J. Elguero, *J. Am. Chem. Soc.*, 2000, **122**, 11154-11161.

124. H.-J. Schneider and A. K. Yatsimirsky, *Principles and Methods in Supramolecular Chemistry*, J. Wiley2000.

125. J. Wu, W. Liu, J. Ge, H. Zhang and P. Wang, *Chem Soc Rev*, 2011, **40**, 3483-3495.

126. Z. G. Chi, X. Q. Zhang, B. J. Xu, X. Zhou, C. P. Ma, Y. Zhang, S. W. Liu and J. R. Xu, *Chem. Soc. Rev.*, 2012, **41**, 3878-3896.

127. Z. C. Hu, B. J. Deibert and J. Li, *Chem. Soc. Rev.*, 2014, **43**, 5815-5840.

128. J. Z. Liu, J. W. Y. Lam and B. Z. Tang, *Chem. Rev.*, 2009, **109**, 5799-5867.

129. Y. N. Hong, J. W. Y. Lam and B. Z. Tang, *Chem. Soc. Rev.*, 2011, **40**, 5361-5388.

130. Y. Hong, J. W. Lam and B. Z. Tang, *Chem. Commun.*, 2009, 4332-4353.

131. H. Deol, S. Pramanik, M. Kumar, I. A. Khan and V. Bhalla, *ACS Catal.*, 2016, **6**, 3771-3783.

132. R. T. Kwok, C. W. Leung, J. W. Lam and B. Z. Tang, *Chem. Soc. Rev.*, 2015, **44**, 4228-4238.

133. D. Ding, K. Li, B. Liu and B. Z. Tang, *Acc. Chem. Res.*, 2013, **46**, 2441-2453.

134. J. Chen, Y. Wang, W. Li, H. Zhou, Y. Li and C. Yu, *Anal. Chem.*, 2014, **86**, 9866-9872.

135. J. Mei, N. L. Leung, R. T. Kwok, J. W. Lam and B. Z. Tang, *Chem. Rev.*, 2015, **115**, 11718-11940.

136. J. Mei, Y. N. Hong, J. W. Y. Lam, A. J. Qin, Y. H. Tang and B. Z. Tang, *Adv. Mater.*, 2014, **26**, 5429-5479.

137. N. B. Shustova, B. D. McCarthy and M. Dinca, *J. Am. Chem. Soc.*, 2011, **133**, 20126-20129.

138. M. Wang, G. Zhang, D. Zhang, D. Zhu and B. Z. Tang, *J. Mater. Chem.*, 2010, **20**, 1858-1867.

139. Z. Li, Y. Q. Dong, J. W. Lam, J. Sun, A. Qin, M. Häußler, Y. P. Dong, H. H. Sung, I. D. Williams and H. S. Kwok, *Adv. Funct. Mater.*, 2009, **19**, 905-917.

140. M. A. Rauf, S. Hisaindee and N. Saleh, *RSC Adv.*, 2015, **5**, 18097-18110.

141. J. S. Wu, W. M. Liu, J. C. Ge, H. Y. Zhang and P. F. Wang, *Chem. Soc. Rev.*, 2011, **40**, 3483-3495.

142. S. S. Babu, V. K. Praveen and A. Ajayaghosh, *Chem. Rev.*, 2014, **114**, 1973-2129.

143. J. Mei, N. L. C. Leung, R. T. K. Kwok, J. W. Y. Lam and B. Z. Tang, *Chem. Rev.*, 2015, **115**, 11718-11940.

144. Y. N. Hong, J. W. Y. Lam and B. Z. Tang, *Chem. Commun.*, 2009, 4332-4353.

145. D. Jana, S. Boxi, P. P. Parui and B. K. Ghorai, *Org. Biomol. Chem.*, 2015, **13**, 10663-10674.

146. Z. Song, R. T. Kwok, E. Zhao, Z. He, Y. Hong, J. W. Lam, B. Liu and B. Z. Tang, *ACS Appl Mater Interfaces*, 2014, **6**, 17245-17254.

147. P. Singh, H. Singh, R. Sharma, G. Bhargava and S. Kumar, *J. Mater. Chem. C*, 2016, **4**, 11180-11189.

148. A. Kundu, P. S. Hariharan, K. Prabakaran, D. Moon and S. P. Anthony, *Cryst. Growth Des.*, 2016, **16**, 3400-3408.

149. A. Malakar, M. Kumar, A. Reddy, H. T. Biswal, B. B. Mandal and G. Krishnamoorthy, *Photochem. Photobiol. Sci.*, 2016, **15**, 937-948.

150. R. Tandon, V. Luxami, H. Kaur, N. Tandon and K. Paul, *Chem. Rec.*, 2017, **17**, 956-993.

151. B. Zhu, C. Gao, Y. Zhao, C. Liu, Y. Li, Q. Wei, Z. Ma, B. Du and X. Zhang, *Chem. Commun.*, 2011, **47**, 8656-8658.

152. N. I. Georgiev, M. D. Dimitrova, Y. D. Todorova and V. B. Bojinov, *Dyes Pigm.*, 2016, **131**, 9-17.

153. J. Shi, Y. Wang, X. Tang, W. Liu, H. Jiang, W. Dou and W. Liu, *Dyes Pigm.*, 2014, **100**, 255-260.

154. W. Chai and R. Jin, *J. Mol. Struct.*, 2016, **1103**, 177-182.

155. L. Tong and Y. Qian, *J. Photochem. Photobiol., A*, 2019, **368**, 62-69.

156. J. F. Zhang, S. Kim, J. H. Han, S.-J. Lee, T. Pradhan, Q. Y. Cao, S. J. Lee, C. Kang and J. S. Kim, *Org. Lett.*, 2011, **13**, 5294-5297.

157. Y. Wang, P.-D. Mao, W.-N. Wu, X.-J. Mao, X.-L. Zhao, Z.-Q. Xu, Y.-C. Fan and Z.-H. Xu, *Sens. Actuators, B*, 2017, **251**, 813-820.

158. C. Hou, A. M. Urbanec and H. Cao, *Tetrahedron Lett.*, 2011, **52**, 4903-4905.

159. P. V. Krasteva, M. D. Dimitrova, N. I. Georgiev and V. B. Bojinov, *J. Chem. Technol. Metall.*, 2018, **53**, 150-158.

160. Y. Xu, S. Mao, H. Peng, F. Wang, H. Zhang, S. O. Aderinto and H. Wu, *J. Lumin.*, 2017, **192**, 56-63.

161. P. Alaei, S. Rouhani, K. Gharanjig and J. Ghasemi, *Spectrochim. Acta, Part A*, 2012, **90**, 85-92.

162. J.-S. Chen, R.-Z. Liu, Y. Yang and T.-S. Chu, *Theor. Chem. Acc.*, 2013, **133**, 1411.

163. R. M. Duke, E. B. Veale, F. M. Pfeffer, P. E. Kruger and T. Gunnlaugsson, *Chem. Soc. Rev.*, 2010, **39**, 3936-3953.

164. T. Gunnlaugsson, P. E. Kruger, P. Jensen, F. M. Pfeffer and G. M. Hussey, *Tetrahedron Lett.*, 2003, **44**, 8909-8913.

165. R. Goel, S. Sharma, K. Paul and V. Luxami, *Sens. Actuators, B*, 2017, **246**, 776-782.

166. X. Li, Y. Lin, Q. Wang, Y. Yuan, H. Zhang and X. Qian, *Eur. J. Med. Chem.*, 2011, **46**, 1274-1279.

167. R. Filosa, A. Peduto, S. Di Micco, P. de Caprariis, M. Festa, A. Petrella, G. Capranico and G. Bifulco, *Biorg. Med. Chem.*, 2009, **17**, 13-24.

168. S.-C. Chang, B. J. Archer, R. E. Utecht, D. E. Lewis, M. M. Judy and J. L. Matthews, *Bioorg. Med. Chem. Lett.*, 1993, **3**, 555-556.

169. G. Berger, J. Soubhye and F. Meyer, *Polym. Chem.*, 2015, **6**, 3559-3580.

170. C. Li, Y. Yang, D. Li and Y. Liu, *Phys. Chem. Chem. Phys.*, 2017, **19**, 4802-4808.

171. K.-C. Tang, C.-L. Chen, H.-H. Chuang, J.-L. Chen, Y.-J. Chen, Y.-C. Lin, J.-Y. Shen, W.-P. Hu and P.-T. Chou, *J. Phys. Chem. Lett.*, 2011, **2**, 3063-3068.

172. H. Lin, X. Chang, D. Yan, W.-H. Fang and G. Cui, *Chem. Sci.*, 2017, **8**, 2086-2090.

173. S. Maity, S. S. Ray, A. Chatterjee, N. Chakraborty and J. Ganguly, *ChemistrySelect*, 2018, **3**, 6575-6580.

174. G. T. Hanson, T. B. McAnaney, E. S. Park, M. E. Rendell, D. K. Yarbrough, S. Chu, L. Xi, S. G. Boxer, M. H. Montrose and S. J. Remington, *Biochemistry*, 2002, **41**, 15477-15488.

175. M. Cotlet, J. Hofkens, F. Köhn, J. Michiels, G. Dirix, M. Van Guyse, J. Vanderleyden and F. C. De Schryver, *Chem. Phys. Lett.*, 2001, **336**, 415-423.

176. O. Vendrell, R. Gelabert, M. Moreno and J. M. Lluch, *Chem. Phys. Lett.*, 2004, **396**, 202-207.

177. D. K. Rana, S. Dhar, A. Sarkar and S. C. Bhattacharya, *J. Phys. Chem. A*, 2011, **115**, 9169-9179.

178. D. Stoner-Ma, E. H. Melief, J. Nappa, K. L. Ronayne, P. J. Tonge and S. R. Meech, *J. Phys. Chem. B*, 2006, **110**, 22009-22018.

179. S. Ghosh, J. Thomas, W. Huang, Y. Xu and W. Jäger, *J. Phys. Chem. Lett.*, 2015, **6**, 3126-3131.

180. C.-C. Hsieh, P.-T. Chou, C.-W. Shih, W.-T. Chuang, M.-W. Chung, J. Lee and T. Joo, *J. Am. Chem. Soc.*, 2011, **133**, 2932-2943.

181. M. Kondo, I. A. Heisler, D. Stoner-Ma, P. J. Tonge and S. R. Meech, *J. Am. Chem. Soc.*, 2009, **132**, 1452-1453.

182. D. Stoner-Ma, A. A. Jaye, K. L. Ronayne, J. Nappa, S. R. Meech and P. J. Tonge, *J. Am. Chem. Soc.*, 2008, **130**, 1227-1235.

183. O. Vendrell, R. Gelabert, M. Moreno and J. M. Lluch, *J. Am. Chem. Soc.*, 2006, **128**, 3564-3574.

184. M. Chattoraj, B. A. King, G. U. Bublitz and S. G. Boxer, *Proc. Natl. Acad. Sci*, 1996, **93**, 8362-8367.

185. I. Serdiuk and A. D. Roshal, *Dyes Pigm.*, 2017, **138**, 223-244.

186. B. Jiang, C.-G. Yang, W.-N. Xiong and J. Wang, *Bioorg. Med. Chem.*, 2001, **9**, 1149-1154.

187. R. Goel, V. Luxami and K. Paul, *RSC Adv.*, 2014, **4**, 9885-9892.

188. R. G. Parr and W. Yang, *J. Am. Chem. Soc.*, 1984, **106**, 4049-4050.

189. H. H. Freedman, *J. Am. Chem. Soc.*, 1961, **83**, 2900-2905.

190. R. M. Silverstein and G. C. Bassler, *J. Chem. Educ.*, 1962, **39**, 546.

191. C. F. Matta, J. Hernández-Trujillo, T. H. Tang and R. F. Bader, *Eur. J. Chem.*, 2003, **9**, 1940-1951.

Annex

Determination of Binding constant

The binding constants of compounds for the different analyte are determined using the following Benesi-Hildebrand equation

$$\frac{1}{I - I_0} = \frac{1}{K_a(I_{max} - I_0)[C]^n} + \frac{1}{I_{max} - I_0}$$

Where I_0, I, and I_{max} are the absorption/emission intensities of the compound in the absence of an analyte, at an intermediate analyte concentration, and a concentration of complete interaction with analyte respectively. K_a is the binding constant, C is the concentration of the analyte, and n is the number of analytes bound per compound molecule.

An example is demonstrated here to determine the binding constant

1. First, an absorption/emisison peak is selected, where does the change occurs with respect to addition of analyte.
2. We proceed with intensity and concentration data at selected wavelength.

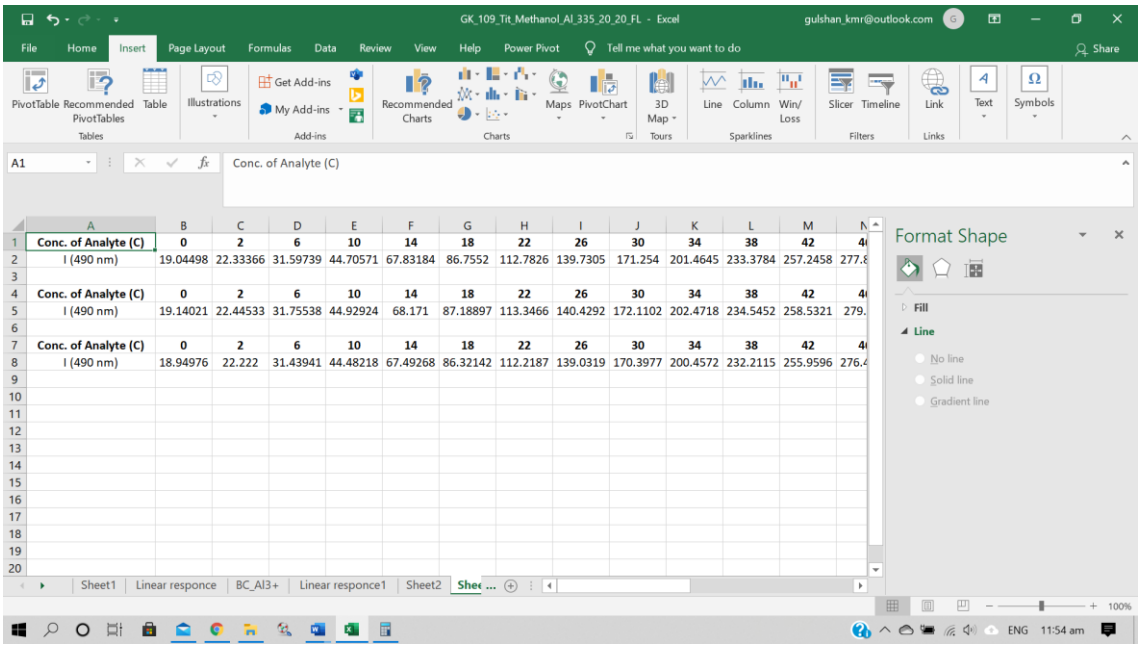

3. Then we calculate the reciprocal of concentration and ($I-I_0$).

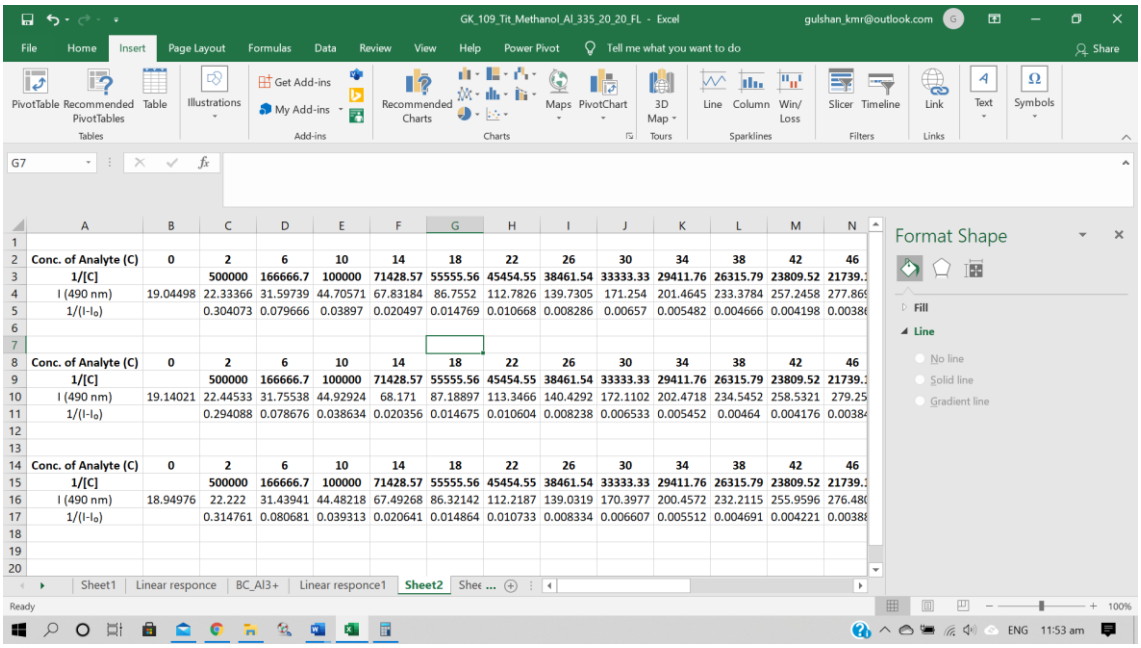

4. Plot the graph between the reciprocal of concentration and ($I-I_0$) and draw the trendline with linear fitting.

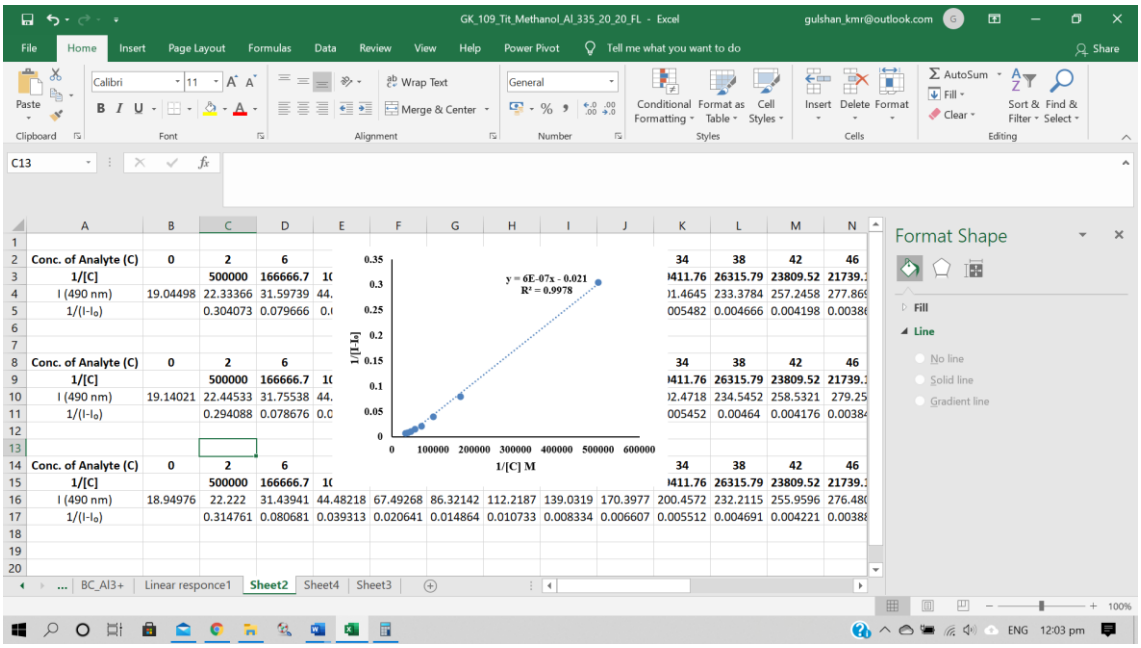

The slope and intercept for linear fitting can be obtained by using slope and intercept formula in excel.

5. The ratio of intercept and slope present the Benesi-Hildebrand association constant. e.g. in this example association constant will be $3.5 \times 10^4\ M^{-1}$.

List of Publication, conferences and workshop

Publications

1. **Kumar, G.**; Rani, R.; Paul, K.; Luxami, V., Single molecular platform displaying PET and hydrolysis sensing mechanism for differential detection of metal ions. *J. Photochem. Photobiol., A* 2019, **380**, 111845.
2. **Kumar, G.**; Paul, K.; Luxami, V., Aggregation induced emission-excited state intramolecular proton transfer based "off-on" fluorescent sensor for Al^{3+} ions in liquid and solid state. *Sens. Actuators, B* 2018, **263**, 585-593.
3. **Kumar, G**.; Goel, R.; Paul, K.; Luxami, V., Investigation of rotameric conformations of substituted imidazo-[1, 2-a] pyrazine: experimental and theoretical approaches. *RSC Adv.* 2018, **8**, 9707-9717.
4. **Kumar, G.**; Gupta, N.; Paul, K.; Luxami, V., Acrylonitrile embedded benzimidazole-anthraquinone based chromofluorescent sensor for ratiometric detection of CN^- ions in bovine serum albumin. *Sens. Actuators, B* 2018, **267**, 549-558.
5. **Kumar G.**; and Luxami, V., Deciphering the excited state intramolecular charge-coupled double proton transfer in an asymmetric quinoline-benzimidazole system. *New J. Chem.*, 2020, **44**, 12866-12874
6. **Kumar G.**; Paul, K., and Vijay Luxami, Dual-channel ratiometric recognition of Al^{3+} and F^- ions through an ESIPT-ESICT signalling mechanism (Spectrochim. Acta A, 2021, **247**, 119112)
7. **Kumar G.**; and Luxami, V., Excited-state intramolecular proton transfer in C_2 symmetrical bis(diphenylmethylene)hydrazine-based Schiff bases (Under preparation)
8. **Kumar, G.**; and Vijay Luxami, Supremacy of charge transfer over proton transfer in symmetrical bis(diphenylmethylene)hydrazine-based Schiff base (Manuscript prepared)
9. **Kumar G.**; Paul, K.; and Luxami, V., Excited state intramolecular proton and twisted charge transfer mechanism for dual emission of naphthalimide based Schiff base (Under preparation)
10. **Kumar, G.**; Rani, R.; Paul, K.; Luxami, V., Donor–π–acceptor (D–π–A) dyad for ratiometric detection of Hg^{2+} and PPi. *New J. Chem.* 2018, **42**, 12729-12736.
11. **Kumar, G.**; Puri, P.; Paul, K.; Luxami, V., Self-agglomerated crystalline needles harnessing ESIPT and AIEE features for the 'turn-on' fluorescence detection of Al^{3+} ions. *New J. Chem.* 2018, **42**, 18550.

12. Gupta, A. S.; **Kumar, G.**; Paul, K.; Luxami, V., BINOL-based differential chromo-fluorescent sensor and its application in miniaturized 1-2/4-2 bit encoders and decoders. *New J. Chem*. 2018, **42**, 2491-2497

13. Rani, R.; **Kumar, G.**; Paul, K.; Luxami, V., Thiazolidine based differential chromo-fluorescent sensor for Cu^{2+} and CN^{-} ions: Elaboration as logic devices. *J. Lumin.* 2016, **180**, 292-300.

14. Dhiman, S.; **Kumar, G**., Luxami, V.; Singh, P.; Kumar, S., A stilbazolium dye-based chromogenic and red-fluorescent probe for recognition of 2,4,6-trinitrophenol in water. *New J. Chem.*, 2020, **44**, 10870-10877.

15. Dhiman, S.; Ahmad, M.; Singla, N.; **Kumar, G**., Singh, P.; Luxami, V.; Kaur, N.; Kumar, S., Chemodosimeters for optical detection of fluoride anion. *Coord. Chem. Rev.* 2020, **405**, 213138.

Conferences and Workshops

1. **Virtual Conference**: "Organic optoelectronic sensors for biomedical applications" Mangalayatan, Aligarh & Himalayan University, Itanagar, 27th June 2020.
2. **Virtual Conference**: "Photochemistry Spotlight-2020"
3. **Virtual Conference**: "Metabolomics approaches for the development of newer biomarkers" Sharaad Chandra Pawar College of Pharmacy, Pune; 6th June 2020.
4. **Poster presentation:** "An asymmetric quinoline-benzimidazole system undergoing intramolecular charge-coupled double proton transfer in the excited state" Gulshan Kumar, and Vijay Luxami; 3rd Asian Conference on Chemosensors & Imaging Probes (AsianChIP-2019), at Guru Nanak Dev University, Amritsar- Punjab, Nov 2019.
5. **Poster presentation:** "A quinoline-benzimidazole-based system undergoing intramolecular charge transfer and relay double proton transfer system in the excited state" **Gulshan Kumar**, and Vijay Luxami; *Recent Trends in Chemical and Environmental Science 2019" at Punjabi University, Patiala,* Feb 2019 (**Best Poster award**).
6. **Poster presentation:** "Investigating excited state intramolecular double proton transfer of 8-(1H-benzo[d]imidazol-2-yl) quinolin-7-ol for dual emission" **Gulshan Kumar**, and Vijay Luxami; *Frontier in chemical sciences-2018, at IIT Guwahati, Dec 2018.*

7. **Poster presentation:** "Excited state intramolecular proton transfer of azine-linked probe for detection of Fe^{3+} ions*"* **Gulshan Kumar**, Kamaldeep Paul, and Vijay Luxami; *National Conference on Chemical and Environmental science: Innovation and advances 2018" at Punjabi University, Patiala, Feb 2018.*
8. **Poster presentation:** "Turn-on fluorescent sensor with aggregation-induced emission and excited state proton transfer for detection of Al^{3+} and CN^{-} ions*"* **Gulshan Kumar**, Kamaldeep Paul, and Vijay Luxami; *The 21st CRSI National Symposium in Chemistry (CRSI-NSC-21)" at IICT Hyderabad, July 13, 2017.*
9. **Poster presentation:** "Conformational Analysis of Phenol Substituted Imidazo-[1,2-a]pyrazines*"* **Gulshan Kumar**, Kamaldeep Paul, and Vijay Luxami; *Impact of pharmaceutical biotechnology on the future of medicine" at Geetanjali University, Udaipur, March 24-25, 2017*
10. **Attended:** National workshop on "Single Crystal Structure Determination of Small Molecules" at *Panjab University, Chandigarh Nov. 20-21, 2018*
11. **Attended:** National workshop on "Advanced Materials and Characterization Techniques" at *NIT Jalandhar, 2015, June 1-7, 2015*